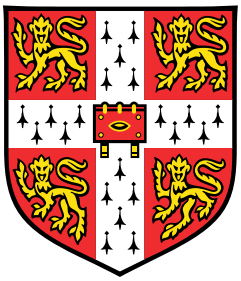

Simulations of Nanoparticle Synthesis in Laminar Stagnation Flames

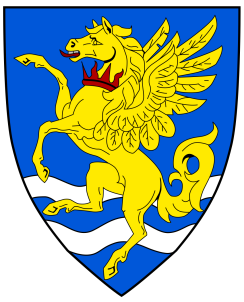

Eric James Bringley

Department of Chemical Engineering and Biotechnology
University of Cambridge

This dissertation is submitted for the degree of
Doctor of Philosophy

Robinson College

March 2021

To my friends and family, all of whom I would be lost without.

Declaration

I hereby declare that except where specific reference is made to the work of others, the contents of this dissertation are original and have not been submitted in whole or in part for consideration for any other degree or qualification in this, or any other university. This dissertation is my own work and contains nothing which is the outcome of work done in collaboration with others, except as specified in the text and Acknowledgements.

This dissertation contains approximately 36,000 words, 73 figures and 8 tables. Some of the work in this thesis has been published or submitted for publication:

1. Jochen A.H. Dreyer, **Eric J. Bringley**, Manoel Y. Manuputty, Jethro Akroyd and Markus Kraft (2021). Temperature and CH* Measurements and Simulations of Laminar Premixed Ethylene Jet-Wall Stagnation Flames. *Proceedings of the Combustion Institute*, 38(2):2083-2091. doi:10.1016/j.proci.2020.06.106.

2. **Eric J. Bringley**, Manoel Y. Manuputty, Casper S. Lindberg, Gustavo Leon, Jethro Akroyd and Markus Kraft. Simulations of TiO_2 nanoparticle synthesised off-centreline in jet-wall stagnation flames. *In Preparation*.

Other works not presented in this thesis include:

1. Gustavo Leon, Jacob W. Martin, **Eric J. Bringley**, Jethro Akroyd, and Markus Kraft (2021). The role of oxygenated species in the growth of fullerenes and graphene. *Carbon*, 182:203–213. doi:10.1016/j.carbon.2021.05.052.

2. Jiaru Bai, Rory M Geeson, Feroz Farazi, Sebastian Mosbach, Jethro Akroyd, **Eric J. Bringley**, and Markus Kraft (2021). Automated calibration of a poly(oxymethylene) dimethyl ether oxidation mechanism using knowledge-graph technology. *Journal of Chemical Information and Modeling*, 61(4):1701–1717. doi:10.1021/acs.jcim.0c01322.

3. Gustavo Leon, Angiras Menon, Laura Pascazio, **Eric J. Bringley**, Jethro Akroyd, and Markus Kraft (2021). Kinetic Monte Carlo statistics of curvature integration by HACA growth and bay closure reactions for PAH growth in a counterflow diffusion flame. *Proceedings of the Combustion Institute*, 38:1449–1457. doi:10.1016/j.proci.2020.06.352.

4. Manoel Y. Manuputty, Jochen A.H. Dreyer, Yuan Sheng, **Eric J. Bringley**, Maria Botero, Jethro Akroyd and Markus Kraft (2019). Polymorphism of nanocrystalline TiO_2 prepared in a stagnation flame: Formation of TiO_2-II phase. *Chemical Science*, 10:1342–1350. doi:10.1039/C8SC02969E.

5. Andrew D. McGuire, Sebastian Mosbach, Gavin Reynolds, Robert I. A. Patterson, **Eric J. Bringley**, Nick A. Eaves, Jochen Dreyer, and Markus Kraft (2019). Analysing the effect of screw configuration using a stochastic twin-screw granulation model. *Chemical Engineering Science*, 203:358–379. doi:10.1016/j.ces.2019.03.078.

Eric James Bringley
March 2021

Simulations of Nanoparticle Synthesis in Laminar Stagnation Flames

Eric James Bringley

A new implementation of a multidimensional solver for studying nanoparticle synthesis in laminar flames is presented. The governing equations are convective-diffusive-reactive partial differential equations that are discretised using the finite volume method. Detailed chemical source terms and transport coefficients are used to close the equations. The implementation of these governing equations is discussed and the numerical algorithm used to solve them is presented. The new solver is verified against analytic solutions and numerical solutions from 1D models for counterflow diffusion flames.

The new solver was used to calculate the flame location, shape and temperature of laminar premixed ethylene jet-wall stagnation flames when the equivalence ratio, exit gas velocity and burner-plate separation distance are varied. The simulation results were compared to new experimental 2D measurements of CH* chemiluminescence and temperature. The 2D simulations showed excellent agreement, and correctly predicted the flame shape, location and temperature as the experimental conditions were varied.

The new solver was used to study growth of inorganic nanoparticles in premixed, jet-wall stagnation flames. Titanium dioxide, also known as titania and TiO_2, is a white powder than has many uses as a pigment, including in paper and cosmetics, and was selected as the system to apply the new solver. TiO_2 nanoparticles formed from titanium tetraisopropoxide (TTIP) were simulated using a two step methodology, which enabled insight into the variations of particle properties as a function of the deposition radius. Two different TTIP loadings (280 and 560 ppm) were studied in two flames, a lean flame (equivalence ratio, $\phi = 0.35$) and a stoichiometric flame ($\phi = 1.0$). First, the growth of particles was described with a spherical particle model fully coupled to the conservation equations of chemically reacting flow. Second, particle trajectories were extracted from the 2D simulations and post-processed using a detailed particle model solved with a stochastic numerical method. The simulation produced gas phase predictions of flame location that are in good agreement with available literature. The particle morphologies and size distributions were examined and found to be dependent on the deposition radius. Particles began to have different size distributions at a deposition radius of approximately one and a half times the nozzle radius (1.0 cm), which should be kept in mind when synthesising and modelling nanoparticles for novel applications. This coincided with the growth of total residence time along particle trajectories. It is suggested that experiments critically examine the radially uniformity of deposited particles do not affect the performance for their intended application.

Acknowledgements

This work would not have been completed without the guidance I received, professional and personal, encouraging and demanding, from numerous advisers. The first thanks goes to the CoMo Trinity: To Markus Kraft, the Chaos: you were tough, you were unpredictable, and you pushed hard, but only because you demanded the best of us. Thank you. To Jethro Akroyd, the Order: you have been a role model and an important lifeline during my time here; I owe you more gratitude than I could ever express. To Sebastian Mosbach, the Truth: I owe you a great deal of thanks for your guidance on the vast array of technical problems I faced over the years. Additional gratitude is extended to Paul Griffiths, whose unwavering support and encouragement helped me successfully complete this degree to the best of my abilities.

I would like to acknowledge Jochen A.H. Dreyer and Manoel Y. Manuputty for their experimental work that was a vital source of comparison. Without their expertise, data, and insight, this work would have been incomplete.

A special thanks must be said to all the members of the CoMo group, past, present and adopted, whose company made many long, painful and frustrating days in the office not just bearable, but truly enjoyable.

There are several groups of people to thank for keeping me busy (read: sane) outside the office. First, there are all the friends who I have created countless memories with - here's to all the boardgames, badminton, tichu and gatherings. Second, the Robinson College community, whose many MCR and academic events created a community that I could call home. Lastly, the Newnham $11^{th}/9^{th}$ Explorers, both kids and adults, who kept me smiling.

Words will fail and yet I will try: Most thanks and gratitude must be extended to the family that crafted me into who I am. Mom, Dad, Alex, distance was no match when it came to feeling your love and support. And to Kaitlin, whose daily love, support, and patience makes me a better man.

Lastly, I would like to acknowledge the Gates Cambridge Foundation who provided funding through the Gates Cambridge Scholarship (OPP1144) to make this opportunity possible.

Table of contents

List of figures

List of tables

Chapter 1

Introduction

This chapter presents the motivation, the novelty, and the structure of the thesis.

1.1 Motivation

Nanoparticles and functionalised materials are an ever-growing field of study with a wide body of applications. Inorganic nanoparticles have found applications in batteries [227], photovoltaics [97, 121], and catalysis amongst other fields. At the industrial level, production of inorganic materials is accomplished using continuous processes of fluidised bed reactors [121] and flame aerosol synthesis [284].

Titanium dioxide, TiO_2 or titania, is one of the most important inorganic materials and is frequently produced industrially by flame aerosol synthesis. It is a white powder that is used as a pigment in many industries including paper, cosmetics and food [121]. The synthesis conditions have been shown to influence the particle properties. The properties that are of interest are particle size, polydispersity, morphology, composition, and crystallinity. Titania is commonly produced from titanium tetrachloride, $TiCl_4$, and titanium tetraisopropoxide, $Ti(OC_4H_7)_4$ (TTIP). $TiCl_4$ is the source for pigment production while TTIP is used for specialised products.

Different methods are used to study synthesis of inorganic nanoparticles in laboratory settings. Furnace reactors are common bench-top experiments; for example, two-stage furnace apparatus has been used to study sintering [309]. Chemical vapour deposition reactors have been used to study the decomposition rate of TiO_2 gas phase precursors [265]. Premixed stretch-stabilised, jet-wall stagnation flames have been used to synthesise ultrafine TiO_2 [417, 345, 239, 215]. In the flame experiments, the wall (also known as the stagnation surface) is generally either water-cooled [215] or air-cooled [345, 239]. In air-cooled experiments, a rotating surface is sometimes used to control temperature as well as collect nanoparticles [345].

The experimental synthesis of inorganic nanoparticles is complemented by modelling studies to test models under conditions where it is challenging to perform experiments, such as high temperatures and short residence times in flames. Individual processes are studied using *ab initio* calculations or molecular dynamics simulations. For example, the detailed mechanism and thermochemistry of TTIP decomposition has been studied from first principles [47, 48] and the rates of sintering [50] and phase transformations [219] have been studied using molecular dynamics. Modelling the growth of a distribution of nanoparticles is done by solving population balance equations (PBE). The rates of sintering and coalescence have been studied through a bivariate surface area-volume model [310]. Production of TiO_2 can be examined by coupling population balance equations to equations for convection-diffusion-reaction problems, such as in the case of jet-wall stagnation flames [216, 218].

It is convenient to study systems where the dimensionality of the problem can be reduced. The dimensionality of the problem has many forms such as the spatial dimensions, the number of chemical species, and description of the particulate phase. One such method to simplify the problem is to take advantage of symmetry and well defined flow structure of the flame. The reduction of the dimensionality of the problem produces a saving in computational cost. One such reduction is commonly made in literature when studying stagnation flames. The flow of stagnation flames can be approximated using a stream function assumption that is radially independent, thus reducing the azimuthally symmetric system to a one dimensional system that is a function of the axial direction alone [164]. A similar assumption can be made for another common flame apparatus: the freely propagating premixed flame [163]. These 1D approximations have been integral to studying detailed reaction mechanisms of hydrocarbons and have yielded key insights into carbonaceous nanoparticle (soot) formation, for example: [402].

There are many systems that are currently used where the assumptions of one dimensionality are questionable at best [145, 159, 302, for example]. One such example is the flame stabilised on a rotating surface (FSRS) used to study TiO_2 nanoparticle synthesis [345]. The choice to neglect the influence of the rotating surface in the model analysis was justified by arguing that the thin boundary layer created on the rotating surface would not affect the flame. Experimentally, Tolmachoff et al. [345] observed that the flame front location in their experiments was not affected by the rotating surface. A full three dimensional study that included the rotating surface and a one-step chemical mechanism to represent the flame has shown that the entrained flow from the rotating surface changes the chemical environment between the flame front and the stagnation surface [145]. A detailed analysis of the effect that the rotating surface has on nanoparticle synthesis is an open research question. Therefore, it is important to

develop computational tools that are flexible enough to be able to study systems in multiple dimensions with complex geometries.

The **objective of this thesis** is to study nanoparticle synthesis in laminar flow systems in multiple spatial dimensions. The synthesis of titania nanoparticles in stagnation flames is studied to examine how nanoparticles change along the radius of the flame and demonstrate the capability of the newly implemented solver. The difference in how particles grow along different radial streamlines is presented. The methods and solvers developed in this work can be applied to other systems in the future.

1.2 Novelty of the thesis

The following novelties are demonstrated in this thesis:

- New simulations of premixed, jet-wall stagnation flames are compared to new experimental measurements of flame temperature and shape. The experimental parameters tested are the premixed gas equivalence ratio, volumetric flow rate, and burner-surface separation distance. The flame location and shape is assessed using CH* chemiluminescence and compared to experimental chemiluminescence measurements. Thin filament pyrometry is used to calculate the experimental gas phase temperature; the simulations provide detailed multicomponent mixture properties that are used in the energy balance between the gas and filament. The ability of the solver to predict premixed, jet-wall stagnation flames over a wide array of experimental parameters is demonstrated.

- TiO_2 nanoparticle synthesis is studied in two dimensions in premixed, jet-wall stagnation flames. Titanium tetraisoproproxide (TTIP) is used as the particle precursor with two loadings: 280 and 560 ppm. A lean $C_2H_4-O_2-AR$ flame with equivalence ratio, ϕ, of 0.35 and a stoichiometric flame ($\phi = 1.0$) provide the thermochemical environment for conversion of TTIP from the gas phase to the particulate phase. The TiO_2 nanoparticle phase is described by a spherical particle model and solved using the method of moments when coupled to the conservation equations. Lagrangian particle trajectories starting from different burner radii are post-processed using a hybrid particle-number/detailed particle model. The model is able to resolve detailed information about particle morphology by evolving an ensemble of particles. The uniformity of the particles are assessed using particle diameter as a surrogate for particle performance. The particle size distributions are resolved and compared at different deposition radii and shown to differ beyond a deposition radius of 1 cm. This is an important result for experimental studies seeking to use premixed jet-wall, stagnation flames for material synthesis applications.

- It was necessary to develop a numerical solver to be able to study particle synthesis in flames in multiple dimensions. The new implementation of a multidimensional solver for multicomponent convective-diffusive-reactive problems with detailed transport and detailed chemical source terms is presented. This is accomplished by coupling OpenFOAM [343] to the *k*inetics application programming interface [65]. OpenFOAM handles the discretisation of the transport equations using the finite volume method, while *k*inetics handles calculating the mixture properties and the integration of chemical source terms to obtain averaged source terms for the transport equations. The algorithm is presented in full in this thesis. To ensure the implementation is correct, the solver is verified in a term-by-term analysis of its implementation in a series of test systems and compared against the pseudo 1D model for opposed flow diffusion flames.

1.3 Structure of the thesis

The thesis is structured as follows. Chapter 2 presents the background material to contextualise the thesis and its contributions. Chapter 3 describes the model equations, algorithms used, and details regarding the implementation. Chapter 4 demonstrates the use of the implemented models to study stagnation flames while varying three common design parameters: cold gas velocity, nozzle-plate separation distance and the premixed gas equivalence ratio. The simulations are compared to experimental measurements of temperature and CH* chemiluminescence. Chapter 5 studies particle formation in flames using the Method of Moments with Interpolative Closure (MOMIC). Particle trajectories are extracted from the simulation and post-processed using a hybrid particle-number/detailed particle model solved with Monte Carlo methods. The differences in particle formations due to the radial coordinate (along different particle trajectories) is examined for consideration in material synthesis applications. The conclusions and suggestions for future work are presented in Chapter 6. The bibliography and appendices follow thereafter. The appendices contain information relevant to the work, including the method used to design the aerodynamic nozzle and additional experimental details.

Chapter 2

Background

This chapter discusses titanium dioxide characterisation and precursor chemistry, flame synthesis of nanoparticles, modelling of laminar flames, and the construction and numerical solution of population balance equations.

2.1 Titania

Titanium dioxide, also referred to as titania or TiO_2, is a white powder that has many uses as a pigment in many industries including paper, cosmetics and food [121]. TiO_2 is one example of a transition metal oxide that has wide applications in many different fields [240]. Titania has many crystal phases that it can take on and is a subset of the Ti-O family of compounds [264].

Several methods exist to produce TiO_2 including liquid phase methods (e.g. sol-gel [131, 210] or electrodeposition [97]) and gas phase methods (chemical vapour deposition [87, 192, 265], and aerosol synthesis [190]). Industrial production of titania is primarily via aerosol synthesis due to its rapid scaling [121]. During aerosol synthesis routes, TiO_2 particles undergo inception, surface growth, coagulation, sintering and coalescence to create particles of different shapes and sizes.

The following sections discuss particle morphology, TiO_2 crystal phases, gas phase precursor chemistry, and particle dynamics via aerosol synthesis routes.

2.1.1 Morphology

It is necessary to examine particle morphology when discussing nanoparticles due to its effect on physical and chemical properties. Many aerosol nanoparticles are used in semiconductor gas sensors [259, 117] whose sensitivity depends on particle properties including grain size [299], neck morphology [349, 298], surface area to volume ratio, porosity and film thickness [344].

When nanoparticles are dispersed in liquid, they are termed nanofluids [62]. The properties of nanofluids, such as nanofluid thermal conductivity, have been shown to be dependent on TiO_2 nanoparticle shape [254]. Therefore, being able to describe nanoparticle shape and structure is essential to understanding the properties of nanoparticles.

The simplest shape a particle can take is a sphere, which is most common in incipient particles and high temperature growth particles. Aggregate particles are made up of primary particles and can be thought of as overlapping spheres. When there are two primary particles, the particle morphology can be described exactly. The addition of more primary particles (totalling three or more) results in ambiguous shape descriptions [329]; the example of three primaries is used by Sorensen [329]: the aggregate particle may take a rod shape, a triangular shape, or somewhere in between. As the particles grow, they are then described as fractal-like. Although aggregate particles do not satisfy fractal theory (specifically, the primary particles must be monodisperse, in point contact, and approach an infinite number of primary particles to truly be called fractals [329]), they can still be described as fractal-like. The structure of fractal-like particles are self-similar or scale invariant as seen by experiments [113] and simulations [388, 169]. Due to self-similarity, the number of primary particles is equal to the radius of gyration, r_g [153], divided by the monomer radius r_0 to the power of the fractal dimension, D_f, scaled by a scaling factor k_0 [329]:

$$N_p = k_0(r_g/r_0)^{D_f}. \tag{2.1}$$

This relation gives an upper limit to the number of primary particles in an aggregate of a given radius of gyration.

Power law relationships between the size and number of primary particles exist with non-integer exponents of fractal dimensions between 1 and 3 [388]. The mechanism by which particles coagulate uniquely influences the fractal dimension [233]. When particle coagulation is driven by Brownian motion, the particles undergo diffusion limited cluster aggregation (DLCA); the process is as follows: the particles undergo random walks, collide, and stick together [232, 170]. From a wide range of experimental [153, 54], simulated [234, 330, 186, 278] and analytical [328] work, DLCA in three dimensional spaces results in a fractal dimension of 1.78. Another important coagulation mechanism is the ballistic cluster-cluster agglomeration (BCCA) that results in $D_f \approx 1.9$ [234].

A constant fractal dimension does not mean particles have the same shape [136] and additional shape information lies in the particle anisotropy [201]. The eigenvalues of the moment of inertia tensor [101] can be used to describe the principle radii of gyration [41]. These principle radii can be used to calculate the gyration radius and anisotropy of the particle [41]. The DCLA aggregation mechanism has been found to have the largest particle anisotropy [120].

When the primary particles are no longer monodisperse, the value of D_f decreases as the width of the primary particle distribution increases [89].

The use of fractal concepts when describing aerosols [113, 214] contributed to collision rates that account for particle morphology [251, 154]. Fractal particles can also be described by a mobility diameter (or radius) [329]. The mobility diameter of an irregular particle is the equivalent diameter of a sphere experiencing the same drag force [118].

2.1.2 Crystal phase

The crystal structure of inorganic nanoparticles is also essential to understanding the particle properties. Titanium dioxide exists in twelve known crystal phases and three amorphous phases [414]. Crystalline polymorphs of titania exist in distorted octahedron units where Ti^{4+} is coordinated with two to six O^{2-} ions (the one exception is 7-coordinated Ti in Baddeleyite [307]). The most thermodynamically stable phase is rutile. At atmospheric pressure, other metastable phases exist and can be synthesised. These phases include anatase, brookite, TiO_2-B and TiO_2-II. The thermodynamic stability of metastable anatase and brookite in nanosized particles is attributed to their lower surface enthalpies when compared to rutile [291, 256, 414]. Based on calorimetry measurements of nanosized particles, rutile has a surface energy value of $2.2(\pm 0.2)$ J/m^2, brookite $1.0(\pm 0.2)$ J/m^2, and anatase $0.4(\pm 0.2)$ J/m^2 [291].

A size-dependent stability due to effects of bulk and surface energies can be discussed from a thermodynamic point of view [414]. A crossover stability size of 14 to 15 nm was calculated from a simple thermodynamic description of Gibbs free energy during the anatase-rutile transformation in spherical particles [412]. This calculation was consistent with the previous experimental work and prediction of 13 nm [130]. The work was expanded to include brookite where the size dependent stabilities were found to be < 11 nm for anatase, 11-35 nm for brookite, and > 35 nm for rutile [413].

In contrast to the thermodynamic stability, a kinetic stability of phases can exist, where the phase is trapped in a local equilibrium state due to high potential energy barriers for transformation. From classical homogeneous nucleation theory, nucleation of crystal phases have an energy barrier [155]. A metastable phase can precipitate due to possessing a lower nucleation barrier than the nucleation barrier of a more thermodynamically stable phase. This is the rationale for the formation of anatase nuclei present in a supercooled melt [191]. Two examples of kinetically metastable phases are TiO_2-B [347] and TiO_2-II [129].

Recent work has shown the existence of four crystal phases in stagnation flames [215]. Anatase was shown to be favoured over rutile in dilute $C_2H_4-O_2-Ar$ flames [218]. Three size dependent phase transformation models were tested using a detailed particle model solved

using a stochastic method [218]. The hypothesis of a composition-dependent crossover size was found to be in good agreement with the experimental data, but was strongly influenced by the assumptions about initial particle growth. It was concluded that a better understanding of high temperature particle formation is needed to understand flame synthesised crystal phase formation.

2.1.3 Precursor chemistry

The two most common precursors used for the formation of titania are titanium tetrachloride, $TiCl_4$, and titanium tetraisopropoxide, $Ti(OC_4H_7)_4$ (TTIP). A discussion of each precursor is presented below.

Titanium tetrachloride

The oxidation of $TiCl_4$ is an important industrial process. Impure ore can be chlorinated, purified, and then oxidised to produce TiO_2 particles. The oxidation step occurs in a pure oxygen plasma or flame to produce nanoparticles which can be after-treated to achieve the desired product properties [121]. The global oxidation reaction of $TiCl_4$ is written as follows:

$$TiCl_4 + O_2 \rightarrow TiO_2 + 2\,Cl_2. \tag{2.2}$$

The production of chlorine gas is an inhibitor to using $TiCl_4$ in laboratory studies. Despite this, there are several experimental studies that sought to expand the understanding of the oxidation of $TiCl_4$. Hot-wire experiments conducted to explore surface reactions of $TiCl_4$ with TiO_2 films between 673 K and 1120 K found that the reaction proceeds via an Eley-Rideal mechanism: gas phase $TiCl_4$ collides with chemisorbed atomic oxygen [122]. Studies of the kinetics of the global reaction in a hot wall reactor between 973 K and 1273 K found that the rate is first-order in $TiCl_4$ [287]. The global reaction is found to be zeroth-order in O_2 up to a 10-fold excess where it is found to be half-order in O_2 beyond [287]. Pratsinis et al. [287] proposed a mechanism for $TiCl_4$ oxidation that is consistent with the measured rate-orders and activation energy: thermal decomposition and abstraction reactions lead to radical disproportionation reactions; the radials are oxidised by O_2, leading to TiO_kCl_x collision species that can coagulate to form particles. Pratsinis et al. [287] show that this mechanism produces the experimentally observed rate dependencies, but further thermodynamic and kinetic data are needed before detailed simulations are possible. Experiments of $TiCl_4$ were simulated with the overall reaction rates [287] and surface reaction rates [122] that demonstrated the importance of surface reaction to the resulting particle diameter under high $TiCl_4$ concentrations [286].

A first-principles approach was used to create a thermodynamically consistent gas-phase kinetic model for the oxidation of $TiCl_4$ [379, 378]. The model was further expanded with new species and reaction pathways and used to simulate rapid compression machine and plug-flow reactor experiments [380]. The expanded first-principles model was coupled to a population balance model where the particles are described by surface area-volume type space to explore the particle size distribution's temperature dependence in the plug flow reactor [380].

The experimentally derived particle model of Pratsinis and Spicer [286] was compared to the first-principles model of West et al [380] in a turbulent flame and showed that the two models predict different inception locations [235], which was consistent with other studies [5, 315]. A reduced kinetic mechanism [236] based on the detailed mechanism [380] was proposed to simulate $TiCl_4$ oxidation in turbulent methane flames.

Further work towards a first-principles kinetic model for $TiCl_4$ oxidation include reactions with $AlCl_3$ additives [314], expansion of thermal data for hydrogenated species (e.g. $TiCl_3OH$) [346], and recalculation of thermodynamic data using error balanced reactions of species generated algorithmically [49]. A theoretical investigation of surface growth of $TiCl_4$ adsorption on the [110] surface of rutile was found to proceed via an Eley-Rideal growth mechanism [315], which is consistent with previous experimental findings [122]. The results were found to be very sensitive to surface growth rates and a new kinetic model for surface growth was proposed [315]. Further development of $TiCl_4$ decomposition and surface reaction mechanisms, and experimental studies to corroborate them, are still required to better model TiO_2 formation.

Titanium tetraisopropoxide

Titanium tetraisopropoxide (TTIP) is more frequently used in laboratory investigations because it is easier to handle with less corrosive by-products than $TiCl_4$. The global reaction of TTIP decomposition is

$$Ti(OC_3H_7)_4 \longrightarrow TiO_2 + 4C_3H_6 + 2H_2O. \tag{2.3}$$

Studies of chemical vapour deposition of TiO_2 in seeded flows [265] calculated the global rate constant by measuring the formation of C_3H_6. The first-order rate was proposed to be $k = 3.96 \times 10^5 \exp(-8479.7/T)$ s^{-1} [265], which the authors report to be in good agreement with the previously proposed rate of Kanai et al. [157]. At low temperatures ($T < 400$ K), TTIP may not thermally decompose fully [104] and the reaction may be

$$Ti(OC_3H_7)_4 \longrightarrow TiO_2 + 2C_3H_6 + 2C_3H_7OH. \tag{2.4}$$

At low temperatures (380-688 K), TTIP has been shown to undergo gas-phase hydrolysis and produce fine TiO_2 nanoparticles [105]:

$$Ti(OC_3H_7)_4 + 2H_2O \longleftrightarrow TiO_2 + 4C_3H_7OH. \tag{2.5}$$

Equation 2.3 has been used to study TiO_2 formation in high temperature flame environments and was found to be a fair representation [175]. The rate is found to be in good agreement at temperatures higher than 770 K in furnace experiments [370]. Below 800 K, the reaction was found to have a rate constant $k = 99.1\exp(-1972.6/T)$ s^{-1} due to reactions with the wall of the furnace. Wang et al. [370] made the assumption that the reaction only occurs over an 'effective reaction' zone at the constant, peak temperature region of the furnace, neglecting the decomposition during the preheating. This one step model has been widely used in other high temperature TiO_2 studies [21, 216, 352, 407, 421].

Additional experimental work has studied TTIP decomposition to provide insight into important species. Mass spectrometry work in H_2-O_2-Ar flames doped with TTIP on a flat burner identified major species in the TTIP decomposition [316], such as Ti, TiH, TiO, TiOH and $HTiO_2$. Their work showed that the overall rate constant previously proposed by Okuyama et al. [265] was insufficient to describe the consumption of TTIP in these flames and hydrolysis of TTIP was important to accurately describe its consumption [316]. They propose a bimolecular hydrolysis reaction to consume TTIP,

$$Ti(OC_3H_7)_4 + H_2O \longrightarrow \text{products}, \tag{2.6}$$

with a rate constant of $k = 2\times10^{12}\exp(-6.14\times10^{-3}/T)$ mol^{-1} cm^3 s^{-1}, which is in good agreement with their quantum chemistry calculations [316] at the B3LYP/6-311++G(2df,p) functional level of theory. The work proposes that $Ti(OH)_n$ are the major intermediates before the formation of TiO_2 [316].

More recently, measurements of sub-2 nm particles in flames by Biswas and co-workers [370, 102, 371, 372, 35] have yielded insights into TTIP decomposition. A Half Mini differential mobility analyser was used to measure sub-2 nm particles in a furnace [370]; the work found good agreement with the global reaction rate proposed by [265] as previously discussed. Through the measurements of charged clusters using atmospheric pressure interface time-of-flight (APi-TOF) mass spectrometry in a flat methane flame, identification of charged species $Ti(OH)_4H^+$, $Ti(OH)_3H^+$, and $TiO(OH)_4{}^+$ further supports that $Ti(OH)_4$ is the major decomposition product in TiO_2 particle formation [102]. Additional phenomena were observed from examination of charged clusters: chemi-ionisation can play a principle role in initial stages of particle formation; intermediate organic species, $Ti_nO_xC_yH_z$, may form before complete TTIP conversion;

in addition to $Ti(OH)_4$, $TiO(OH)_4$ and $TiO_2(NO_3)_3^-$ are the most stable negatively charged monomeric Ti species; and CH_2 abstractions dominate hydrocarbon removal in positively charged precursor clusters [102]. Their work asserts that larger Ti complexes need to be included when working towards a complete TTIP decomposition mechanism [102].

C_3H_6 may not always be the main hydrocarbon decomposition product from TTIP. Gas phase mass spectra from chemical vapour deposition experiments of TTIP have provided additional insight into the gas phase intermediates at low temperatures [36]. The mass spectra by Blackburn et al. [36] provides evidence for the formation of isopropanol in atmospheric CVD at 873 K. In ethanol spray flames, acetone has been observed via mass spectrometry, but the authors acknowledge that it is uncertain as to whether this is a direct byproduct of TTIP decomposition or is produced afterwards in the flame [123].

A detailed kinetic mechanism to describe the decomposition of TTIP was developed by utilising first-principles calculations to calculate rate constants [48] and thermochemistry [47]. Three main reaction pathways, motivated by an analogy to isopropanol decomposition [150], were proposed to produce $Ti(OH)_4$: a step-wise release of C_3H_6, CH_3 radical abstraction followed by hydrogen-abstraction, and hydrogen-abstraction followed by C_3H_6 release [48]. The production of $Ti(OH)_4$ as the final species was consistent with findings available at the time [316] as well as the later experimental work of Fang et al. [102].

Discrepancies between ignition delay measurements [2] and predictions [48] indicate that the detailed mechanism does not capture all of the important reaction pathways. An additional reaction pathway of C_3H_6O abstraction to produce less deoxygenated species (e.g. TiO) has been proposed [100], but no kinetic data currently exists for the proposed model. The presence of acetone in ethanol spray flames with TTIP [123] supports the need to explore this route further. Additionally, the observations about chemi-ionisation and intermediate organic species, $Ti_nO_xC_yH_z$, may be important to describing the decomposition of TTIP [102]. These are examples of areas where the precursor chemistry and TiO_2 formation can be studied further.

2.1.4 Particle dynamics

TiO_2 particles undergo aerosol particle dynamics and their growth can be described by a population balance equation. The evolution of the particle size distribution is controlled by the relative rates of competing processes including inception, surface growth, coagulation, coalescence and sintering. The rates are influenced by kinetic parameters including the temperature [147, 12], pressure [421], and precursor concentration or loading [12, 421]. Additionally, other experimental design parameters will influence the particle size distribution and particle properties including burner configuration [403, 424], dopants [3, 188], or external fields [161, 156] due to their complex effect on temperature, residence time and/or the chemical environment.

The physical phenomena are discussed in this section, while the construction and methods to obtain solutions of the population balance equations are discussed in Section 2.4. The particle models presented in Section 3.3 outline the detailed equations used to simulate particle growth in this thesis.

Inception

After the stable precursor is converted through its oxidation or decomposition pathway to particle precursors, the gas-phase species can transfer to the solid particle phase through inception. Inception creates a monomer, the smallest entity that is considered a solid species. Figure 2.1 shows an example of an inception reaction. A general inception equation can be written as

$$\frac{\partial N(\boldsymbol{\xi},t)}{\partial t}_{\text{IN}} = \sum_{i \in R_{\text{IN}}} I_{i,\boldsymbol{\xi}}, \tag{2.7}$$

where $N(\boldsymbol{\xi},t)$ is the number density of a particle of type $\boldsymbol{\xi}$ at time t and $I_{i,\boldsymbol{\xi}}$ is the i^{th} inception reaction that produces a particle of type $\boldsymbol{\xi}$ in the set of R_{IN} inception reactions. Inception can be a physical process (kinetic reaction or collision limited) or an empirical model, thus the exact form of the rate equation is model dependent. The form of the inception models used in this thesis will be discussed in Section 3.3.

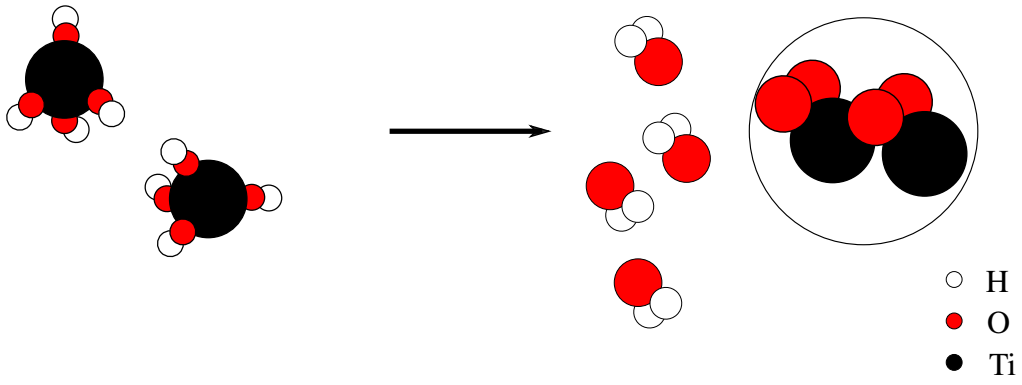

Fig. 2.1 Example of an inception reaction from two $Ti(OH)_4$ molecules that results in the production of a TiO_2 nanoparticle and releases two water molecules to the gas phase.

Coagulation

Coagulation is described by the collision between two particles (particle-particle interaction), leaving them in point contact with one another. Coagulation can be followed by the two primary

particles instantaneously combining into a single particle. The latter is known as coalescence, which frequently happens to small particles or under high temperatures.

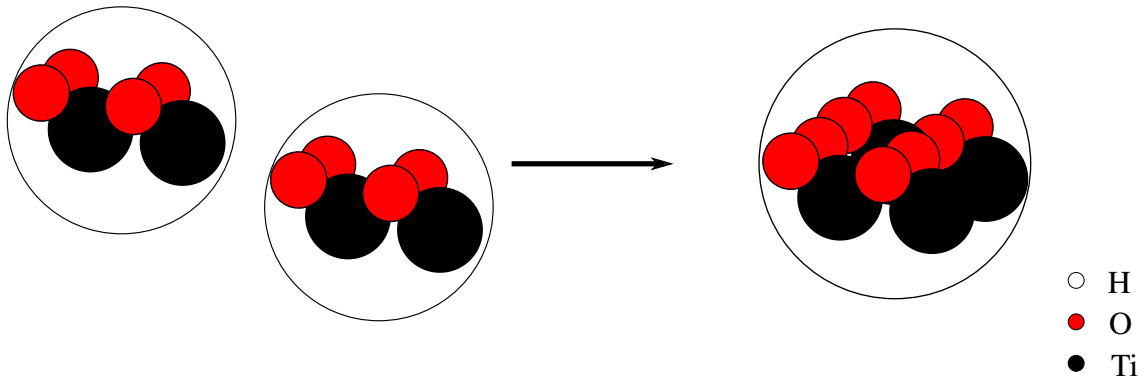

Fig. 2.2 Example of coagulation and coalescence.

The coagulation of particles is described by the Smoluchowski equation [322],

$$\frac{dN(\boldsymbol{\xi},t)}{dt}_{\text{CG}} = \frac{1}{2}\sum_{\boldsymbol{\xi}_2<\boldsymbol{\xi}} \beta(\boldsymbol{\xi}_2,\boldsymbol{\xi}-\boldsymbol{\xi}_2)N(\boldsymbol{\xi}_2)N(\boldsymbol{\xi}-\boldsymbol{\xi}_2) - \sum_{\boldsymbol{\xi}_2\leq\boldsymbol{\xi}} \beta(\boldsymbol{\xi},\boldsymbol{\xi}_2)N(\boldsymbol{\xi})N(\boldsymbol{\xi}_2), \tag{2.8}$$

where the first term is the production of particles of size $\boldsymbol{\xi}$ from particles of size $\boldsymbol{\xi}_2$ and $\boldsymbol{\xi}-\boldsymbol{\xi}_2$ and the second term is the consumption of particles of size $\boldsymbol{\xi}$ from coagulation with particles of size $\boldsymbol{\xi}_2$. Since the particles are assumed to be spherical, instantaneous coalescence occurs upon coagulation of two particles. The coagulation kernel, $\beta(\boldsymbol{\xi}_1,\boldsymbol{\xi}_2)$, maps the number density of a binary pair of particles to their coagulation rates and is dependent on the physical interaction between particles. Possible interactions include gravitational settling, electrostatic potentials, turbulence, and Brownian motion, with only the latter being important in particle synthesis in laminar flames. Different kernels exist for different pressure regimes, and the dimensionless Knudsen number, Kn, aides the classification of the regimes:

$$\text{Kn}(\boldsymbol{\xi}) = \frac{2\lambda_\text{f}}{d_\text{c}(\boldsymbol{\xi})}, \tag{2.9}$$

with

$$\lambda_\text{f} = \frac{\mu}{p}\sqrt{\frac{\pi k_\text{B} T}{2W}}, \tag{2.10}$$

where λ_f is the mean free path of a fluid molecule, W is the average molecular weight, and $d_\text{c}(\boldsymbol{\xi})$ is the particle's collision diameter. Four kernels exist: a continuum regime (CN, $\text{Kn} \leq 0.1$); a slip flow regime (SF, $0.1 < \text{Kn} \leq 1$), a free molecular regime (FM, $\text{Kn} > 10$), and a transition

kernel between slip flow and free molecular (TR, $1 < \mathrm{Kn} \leq 10$). A summary of the four kernels and the range of Kn where they are valid is presented in Figure 2.3.

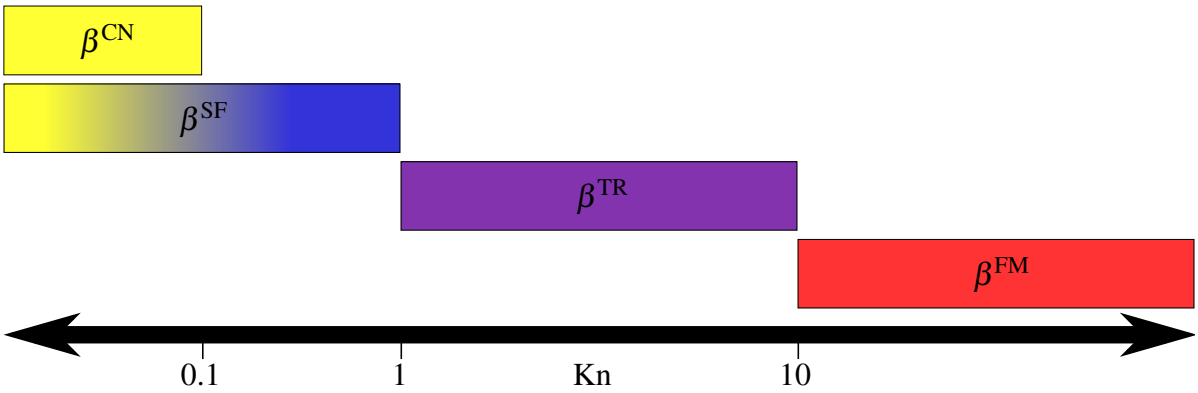

Fig. 2.3 Coagulation collision kernels, β, for the continuum (CN), slip flow (SF), transition (TR), and free molecular (FM) regimes displayed over the range of Knudsen numbers, Kn, for which their equations are valid.

In the continuum regime, the particle size is large when compared to the mean free path of the fluid. Consequently, the particles act as a continuum. This is represented by the yellow region in Fig. 2.3. Coagulation is diffusion-limited and the coagulation kernel in the continuum regime is:

$$\beta^{\mathrm{CN}}(\boldsymbol{\xi}_1, \boldsymbol{\xi}_2) = A^{\mathrm{CN}} \left(d_{\mathrm{c}}(\boldsymbol{\xi}_1) + d_{\mathrm{c}}(\boldsymbol{\xi}_2)\right) \left(\frac{1}{d_{\mathrm{c}}(\boldsymbol{\xi}_1)} + \frac{1}{d_{\mathrm{c}}(\boldsymbol{\xi}_2)}\right), \tag{2.11}$$

and

$$A^{\mathrm{CN}} = \frac{2k_{\mathrm{B}}T}{3\mu}, \tag{2.12}$$

where μ is the viscosity, T is temperature, and k_{B} is the Boltzmann constant.

In the slip flow regime, the particle size approaches the mean free path of the fluid. The diffusion model of the continuum regime is extended to $\mathrm{Kn} = 1$ by applying a correction factor, $C^{\mathrm{SF}}(\boldsymbol{\xi})$. This is represented by the blue-yellow region in Fig. 2.3. The correction factor is defined as:

$$C^{\mathrm{SF}}(\boldsymbol{\xi}) = 1 + A^{\mathrm{SF}}\mathrm{Kn}(\boldsymbol{\xi}), \tag{2.13}$$

$$\beta^{\mathrm{SF}}(\boldsymbol{\xi}_1, \boldsymbol{\xi}_2) = A^{\mathrm{CN}} \left(d_{\mathrm{c}}(\boldsymbol{\xi}_1) + d_{\mathrm{c}}(\boldsymbol{\xi}_2)\right) \left(\frac{C^{\mathrm{SF}}(\boldsymbol{\xi}_1)}{d_{\mathrm{c}}(\boldsymbol{\xi}_1)} + \frac{C^{\mathrm{SF}}(\boldsymbol{\xi}_2)}{d_{\mathrm{c}}(\boldsymbol{\xi}_2)}\right). \tag{2.14}$$

The correction factor preserves the continuum regime kernel in the limit of $\mathrm{Kn} \to 0$. This is noted by the presence of the solid yellow region of the slip flow collision kernel in Fig. 2.3. The

value of A^{SF} parameter depends on the correction factor used. In this work, the Cunningham correction factor [70] with $A^{\mathrm{SF}} = 1.257$ is used.

In the free molecular regime, the particles are relatively small compared to the mean free path of the fluid, which is represented by the red region in Fig. 2.3. The collision rate is calculated using statistical mechanics by averaging over the velocity distribution of the fluid. The free molecular kernel is

$$\beta^{\mathrm{FM}}(\boldsymbol{\xi}_1, \boldsymbol{\xi}_2) = A^{\mathrm{FM}} \varepsilon(\boldsymbol{\xi}_1, \boldsymbol{\xi}_2) \left(d_{\mathrm{c}}(\boldsymbol{\xi}_1) + d_{\mathrm{c}}(\boldsymbol{\xi}_2)\right)^2 \bar{m}(\boldsymbol{\xi}_1, \boldsymbol{\xi}_2)^{-1/2}, \tag{2.15}$$

where $\varepsilon(\boldsymbol{\xi}_1, \boldsymbol{\xi}_2)$ is a size-dependent coagulation enhancement factor due to inter-particle forces, $\bar{m}(\boldsymbol{\xi}_1, \boldsymbol{\xi}_2)$ is the reduced mass,

$$\bar{m}(\boldsymbol{\xi}_1, \boldsymbol{\xi}_2) = \left(m(\boldsymbol{\xi}_1)^{-1} + m(\boldsymbol{\xi}_2)^{-1}\right)^{-1} \tag{2.16}$$

and

$$A^{\mathrm{FM}} = \left(\frac{\pi k_{\mathrm{B}} T}{2}\right)^{1/2}. \tag{2.17}$$

The transition regime handles the transition between the slip flow and free molecular regime ($1 < \mathrm{Kn} \leq 10$), which is represented by the purple region in Fig. 2.3. The kernel is calculated as half of the harmonic mean of the two regimes:

$$\beta^{\mathrm{TR}}(\boldsymbol{\xi}_1, \boldsymbol{\xi}_2) = \left(\frac{1}{\beta^{\mathrm{SF}}(\boldsymbol{\xi}_1, \boldsymbol{\xi}_2)} + \frac{1}{\beta^{\mathrm{FM}}(\boldsymbol{\xi}_1, \boldsymbol{\xi}_2)}\right)^{-1}. \tag{2.18}$$

Surface growth

Surface processes change an existing particle through an interaction with the gas phase. For example, this may occur as a growth of a particle if mass is added (Fig. 2.4) or a shrinkage if mass is released back to the gas phase. Surface processes can be kinetically limited, collision limited, or free-energy controlled. Surface growth has also been shown to be an important process in high temperature TiO_2 particle formation when compared to experimental data [352]. The change to the population from a general surface process (both production and depletion) can be written as

$$\left.\frac{\partial N(\boldsymbol{\xi}, t)}{\partial t}\right|_{\mathrm{SG}} = \sum_{i \in R_{\mathrm{SG}}} S_{\mathrm{SG},i} \left(N(\boldsymbol{\xi} - \Delta\boldsymbol{\xi}_i) s(\boldsymbol{\xi} - \Delta\boldsymbol{\xi}_i) - N(\boldsymbol{\xi}) s(\boldsymbol{\xi})\right), \tag{2.19}$$

where S_i is the i^{th} surface growth reaction that changes a particle by $\Delta\boldsymbol{\xi}_i$ in the set of R_{SG} surface reactions. The form of S_i is model dependent and are discussed in the TiO_2 particle model descriptions in Section 3.3.

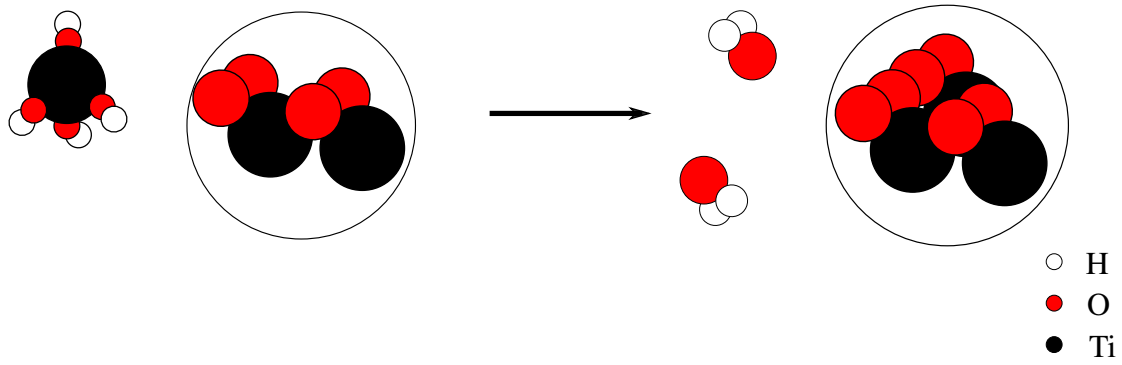

Fig. 2.4 Example of a surface growth reaction from $Ti(OH)_4$ molecules.

Sintering

After the depletion of gas-phase precursor species, the particles can no longer grow by surface growth and the particles instead evolve through coagulation and sintering [91, 90, 79]. Sintering is described by the two primary particles in contact moving closer to each other [200] and is an intra-particle process. An example of this can be seen in Figure 2.5. The primaries begin to merge and a 'neck' is created between them. Sintering of two primary particles can lead to coalescence when the smaller primary is below a critical size. It has two effects on the particles: first, the agglomerate particle size distributions become consistently narrower during sintering; second, the trend for the measured primary particle size distribution varies [310]. Primary particle size distributions are usually obtained by manually counting TEM images where it can be difficult to determine unique primaries [88].

There are many mechanisms that are used to describe sintering. Sintering is driven by the minimisation of free surface energy by eliminating interfaces, grain boundaries, and defects [66]. Sintering of TiO_2 nanoparticles has been studied by several authors [309, 310, 255, 263, 61]. The effect of sintering was studied by classifying, reheating, and reclassifying the particles to measure the reduction in surface area [309]. Different sintering mechanisms were compared with the models based on experiments which studied simultaneous coagulation, surface growth and sintering [309]. The model found to be in best agreement was the surface diffusion model of Kobata et al. [167] based on the expression for the neck size obtained by Hiram and Nir [137]. This phenomenological model is frequently used in modelling studies of TiO_2 [352, 398, 309, 310, 255]. The same study found that carrier gas did not influence TiO_2

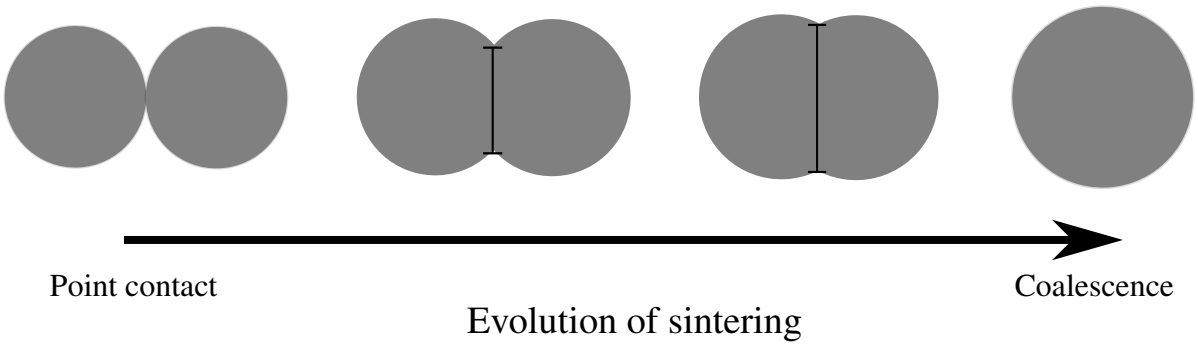

Fig. 2.5 An example of two primary particles sintering from point contact to full coalescence. The necks are shown in black lines.

sintering [309]. Grain boundary diffusion is the dominant mechanism for TiO_2 sintering [9], but for small TiO_2 particles ($r < 5$ nm), surface diffusion has been found to be the dominant sintering mechanism [50].

Molecular dynamic simulations have also been used to investigate sintering of TiO_2. Surface diffusion was found by multiple studies to be the primary mechanism by which sintering takes place [68, 50, 174] which is in contrast to experimental work that suggested grain boundary diffusion is dominant [9]. The simulations of 2-4 nm rutile to full coalescence showed that sintering by grain boundary diffusion takes place to a lesser extent that surface diffusion [50]. Buesser et al. [50] note that surface diffusion could be limited by compacted particles or larger particles which may help explain the conflicting results. Both models have a quartic dependence on particle size, thus late stage sintering was shown to agree well [50] with the commonly used phenomenological model [168].

2.2 Flame synthesis of nanoparticles

The production of nanoparticles using flames is referred to as flame synthesis or flame aerosol synthesis [190]. Both laminar and turbulent flames have been applied to the production of nanoparticles. Some of the advantages of flame synthesis are the high throughputs [342] and the lack of filtering and drying equipment required by wet chemistry methods [285], as well as process continuity and purity of material composition. Flame synthesis of nanoparticles has a very long history, with some of the first uses being the production of carbon black for paints in ancient times. For example, lampblack was produced by burning vegetable oils in oxygen-starved environments and scraping the soot deposits off the surrounding surfaces [355]. The first industrial flame synthesis of ceramic or metal oxide particles was fumed silicon dioxide (silica) [283].

Early work into studying flame synthesised silica particles in a flat-flame burner was completed by Ulrich and co-workers [356, 358, 357] and the production of other metal oxides (including TiO_2) produced in a burner similar to an inverse diffusion flame quickly followed [111]. The prior notion that only nucleation and surface growth dominate the particle size distribution was refuted by Ulrich [356], who suggested that coagulation and coalescence are important factors as well. The work also comments that the influences of ionising additives and electric fields that affected the size distributions will also influence the coagulation rates instead of just the nucleation rate as previously thought [356]. Current experimental work in flame synthesised materials aims to produce novel materials for a wide array of applications including the deposition of catalytic surfaces to serve as dye sensitised solar cells [257, 258], photocatalysts [40, 393] and antimicrobial coatings [74]. Many other works have shown a desirable ability to control properties of flame synthesised nanoparticles by changing experimental design parameters. These parameters include flow rates, burner configuration, precursor concentration, gas composition, dopants and electric fields.

Flame aerosol synthesis is commonly divided into two categories based on the metal oxide precursor feed: vapour-fed aerosol flame synthesis (VAFS) and liquid-fed aerosol flame synthesis (LAFS) [190]. Both VAFS and LAFS are considered gas-gas combustion synthesis because nanoparticles form through reactions of gaseous species [46].

2.2.1 Flame burners

An important aspect of flame synthesis of nanoparticles is the choice of gas flow profile, which is implemented through different gas delivery systems or burner configurations [190]. Different configurations will have different flammability ranges as well as different quenching rates; for example, free jet burners have quenching rates of < 100 K/cm and premixed stagnation burners have quenching rates in excess of 10^4 K/cm [190]. These quenching rates will influence the temperature-residence time profiles, which significantly influences particle formation and growth [350]. A comprehensive review of burner configurations, their properties, and their application was recently completed by Li et al. [190].

Figure 2.6 presents different burner configurations used for studying flame synthesis of metal oxide materials [190]. The first three flame types to be used were coflow diffusion flames (and inverse coflow diffusion flames), McKenna burners and Hencken burners. These three systems operate using a single ‘free jet’ in the laminar regime. The fourth type of laminar burner to be applied to nanoparticles is a counterflow flame which can operate in premixed or non-premixed configurations and has been commonly used by Katz and co-workers [63, 160, 301] as well as Rosner and co-workers [396, 397]. The last ‘free jet’ system is a turbulent system commonly known as flame spray pyrolysis [253]. These systems are unbounded downstream,

which can lead to long exposure to high temperatures and to uncontrolled particle growth [190]. One method to limit the time during which particles can grow is to use a stagnation surface. As seen in Figure 2.6, the laminar flame can be burner stabilised, inner-tube stabilised, divergence-stabilised or swirl stabilised.

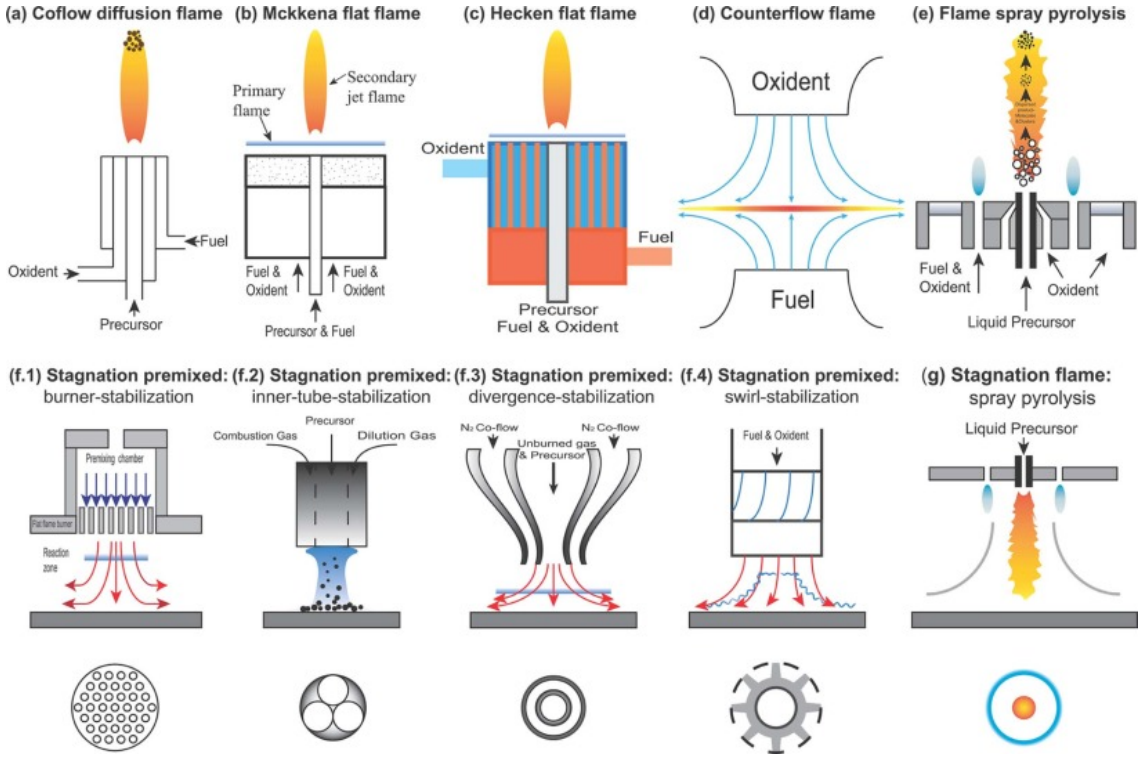

Fig. 2.6 Different burners used in nanoparticle synthesis. Reprinted from Li et al. [190] with permission from Elsevier.

The counterflow apparatus and the wall limited flows are two types of stagnation flames. In the counterflow apparatus, the two opposed jets impinge against each other, creating a stagnation plane which may not always be well defined. This configuration can be operated such that the impinging flows are homogeneous or non-homogeneous. Some of the configurations include a (diluted) fuel stream impinging against an oxidiser stream, two premixed streams, or a premixed and an inert stream. Due to the separation between the flame and the burners, the system is considered adiabatic. Replacing one jet with a wall, thus creating a jet-wall configuration, has some experimental advantages. A reduced amount of gas is needed while a well-defined stagnation surface is created. This surface can be cooled and can act as a heat sink, creating large temperature gradients even to the point of extinction [194]. Fuel and oxidiser are delivered together, thus jet-wall stagnation flames are often referred to as premixed stagnation flames.

Jet-wall stagnation flames

Jet-wall stagnation flames have several advantages when employed to study the fundamental physics of nanoparticle synthesis. First, they are a laminar and stable system with a well-defined stagnation plane. This makes them easy to model, simulate, and study experimentally. Second, they provide short residence times and high temperature gradients between the flame and a cooled stagnation surface. This facilitates narrow nanoparticle size distributions and thermophoretic deposition. Third, changing experimental parameters has been shown to produce nanoparticles with different properties, such as average particle size [202], crystalline phase [202, 215, 218], and oxygen-vacancies [394]. This provides a simple route to produce and test particles with specific properties.

It is generally advantageous to perform experiments where the flow conditions are well defined. One advantage of the jet-wall configuration is that the stagnation plane is well defined. This is contrast to opposed-flow stagnation flames where the stagnation plane is dependent on the balance of two opposing jets, which may not have the same total momentum. The imbalance makes the location of the stagnation plane uncertain in opposed-flow configurations. Will a well defined stagnation plane, the boundary layer can be easily examined. Figure 2.7 shows the radial velocity profiles at different radial points off-centreline. It can be see that the boundary layer at the stagnation surface is less than 1 mm. This thin boundary layer is, therefore, not expected to disturb the flame front.

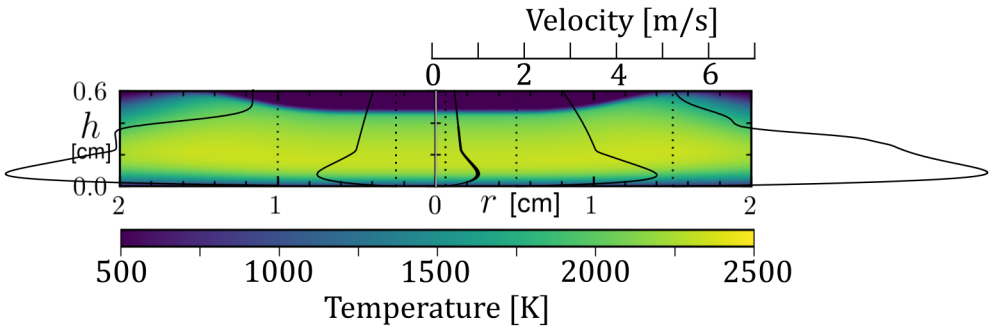

Fig. 2.7 Radial velocity profiles as a function of height above surface, h at different radial locations.

As will be discussed in Section 2.3, the counterflow diffusion flames and premixed stagnation flames can be modelled under an assumed one-dimensional hydrodynamic model [164]. The model uses a streamfunction to describe the flow to eliminate the radial dimension from the transport equations. This reduces the overall computational effort required to describe the flame produced using a detailed reaction mechanism.

Wang and co-workers have demonstrated the use of premixed, jet-wall stagnation flames to produce TiO_2 nanoparticles [417, 418, 345, 239, 257] above a rotating surface (FSRS). The rotating stagnation surface, with the axis of rotation offset 12 cm from the flame centreline, cools the substrate and minimises further particle processes while on the surface. The influence of the stagnation surface is neglected for one-dimensional computational studies because of the minimally thin boundary layer and consistent flame position [345]. The hypothesis is that the rotating surface (and its entrained flow) does not break the one-dimensional hydrodynamic assumption in the 1D model. To assess this hypothesis, the flame must be studied numerically in a full 3D simulation. A step forward has been made where the experimental conditions of Tolmachoff et al. [345] were studied using a simplified chemical mechanism [381] and found that the composition and temperature fields under the flame are significantly affected [145]. The authors highlight differences in deposition time and local thermochemical composition created by streamlines from the sum of thermophoretic and convective velocities, noting that significant differences would exist along different radial streamlines [145], though no particle model is included in the analysis.

Temperature-residence time is a key variable of nanoparticle synthesis and is widely researched [356, 167, 4, 338, 376]. Ulrich [356] discussed that the final particle size was dependent on its temperature and residence time when proposing Brownian growth to dominate particle growth. In addition to particle size, other properties are well known to be affected. The titania phase transformation between anatase and rutile is dependent on the temperature-residence time [167, 4]. The crystal phase and particle size have been shown to be sensitive to the temperature-time histories in a lab-scale, swirl-stabilised tubular reactor that impinges on a stagnation surface [376].

In premixed jet-wall stagnation flames, the nanoparticles produced in the gas phase are collected in a finite area. This area is typically 2 cm in radius but becomes wider if the collection surface rotates during the flame synthesis. The one-dimensional model is unable to describe particles at different deposition radii. For this reason, solving the Navier-Stokes equations is deemed to be necessary. Three dimensional simulations of jet-wall stagnation flames have shown that the total residence time and deposition temperature vary along different particle trajectories depending on their starting inlet radius [145]. In nanoparticle synthesis in burner stabilised stagnation flames, large variation in nanoparticles have been observed at different radii [156]. How the radial variation in the temperature-residence time affects the properties of nanoparticles in jet-wall stagnation flames remains an open question.

2.3 Simulating laminar flames

Simulating nanoparticle synthesis in flames requires descriptions of the thermochemical environment of the flame as well as the nanoparticles themselves. The partial differential equations that govern fluid flow (conservation of mass, momentum, and energy) are generally known as the Navier-Stokes equations. These equations have different closure models for laminar and turbulent conditions, but turbulence is outside the scope of this thesis and will not be discussed. The solution of these PDEs by the finite volume method is commonly known as computational fluid dynamics (CFD).

Laminar flames (and combustion more generally) are one example of chemically reacting flow and are described by convective-diffusive-reactive partial differential equations [281]. Fuel and oxidiser, usually a hydrocarbon species and oxygen, react to produce heat and byproducts on very fast time scales. The incomplete combustion of hydrocarbons produces carbonaceous soot and involves mass transfer from the gas phase to the solid phase. Many different species are produced in the process, including chemi-ions, radicals and numerous isomers that grow with the number of atoms in the molecule. Each species used in the combustion model requires kinetic, thermodynamic and transport data to close its convective-diffusive-reactive PDE. The conservation equations are for mass,

$$\frac{\partial \rho}{\partial t} + \nabla \cdot (\rho U) = 0; \tag{2.20}$$

momentum,

$$\frac{\partial \rho U}{\partial t} + \nabla \cdot (\rho U U) = -\nabla p - \mu \left(\nabla U + (\nabla U)^{\intercal}\right); \tag{2.21}$$

species,

$$\frac{\partial \rho Y_i}{\partial t} + \nabla \cdot (\rho U Y_i) + \nabla \cdot (\rho V_i^{\mathrm{c}} Y_i) = \dot{\omega}_i; \tag{2.22}$$

and energy,

$$c_{\mathrm{p}} \frac{\partial \rho T}{\partial t} + c_{\mathrm{p}} \nabla \cdot (\rho U T) = \nabla \cdot (\lambda \nabla T) - \left(\rho \sum_{i=1}^{N} c_{\mathrm{p}_i} Y_i V_i^{\mathrm{c}} \right) \cdot \nabla T + \dot{\omega}_{\mathrm{T}}; \tag{2.23}$$

where ρ is density, U is velocity, Y_i is the mass fraction of species i, T is temperature, p is pressure, V_i^{c} is the corrected diffusive velocity of species i, $\dot{\omega}_i$ is the rate of formation of species i, $\dot{\omega}_{\mathrm{T}}$ is the enthalpy heat release, μ is mixture viscosity, λ is the mixture thermal conductivity, and c_{p} is the mixture heat capacity.

The following sections aim to discuss the models widely used for solving laminar flames under asymptotic analysis, reduction to one spatial dimension, or models of two or more

spatial dimensions. Each section includes a brief discussion of when and why models of these classifications are popular and major accomplishments or milestones that are enabled through each model.

2.3.1 Asymptotic analysis

In the early days of examining laminar flames, many simplifications were made to allow the solution of the governing equations to become tractable with methods and resources of the time. Notably, these simplifications included assuming steady-state; using single-step, irreversible chemistry with a limited number of species; neglecting physics (such as radiation, Soret and Dufour effects); and using ideal boundary conditions that can neglect some effects (like flame stretch). These assumptions lead to *coupling functions* analysis. Burke and Shumann [52] study a confined coflow diffusion flame using coupling functions to predict flame height. Zeldovich and Barenblatt [411] discussed the importance of finite rate chemistry compared to the assumption of infinitely fast chemistry in the asymptotic models. The analysis showed the flame velocity is dependent on the diffusion and characteristic reaction time [411].

Mixture fractions are another example of coupling functions [387] which, under the assumption of equal diffusivities, can describe species and temperature profiles through the mixing of fuel and oxidiser streams. The mixture fraction, γ, is defined as:

$$\gamma = \frac{Z_i - Z_{i,2}}{Z_{i,1} - Z_{i,2}}, \tag{2.24}$$

where Z_i is the element mass fraction in the fuel stream (subscript 1), oxidiser stream (subscript 2) or locally (no subscript). Mixture fractions are a conserved quantity (as they are not affected by reactions) and thus are described by a transient convective-diffusive equation. With a unity Lewis number assumption (equal mass and thermal diffusivity), negligible radiation, and constant pressure, the total enthalpy can also be described as a linear function of mixture fraction. The mixture fraction approach is a more general example of a coupling function as it does not assume steady flow or single step chemistry as in works by Zeldovich [410]. Mixture fractions are leveraged in 'flamelet' methods [280, 384].

Asymptotic analysis of flames is still used to provide valuable insight into complex systems. For example, the combustion of magnesium aerosol clouds was studied using an asymptotic model based on the combustion behaviour of a single particle by Maghsoudi et al. [212]. The flame consisted of four zones: a preheat region, a liquid magnesium region, a vapourised magnesium region, and a post-flame zone. The analysis resulted in insight into the combustion of these clouds: the flame location is proportional to particle diameter while the flame temperature has an inverse square dependence on particle diameter.

2.3.2 One dimensional models

To explore more detailed physics, model formulations that allowed for more generalised physics were published by many authors ([331, 334, 333, 163–165]). These formulations rely on the flame symmetry to reduce the dimensionality of the governing conservation equations. Early work by Spalding is discussed before two widely used models are presented in detail below.

Spalding introduced a model that examined heat transfer in a coordinate system relative to the flame front [331] and later a model that described flames based on their 'reactedness' [334]. The later formulation was the first that did not rely on describing the flame with a single step reaction, but allowed for an arbitrary reaction mechanism. Dixon-Lewis studied the transport coefficients based on Chapman-Enskog theory for non-polar mixtures and mixtures with one polar component [77], thus introducing the multicomponent transport formulation to the combustion community. Spalding et al. [333] transformed the governing equations for a freely propagating flame into two-dimensional boundary-layer equations. This allowed Spalding et al. [333] to use more physically realistic transport and thermodynamic parameters than in previous literature [204]. These models were solved using fully transient methods (e.g. graphical methods in Spalding [334], ODE integration by Runge-Kutta Methods in Dixon-Lewis [78], and the SIMPLE algorithm [332] in Spalding et al. [333]).

Two more popular models widely used in literature today use a boundary layer approximation to describe the flow. The premixed flame model relies on describing the flame with constant mass flux along the axial direction and neglects any radial effects. The opposed flow flame model reduces the dimensionality of the problem by imposing a stagnation point flow. By changing the boundary conditions in the models, a wide array of laboratory scale flame configurations can be modelled. These models are widely used to predict flame characteristics, such as laminar flame speed [93] or flame front location [374], to assist mechanism development [369, 19], or study particle formation (such as titania [216, 218]) in flames. They allow for an arbitrary level of detail in the thermophysical and reaction models, thus allowing researchers to probe the coupling between these models and flame characteristics. These models are available as commercial codes (Chemkin [292] and *k*inetics [65]) as well as in open-source implementations (Cantera [125]). They have become widely popular due to their associated numerical method that makes them computational tractable: a pseudo-transient assisted Newton search for solving one-dimensional problems with two boundary values [127]. The solution is solved on an adaptive grid which allows for a more accurate solution on a reduced number of grid points and requires a lower computational cost [128].

Premixed flat flames

In premixed flames at steady state, the governing equation for mass is a special case, where the mass flux $\dot{m}''$ is constant along the axial direction z:

$$\dot{m}'' = \rho U_z. \tag{2.25}$$

The pressure variations in the flame are generally small, allowing the velocity to be described as a function of temperature and local composition. Therefore, the momentum equation is generally not needed in this formulation. The resulting species and energy equations are reduced to the following form:

$$\rho \frac{\partial Y_i}{\partial t} + \dot{m}'' \frac{\partial Y_i}{\partial z} + \frac{\partial j_{i,z}}{\partial z} + \omega_i \quad \text{for } i = 1,..,\mathrm{N_{sp}}, \tag{2.26}$$

and

$$\rho c_\mathrm{p} \frac{\partial T}{\partial t} + \dot{m}'' c_\mathrm{p} \frac{\partial T}{\partial z} - \frac{\partial}{\partial z}\left(\lambda \frac{\partial T}{\partial z}\right) + \sum_{i=1}^{\mathrm{N_{sp}}} c_{\mathrm{p},i} j_{i,z} \frac{\partial T}{\partial z} = \sum_{i=1}^{\mathrm{N_{sp}}} h_i \omega_i, \tag{2.27}$$

where Y_i is the species mass fraction, $j_{i,z}$ is the diffusive mass flux and ω_i is the mass rate of formation. Depending on the exact geometry being modelled, the mass flow rate is either fixed as a boundary condition or is solved as an eigenvalue of the solution [165].

Premixed flat flames have been used to study many different fundamental aspects of combustion and aerosol physics. Important properties, like laminar flame speeds [171, 173], species compositions [171], and pressure effects [369], are studied in premixed flat flames. The fundamental physics of soot formation are widely studied in premixed flame flames [276, 405].

Opposed flow stagnation flames

The Navier-Stokes equations in cylindrical coordinates are reduced to a set of one-dimensional ordinary differential equations by applying the stream function of the form [164, 206, 165]

$$\Psi(z,r) = r^2 F(z), \tag{2.28}$$

where z is the axial direction and r is the radial direction. $F(z)$ is the axial component of the stream function which is only a function of the axial coordinate, z. The Navier-Stokes equations are reduced to a set of one-dimensional ordinary differential equations by applying the stream

function assumption [164, 206]. By applying the following transformation variables,

$$F(z) = \frac{\rho u_z}{2}, \text{ and} \tag{2.29}$$

$$G(z) = -\frac{\rho u_r}{r}, \tag{2.30}$$

the mass conservation (continuity) equation becomes the following:

$$\frac{\mathrm{d}F}{\mathrm{d}z} = G(z). \tag{2.31}$$

Assuming the radial pressure-gradient Λ is a constant value (determined by an eigenvalue of the system)

$$\Lambda = -\frac{1}{r}\frac{\partial p}{\partial r}, \tag{2.32}$$

$$\frac{\mathrm{d}\Lambda}{\mathrm{d}z} = 0, \tag{2.33}$$

the axial momentum equation becomes

$$\Lambda - 2\frac{\mathrm{d}}{\mathrm{d}z}\left(\frac{FG}{\rho}\right) + \frac{3G^2}{\rho} + \frac{\mathrm{d}}{\mathrm{d}z}\left[\mu\frac{\mathrm{d}}{\mathrm{d}z}\left(\frac{G}{\rho}\right)\right] = 0. \tag{2.34}$$

The energy and species conservation equations are as follows:

$$2F\frac{\mathrm{d}T}{\mathrm{d}z} - \frac{1}{c_\mathrm{p}}\frac{\mathrm{d}}{\mathrm{d}z}\left(\lambda\frac{\mathrm{d}T}{\mathrm{d}z}\right) + \frac{\rho}{c_\mathrm{p}}\sum_{i=1}^{\mathrm{N_{sp}}} Y_i c_{\mathrm{p},i} V_i^\mathrm{c}\frac{\mathrm{d}T}{\mathrm{d}z} + \frac{1}{c_\mathrm{p}}\sum_{i=1}^{N_\mathrm{sp}} h_i\dot{\omega}_i + \frac{1}{c_\mathrm{p}}\dot{Q}_\mathrm{rad} = 0, \tag{2.35}$$

$$2F\frac{\mathrm{d}Y_i}{\mathrm{d}z} + \frac{\mathrm{d}}{\mathrm{d}z}(\rho Y_i V_i^\mathrm{c}) - \dot{\omega}_i = 0 \quad \text{for } i = 1,\ldots,\mathrm{N_{sp}}. \tag{2.36}$$

This model is implemented in many different commercial [65, 292] and open source codes [125]. It is used frequently in this work for comparison.

The model has been expanded to describe the transport of a dilute particulate phase. For simple particle descriptions, integral values of the distribution can be solved for using the method of moments. The moment transport equation can be solved coupled to the 1D equations. With a univariate, spherical particle model based on particle size, the number density transport equations for particles can be transformed into a smaller set of moment transport equations [280]. Under the stream function assumption, the j^{th} moment transport equation in logarithmic form

is [216]:

$$2F\frac{\mathrm{d}}{\mathrm{d}z}\left(\frac{1}{\rho}\right)+\frac{2F}{\rho}\frac{\mathrm{d}\log M_j}{\mathrm{d}z}+\frac{2}{\rho}\frac{\mathrm{d}F}{\mathrm{d}z}-\frac{2G}{\rho}+V_{\mathrm{T},z}\frac{\mathrm{d}\log M_j}{\mathrm{d}z}+\frac{\mathrm{d}V_{\mathrm{T},z}}{\mathrm{d}z}$$
$$-\frac{1}{M_j}\frac{\mathrm{d}}{\mathrm{d}z}\left[\rho D_{\mathrm{p},1}\frac{\mathrm{d}}{\mathrm{d}z}\left(\frac{M_{j-2/3}}{\rho}\right)\right]-\frac{\dot{\omega}_j}{M_j}=0 \quad \text{for } j=0,\ldots,\mathrm{N_{mom}}-1. \quad (2.37)$$

The definitions of the thermophoretic velocity, V_{T}, and diffusion coefficient of the smallest monomer, $D_{\mathrm{p},1}$, can be found in Section 3.2.1. The exact form of the moment source term, $\dot{\omega}_j$, depends on the model being used; see Section 3.3.1.

The upstream boundary does not always need to be the nozzle inlet, as is the case in the work of Bergthorson and co-workers [29, 28, 25, 361, 373]. This makes the determination of the upstream boundary conditions difficult to determine without extensive effort being devoted to taking velocimetry measurements. This leads some authors to tune the upstream strain G_0 until the flame location matches the experimentally observed flame location. This method has the inherent assumption that the thermochemical model correctly predicts the flame location, which may not always be the case.

2.3.3 Multidimensional models

There are several reasons why higher dimensional descriptions of flames are required. First, not all flames are described by a singular dimension. This includes laminar coflow diffusion flames where the fuel and oxidiser streams are separated and mix through radial diffusion [326, 86]. Second, higher dimensional models do not have as restrictive assumptions as one-dimensional models. Lastly, comparisons can be made against the one-dimensional models to test the assumptions and applicability of the models to experiments.

Two challenges to modelling laminar flames in multiple dimensions are handling the pressure-velocity coupling [363] and the calculation of chemical source terms. The pressure-velocity coupling can be solved by transforming the conservation equations [326, 98, 85] or by devising algorithms to iteratively handle the coupling [271, 148]. The difficulties of chemical source terms are rooted in the nature of combustion having stiff chemistry. Numerical methods, such as operator splitting, are typically used to address this problem and will be discussed in the methods section (Section 2.3.5).

Vorticity-stream function formulation

One example of a transformation is the vorticity-stream function formulation [383] used by Smooke and co-workers [326, 323, 325]. The definition of vorticity is:

$$\omega_v = \nabla \times U. \tag{2.38}$$

The stream function Ψ can be defined as follows:

$$r\rho U_z = -\frac{\partial \Psi}{\partial z}, \tag{2.39}$$

$$r\rho U_r = -\frac{\partial \Psi}{\partial r}, \tag{2.40}$$

where U_z is velocity in the axial direction ($\hat{z}$) and U_r is the velocity in the radial directon ($\hat{r}$). These definitions can be used to transform the Navier-Stokes equations. The advantage of this model formulation is the pressure equation does not need to be solved. The downside of this method is that the vorticity boundary conditions are difficult to describe [295, 326]. The vorticity boundary conditions at walls require additional assumptions, such as a fixed linear gradient at no-slip walls, or integral (non-local) boundary conditions [289, 8].

This model formulation has been widely applied to laminar combustion. For example, Smooke et al. [326] were among the first to study two-dimensional, axisymmetric coflow laminar diffusion flames with full treatment of the elliptic diffusion terms (unlike the previous work where axial diffusion was neglected [244]) using vorticity-stream function formulation [383]. This method was later parallelised to take advantage of more processing power [323, 99] and was shown to converge faster than the SIMPLER algorithm [399]. It has also been used to study counterflowing hydrogen-air flames [348].

Vorticity-velocity formulation

An alternative approach is to use a vorticity-velocity formulation to generalise to the third spatial dimension where the velocity is taken from the Poisson equations [98]. This formulation is solved using the finite difference method. Many improvements were made to these methods, including guidelines to handle the vorticity boundary conditions as well as ensuring mass conservation [85].

Low Mach number approximation

In a low Mach number approximation, the characteristic fluid velocity is small compared to the speed of sound, such that the Mach number, M, is less than 0.1. Under these conditions, the acoustic wave propagation is unimportant to the dynamics of the system [73, 260]. The approach decomposes the total pressure, p, into an ambient pressure, p_0, and a perturbational

pressure field π such that π/p_0 $\mathscr{O}(\mathrm{M}^2)$. The total pressure is replaced in all equations except the momentum equation. The decomposition is as follows:

$$p(\boldsymbol{x},t) = p_0(t) + \pi(\boldsymbol{x},t). \tag{2.41}$$

The decomposition is rooted in a Taylor-series expansion of the pressure where the acoustic changes are related to π [238]. The advantage of this formulation is that a much larger time step can be used. This model is widely used in combustion (e.g. [73, 260]), but is not valid for detonation problems.

Lattice Boltzmann

The lattice Boltzmann method (LBM) [288, 177] is an alternative approach for solving challenging flow problems. The method is rooted in the fundamentals of the kinetic theory of gases, where the moments of a distribution function, $f(\boldsymbol{x},\boldsymbol{\eta},t)$ where $\boldsymbol{x}$ is position, $\boldsymbol{\eta}$ is velocity and t is time, are used to calculate integral properties, such as mass density, or momentum density, depending on the test function used for the moment calculation [177]. The advantages of this method are that it is simple to implement and parallelise as well as being well-suited to handle complex geometries [177]. Additionally, LBM has taken advantage of graphical processing units to simulate the flow of stirred tanks [318].

The application of LBM to combustion is more limited than that of FDM, FEM and FVM. Some important works towards LBM in combustion have been made by Hänel and coworkers [107, 109, 108, 133]. A two phase lattice Boltzmann scheme has been used to simulate droplet combustion [14]. Hybrid methods are sometimes used, where the fluid flow is solved by LBM and the species and energy equations are solved using the FDM [142, 143]. It has recently been used to study coke combustion in porous media [187] and has been expanded to include Stefan-Maxwell diffusion [308]. The lattice Boltzmann method provides an interesting alternative to solving multicomponent and multiphase equations of combustion.

2.3.4 Comparing one- and two-dimensional models

Examining the concept of how well experimental flames hold up to their assumptions of 'flatness' [243] or 'one-dimensionality' [266, 43] is an active research question. Multidimensional studies of flames have assisted these investigations into the applicability of 1D models for burner stabilised, premixed flames (McKenna burners) [172, 402, 55, 209], counterflow flames [246, 151] and jet-wall, stagnation flames [26, 43, 327]. Discrepancies between 1D and 2D models have largely been attributed to differences in the non-uniform pressure curvature [246, 327, 43] because it is assumed to be constant in the 1D model. Flow instabilities

in atmospheric and low pressure McKenna burner flames were studied using particle image velocimetry and two-dimensional simulations, which concluded that diffusive losses of H atoms at low pressures was more important than the diffusive loss of fuel. A study of burner stabilised premixed flames (McKenna burner) by laser absorption spectroscopy and CFD [209] found that temperature and species were radially uniform up to a scaled radius of $r/R_{\max}$ of 2/3 at low height above burners. Ma et al. [209] also found that the flow rates of the premixed gas and coflow had more significant effects than chemical composition on the uniformity. Bergthorson and co-workers [29, 27, 30] have shown that the assumptions made in the 1D model are satisfied if the boundary conditions are specified appropriately after the free-jet region. Bouvet et al. [43] studied a jet-wall, stagnation flame confined by a cooling jacket and also found the 1D simulation was unable to simulate the free-jet due to the non-uniform pressure curvature. Johnson et al. [151] showed that the 1D approach is applicable for counterflow streams from contoured nozzles of greater than 13 mm diameter because of the negligible contribution of radial terms on the momentum and energy equations.

2.3.5 Methods

Many different numerical methods exist to discretise the partial differential equations to solve the convective-diffusive-reactive equations. Among them are the finite difference method (FDM), the finite volume method (FVM), and the finite element method (FEM). All three of these methods are very popular for solving flames and PDEs more generally. The finite volume method and the increase in computational computing power has led to the rise of 'Computational Fluid Dynamics' (CFD), where the Navier-Stokes PDEs are solved using the FVM with a variety of different closure models. Two other methods that are growing in popularity are the lattice Boltzmann method (LBM) and radial basis method (RBM).

An overview of these methods is presented below. These methods, their developments, and their applications are vast. There are numerous textbooks written about these method (e.g. [103, 270, 250]) and this section does not seek to act as a replacement. An additional discussion of the Newton based methods for finding steady state solutions is also presented.

Finite difference

Finite difference methods discretise the domain into a series of points at which the operators of the PDEs are approximated by linear approximations. It can be applied to any type of grid, but is traditionally applied to structured grids [103]. The advantage of the FDM method is that it is simple to implement [270] and can easily be expanded to higher-order schemes on regular grids [103]. The disadvantages of the method is that numerical error can be large,

with conservation not inherently being enforced [103] as well as being subject to numerical diffusion [270].

Because of the finite difference method's simplicity, it has been widely used in modelling of combustion. The aforementioned one-dimensional models for premixed flat flames [163] and opposed flow flames [206] are discretised using FDM and, as such, the applications of FDM to laminar flames are numerous.

Finite volume

The finite volume method discretises the spatial domain into a set of control volumes which is used to solve the fields. Its principles and applications are well covered in many textbooks, such as Versteeg and Malalasekera [363], Moukalled et al. [250], and Ferziger and Perić [103]. The conservation equations are applied to each control volume [103]. The FVM relies on the use of the divergence theorem (or Gauss' Theorem) to express a volume integral as a surface integral:

$$\int_V \nabla \cdot \phi dV = \int_A \mathbf{n} \cdot \phi dA, \tag{2.42}$$

where $\int_V dV$ is a volume integral, $\int_A dA$ is a surface integral, ϕ is an arbitrary vector field, and $\mathbf{n}$ is the normal vector over the surface. The fields are stored at the centre of each control volume and interpolation schemes are used to express variables at the control surfaces. The advantages of the FVM are that it can handle various grid types allowing for complex geometries and that it is conservative by its construction. The disadvantage is that higher order schemes are more difficult to develop for generalised 3D systems with irregular, non-orthogonal grids than in the FDM [103].

The applications of FVM to laminar flames are numerous. It has been used to study different aspects of laminar flames, such as the influence of thermochemistry [197], soot formation [276], and buoyancy effects [402].

Finite element

The finite element method approximates an unknown function over a discretised spatial domain. The equations are multiplied by a weight function before they are integrated over the domain. The advantage of FEM is that it is able to deal with complex and arbitrary geometries. The drawback of this method is that efficient numerical solutions are difficult to achieve with unstructured grids.

The FEM method has been successfully applied to combustion. For example, FEM has been applied to study laminar flame propagation [241, 242] and has been applied by Becker et al. [23] on adaptive grids.

A hybrid method is the control-volume-based finite element method (CV-FEM) [103]. Control volumes are formed around the nodes of the mesh. Because the variables are analytically described (e.g. linear function [72]) from the FEM weight function, the control volume integrals can easily be calculated [103]. The extension to three dimensions has been used in modelling laminar diffusion flames, with a fast convergence algorithm [72].

Radial basis

In the radial basis method, an unknown function is approximated using linear combinations of radial basis functions (RBF) interpolated onto a set of points. The RBFs are selected such that they are infinitely differentiable [51]. It is similar to a finite element method, but is generally considered a meshless method as the RBFs can be used to recast the original partial differential equation in a new form [317, 60]. RBFs have been used to solve the Navier-Stokes equations [1, 53]. The application of RBM for solving laminar flames is sparse. It was used to study laminar flame propagation by Kindelan and Bayona [166]. A RBF-FD method has been described as a natural generalisation of finite difference methods [112]. The most recent application of RBM-FD to micro-combustion was for reactive flows in complex geometries [22]. It is a method that is worth noting due to its recent application to solving detailed population balance equations [6].

Newton-based method considerations

Many methods for solving systems of algebraic equations exist. One method is Newton searches which can be used to solve steady state problems. The method requires calculation of a Jacobian matrix, which is an expensive part of the solution method [325]. Many researchers have sought to speed up the repeated calculation of the Jacobian such as developing sparse, iterative methods [183, 184] or adaptive preconditioning [230].

When one-dimensional models are used with fixed boundary conditions, the model equations are a class of problems known as boundary value problems. Solving this special class of equations led to a modified Newton solver with a psuedo-transient numerical method, known as TWOPNT [127]. In this method, the governing equations are discretised using the finite difference method. An initial guess, such as a flamelet solution solved using simplified transport properties, is supplied and used as the starting point for the damped Netwon search to seek the steady state solution. If a solution cannot be found, the solution is evolved using a transient

solver to advance the initial starting point of the Newton search closer to the true solution before attempting another Newton search.

In order to find a grid-independent solution, the TWOPNT method was solved on an adaptive grid. The criteria for applying grid refinement are based on first and second derivatives of the solution. It was shown that the adaptive grid refinement provides a solution method that is equally as accurate at a lower computational cost than on a fixed grid with a larger number of points [128].

In two spatial dimensions, the use of Newton methods is still possible. The Jacobian in these cases is very sparse, and the system of discretised partial differential equations becomes a system of linear equations. Gaussian elimination becomes intractable, so iterative methods are used.

Methods for chemistry

The inclusion of explicit source terms of stiff reaction chemistry in the transport equations can be challenging. While the low computational cost of explicit calculations of chemical source terms is desired, it can lead to large errors unless appropriate care is taken [249]. For example, in regions where ignition takes place, the chemical source terms are generally very small, but rapidly grow over a short period of time. The reaction rates at both the beginning and end of a time step for ignition are not appropriate for use in the chemical source term of the governing equations.

One method to address this, as is done in OpenFOAM [343], is to integrate the chemistry separately (e.g. with a detailed ODE solver) and average the source term over the time step. The averaged reaction operator can then be used to solve all operators in the convective-diffusive-reactive equation simultaneously. For a flow $\mathscr{F}$ and reaction $\mathscr{R}$ operator, the averaged reaction operator scheme is as follows:

$$\begin{aligned}
\frac{\mathrm{d}\Phi_n}{\mathrm{d}t} &= \mathscr{F}(\Phi_n, x, t) + \mathscr{R}(\Phi_n, t), \\
\frac{\mathrm{d}\Phi^*}{\mathrm{d}t} &= \mathscr{R}(\Phi^*, t), \quad \Phi^*(t_n) = \Phi_n, \\
\tilde{\mathscr{R}} &= \frac{\Phi^*(t_n + \Delta t) - \Phi^*(t_n)}{\Delta t}, \\
\frac{\mathrm{d}\Phi^{**}}{\mathrm{d}t} &= \mathscr{F}(\Phi^*, x, t) + \tilde{\mathscr{R}}, \quad \Phi^*(t_n) = \Phi_n, \\
\Phi_{n+1} &= \Phi^{**}(t_n + \Delta t).
\end{aligned} \tag{2.43}$$

This will provide a more accurate prediction of the source term by using implicit ODE methods to calculate Φ^* while removing the complication of the transport equation. The transport equation Φ^{**} can be discretised using the FVM and solved with linear algebra solvers.

An alternative approach is to use different splitting methods, such as Strang splitting [337], balanced Strang splitting [335], and iterative predictor-corrector approaches [158], to solve the system of stiff differential equations to produce a chemical source term. The operator splitting allows for appropriate numerical methods to be used for each operator. Although operator splitting is a source of error in solving convective-diffusive-reactive problems [336, 71, 335], it is generally required to make the problem more computationally tractable.

One such example of this hard operator splitting method is the chemistry-flow-chemistry Strang splitting scheme in the work by Cuoci et al. [71]. Their operator splitting separates the flow (convection diffusion) operators, $\mathscr{F}$, from the reaction operators, $\mathscr{R}$. Inverting these steps is possible but leads to less accurate solutions [336]. The splitting scheme is presented below for an arbitrary scalar, Φ, over a time step Δt:

$$\begin{aligned}
\frac{\mathrm{d}\Phi^*}{\mathrm{d}t} &= \mathscr{R}(\Phi^*,t), \quad \Phi^*(t_n) = \Phi_n, \\
\frac{\mathrm{d}\Phi^{**}}{\mathrm{d}t} &= \mathscr{F}(\Phi^{**},x,t), \quad \Phi^{**}(t_n) = \Phi^*\left(t_n + \frac{\Delta t}{2}\right), \\
\frac{\mathrm{d}\Phi^{***}}{\mathrm{d}t} &= \mathscr{R}(\Phi^{***},t), \quad \Phi^{***}(t_n + \frac{\Delta t}{2}) = \Phi^{**}\left(t_n + \Delta t\right), \\
\Phi_{n+1} &= \Phi^{***}(t_n + \Delta t).
\end{aligned} \tag{2.44}$$

Another splitting method which aims to reduce error in the steady-state solution was recently published and is known as rebalanced operator splitting [335]. A balanced vector c_n is introduced into each step of the Strang splitting:

$$\begin{aligned}
c_n &= \frac{1}{2}\left[\mathscr{F}(\Phi_n,x,t) + \mathscr{R}(\Phi_n,t)\right], \\
\frac{\mathrm{d}\Phi^*}{\mathrm{d}t} &= \mathscr{R}(\Phi^*,t_n) + c_n, \quad \Phi^*(t_n) = \Phi_n, \\
\frac{\mathrm{d}\Phi^{**}}{\mathrm{d}t} &= \mathscr{F}(\Phi^{**},x,t) - c_n, \quad \Phi^{**}(t_n) = \Phi^*\left(t_n + \frac{\Delta t}{2}\right), \\
\frac{\mathrm{d}\Phi^{***}}{\mathrm{d}t} &= \mathscr{R}(\Phi^{***},t) + c_n, \quad \Phi^{***}(t_n + \frac{\Delta t}{2}) = \Phi^{**}\left(t_n + \Delta t\right), \\
\Phi_{n+1} &= \Phi^{***}(t_n + \Delta t).
\end{aligned} \tag{2.45}$$

This operator splitting has been used for the calculation of extinction rates in counterflow diffusion flames [203].

An alternative formulation called the mid-point splitting method [205] has been proposed for near-limit flame simulations and adopted for a general convective-diffusive-reactive solver, reactingFOAM-SCI [404]. In this formulation, the transport terms are held constant over the time steps:

$$\begin{aligned}
&\frac{\mathrm{d}\Phi^{*}}{\mathrm{d}t} = \mathscr{F}(\Phi_n, x, t) + \mathscr{R}(\Phi^{*}, t), \quad \Phi^{*}(t_n) = \Phi_n, \\
&\frac{\mathrm{d}\Phi^{**}}{\mathrm{d}t} = \mathscr{F}(\Phi_{n+\frac{1}{2}}, x, t_{n+\frac{1}{2}}) + \mathscr{R}(\Phi^{**}, t), \quad \Phi_{n+\frac{1}{2}} = \Phi^{*}\left(t_n + \frac{\Delta t}{2}\right), \Phi{**} = \Phi_n, \\
&\Phi_{n+1} = \Phi^{**}(t_n + \Delta t).
\end{aligned} \tag{2.46}$$

The first step is integrated to the mid-point of the time step $t_n + \Delta t/2$. The second step is integrated over the full time step $(t_n, t_n + \Delta t]$ using the updated transport from the mid-point.

Solving pressure-linked equations

In contrast to transforming the model equations, another approach to handling the pressure-velocity coupling is to solve the pressure-linked equations using guess-and-correct procedures [363]. The two algorithms that dominate computational fluid dynamics are the SIMPLE algorithm (Semi-Implicit Method for Pressure Linked Equations) by Patankar and Spalding [271] and the transient PISO aglorithm (Pressure Implicit with Splitting of Operators) by Issa [148], which can be seen as an additional corrector step on a SIMPLE algorithm. There are many variations of these algorithms in literature, but the details of these are outside the scope of this thesis. The SIMPLE algorithm and the PISO algorithm are easily extended to solve additional transport equations at well-defined points in the algorithm, specifically after the predictor step and before the pressure corrector steps. This allows for the inclusion of multicomponent flow very easily. The PISO algorithm is shown below in Figure 2.8.

2.4 Population balances models and methods

2.4.1 Population balance equations

Population balance equations (PBE) are a means to describing the changes of a population over time and space. Many fields use PBEs including granulation [229], polymerisation [395], crystallisation [267], and multiphase flow [290]. A population is described using internal coordinates (also known as the type space), such as mass or shape, and external coordinates,

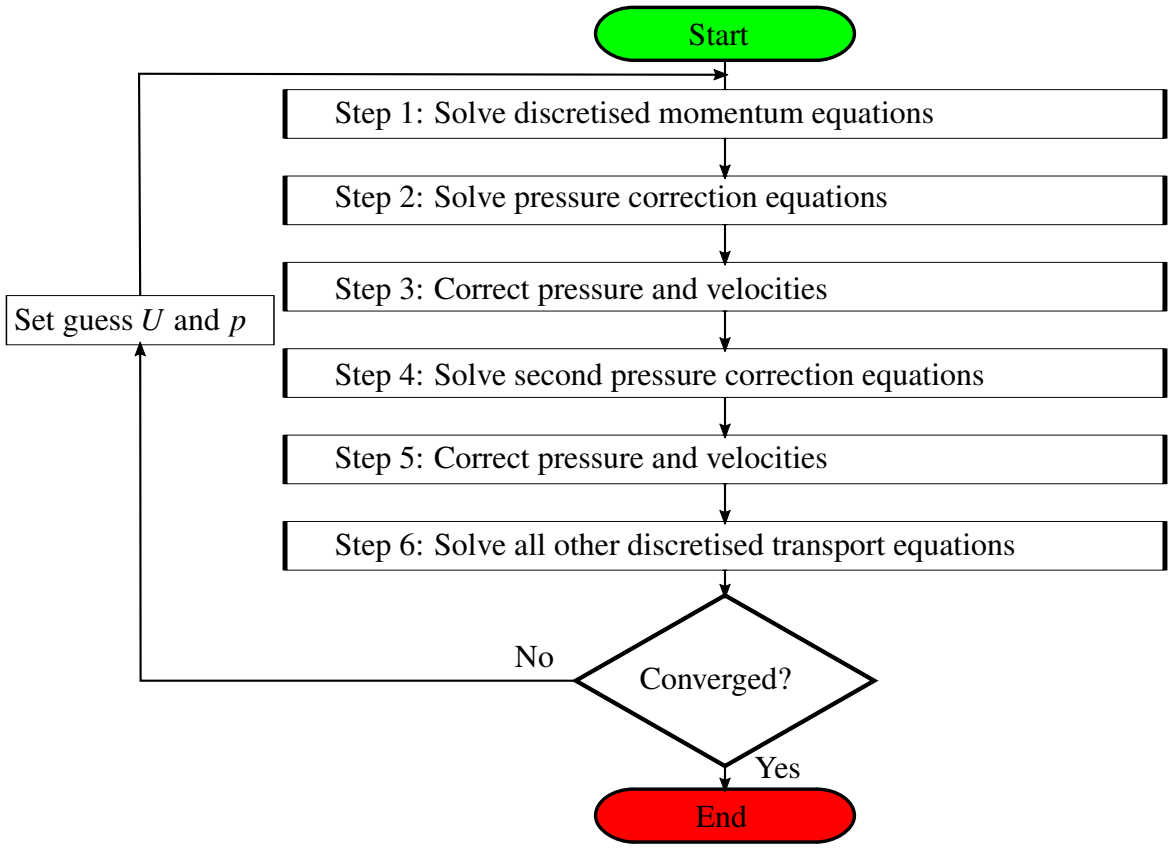

Fig. 2.8 Pressure Implicit with Splitting of Operators (PISO) Algorithm [148].

such as position and time. The choice of internal coordinates and method used to solve the PBE is dictated by the desired level of detail and computational expense. One of the most widely known population balance equations is the Boltzmann kinetic equation for the kinetic theory of gases [58].

As described in Section 2.1.4, titania nanoparticles undergo simultaneous inception, coagulation, surface growth, and coalescence. For an arbitrary internal coordinate $\boldsymbol{\xi}$ and external coordinates $\boldsymbol{\zeta}$, the general population balance equation for the number density of a population N is written as [220]:

$$\frac{\partial N(\boldsymbol{\xi})}{\partial t} + \frac{\partial}{\partial \boldsymbol{\zeta}} \cdot \left(\dot{\boldsymbol{\zeta}} N(\boldsymbol{\xi}) \right) + \frac{\partial}{\partial \boldsymbol{\xi}} \cdot \left(\dot{\boldsymbol{\xi}} N(\boldsymbol{\xi}) \right) = h(\boldsymbol{\xi}). \tag{2.47}$$

The first term is the accumulation over time. The second and third terms are the rates of change from continuous processes in the external and internal coordinates, respectively. The last term corresponds to changes in particle due to discrete events. In the context of TiO_2, surface growth and coalescence are continuous processes and coagulation and inception are discrete

events. Coagulation is described in the TiO_2 (and aerosol particle) synthesis using a generalised Smoluchowski equation [322].

The choice of internal coordinates will determine the exact form of the population balance equations [176]. In the simplest models, the internal coordinate used to describe particles is a single number corresponding to measure size ($\boldsymbol{\xi} = k, k \in \mathbb{R}$) [216, 198]. This is usually expressed in terms of particle mass. Restrictive assumptions, such as constant density or spherical particles, can relate particle size to particle shape. In univariate models, coalescence and particle morphology cannot be studied. The simple models can be easily solved with the method of moments or sectional methods, making them computationally tractable over a wide range of systems from spatially homogeneous to coupled to multi-dimensional flow systems [220]. In this case, the PBE of a spatially homogeneous system can be written as follows:

$$\frac{\partial N(k)}{\partial t} = \frac{\partial N(k)}{\partial t}_{\text{IN}} + \frac{\partial N(k)}{\partial t}_{\text{SG}} + \frac{\partial N(k)}{\partial t}_{\text{CG}}, \tag{2.48}$$

where $N(k)$ is the number density of a particle of size k. The subscripts on the right hand side refer to inception, surface growth, and coagulation. Notably, coalescence is not present in Equation 2.48 because the spherical description of particles cannot capture changes in particle morphology.

A more complex description of particles uses bivariate models, such as the surface-volume models [398, 178]. By considering the particle volume and surface area independently, a non-spherical morphology can be captured. This description is still unable to describe particle properties like primary particle size. The calculation of these properties is only possible when assumptions are made about primary particle size distributions (e.g. monodispersity) and point contact of primaries. An alternative to surface area-volume models is one that describes aggregate size and primary particle size [135].

To capture a more complete description of particle morphology, multivariate models are required. These models can capture an arbitrary level of detail, including descriptions of primary particles, their connectivity, and level of sintering [305, 311, 59, 405, 200]. These models allow for the most physical description of the particles, including crystal phase [218], but these models can be incredibly computationally expensive to solve. These models have been applied to organic (e.g. soot [59, 405]) and inorganic (e.g. silica [305, 311] and titania [200]) nanoparticles.

2.4.2 Moment methods

In the method of moments [146] (MOM), the conditionality of the PBE is reduced by multiplying the PBE by a test function and integrating over the internal coordinates [20]. The test

function usually takes the form of the internal coordinate raised to integer powers. The method of moments is widely used in aerosol science, material science, and cell biology. The result is that the moments of the population are solved for while the particle size distribution (PSD) is unresolved. An infinite number of moments of the PSD exist, but only a subset of these are solved for, usually around six to twelve. Because the number of differential equations is reduced, the method of moments has the advantage of being computationally efficient. This comes at the cost of needing simplified descriptions of particles and an unresolved PSD [224]. The number of internal coordinates is usually limited to one, but a few extensions of these methods exist with a second internal coordinate.

Recovering the particle size distribution from a set of moments is a non-trivial task as there are an infinite set of distributions that can be reconstructed from a small set of moments. The simplest case is when the PSD takes on a distribution shape that is known *a priori*, such as a log-normal distribution [67] or inverse Gaussian distributions [312]. The parameters of the assumed distribution can then be determined from the first few moments. When the distribution shape is not known, continuous approximations of the PSD that preserve a higher number of moments can be used, such as the Spline method [149], adaptive spline-based method [75], the Maximum-Entropy method [231, 340, 224], or the Kernel Density Element Method [15].

Many of the source terms of the model rely on detailed information about the population that is not available, leaving the equations unclosed. Many closure methods exist, including Quadrature methods (Quadrature Method of Moments, QMOM [228]; Direct Quadrature Method of Moments, DQMOM [221]; Conditional Quadrature Method of Moments [408]; Extended Quadrature Method of Moments, EQMOM [409]), Lagrangian interpolation (Method of Moments with Interpolative Closure, MOMIC [116, 115]), hybrid methods [252], and imposed PSD shapes methods [312].

Quadrature-based methods close the moment equations by representing the PSD as a sum of quadratures. The exact representation of PSD by quadratures and how they are calculated is the core of each method. QMOM [228] and DQMOM [221] represent the PSD as Dirac delta functions but differ on how the weights and abscissas are calculated. EQMOM creates a more explicit form of the PSD through a sum of non-negative weight functions [409], which can take on different forms (see references [220], [211] [409], and [279]). The EQMOM inversion has numerical difficulties; the root finding method is not numerically robust and can fail [279, 392]. In other cases, multiple roots exist [211, 279] or the root is highly sensitive to small changes in moment values when reconstructing the PSD [279]. A *split-based* Extended Quadrature Method of Moments [304] has been proposed to address the numerical difficulties of the moment inversion in the original method of Yuan et al. [409]. The particle size distribution is split into a set of overlaying sub-PSDs each with their own PBE. Each PBE is then solved

within a Monte Carlo framework to find the suitability of log-normal, gamma and inverse Gaussian distributions to approximate the PSD shape by employing the Wasserstein metric to determine the appropriate distribution.

Interpolation based methods close the moment equations by predicting the non-integer moments from a set of integer moments. Lagrangian polynomials based on reduced order moments [116, 115, 385] are most commonly used, but an alternative based on the square root of the logarithms of dimensionless moments has also been shown to work well [406]. It is sometimes required to have negative-order moments. By including a moment of order negative-infinity, all fractional moments can be calculated by interpolation [116]. A second interpolation method has been proposed based on only positive order moments, such that negative order moments are determined by extrapolation [115]. The choice of interpolation has been studied by Wick et al. [385] in laminar and turbulent flames. Directly solving for a negative-order moment to be able to interpolate negative order moments was found to improve the solution in coagulation dominated systems.

Moment methods can be extended to bivariate internal coordinates in limited cases. The numerical methods required to solve bivariate moment methods are still a subject of further research to improve robustness. The most common choice of internal coordinates for bivariate population balance models are size and surface area. QMOM was extended to study simultaneous coagulation and sintering of nanoparticles [391]. It was shown that the extension of the DQMOM method to solve bivariate PBEs yields equivalent results [114] to those of QMOM [391] for an equivalent test problem. A novel method that combines the ability of EQMOM to reconstruct the PSD and the ability of CQMOM to express a bivariate type space (volume-surface area) has also been used to study soot formation in premixed flames [303].

2.4.3 Sectional methods

In sectional methods, the internal coordinates are discretised into a finite number of ‘bins’. The number of differential equations is dependent on the number of bins used. These methods allow for more complex descriptions of particles (such as simultaneously tracking particle size and surface area) and have the advantage of also tracking the PSD. The disadvantage of these methods is that they are more computationally expensive than moment methods and they are subject to numerical diffusion due to internal coordinate discretisation. Three of the most common methods are fixed pivot technique [182], finite volume [110, 319] and cell average [180, 320] sectional methods. The fixed pivot method divides the domain of particle sizes into fixed sections of variable width with a representative size for each section. A moving sectional method [377, 245] is aimed at reducing numerical diffusion. The cell average technique aims to better preserve a chosen moment of the number distribution when handling

aggregation and breakage when assigning weights to cells (sections) for a step [181]. The finite volume methods discretise the population balance equation in the particle descriptions rather than in physical space. The same schemes that approximate convection are then applied to the particle growth. The aforementioned sectional methods were compared to analytical solutions for aggregation, breakage and growth problems and the cell average method was found to have superior performance [181]. Sectional methods have frequently been used to study soot [38, 86, 276, 402] as well as inorganic nanoparticles [352, 398, 293].

2.4.4 Stochastic methods

Stochastic (or Monte Carlo) methods have the advantage of allowing detailed particle type spaces that are otherwise computationally intractable using moment or sectional methods. The population is represented by an ensemble of stochastic particles [33]. The evolution of the population is modelled as a series of discrete events also known as jump processes. Each jump process consists of a mathematical description of the transformation of the type space and a rate (or rate equation) describing how frequently the jump process occurs. Solutions to the Monte Carlo methods have been shown to converge to the solution of the coagulation equation [96].

There have been many improvements to stochastic methods. Majorant kernels and fictitious jumps help reduce the computational expense of coagulation [95, 124, 272]. Single particle processes (also known as linear processes) can be deferred for more efficient treatment of linear processes in the linear process deferment algorithm [274]. Ensemble doubling [196, 213, 321] helps reduce statistical error upon particle depletion. To help study more rare particles, weighted particle methods [273] can be used where the statistical weights of the particles are adjusted upon coagulation. Stochastic methods have been applied to study carbonaceous [144] and inorganic nanoparticles [305, 199].

2.4.5 Radial basis methods

A new method has recently been applied to solve population balance equations, the radial basis method (RBM) [6, 368]. In this method, an unknown function is approximated using a linear combination of radial basis functions (RBF) interpolated onto a set of points. The RBFs have the property that their value depends on the distance from a fixed point and are selected such that they are infinitely differentiable. An example of a Gaussian radial basis function ψ_i is

$$\psi_i(\boldsymbol{\xi}) = \exp([-\alpha||\boldsymbol{\xi} - \boldsymbol{\xi_i}||_2]^2), \tag{2.49}$$

where $\boldsymbol{\xi}_i$ is the point where the i^{th} radial basis function is centred and α is a shape parameter. The unknown function is approximated by a linear sum of RBFs.

It is generally considered a meshless method as the RBFs can be used to recast the original PBE in a new form. RBFs have been used to solve PDEs including the Navier-Stokes equations [1, 53]. An aggregation test problem was studied using RBM but found not to predict the self-preserving distribution that should be recovered at long times [368]. The RBM method was applied to analytical aggregation, nucleation, and breakage problems and found to perform very well [6]. It was found to be numerically efficient and is likely a new method for coupling to non-spatially homogeneous problems in the future.

2.4.6 Mixed methods

Many researchers wish to combine the strengths of different methods while addressing the weaknesses of each method to solve population balance equations. One example is a Moment-Sectional Method, termed the Sectional Quadrature Method of Moments [18]. The PBE is divided into sections and a quadrature based moment method is then applied to each section. The method was extended to handle bivariate internal coordinates and has been applied to mass transfer studies of droplets [7]. The method suffers from numerical diffusion for growth and a fix was proposed in the Cumulative Quadrature Method of Moments [17]. Mixed methods that leverage sectional and stochastic methods [42, 31] have also been proposed which aim to better handle breakage and surface growth.

2.4.7 Coupling of flow and particle models

While the general population balance equation has external (spatial) coordinates, most of the methods discussed above have generally been applied to 0D and 1D spatial problems. Some systems are inherently multi-dimensional such as coflow diffusion flames, engines, or turbulent jet sprays. The effect of the domain and its design on the population is an important aspect of study. Therefore, the population balance methods need to be coupled to methods able to solve complex flow problems.

The most common method used to solve complex flow problems is the finite volume method (FVM). Because of its low cost, moment methods have been coupled to flow solvers. In general, the moments are transported, but quadrature based methods transport the approximated weights and abscissas of the moments [313]. QMOM was coupled to the finite volume method (through user defined functions in Fluent) to study aggregation and breakage in Taylor–Couette flows [222]. EQMOM has recently been coupled to the finite volume method as part of OpenFOAM [269]. MOMIC has been coupled to turbulent flows to study TiO_2 synthesis

from $TiCl_4$ in turbulent reactors [5]. In DQMOM, the weights and abscissas that represent the particle size distribution are transported instead of the moments and have been used to study inorganic nanoparticle synthesis in turbulent flame spray pyrolysis [32]. Depending on the closure method used, the 'realisability' of the moments is a concern when subject to transport equations [390]. Higher-order finite volume schemes to ensure realisability of Quadrature-based Moment Methods were published by Vikas et al. [364].

Sectional methods have also been coupled to finite volume methods [245]. For example, sectional methods have had many applications to study soot formation in coflow diffusion flames [86]. While sectional methods can readily resolve the particle size distribution, they are more computationally expensive than moment models and subject to numerical difficulties. As such, moment methods are more commonly applied than sectional methods.

Stochastic methods have been coupled to finite volume methods as well [419, 420, 134]. The fluid flow is treated an Eulerian framework while the particles are treated in a Lagrangian framework to solve the population balance equations. This method was improved to reduce noise in the simulation by using a particle weighting method [422], which is frequently used to increase the resolution of large particles [273]. The method has been used to study TiO_2 nanoparticles in aerosol reactors [134] and in coflow diffusion flames with simplified chemistry [400]. Xu et al. [401] applied the method to study the phase of TiO_2 nanoparticles synthesised in a coflow diffusion flame. The applications of stochastic methods to solve the PBE in a finite volume framework typically used simplified transport assumptions.

2.5 Scope of this thesis

When using jet-wall stagnation flames for synthesis of new materials, it remains an open question how uniform particles are when moving away from the centreline. More specifically, at what point do particles begin to differ in the radial direction? The objective of this thesis is to address this question through modelling to aid experimental efforts in the future. To accomplish this, a tool is needed to solve the flame in multiple spatial dimensions while including a description of nanoparticles. It is desired to be able to study arbitrary geometries and flow configurations in multiple spatial dimensions. Therefore, the conservation equations are solved using the finite volume method and the PISO algorithm. The description of the models, method and implementation is presented in Chapter 3 and its application to gas-phase only systems is presented in Chapter 4.

In this thesis, titania is used as the test material. The performance of synthesised titania nanoparticles is dependent on its morphology and crystal phase, which are also dependent on particle size. Therefore, multidimensional descriptions of nanoparticles are needed. Due

to the computational expense of solving multidensiomal particle models in flow systems, a two-step approach is used: first, the flame is described using a spherical description of the nanoparticles and solved with the method of moments; second, particle trajectories are extracted and post-processed using a multidimensional model to gain insight into the size distribution and morphology of particles and solved with a stochastic method. The results of this study are presented in Chapter 5.

Chapter 3

Models and Methods

This chapter presents the models and methods used in this thesis. The equations for the new solver used to simulate laminar flames and the models to close the governing equations are discussed. The equations of the two particle models are presented: a univariate spherical particle model is used to describe particle growth when coupled to the transport equations and a hybrid particle-number/detailed particle model is used as a post-process. The numerical methods and their implementation are discussed. Last, a series of test cases that are used to verify the implementation of the new flow solver are presented.

3.1 Acknowledgement

The particle models used in this work are the original work of other authors. The spherical particle model solved with the method of moments with interpolative closure was implemented into *k*inetics© [65] by Manoel Y. Manuputty and Jethro Akroyd. The detailed particle model was developed and implemented into *MOpS Particle Simulator* [69] by Casper S. Lindberg. The hybrid particle-number model was developed and implemented into *MOpS Particle Simulator* [69] by Astrid Boje. The theory and implementation of these models and the numerical methods used to solve the population balance equations are presented here.

3.2 Governing equations

The governing equations for laminar reacting flow [281] are partial differential equations in space and time, t, which describe the conservation of mass,

$$\frac{\partial \rho}{\partial t} + \nabla \cdot (\rho U) = 0; \tag{3.1}$$

momentum,

$$\frac{\partial \rho U}{\partial t} + \nabla \cdot (\rho UU) = -\nabla p - \mu \left(\nabla U + (\nabla U)^{\mathsf{T}}\right); \tag{3.2}$$

gas-phase species mass,

$$\frac{\partial \rho Y_i}{\partial t} + \nabla \cdot (\rho U Y_i) + \nabla \cdot (\rho V_i^c Y_i) = \dot{\omega}_i; \tag{3.3}$$

and energy,

$$c_{\mathrm{p}} \frac{\partial \rho T}{\partial t} + c_{\mathrm{p}} \nabla \cdot (\rho U T) = \nabla \cdot (\lambda \nabla T) - \left(\rho \sum_{i=1}^{N} c_{\mathrm{p}_i} Y_i V_i^c \right) \cdot \nabla T + \dot{\omega}_{\mathrm{T}}, \tag{3.4}$$

where ρ is density, U is velocity, Y_i is the mass fraction of species i, T is temperature, p is pressure, V_i^c is the corrected diffusive velocity of species i, $\dot{\omega}_i$ is the rate of formation of species i, $\dot{\omega}_{\mathrm{T}}$ is the enthalpy heat release, μ is mixture viscosity, λ is the mixture thermal conductivity, and c_{p} is the mixture heat capacity. The source term in the energy equation does not include radiative losses from gas or particulate species, but it is expected that this would change the temperature profile of the flames by approximately 50 K in non-sooting flames studied in this thesis.

Transport equations are needed to describe the particle phase. Even for particles that are described by a single internal coordinate (say, a discrete particle size $k \in [0, \infty)$), an infinite number of transport equations exist because a transport equation is needed for each discrete size, making the problem intractable. In this work, the transport equations to describe the population of TiO_2 particles are transformed using the method of moments. The particles are assumed to be very disperse, have negligible mass, be spherical in shape, and have no influence on the momentum or enthalpy of the gas-phase. The moments of the distribution per unit mass, $\hat{M}_j = \frac{M_j}{\rho}$, are solved for as follows:

$$\frac{\partial \rho \hat{M}_j}{\partial t} + \nabla \cdot (\rho U \hat{M}_j) + \nabla \cdot (\rho V_{\mathrm{T}} \hat{M}_j) = \nabla \cdot \left(\rho D_{\mathrm{p}_1} \nabla \hat{M}_{j-\frac{2}{3}} \right) + \dot{\omega}_j \quad \text{for} \quad j = 0..\mathrm{N}_{\mathrm{mom}} - 1. \tag{3.5}$$

In this equation, D_{p_1} is the diffusion coefficient of the smallest particle (of size $k = 1$), V_{T} is the thermophoretic velocity, and $\mathrm{N}_{\mathrm{mom}}$ is the number of moments solved for (which is typically 6). The source terms of the moment equations $\dot{\omega}_j$ consist of inception, coagulation and surface growth processes described in Section 3.3. The source terms and the $\hat{M}_{j-\frac{2}{3}}$ field are unclosed. The equations are closed using interpolative closure (MOMIC) [116] and are presented in Section 3.4.2.

3.2.1 Physical models

Equation of state

The equation of state is described using the ideal gas law [16]. To ensure consistency between the 1D and 2D simulations, the ideal gas law is used in both sets of simulations:

$$pV = n\mathrm{R}_{\mathrm{g}}T. \tag{3.6}$$

Thermodynamic properties

The heat capacities, c_{p_i}; enthalpy h_i; and entropy, s_i; of species i are described using JANAF polynomials [126]. The nomenclature here follows that of Chemkin [292]: variables in the lower case (h_i) are mass-specific (kg^{-1}), while the molar-specific counterparts are capitalised (H_i). R_{g} is the universal gas constant and W_i is the molecular weight of species i. Mixture averaged properties are mass weighted sums of individual components.

$$c_{\mathrm{p}} = \sum_{i=1}^{\mathrm{N}_{\mathrm{sp}}} Y_i c_{\mathrm{p}_i}, \tag{3.7}$$

$$c_{\mathrm{p}_i} = \frac{C_{\mathrm{p}_i}}{W_i} = \frac{\mathrm{R}_{\mathrm{g}}}{W_i}\left(a_{1,i} + a_{2,i}T + a_{3,i}T^2 + a_{4,i}T^3 + a_{5,i}T^4\right), \tag{3.8}$$

$$h = \sum_{i=1}^{\mathrm{N}_{\mathrm{sp}}} Y_i h_i, \tag{3.9}$$

$$h_i = \frac{H_i}{W_i} = \frac{\mathrm{R}_{\mathrm{g}}}{W_i}\left(a_{1,i}T + \frac{a_{2,i}}{2}T^2 + \frac{a_{3,i}}{3}T^3 + \frac{a_{4,i}}{4}T^4 + \frac{a_{5,i}}{5}T^5 + a_{6,i}\right), \tag{3.10}$$

$$s = \sum_{i=1}^{\mathrm{N}_{\mathrm{sp}}} Y_i s_i, \tag{3.11}$$

$$s_i = \frac{S_i}{W_i} = \frac{\mathrm{R_g}}{W_i}\left(a_{1,i}\log(T) + a_{2,i}T + \frac{a_{3,i}}{2}T^2 + \frac{a_{4,i}}{3}T^3 + \frac{a_{4,i}}{5}T^4 + a_{7,i}\right). \tag{3.12}$$

The heat capacity at constant volume, $c_{\mathrm{v},i}$, is described in terms of C_{p_i}:

$$c_{\mathrm{v}} = \sum_{i=1}^{\mathrm{N_{sp}}} Y_i c_{\mathrm{v}_i}, \tag{3.13}$$

$$c_{\mathrm{v}_i} = \frac{C_{\mathrm{v}_i}}{W_i} = \frac{C_{\mathrm{p}_i} - \mathrm{R_g}}{W_i}. \tag{3.14}$$

Viscosity

The viscosity of each species, μ_i, is described by the standard kinetic theory expression where W_i is molecular weight, k_B is the Boltzmann constant, σ_i is the Lennard-Jones collision diameter [34], and $\Omega^{(2,2)*}$ is the collision integral based on reduced temperature [247]:

$$\mu_i = \frac{5}{16}\frac{\sqrt{\pi W_i k_{\mathrm{B}} T}}{\pi \sigma_i^2 \Omega^{(2,2)*}}. \tag{3.15}$$

The mixture viscosity is defined by a semi-empirical formula by Wilke [386] that has been modified by Bird et al. [34]:

$$\mu = \sum_{i=1}^{\mathrm{N_{sp}}} \frac{X_i \mu_i}{\sum_{j=1}^{\mathrm{N_{sp}}} X_j \phi_{ij}}, \tag{3.16}$$

where μ_i, X_i, and W_i are the viscosity, mole fraction, and molecular weight of species i and

$$\phi_{ij} = \frac{1}{\sqrt{8}}\left(1 + \frac{W_i}{W_j}\right)^{-\frac{1}{2}}\left(1 + \left(\frac{\mu_i}{\mu_j}\right)^{\frac{1}{2}}\left(\frac{W_j}{W_i}\right)^{\frac{1}{4}}\right)^2. \tag{3.17}$$

Thermal conductivity

The thermal conductivities of individual species are composed of translational, rotational, and vibrational contributions which are functions of the species geometry and properties [277]:

$$\lambda_i = \frac{\mu_i}{W_i}\left(f_{\mathrm{trans}} C_{\mathrm{v,trans}} + f_{\mathrm{rot}} C_{\mathrm{v,rot}} + f_{\mathrm{vib}} C_{\mathrm{v,vib}}\right), \tag{3.18}$$

$$
\begin{aligned}
f_{\text{trans}} &= \frac{5}{2}\left(1-\frac{2}{\pi}\frac{C_{\text{v,rot}}}{C_{\text{v,trans}}}\frac{\left(\frac{5}{2}-\frac{\rho D_{i,i}}{\mu_i}\right)}{Z_{\text{rot}}+\frac{2}{\pi}\left(\frac{5}{3}\frac{C_{\text{v,rot}}}{R_{\text{g}}}+\frac{\rho D_{i,i}}{\mu_i}\right)}\right),\\
f_{\text{rot}} &= \frac{\rho D_{i,i}}{\mu_i}\left(1+\frac{2}{\pi}\frac{\left(\frac{5}{2}-\frac{\rho D_{i,i}}{\mu_i}\right)}{Z_{\text{rot}}+\frac{2}{\pi}\left(\frac{5}{3}\frac{C_{\text{v,rot}}}{R_{\text{g}}}+\frac{\rho D_{i,i}}{\mu_i}\right)}\right),\\
f_{\text{vib}} &= \frac{\rho D_{i,i}}{\mu_i}.
\end{aligned}
\tag{3.19}
$$

If the species is a single atom, there are no rotational or vibrational contributions and $f_{\text{trans}} = \frac{5}{2}$:

$$
C_{\text{v,trans}} = \frac{3}{2}\text{R}_{\text{g}}. \tag{3.20}
$$

If the species is linear:

$$
\begin{aligned}
C_{\text{v,trans}} &= \tfrac{3}{2}\text{R}_{\text{g}},\\
C_{\text{v,rot}} &= \text{R}_{\text{g}},\\
C_{\text{v,vib}} &= C_{\text{v}} - \tfrac{5}{2}\text{R}_{\text{g}}.
\end{aligned}
\tag{3.21}
$$

If the species is non-linear:

$$
\begin{aligned}
C_{\text{v,trans}} &= \tfrac{3}{2}\text{R}_{\text{g}},\\
C_{\text{v,rot}} &= \tfrac{3}{2}\text{R}_{\text{g}},\\
C_{\text{v,vib}} &= C_{\text{v}} - 3\text{R}_{\text{g}}.
\end{aligned}
\tag{3.22}
$$

The rotational relaxation collision number, $Z_{\text{rot}}(T)$ is available at 298 K and has the following temperature dependence [268, 45]:

$$
Z_{\text{rot}}(T) = Z_{\text{rot}}(298)\frac{F(298)}{F(T)}, \text{ where} \tag{3.23}
$$

$$
F(T) = 1+\frac{\pi^{\frac{3}{2}}}{2}\left(\frac{\varepsilon/\text{k}_{\text{B}}}{T}\right)^{\frac{1}{2}}+\left(\frac{\pi^2}{4}+2\right)\left(\frac{\varepsilon/\text{k}_{\text{B}}}{T}\right)+\pi^{\frac{3}{2}}\left(\frac{\varepsilon/\text{k}_{\text{B}}}{T}\right)^{\frac{3}{2}}. \tag{3.24}
$$

The mixture thermal conductivity is given by [225]:

$$
\lambda = \frac{1}{2}\left(\sum_{i=1}^{\text{N}_{\text{sp}}} X_i\lambda_i + \left[\sum_{i=1}^{\text{N}_{\text{sp}}} X_i/\lambda_i\right]^{-1}\right). \tag{3.25}
$$

Species diffusion

A model is needed to describe mass flux due to concentration gradients in a multicomponent gas mixture. A mixture-averaged approach is used to get a single diffusion coefficient for each species to be used in the transport equation. The binary diffusion coefficient, $D_{i,j}$, given below, is a function of temperature and pressure; the reduced molecular weight, $\bar{W}_{i,j}$; the reduced collision diameter, $\sigma_{i,j}$; and a collision integral, $\Omega^{(1,1)*}$ [140]:

$$D_{i,j} = \frac{3}{16} \frac{\sqrt{2\pi k_B^3 T^3 / \bar{W}_{i,j}}}{p\pi\sigma_{i,j}^2 \Omega^{(1,1)*}}. \tag{3.26}$$

The mixture-averaged approach of Hirschfelder and Curtiss [138] is used to calculate the mixture diffusion coefficient, D_i. This approach is not inherently mass conserving, so a corrective velocity, V_c, is applied to each species to ensure that mass conservation is followed. The final, corrected diffusion velocity, V_i^c, is the sum of the mass flux and the corrective velocity:

$$D_i = \frac{1 - Y_i}{\sum_{j \neq i}^{N_{sp}} \frac{X_j}{D_{i,j}}}, \tag{3.27}$$

$$V_i^c = V_i + V_c, \quad V_i = -D_i \frac{\nabla X_i}{X_i}, \quad V_c = -\sum_i^{N_{sp}} Y_i V_i. \tag{3.28}$$

Particle diffusive and thermophoretic transport

The diffusion coefficient of particles of size k due to Brownian motion in the free-molecular regime, D_{p_k}, can be expressed as [118]:

$$D_{p_k} = \frac{3}{2\rho} \left(1 + \frac{\pi\alpha_T}{8}\right)^{-1} \sqrt{\frac{W k_B T}{2\pi N_A}} \frac{1}{d_k^2}, \tag{3.29}$$

where α_T is a thermal accommodation factor (fraction of gas molecules that leave the surface in equilibrium), N_A is Avagadro's constant, and d_k is the diameter of a particle of size k. The thermal accommodation factor usually takes a value of 0.9 [118]. Under the spherical particle assumption, the diameter of a particle of size k scales by $k^{1/3}$. This can be used to describe D_{p_k} as a function of k and D_{p_1}:

$$\begin{aligned} D_{\mathrm{p}_k} &= \frac{3}{2\rho}\left(1+\frac{\pi\alpha_{\mathrm{T}}}{8}\right)^{-1}\sqrt{\frac{Wk_{\mathrm{B}}T}{2\pi \mathrm{N_A}}}\frac{1}{(d_1k^{1/3})^2} \\ &= \frac{3}{2\rho}\left(1+\frac{\pi\alpha_{\mathrm{T}}}{8}\right)^{-1}\sqrt{\frac{Wk_{\mathrm{B}}T}{2\pi \mathrm{N_A}}}\frac{1}{d_1^2}k^{-2/3} \\ &= D_{\mathrm{p}_1}k^{-2/3}. \end{aligned} \tag{3.30}$$

When applying the definition of moments to the infinite number of particle transport equations, the diffusion transport term of moment $\hat{M}_j$ becomes

$$\nabla\cdot\left(\rho D_{\mathrm{p}_1}\nabla\hat{M}_{j-\frac{2}{3}}\right) \tag{3.31}$$

in Eqn. 3.5.

The thermophoretic velocity of particles, V_{T}, is assumed to be size independent and is expressed as [118]:

$$V_{\mathrm{T}} = -\frac{3}{4}\left(1+\frac{\pi\alpha_{\mathrm{T}}}{8}\right)^{-1}\frac{\mu}{\rho T}\nabla T. \tag{3.32}$$

V_{T} acts as an additional convective flux term in Eqn. 3.5.

Chemical source terms

The chemical source terms are calculated using detailed chemical models, which is a very challenging task [326]. Therefore, the chemical source terms are calculated using an averaged production rate after integrating the chemistry as a closed, constant pressure batch reactor. For a given time step, Δt, the average source terms to be included in the transport equations are calculated as follows:

$$\dot{\omega}_i = W_i\frac{C_i(t+\Delta t)-C_i(t)}{\Delta t}, \quad \text{for } i=1,..,\mathrm{N_{sp}}, \tag{3.33}$$

$$\dot{\omega}_{\mathrm{T}} = \sum_{i=1}^{\mathrm{N_{sp}}}\dot{\omega}_i h_i, \quad \text{and} \tag{3.34}$$

$$\dot{\omega}_j = \frac{M_j(t+\Delta t)-M_j(t)}{\Delta t}, \quad \text{for } j=0,..,\mathrm{N_{mom}}-1, \tag{3.35}$$

where C_i is the concentration of species i, $\dot{\omega}_i$ is the mass production rate of species i, $\dot{\omega}_{\mathrm{T}}$ is the enthalpy production rate, and $\dot{\omega}_j$ is the volumetric moment production rate.

The concentrations and moment values at time $t+\Delta t$ are calculated by integrating a constant pressure batch reactor with an ODE solver with a variable internal time step. This allows for the stiff chemistry to be accurately resolved. The equations for the batch reactor are as follows. The number of moles of species i, n_i is solved for:

$$\frac{\mathrm{d}n_i}{\mathrm{d}t} = V_{\mathrm{smp}}(\dot{\Omega}_i^{\mathrm{GP}} + \dot{\Omega}_i^{\mathrm{P}}), \tag{3.36}$$

where V_{smp} is the sample volume of the batch reactor and $\dot{\Omega}_i$ is the molar production rate per unit volume with contributions from the gas-phase reactions (GP) and particle phase reactions (P).

A general gas-phase chemical reaction can be written in the following form:

$$\sum_{i=1}^{\mathrm{N_{sp}}} \nu_{i,j}^{'} \chi_i \overset{\mathrm{k}_j}{\rightleftharpoons} \sum_{i=1}^{\mathrm{N_{sp}}} \nu_{i,j}^{''} \chi_i, \tag{3.37}$$

where χ_i is the symbol for species i and ν_j are the stoichiometric coefficients for the forward ($\nu_{i,j}^{'}$) and the reverse ($\nu_{i,j}^{''}$) directions of the j^{th} reaction with a rate constant k_j. The reactions are assumed to be reversible unless specified as an irreversible reaction. For an arbitrary species i, the molar production rate from gas-phase reactions, $\dot{\Omega}_i^{\mathrm{GP}}$, is calculated as

$$\dot{\Omega}_i^{\mathrm{GP}} = \sum_{j=1}^{\mathrm{N_{rxn}}} \left(\nu_{i,j}^{''} - \nu_{i,j}^{'}\right) q_j, \tag{3.38}$$

where j is the reaction out of $\mathrm{N_{rxn}}$ gas-phase reactions and q_j is the extent of reaction j. For elementary reactions, the extent of reaction is calculated as:

$$q_j = k_{\mathrm{f},j} \prod_{i=1}^{\mathrm{N_{sp}}} C_{\chi_i}^{\nu_{i,j}^{'}} - k_{\mathrm{r},j} \prod_{i=1}^{\mathrm{N_{sp}}} C_{\chi_i}^{\nu_{i,j}^{''}}. \tag{3.39}$$

where $k_{\mathrm{f},j}$ and $k_{\mathrm{r},j}$ are the forward and reverse rate constants and C_{χ_i} is the concentration of species i. If no reverse reaction rate is defined, the reverse rate constants are calculated from chemical equilibrium:

$$k_{\mathrm{r},j} = \frac{k_{\mathrm{f},j}}{K_{\mathrm{c},j}^{\mathrm{EQ}}}, \tag{3.40}$$

where the equilibrium constant $K_{\mathrm{c},j}^{\mathrm{EQ}}$ is calculated as:

$$K_{\mathrm{c},j}^{\mathrm{EQ}} = \prod_{i=1}^{\mathrm{N_{sp}}} C_{\chi_i}^{\nu_{i,j}^{''} - \nu_{i,j}^{'}}, \tag{3.41}$$

when the Gibbs free energy is at its minimum. If a reverse reaction rate is explicitly defined, the reactions are treated as two irreversible reactions with no reverse reaction ($k_{\mathrm{r},j} = 0$).

The enthalpy balance of the control volume is:

$$C_{\mathrm{p}} \frac{\mathrm{d}T}{\mathrm{d}t} = V_{\mathrm{smp}} (\dot{Q}^{\mathrm{GP}}_{\mathrm{chem}} + \dot{Q}^{\mathrm{P}}_{\mathrm{chem}}), \tag{3.42}$$

where $\dot{Q}^{\mathrm{GP}}_{\mathrm{chem}}$ and $\dot{Q}^{\mathrm{P}}_{\mathrm{chem}}$ are the enthalpy released from gas-phase reactions and particle processes, respectively. The terms are calculated as follows:

$$\dot{Q}^{\mathrm{GP}}_{\mathrm{chem}} = \sum_{i=1}^{\mathrm{N_{sp}}} \dot{\Omega}^{\mathrm{GP}}_i H_i, \quad \text{and} \tag{3.43}$$

$$\dot{Q}^{\mathrm{P}}_{\mathrm{chem}} = \sum_{i=1}^{\mathrm{N_{sp}}} \dot{\Omega}^{\mathrm{P}}_i H_i. \tag{3.44}$$

The equations for the particle phase in the batch reactor are as follows:

$$\frac{\mathrm{d}M_j}{\mathrm{d}t} = \dot{\omega}_{j,\mathrm{IN}} + \dot{\omega}_{j,\mathrm{SG}} + \dot{\omega}_{j,\mathrm{CG}}, \quad \text{for} \quad j = 0, .., \mathrm{N_{mom}} - 1, \tag{3.45}$$

where $\dot{\omega}_j$ is the source term due to particle processes. The processes are inception (IN), surface growth (SG), and coagulation (CG) and are explained in Section 3.3.1 for the spherical particle model used in this work.

To get a source term for each cell, the mole balance (Eqn. 3.36), enthalpy balance (Eqn. 3.42), and moment (Eqn. 3.45) equations are integrated over the time step Δt from the initial condition of the cell. The initial and final values of the species concentrations and moment number densities are used to calculate the average source terms in Equations 3.33 and 3.35.

3.3 Titania particle models

As introduced in Section 2.4, population balance equations are a means of tracking the changes of a population over time (and space). Titania nanoparticles undergo simultaneous coagulation, inception, surface growth, and coalescence as presented in Section 2.1.4. Three particle models are used in this work. A spherical particle model with detailed chemistry is used to describe particle growth fully coupled to the gas phase. A simplified spherical particle model that uses one-step chemistry to model the conversion from TTIP to TiO_2 is used in the verification of the flow slover and is also described here. As a post-processing step, a hybrid particle-

number/detailed particle model is used to simulate particle growth along different Lagrangian trajectories in the 2D simulations. These three models are presented below.

3.3.1 Spherical particle model with complex chemistry

This model tracks the number of Ti atoms undergoing coagulation, inception, and surface growth ($\xi = k$, $k \in \mathbb{N}$). The bulk density is assumed to be that of rutile ($\rho_{\text{rutile}} = 4250$ kg m^{-3}). The particle inception and surface growth are modelled as collision-limited processes. The collision species is $Ti(OH)_4$ with the collision diameters assumed to be $d_{Ti(OH)_4} = 0.5128$ nm [47]. Instantaneous coagulation and coalescence is assumed for the particles to maintain their spherical shape. Because this model is solved using the method of moments with interoplative closure (Section 3.4.2), the rate equations for the particle processes are transformed into their corresponding moment source terms.

Precursor chemistry

The gas phase decomposition of TTIP is described by 25 species containing titanium and 61 reactions. Titanium (IV) hydroxide, $Ti(OH)_4$, is formed from TTIP through C_3H_6 and CH_3 abstraction pathways identified by Buerger et al. [48]. Further dissociation reactions of $Ti(OH)_4$ to TiO_xH_y as proposed by Shmakov et al. [316] are included and are assumed to be barrierless reactions. An alternative decomposition pathway through C_3H_6O abstraction proposed by Ershov et al. [100] is not included due to lack of kinetic information.

Coagulation

Coagulation is described by the Smoluchowski equation [322] as described in Section 2.1.4. Because this model has a single internal coordinate, instantaneous coagulation and coalescence is assumed (Fig. 2.2). The choice of internal coordinates and assumed spherical shape allows a relationship between particle size k and the collision diameter, $d_c(k)$ to be leveraged:

$$d_c(k) = d_1 k^{\frac{1}{3}},$$

where d_1 is the collision diameter of the monomer. This leads to the following forms of the coagulation kernel:

$$\beta(k_1,k_2)=\begin{cases} A^{\mathrm{CN}}\left(k_1^{\frac{1}{3}}+k_2^{\frac{1}{3}}\right)\left[\frac{1}{k_1^{\frac{1}{3}}}+\frac{1}{k_2^{\frac{1}{3}}}+A^{\mathrm{SF}\prime}\left(\frac{1}{k_1^{\frac{2}{3}}}+\frac{1}{k_2^{\frac{2}{3}}}\right)\right] & \text{slip flow} \\ A^{\mathrm{FM}\prime}\varepsilon_{k_1,k_2}\left(k_1^{\frac{1}{3}}+k_2^{\frac{1}{3}}\right)^2\left(\frac{1}{k_1}+\frac{1}{k_2}\right)^{\frac{1}{2}} & \text{free molecular,} \end{cases} \tag{3.46}$$

where

$$A^{\mathrm{CN}}=\frac{2k_{\mathrm{B}}T}{3\mu}, \tag{3.47}$$

$$A^{\mathrm{SF}\prime}=\frac{2A^{\mathrm{SF}}\lambda_f}{d_1}, \tag{3.48}$$

$$A^{\mathrm{FM}\prime}=\frac{A^{\mathrm{FM}}d_1^2}{m_1^{\frac{1}{2}}}. \tag{3.49}$$

The resulting moment coagulation source term, $\dot{\omega}_{j,\mathrm{CG}}$, to be included in the moment transport equation (Eqn. 3.5) can be written as follows [115]:

$$\dot{\omega}_{j,\mathrm{CG}}=\frac{\dot{\omega}^{\mathrm{SF}}_{j,\mathrm{CG}}\dot{\omega}^{\mathrm{FM}}_{j,\mathrm{CG}}}{\dot{\omega}^{\mathrm{SF}}_{j,\mathrm{CG}}+\dot{\omega}^{\mathrm{FM}}_{j,\mathrm{CG}}}, \tag{3.50}$$

where

$$\dot{\omega}^{\mathrm{SF}}_{j,\mathrm{CG}}=\begin{cases} -A^{\mathrm{CN}}\left(1+\mu_{\frac{1}{3}}\mu_{-\frac{1}{3}}+A^{\mathrm{SF}\prime}\left[\mu_{-\frac{1}{3}}+\mu_{\frac{1}{3}}\mu_{-\frac{2}{3}}\right]\right)M_0^2, & j=0 \\ 0, & j=1 \\ \frac{1}{2}A^{\mathrm{CN}}\sum_{r=1}^{j-1}\binom{j}{r}\Big(\mu_{r+\frac{1}{3}}\mu_{j-r-\frac{1}{3}}+\mu_{r-\frac{1}{3}}\mu_{j-r+\frac{1}{3}} & \\ \quad +2\mu_r\mu_{j-r}+A^{\mathrm{SF}\prime}\Big[\mu_{r+\frac{1}{3}}\mu_{j-r-\frac{2}{3}}+\mu_r\mu_{j-r-\frac{1}{3}} & j>1, \\ \qquad +\mu_{r-\frac{1}{3}}\mu_{j-r}+\mu_{r-\frac{2}{3}}\mu_{j-r+\frac{1}{3}}\Big]\Big)M_0^2, & \end{cases} \tag{3.51}$$

and under the assumption that the enhancement factor is size independent, where

$$\dot{\omega}^{\mathrm{FM}}_{j,\mathrm{CG}}=\begin{cases} -A^{\mathrm{FM}\prime}\bar{\varepsilon}\left(\frac{1}{2}f_{0,0}\right)M_0^2, & j=0 \\ 0, & j=1 \\ A^{\mathrm{FM}\prime}\bar{\varepsilon}\sum_{r=1}^{j-1}\binom{j}{r}\left(\frac{1}{2}f_{r,j-r}\right)M_0^2, & j>1, \end{cases} \tag{3.52}$$

and

$$ {}^{m}f_{x,y} = \sum_{k_1=k_{min}}^{\infty} \sum_{k_2=k_{min}}^{\infty} \frac{k_1^x k_2^y}{\sqrt{k_1 k_2}} (k_1+k_2)^m \left(k_1^{\frac{1}{3}} + k_2^{\frac{1}{3}} \right)^2 \frac{N(k_1)N(k_2)}{M_0^2}, \quad m = \frac{1}{2}. \tag{3.53} $$

There are terms in the coagulation source term equations ($\frac{1}{2} f_{r,j-r}$) that are unclosed. To close these terms, Lagrangian interpolation is used as described in Section 3.4.2.

Inception

Inception is modelled as a collision-limited process where the rate is described from the kinetic theory of gases. $Ti(OH)_4$ is the collision species. The generalised inception reaction can be written as follows:

$$ 2\mathrm{Ti(OH)_{4(g)}} \xrightarrow{k_{IN}} \mathrm{Ti_2O_{4(s)}} + 4\,\mathrm{H_2O_{(g)}}. \tag{3.54} $$

The inception rate, k_{IN}, is calculated by the free molecular collision kernel (Eqn. 2.15),

$$ k_{IN} = \varepsilon \sqrt{\frac{\pi k_B T}{2} \left(\frac{1}{m_i} + \frac{1}{m_i} \right)} (d_i + d_i)^2, \tag{3.55} $$

where m_i and d_i are the mass and collision diameter of the collision species ($Ti(OH)_4$). The collision diameter is assumed to be the same as calculated in Buerger et al. [47]: 0.5218 nm. The moment inception source term can be written as:

$$ \dot{\omega}_{j,IN} = \frac{1}{2} k_{IN} N_A 2^j C^2_{Ti(OH)_4}, \tag{3.56} $$

where $C_{Ti(OH)_4}$ is the concentration of the inception species, $Ti(OH)_4$. The factor of 2^j is rooted in the fact that two Ti atoms are added to the particle phase from the inception reaction. The subsequent source term for moment j is 2^j.

Surface growth

Surface growth is modelled as a collision limited process where $Ti(OH)_4$ is the possible collision species:

$$ \mathrm{Ti(OH)_{4(g)}} + [\mathrm{Ti}_x\mathrm{O}_y]_{(s)} \xrightarrow{k_{SG}} [\mathrm{Ti}_{x+1}\mathrm{O}_{y+2}]_{(s)} + 2\,\mathrm{H_2O_{(g)}}. \tag{3.57} $$

The surface growth rate constant, k_{SG} is estimated using the free-molecular coagulation rate (Eqn. 2.15) between spherical particles of size k_1 and size k_2 [115]. The collision species are

approximated by a spherical particle containing one TiO_2 unit ($k_1 = 1$). Under the assumption that $k_2 >> k_1$,

$$\begin{aligned} k_{\mathrm{SG}} &= \varepsilon \left(\frac{6k_{\mathrm{B}}T}{\rho_{\mathrm{TiO_2}}}\right)^{\frac{1}{2}} \left(\frac{3m_{k_{\min}}}{4\pi\rho_{\mathrm{TiO_2}}}\right)^{\frac{1}{6}} \sqrt{\frac{1}{k_1}+\frac{1}{k_2}} \left(k_1^{1/3}+k_2^{1/3}\right)^2 \\ &\approx \varepsilon \left(\frac{6k_{\mathrm{B}}T}{\rho_{\mathrm{TiO_2}}}\right)^{\frac{1}{2}} \left(\frac{3m_{k_{\min}}}{4\pi\rho_{\mathrm{TiO_2}}}\right)^{\frac{1}{6}} (k_2^{2/3}). \end{aligned} \tag{3.58}$$

The moment source term due to surface growth can be written as:

$$\dot{\omega}_{j,\mathrm{SG}} = \begin{cases} 0, & \text{for } j = 0, \\ C_{\mathrm{Ti(OH)_4}} \mathrm{N_A} \varepsilon \left(\frac{6k_{\mathrm{B}}T}{\rho_{\mathrm{TiO_2}}}\right)^{\frac{1}{2}} \left(\frac{3m_{k_{\min}}}{4\pi\rho_{\mathrm{TiO_2}}}\right)^{\frac{1}{6}} \sum_{r=0}^{j-1} \binom{j}{r} \mu_{r+\frac{2}{3}} M_0, & \text{for } j \geq 1, \end{cases} \tag{3.59}$$

where k_{B} is the Boltzmann constant, $\rho_{\mathrm{TiO_2}}$ is the bulk density of TiO_2, and $m_{k_{\min}}$ is the mass of the monomer unit. The fractional moments are determined by Lagrangian interpolation (Section 3.4.2).

3.3.2 Spherical particle model with one-step chemistry

A second spherical particle model with one-step chemistry is used in the verification of the new solver. This model tracks the number of Ti atoms undergoing coagulation, inception, and surface growth ($\xi = k$, $k \in \mathbb{N}$). The bulk density is assumed to be that of rutile ($\rho_{\mathrm{rutile}} = 4250$ kg m^{-3}). The particle inception and surface growth are modelled as kinetically-limited processes. Instantaneous coagulation and coalescence is assumed for the particles to maintain their spherical shape. Because this model is solved using the method of moments with interpolative closure (Section 3.4.2), the rate equations for the particle processes are transformed into their corresponding moment source terms.

Coagulation

The coagulation source term is the same as described in Section 3.3.1.

Precursor chemistry

The simplified one-step reaction is used to describe the consumption of TTIP from the gas phase [265]:

$$\mathrm{Ti(OC_3H_7)_{4(g)}} \longrightarrow \mathrm{TiO_{2(s)}} + 4\,\mathrm{C_3H_{6(g)}} + 2\,\mathrm{H_2O_{(g)}}. \tag{3.60}$$

The overall reaction rate constant, k'_{ov}, is a first-order reaction rate constant,

$$k'_{ov} = 3.96 \times 10^5 \exp\left(\frac{-8479.7\text{K}}{T}\right) \text{s}^{-1}, \tag{3.61}$$

and includes contributions from inception and surface growth. The use of an overall TTIP consumption rate means the TTIP gas phase consumption is independent of the particle state. This provides the numerical advantage that the gas phase chemistry can be decoupled from the particle physics while still accounting for the gas phase sink terms to TTIP.

Particle surface growth and inception

The smallest particle size is $k = 1$, a single TiO_2 monomer, and is the only particle that can incept. Additionally, only a single surface growth reaction exists.

$$\text{Ti}(\text{OC}_3\text{H}_7)_{4(\text{g})} \xrightarrow{k_{IN}} \text{TiO}_{2(\text{s})} + 4\,\text{C}_3\text{H}_{6(\text{g})} + 2\,\text{H}_2\text{O}_{(\text{g})}, \tag{3.62}$$

$$\text{Ti}(\text{OC}_3\text{H}_7)_{4(\text{g})} + (\text{TiO}_2)_{k-1(\text{s})} \xrightarrow{k_{SG}} (\text{TiO}_2)_{k(\text{s})} + 4\,\text{C}_3\text{H}_{6(\text{g})} + 2\,\text{H}_2\text{O}_{(\text{g})}. \tag{3.63}$$

The surface growth reaction rate is a first-order rate model [21] with rate constant, k'_{SG} [352]

$$k'_{SG} = 1 \times 10^9 \exp\left(\frac{-15155.16\text{K}}{T}\right) \text{m s}^{-1}. \tag{3.64}$$

The inception of particles is calculated as the balance between the overall TTIP consumption rate and the surface growth consumption. If the surface growth rate exceeds the overall TTIP consumption rate, the inception rate is set to 0 and the surface growth is limited by the overall consumption rate. The gas-phase reaction rate constant, k_{IN}, and the surface reaction rate constant, k_{SG}, are given by

$$k_{IN} = \begin{cases} k'_{ov} - Ak'_{SG} & \text{for } k'_{ov} \geq Ak'_{SG} \\ 0 & \text{for } k'_{ov} < Ak'_{SG}, \end{cases} \tag{3.65}$$

$$k_{SG} = \begin{cases} k'_{SG} & \text{for } k'_{ov} \geq Ak'_{SG} \\ k'_{ov}/A & \text{for } k'_{ov} < Ak'_{SG}, \end{cases} \tag{3.66}$$

where A is the total particle surface area per unit volume. These rate constants feed into the inception and surface growth terms of the PBE:

$$\left.\frac{\partial N(k)}{\partial t}\right|_{\mathrm{IN}} = k_{\mathrm{IN}} C_{\mathrm{TTIP}} \mathrm{N_A}, \tag{3.67}$$

$$\left.\frac{\partial N(k)}{\partial t}\right|_{\mathrm{SG}} = k_{\mathrm{SG}} A C_{\mathrm{TTIP}}. \tag{3.68}$$

The corresponding moment source terms are:

$$\dot{\omega}_{j,\mathrm{IN}} = k_{\mathrm{IN}} C_{\mathrm{TTIP}} \mathrm{N_A} \qquad \text{for } j \geq 0 \tag{3.69}$$

$$\dot{\omega}_{j,\mathrm{SG}} = \begin{cases} 0 & \text{for } j = 0 \\ k_{\mathrm{SG}} A C_{\mathrm{TTIP}} \mathrm{N_A} \sum_{r=0}^{j-1} \binom{k}{r} \mu_{r+\frac{2}{3}} M_0 & \text{for } j \geq 1 \end{cases} \tag{3.70}$$

where C_{TTIP} is the molar concentration of TTIP in the gas phase. The inception source term is independent of the moment order (j) because a single TiO_2 monomer ($k = 1$) is added to the particle phase.

3.3.3 Hybrid particle-number/detailed particle model

The detailed particle model used in this work was developed and previously published by Lindberg et al. [200]. This detailed description of particles allows for inception, surface growth, coagulation, sintering and coalescence to be studied simultaneously. To address the numerical stiffness created by high levels of inception, an additional hybrid particle-number model is used in addition to the detailed particle model [39]. In short, the particle-number model is used to track the frequency of a subset of spherical monomers before being transferred to the full detailed particle model. More details regarding this formulation can be found in Boje et al. [39].

Particle type space

This model contains two particle descriptions: a particle-number model and a detailed particle model. These are described below.

Particle-number model: This model tracks the quantity of a set of spherical monomers up to a critical size, N_{thresh}. The phase space is defined as $\mathbb{M}$. Particles in this space have a single internal coordinate with different sizes $k \in [1, N_{\mathrm{thresh}}]$, where $k = 1$ is a single molecular unit

and N_{thresh} is the size of the largest particle. Particles larger than this are transferred to the space of aggregate particles, $\mathbb{X}$. The particle-number (PN) system, $z_{\mathbb{M}}$, is written as:

$$z_{\mathbb{M}}(t) = \left(\boldsymbol{\xi}_1, \ldots, \boldsymbol{\xi}_{N_{\text{thresh}}}\right), \tag{3.71}$$

where

$$\boldsymbol{\xi}_k(t) \in \mathbb{M}, \quad k = 1, \ldots, N_{\text{thresh}}, \quad t \geq 0, \tag{3.72}$$

and $N_k = N(\boldsymbol{\xi}_k)$ is the number of particles that have type $\boldsymbol{\xi}_k$. More details regarding this formulation can be find in Boje et al. [39].

Large aggregate particles: Let $\mathbb{X}$ be the phase space for spherical particles larger than that tracked by $\mathbb{M}$ and all possible aggregate particles. The particle system, $z_{\mathbb{X}}$, is comprised of $N(t) \leq \mathrm{N}_{\max}$ such particles (at time t):

$$z_{\mathbb{X}}(t) = \left(\boldsymbol{\xi}_1, \ldots, \boldsymbol{\xi}_{N(t)}\right), \tag{3.73}$$

where

$$\boldsymbol{\xi}_i(t) \in \mathbb{X}, \quad i = 1, \ldots, N(t), \quad t \geq 0. \tag{3.74}$$

Particles in $\mathbb{X}$ are to be described by the detailed particle model from Lindberg et al. [200], which is outlined below. Primary particles, p_i, are described by their composition, η, their position relative to the aggregate centre of mass, $\mathbf{x}$, and their radius, r. They are assumed to be overlapping spheres [91]:

$$p_i = p_i(\eta, r, \mathbf{x}). \tag{3.75}$$

The particle composition, η, has the ability to track the composition to an arbitrary level of detail. In this work, the composition tracks the number of Ti and O atoms. An aggregate particle, $P_q \in \mathbb{X}$, is made up of $n_{\text{p}}(P_q)$ overlapping primary particles and a matrix $\mathbf{C}$ of the primary particle connectivity:

$$P_q = P_q\left(p_1, p_2, ..., p_{n_{\text{p}}(P_q)}, \boldsymbol{C}\right) \in \mathbb{X}. \tag{3.76}$$

The connectivity matrix is a binary lower triangular matrix (of size $n_{\text{p}}(P_q) \times n_{\text{p}}(P_q)$) that represents if there is ($C_{ij} = 1$) or is not ($C_{ij} = 0$) a connection between primary p_i and primary p_j. The connectivity matrix is used to form a binary tree structure [305] that can be used

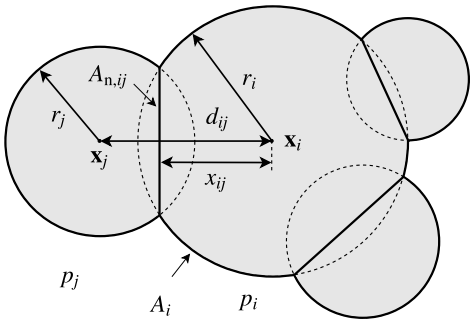

Fig. 3.1 An illustration depicting the derived quantities in the detailed particle model. The primary particles are represented by spheres and the aggregates are modelled as overlapping spheres. The derived quantities d_{ij}, x_{ij}, A_i, and $A_{n,ij}$ are labelled as well for p_i. Reprinted from Lindberg et al. [200] with permission from Elsevier.

to efficiently sum over neighbours of a primary to calculate properties such as volume, free surface, and neck area. There are limitations to the binary tree structure, such as multiple overlaps and connectivity cycles, which are not considered.

Derived quantities

When aggregate particles are described by overlapping spheres, a number of properties can be calculated [91]. Figure 3.1 shows an example of the derived quantities.

The distance between two primaries is calculated as:

$$d_{ij} = |\mathbf{x}_i - \mathbf{x}_j|. \tag{3.77}$$

The distance between the centre of primary p_i and the neck with neighbour p_j is calculated as:

$$x_{ij} = \frac{d_{ij}^2 - r_j^2 + r_i^2}{2d_{ij}}. \tag{3.78}$$

The volume of p_i can then be calculated as the volume of the sphere minus the 'caps' created from overlaps with the neighbour primaries [91]:

$$v_i = V_{\text{sphere}}(r_i) - \sum_j V_{\text{cap}}(r_i, x_{ij}) \tag{3.79}$$

$$= \frac{4}{3}\pi r_i^3 - \frac{1}{3}\pi \sum_j \left(2r_i^3 + x_{ij}^3 - 3r_i^2 x_{ij}\right). \tag{3.80}$$

Alternatively, the volume can be calculated from the composition under assumed density (assumed to be that of bulk TiO_2) and the average molecular weight as calculated from the composition η. For example, when TiO_2 monomers are tracked:

$$v_i = \frac{\eta_{\mathrm{TiO_2},i} W_{\mathrm{TiO_2}}}{\rho_{\mathrm{TiO_2}} \mathrm{N_A}}. \tag{3.81}$$

The volume can be used to calculate other primary properties. The area of a neck created by the overlap with a neighbour p_j can be calculated by the partial derivative of particle volume with respect to x_{ij}:

$$A_{n,ij} = \frac{\partial v_i}{\partial x_{ij}} = \pi(r_i^2 - x_{ij}^2). \tag{3.82}$$

The free surface area of a primary is calculated as the area of a sphere, minus the area of the 'caps' from particle overlap:

$$A_i = \frac{\partial v_i}{\partial r_i} = 4\pi r_i^2 - 2\pi \sum_j \left(r_i^2 - r_i x_{ij}\right). \tag{3.83}$$

Because the model tracks the location and size of primaries, the diameter of gyration d_g and collision diameter d_c can be directly calculated. The diameter of gyration is defined [185] as

$$d_\mathrm{g}^2 = \frac{4}{\sum_i m_i} \sum_i m_i (|\boldsymbol{x}_i|^2 + r_{\mathrm{gp},i}^2), \tag{3.84}$$

where $r_{\mathrm{gp},i}$ is the radius of gyration of primary p_i and $|\mathbf{x}_i|$ is the distance from the centre of mass of the aggregate to the centre of the primary. For a sphere $r_{\mathrm{gp},i} = \sqrt{3/5} r_i$; however, it was chosen that $r_{\mathrm{gp},i} = r_i$, the radius of the primary, so that the collision diameter yields the primary diameter in the limit of $n_\mathrm{p} = 1$ as previously done in literature [106]. The collision diameter can then be defined as:

$$d_\mathrm{c}^2 = \frac{4}{\sum_i m_i} \sum_i m_i (|\mathbf{x}_i|^2 + r_i^2). \tag{3.85}$$

Mobility diameter is another common metric used to describe aggregates. In this thesis, the aerodynamic mobility diameter is used (in contrast to the electrical mobility diameter). Its physical meaning is the diameter of a spherical particle that experiences the same drag force and it is frequently measured in aerosol experiments [217]. The mobility diameter, d_m, is calculated according to the following equation under the assumption that the particle is in the

free-molecular regime [296, 56]:

$$d_{\mathrm{m}} = \frac{\sqrt{0.802(n_{\mathrm{p}}(P_q)-1)+1}}{n_{\mathrm{p}}(P_q)} \sum_{i=1}^{n_{\mathrm{p}}(P_q)} d_{\mathrm{p}}(p_i). \tag{3.86}$$

This equation was originally derived for linear chains of spheres. The review of mobility diameters in different regimes by Sorensen [329] suggests a power-law relationship of the form: $d_{\mathrm{m}} = r_0 * n_{\mathrm{p}}^c$ where r_0 is the primary radius assumed to be a uniform size and c is the exponent between 0.46 and 0.56. Sorensen [329] compared the power-law relationship with the relationship in Eqn. 3.86 and showed it is in good agreement when the number of primaries is small (<10). As the number of primaries in aggregates is small in this work, Eqn. 3.86 is a fair representation of the mobility diameter for comparison with experimental measurements.

Particle coagulation

The coagulation process is described in detail in Lindberg et al. [200]. Details of coagulation with the particle-number model can be found in Boje et al. [39]. In the free molecular regime, the orientations and point of contact are determined by ballistic cluster-cluster aggregation (BCCA) with a random impact parameter [152]. This is shown in Figure 3.2.

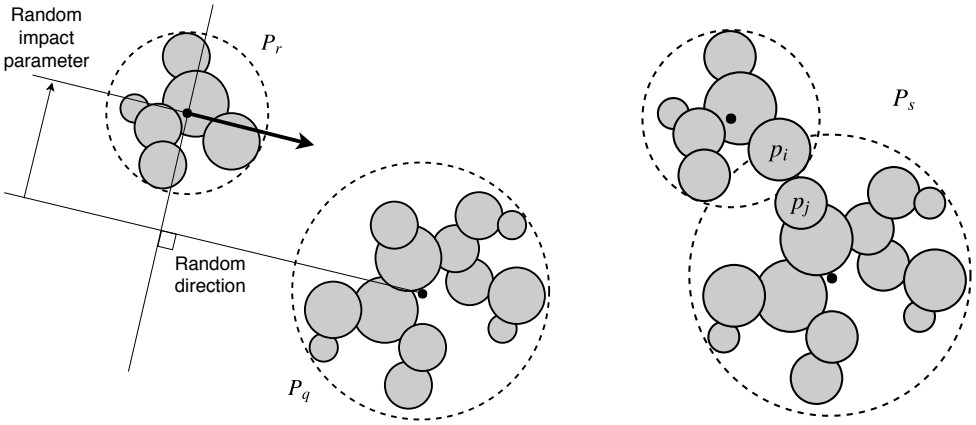

(a) Particles P_r and P_q before collision.

(b) New particle P_s following collision. Point contact between primary p_i from P_r and p_j from P_q.

Fig. 3.2 Ballistic cluster-cluster aggregation with a random impact parameter. Reprinted from Lindberg et al. [200] with permission from Elsevier.

The coagulation rate is given by a transition kernel, β^{TR}, which is half of the harmonic mean of the slip-flow kernel, β^{SF}, and free-molecular kernel, β^{FM} [162, 272]:

$$\beta^{\mathrm{SF}}(P_q,P_r)=\frac{2k_{\mathrm{B}}T}{3\mu}\left(\frac{1+1.257\mathrm{Kn}(P_q)}{d_c(P_q)}+\frac{1+1.257\mathrm{Kn}(P_r)}{d_c(P_r)}\right)\left(d_c(P_q)+d_c(P_r)\right), \tag{3.87}$$

$$\beta^{\mathrm{FM}}(P_q,P_r)=\varepsilon\sqrt{\frac{\pi k_{\mathrm{B}}T}{2}\left(\frac{1}{m(P_q)}+\frac{1}{m(P_r)}\right)}\left(d_c(P_q)+d_c(P_r)\right)^2, \tag{3.88}$$

$$\frac{1}{\beta^{\mathrm{TR}}(P_q,P_r)}=\frac{1}{\beta^{\mathrm{SF}}(P_q,P_r)}+\frac{1}{\beta^{\mathrm{FM}}(P_q,P_r)}. \tag{3.89}$$

The collision enhancement factor, ε, is assumed to be size independent and takes a value of 2.64 [415].The Knudsen number of the particles is calculated as:

$$\mathrm{Kn}(P_q)=\frac{2\lambda_{\mathrm{f}}}{d_{\mathrm{c}}(P_q)}. \tag{3.90}$$

The mean free path, λ_{f}, and viscosity, μ, are taken to be that of air at a given temperature T and pressure p. The temperature dependence of viscosity is described using the Sutherland's transport parametrisation [339]:

$$\lambda_{\mathrm{f}}=2.371\times10^{-5}\frac{T}{p}\ \ \mathrm{m}, \tag{3.91}$$

$$\mu=1.458\times10^{-6}\frac{T\sqrt{T}}{T+110.4}\ \mathrm{kg\,m^{-1}s^{-1}}. \tag{3.92}$$

The coagulation jump process is:

$$P_q(p_1,...,p_{n_{\mathrm{p}}(P_q)},\mathbf{C}(P_q))+P_r(p_1^*,...,p_{n_{\mathrm{p}}(P_r)}^*,\mathbf{C}(P_r))\rightarrow P_s(p_1,...,p_{n_{\mathrm{p}}(P_q)},p_1^*,...,p_{n_{\mathrm{p}}(P_r)}^*,\mathbf{C}(P_s)). \tag{3.93}$$

The connectivity matrix is updated as follows:

$$\mathbf{C}(P_s)=\begin{pmatrix} & & \vdots & \\ \mathbf{C}(P_q) & \cdots & 0 & \cdots \\ & & \vdots & \\ \vdots & & & \\ \cdots\ C_{ij} & \cdots & \mathbf{C}(P_r) & \\ \vdots & & & \end{pmatrix}, \tag{3.94}$$

where $C_{ij} = 1$.

A coagulation operator $\mathbb{K}$ acts on $(\mathbb{M} \cup \mathbb{X})$ to produce particles in $\mathbb{X}$. The total coagulation rate is as follows:

$$\begin{aligned} R_{\text{coag}} &= \frac{1}{2V_{\text{smp}}} \iint_{(\mathbb{M}\cup\mathbb{X})^2} \beta\left(\boldsymbol{\xi}_1, \boldsymbol{\xi}_2\right) N\left(d\boldsymbol{\xi}_1\right) N\left(d\boldsymbol{\xi}_2\right) \\ &= \frac{1}{V_{\text{smp}}} \left[\frac{1}{2} \sum_{\substack{i=1 \\ \boldsymbol{\xi}_i \in \mathbb{X}}}^{N(t)} \sum_{\substack{j=1; j\neq i \\ \boldsymbol{\xi}_j \in \mathbb{X}}}^{N(t)} \beta\left(\boldsymbol{\xi}_i, \boldsymbol{\xi}_j\right) + \sum_{\substack{i=1 \\ \boldsymbol{\xi}_i \in \mathbb{X}}}^{N(t)} \sum_{\substack{j=1 \\ \boldsymbol{\xi}_j \in \mathbb{M}}}^{N_{\text{thresh}}} \beta\left(\boldsymbol{\xi}_i, \boldsymbol{\xi}_j\right) N_j \right. \\ &\qquad \left. + \frac{1}{2} \sum_{\substack{i=1 \\ \boldsymbol{\xi}_i \in \mathbb{M}}}^{N_{\text{thresh}}} \sum_{\substack{j=1; (N_i<2 \iff j\neq i) \\ \boldsymbol{\xi}_j \in \mathbb{M}}}^{N_{\text{thresh}}} \beta\left(\boldsymbol{\xi}_i, \boldsymbol{\xi}_j\right) N_i N_j \right]. \end{aligned} \tag{3.95}$$

Particle inception

Inception is modelled as a collision limited process where $Ti(OH)_4$ is the collision species. It occurs at a rate, $\beta_{\text{IN}}^{\text{FM}}$, that depends on the gas phase concentrations and the temperature. The inception process only acts on the space of spherical primaries, $\mathbb{M}$, and not on the space of large particles, $\mathbb{X}$. Primary particles of type $\boldsymbol{\xi}_1 \in \mathbb{M}$ are created and this is modelled by incrementing the count at index 1 in the particle-number model:

$$2\text{Ti(OH)}_{4(\text{g})} \longrightarrow P_N(x_1) + 4\,\text{H}_2\text{O}_{(\text{g})}. \tag{3.96}$$

The inception rate is calculated using the free molecular kernel (Eqn. 3.88):

$$\beta_{\text{IN}}^{\text{FM}} = \varepsilon \sqrt{\frac{\pi k_{\text{B}} T}{2} \left(\frac{1}{m_i} + \frac{1}{m_i} \right)} \left(d_i + d_i\right)^2, \tag{3.97}$$

where m_i and d_i are the mass and collision diameter of the collision species, $Ti(OH)_4$. The collision diameters are assumed to be the same as calculated in Buerger et al. [47]: 0.5218 nm. The collision enhancement factor, ε, is assumed to be size independent and takes a value of 2.64.

Particle surface growth

The surface growth of particles is assumed to be collision limited with a rate that is determined by the free molecular kernel (Eqn. 3.88). The collision species (e.g. $Ti(OH)_4$) is consumed from the gas phase and condenses on the surface of a particle as TiO_2. The process is described

in full in Lindberg et al. [200]. The collision species are approximated by a spherical particle containing one TiO_2 unit. Therefore, the addition to a primary p_i, $\Delta\eta_i$, is equal to the composition of one TiO_2 unit. Under the assumption that the mass of the condensing species is that of TiO_2, the rate is:

$$\beta_{\mathrm{SG}}^{\mathrm{FM}} = \varepsilon \sqrt{\frac{\pi k_{\mathrm{B}} T}{2 m_{\mathrm{TiO_2}}}} \left(d_{\mathrm{c}}(P_q)\right)^2. \tag{3.98}$$

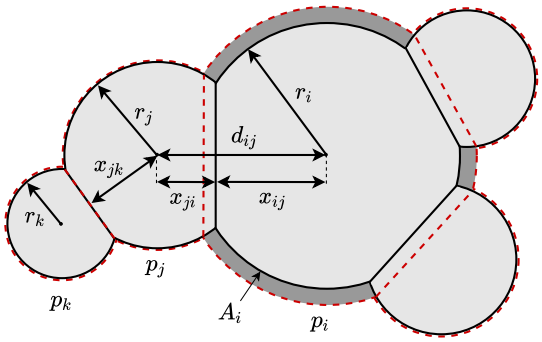

Fig. 3.3 A surface growth event. Mass is added to the free surface of primary p_i (dark shaded region). The new particle geometry is shown by the red dashed line. Immediate neighbours of p_i are labeled p_j, and neighbours of neighbours are labeled p_k. Reprinted from Lindberg et al. [200] with permission from Elsevier.

When a particle undergoes surface growth, the primary particle is randomly chosen with a probability of its free surface area divided by the total particle surface area: $A_i/A(P_q)$. The change in radius is proportional the volume added to the particle:

$$\frac{\mathrm{d}r_i}{\mathrm{d}t} = \frac{1}{A_i} \frac{\mathrm{d}V(P_q)}{\mathrm{d}t}. \tag{3.99}$$

Due to the change in radius of the primary particle, mass is transferred from the neighbours to the primary particle. This is a consequence of the model assumptions rather than a fundamental physical process. In this model, only a discrete number of atoms is transferred between neighbours. The following equations govern the mass transfer from neighbour p_j to p_i due to surface growth. Under the model assumptions, the change in volume of neighbour p_j with a set of $p_k \neq p_i$ neighbours is

$$\frac{\mathrm{d}v_j}{\mathrm{d}t} = -A_{n,ij} \frac{r_i}{d_{ij}} \frac{\mathrm{d}r_i}{\mathrm{d}t}, \tag{3.100}$$

from which the discrete change can be determined:

$$\Delta\eta_j = \frac{\Delta v_j}{v_{\mathrm{TiO_2}}}. \tag{3.101}$$

The jump process for surface growth is written as:

$$\begin{aligned} P_q(p_1,\ldots,p_i,p_j,\ldots,p_{n_p(P_q)},\mathbf{C}(P_q)) \rightarrow \\ P_q(p_1,\ldots,&p_i(\eta_i+\Delta\eta_i+\Delta\eta_j,r_i+\Delta r_i,\mathbf{x}_i),\\ &p_j(\eta_j-\Delta\eta_j,r_j,\mathbf{x}_j),\\ \ldots,&p_{n_p(P_q)},\mathbf{C}(P_q)), \end{aligned} \tag{3.102}$$

where p_j are neighbours of p_i, which each transfer $\Delta\eta_j$ from p_j to p_i.

Sintering

Sintering is described as two primary particles, p_i and p_j, moving closer to each other. The primary radii r_i and r_j will grow as the particles move toward each other due to mass conservation, while the neighbours p_k remain unchanged. The grain diffusion model is used to evaluate the sintering [92]. The full details of the sintering process are described in Lindberg et al. [200]. The model has three parameters that are explained below: a critical sintering diameter $d_{\mathrm{p,crit}}$, a sintering prefactor A_{s}, and a critical exponent, α_{crit}. Sintering happens according to the function g_{SC}:

$$g_{\mathrm{SC}}\left(P_j(\boldsymbol{\xi})\right) = P_i(\boldsymbol{\xi}). \tag{3.103}$$

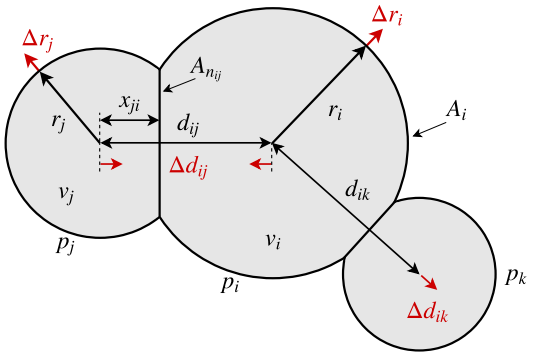

Fig. 3.4 Sintering of a single neck between primaries p_i and p_j. Neighbours not sintering are labelled p_k. The centre to centre separation decreases by Δd_{ij}. To conserve mass, the radii of the sintering primaries increase by Δr_i and Δr_j respectively and the separation with neighbouring primary p_k increases by Δd_{ik}. Reprinted from Lindberg et al. [200] with permission from Elsevier.

The rate of change in the distance between primary particles p_i to the neck formed with p_j is

$$\frac{\mathrm{d}x_{ij}}{\mathrm{d}t} = -\frac{d_\mathrm{p}^4}{16\theta A_{\mathrm{n},ij}}\left(\frac{1}{r_i - x_{ij}} - \frac{1}{a_{ij}}\right), \tag{3.104}$$

where a_{ij} is the neck radius, $A_{\mathrm{n},ij}$ is the neck area, r_i is the radius of the primary particle p_i, and $d_\mathrm{p} = \min(d_\mathrm{p}(p_i), d_\mathrm{p}(p_j))$ is the smaller primary diameter. The characteristic time is

$$\theta = 9.11 \times 10^{17} d_\mathrm{p}^4 T A_\mathrm{s} \exp\left(\frac{258\ \mathrm{kJ\ mol^{-1}}}{\mathrm{R_g} T}\left(1 - \left(\frac{d_{\mathrm{p,crit}}}{d_\mathrm{p}}\right)^{\alpha_\mathrm{crit}}\right)\right)\ \ \mathrm{s}, \tag{3.105}$$

where A_s is a sintering prefactor.
The rate of change in primary particle separation d_{ij} is:

$$\begin{aligned}\beta_\mathrm{SC}\left(p_i, p_j\right) = \frac{\mathrm{d}d_{ij}}{\mathrm{d}t} &= \frac{\mathrm{d}x_{ij}}{\mathrm{d}t} + \frac{\mathrm{d}x_{ji}}{\mathrm{d}t}, \\ &= -\frac{d_\mathrm{p}^4}{16\theta A_{\mathrm{n},ij}}\left(\frac{1}{r_i - x_{ij}} + \frac{1}{r_j - x_{ji}} - \frac{2}{a_{ij}}\right) \\ &\times \exp\left(\frac{-258\ \mathrm{kJ\ mol^{-1}}}{\mathrm{R_g} T}\left(1 - \left(\frac{d_{\mathrm{p,crit}}}{d_\mathrm{p}}\right)^{\alpha_\mathrm{crit}}\right)\right).\end{aligned} \tag{3.106}$$

Small particles have been observed to sinter and coalesce faster than larger particles [50, 309]. The critical sintering diameter $d_{\mathrm{p,crit}}$ [351] is the threshold at which instantaneous coalescence of primaries with $d_\mathrm{p} < d_{\mathrm{p,crit}}$. The threshold is taken to be 4 nm, which is consistent with modelling [50] and experimental [309] studies of sintering and coalescence of small nanoparticles. The exponent α_crit is the critical exponent that is treated as a model parameter that affects the sintering rate of small particles [199]. Lindberg et al. [199] suggested a value of 3 to be an appropriate value. This is close to the value 3.76 suggested by Buesser et al. [50] where there was an addition temperature dependent term in the non-linear fitting.

As two particles sinter closer together, mass is conserved. Assuming that the density does not change, this implies that the volume is conserved as well. As a consequence, the radii of primary particles i and j must increase to conserve mass. By defining an intermediate term,

$$B_{ij} = A_i + \sum_{k \neq j} A_{n,ik}\frac{r_i}{x_{ik}}, \tag{3.107}$$

the change of particle radii is described by [200]

$$\frac{\mathrm{d}r_i}{\mathrm{d}t} = \frac{-r_j A_{n_i j}^2 - x_{ji} B_{ji} A_{\mathrm{n},ij}}{d_{ij} B_{ij} B_{ji} + r_j A_{n,ij} B_{ij} + r_i A_{n,ij} B ji}\frac{\mathrm{d}d_{ij}}{\mathrm{d}t}. \tag{3.108}$$

The position of neighbours of particles i and j are shifted due to the change in radii and positions of particles i and j during sintering. Their change is calculated by

$$\frac{\mathrm{d}x_{ik}}{\mathrm{d}t} = \frac{r_i}{x_{ik}}\frac{\mathrm{d}r_i}{\mathrm{d}t} \text{ for } k \neq j. \tag{3.109}$$

The jump process for surface growth, assuming $\min(d_{p,i}, d_{p,j}) > d_{p,\mathrm{crit}}$, is

$$\begin{aligned} P_q(p_1,...,p_i,p_j,p_k,...,p_{n_p(P_q)},\mathbf{C}(P_q)) \rightarrow \\ P_q(p_1,...,p_i(\eta_i, r_i+\Delta r_i, \mathbf{x}_i+\Delta\mathbf{d}_{ij}), \\ p_j(\eta_j, r_j+\Delta r_j, \mathbf{x}_j+\Delta\mathbf{d}_{ij}), \\ p_k(\eta_k, r_k, \mathbf{x}_k+\Delta\mathbf{d}_{ij}),...,p_{n_p(P_q)},\mathbf{C}(P_q)), \end{aligned} \tag{3.110}$$

where

$$\Delta\mathbf{d}_{ij} = -\Delta d_{ij}\frac{\mathbf{x}_j-\mathbf{x}_i}{|\mathbf{x}_j-\mathbf{x}_i|}. \tag{3.111}$$

The sintering level is used to quantify how sintered two primary particles are to each other. For a neck with radius a_{ij}, the sintering level, s_{ij}, is defined as

$$s_{ij} = \frac{a_{ij}}{r_j} \text{ where } r_j \leq r_i, \tag{3.112}$$

which ranges from $0 \leq s_{ij} \leq 1$. Two processes can change the sintering level: surface growth and sintering.

Coalescence

As two particles sinter closer together, they will eventually coalesce. The coalescence process is the merger of two primary particles, with the smaller primary being added to the larger primary. The full details of the coalescence process are described in Lindberg et al. [200]. When two primaries p_i and p_j are merged, the neck radii of neighbours of p_j are preserved with the new primary p_i: $R_{ik,\mathrm{new}} = R_{kj}$. The neighbours are translated along the vector $\mathbf{x}_k - \mathbf{x}_j$. The volume of the new primary $p_{i,\mathrm{new}}$ is

$$v_{i,\mathrm{new}} = v_i + v_j. \tag{3.113}$$

The new radius $r_{i,\mathrm{new}}$ is one that satisfies

$$v_{i,\mathrm{new}} = \frac{4}{3}\pi r_{i,\mathrm{new}}^3 + \frac{\pi}{3}\sum_{(m\in k,l)}\left(2r_{i,\mathrm{new}}^3 + \left(r_{i,\mathrm{new}}^2 - \frac{A_{n,im}}{\pi}\right)^{\frac{3}{2}} - 3r_{i,\mathrm{new}}^2\left(r_{i,\mathrm{new}}^2 - \frac{A_{n,im}}{\pi}\right)^{\frac{1}{2}}\right), \tag{3.114}$$

where l and k are new neighbours. $r_{i,\mathrm{new}}$ is solved for using a Newton-Raphson method.

The jump process for coalescence can be described as follows:

$$\begin{aligned} P_q(p_1,...,p_i,p_j,p_k,p_l,...,p_{n_p(P_q)},\mathbf{C}(P_q)) \rightarrow \\ P_s(p_1,...,p_i(\eta_i+\eta_j,r_{\text{new}},\mathbf{x}_i), \\ p_k(\eta_k,r_k,\mathbf{x}_k+\Delta\mathbf{d}_{ik}), \\ p_l(\eta_l,r_l,\mathbf{x}_l+\Delta\mathbf{d}_{il}), \\ ...,p_{n_p(P_s)=n_p(P_q)-1},\mathbf{C}(P_s)), \end{aligned} \tag{3.115}$$

where $p_k \neq p_j$ are the neighbours of p_i, $p_l \neq p_i$ are the neighbours of p_j,

$$x_{ki} = \frac{d_{ik}^2 - r_i^2 + r_k^2}{2d_{ik}}, \tag{3.116}$$

$$\Delta\mathbf{d}_{ik} = -\left(\max\left(x_{ki} \pm \sqrt{x_{ki}^2 - r_k^2 + r_{i,\text{new}}}\right) - d_{ik}\right)\frac{\mathbf{x}_k - \mathbf{x}_i}{|\mathbf{x}_k - \mathbf{x}_i|}, \tag{3.117}$$

and

$$x_{lj} = \frac{d_{jl}^2 - r_j^2 + r_l^2}{2d_{jl}}, \tag{3.118}$$

$$\Delta\mathbf{d}_{il} = -\left(\max\left(x_{lj} \pm \sqrt{x_{lj}^2 - r_l^2 + r_{i,\text{new}}}\right) - d_{il}\right)\frac{\mathbf{x}_l - \mathbf{x}_i}{|\mathbf{x}_l - \mathbf{x}_i|}. \tag{3.119}$$

Population balance equations

Population balance equations can be formed for the number density $n(x)$ of particles of each type, $\boldsymbol{\xi} \in \mathbb{M}$ and $\boldsymbol{\xi} \in \mathbb{X}$. Let $\mathbb{I}$, $\mathbb{K}$, $\mathbb{S}$, and $\mathbb{C}$ in Eqs. (3.120)-(3.122) be the inception, coagulation, surface growth and sintering/coalescence operators respectively and let the subscript on the operator denote the relevant type space(s) involved in each case.

For $\boldsymbol{\xi}_1 \in \mathbb{M}$:

$$\begin{aligned} \frac{\mathrm{d}N_1}{\mathrm{d}t} =& \mathbb{I}_{\boldsymbol{\xi}_1\in\mathbb{M}} - \left(\mathbb{K}_{\boldsymbol{\xi}_1\in\mathbb{M}\leftrightarrow\mathbb{X}} + \mathbb{K}_{\boldsymbol{\xi}_1\in\mathbb{M}\leftrightarrow\mathbb{M}}\right) - \mathbb{S}_{\boldsymbol{\xi}_1\in\mathbb{M}} \\ \frac{\mathrm{d}N(\boldsymbol{\xi}_1)}{\mathrm{d}t} =& I(\boldsymbol{\xi}_1) - \sum_{\substack{j=1 \\ \boldsymbol{\xi}_j\in\mathbb{X}}}^{N(t)} \beta\left(\boldsymbol{\xi}_1,\boldsymbol{\xi}_j\right)N(\boldsymbol{\xi}_1)N\left(\boldsymbol{\xi}_j\right) - \sum_{\substack{j=1;(N_1<2 \iff j\neq 1) \\ x_j\in\mathbb{M}}}^{N_{\text{thresh}}} \beta\left(\boldsymbol{\xi}_1,\boldsymbol{\xi}_j\right)N(\boldsymbol{\xi}_1)N\left(\boldsymbol{\xi}_j\right) \\ & - \beta_{\text{SG}}(\boldsymbol{\xi}_1)N(\boldsymbol{\xi}_1). \end{aligned} \tag{3.120}$$

For $\boldsymbol{\xi}_i \in \mathbb{M}$, $i = \{2,3,\ldots,N_{\text{thresh}}\}$:

$$\begin{aligned}
\frac{\mathrm{d}N_i}{\mathrm{d}t} =& -\left(\mathbb{K}_{\boldsymbol{\xi}_i \in \mathbb{M}\leftrightarrow\mathbb{X}} + \mathbb{K}_{\boldsymbol{\xi}_i \in \mathbb{M}\leftrightarrow\mathbb{M}}\right) + \left(\mathbb{S}_{\mathbb{M}} - \mathbb{S}_{\boldsymbol{\xi}_i \in \mathbb{M}\cup\mathbb{X}}\right) \\
\frac{\mathrm{d}N(\boldsymbol{\xi}_i)}{\mathrm{d}t} =& -\sum_{\substack{j=1 \\ \boldsymbol{\xi}_j\in\mathbb{X}}}^{N(t)} \beta\left(\boldsymbol{\xi}_i,\boldsymbol{\xi}_j\right) N(\boldsymbol{\xi}_i) N\left(\boldsymbol{\xi}_j\right) - \sum_{\substack{j=1;(N_i<2 \iff j\neq i) \\ \boldsymbol{\xi}_j\in\mathbb{M}}}^{N_{\text{thresh}}} \beta\left(\boldsymbol{\xi}_i,\boldsymbol{\xi}_j\right) N(\boldsymbol{\xi}_i) N\left(\boldsymbol{\xi}_j\right) \\
& - \beta_{\text{SG}}(\boldsymbol{\xi}_i) N(\boldsymbol{\xi}_i) + \sum_{\substack{j=1 \\ \boldsymbol{\xi}_j\in\mathbb{M}}}^{i-1} \beta_{\text{SG}}\left(\boldsymbol{\xi}_j\right) N\left(\boldsymbol{\xi}_j\right) 1_{g_{\text{SG}}(\boldsymbol{\xi}_j)=\boldsymbol{\xi}_i}.
\end{aligned} \tag{3.121}$$

For $\boldsymbol{\xi}_i \in \mathbb{X}$, $i = \{1,2,\ldots,N(t)\}$:

$$\begin{aligned}
\frac{\mathrm{d}N_i}{\mathrm{d}t} =& \left(\mathbb{K}_{\mathbb{M}\leftrightarrow\mathbb{M}} + \mathbb{K}_{\mathbb{X}\leftrightarrow\mathbb{M}} + \mathbb{K}_{\mathbb{X}\leftrightarrow\mathbb{X}} - \mathbb{K}_{\boldsymbol{\xi}_i\in\mathbb{X}\leftrightarrow\mathbb{M}} - \mathbb{K}_{\boldsymbol{\xi}_i\in\mathbb{X}\leftrightarrow\mathbb{X}}\right) \\
& + \left(\mathbb{S}_{\mathbb{M}\cup\mathbb{X}} - \mathbb{S}_{\boldsymbol{\xi}_i\in\mathbb{X}}\right) + \left(\mathbb{C}_{\mathbb{X}} - \mathbb{C}_{\boldsymbol{\xi}_i\in\mathbb{X}}\right) \\
\frac{\mathrm{d}N(\boldsymbol{\xi}_i)}{\mathrm{d}t} =& \beta_{\text{SG}}(\boldsymbol{\xi}_{\text{thresh}}) N(\boldsymbol{\xi}_{\text{thresh}}) 1_{g_{\text{SG}}(\boldsymbol{\xi}_{\text{thresh}})=\boldsymbol{\xi}_i} \\
& + \frac{1}{2} \sum_{\substack{j=1 \\ \boldsymbol{\xi}_j\in\mathbb{M}}}^{N_{\text{thresh}}} \sum_{\substack{k=1;(N_j<2 \iff k\neq j) \\ \boldsymbol{\xi}_k\in\mathbb{M}}}^{N_{\text{thresh}}} \beta\left(\boldsymbol{\xi}_j,\boldsymbol{\xi}_k\right) N\left(\boldsymbol{\xi}_j\right) N(\boldsymbol{\xi}_k) 1_{\boldsymbol{\xi}_j+\boldsymbol{\xi}_k=\boldsymbol{\xi}_i} \\
& + \sum_{\substack{j=1 \\ \boldsymbol{\xi}_j\in\mathbb{M}}}^{N_{\text{thresh}}} \sum_{\substack{k=1 \\ \boldsymbol{\xi}_k\in\mathbb{X}}}^{N(t)} \beta\left(\boldsymbol{\xi}_j,\boldsymbol{\xi}_k\right) N\left(\boldsymbol{\xi}_j\right) N(\boldsymbol{\xi}_k) 1_{\boldsymbol{\xi}_j+\boldsymbol{\xi}_k=\boldsymbol{\xi}_i} \\
& + \frac{1}{2} \sum_{\substack{j=1 \\ \boldsymbol{\xi}_j\in\mathbb{X}}}^{N(t)} \sum_{\substack{k=1;k\neq j \\ \boldsymbol{\xi}_k\in\mathbb{X}}}^{N(t)} \beta\left(\boldsymbol{\xi}_j,\boldsymbol{\xi}_k\right) N\left(\boldsymbol{\xi}_j\right) N(\boldsymbol{\xi}_k) 1_{\boldsymbol{\xi}_j+\boldsymbol{\xi}_k=\boldsymbol{\xi}_i} \\
& - \sum_{\substack{j=1;j\neq i \\ \boldsymbol{\xi}_j\in\mathbb{X}}}^{N(t)} \beta\left(\boldsymbol{\xi}_i,\boldsymbol{\xi}_j\right) N(\boldsymbol{\xi}_i) N\left(\boldsymbol{\xi}_j\right) - \sum_{\substack{j=1 \\ \boldsymbol{\xi}_j\in\mathbb{M}}}^{N_{\text{thresh}}} \beta\left(\boldsymbol{\xi}_i,\boldsymbol{\xi}_j\right) N(\boldsymbol{\xi}_i) N\left(\boldsymbol{\xi}_j\right) \\
& + \sum_{\substack{j=1 \\ \boldsymbol{\xi}_j\in\mathbb{X}}}^{i-1} \beta_{\text{SG}}\left(\boldsymbol{\xi}_j\right) N\left(\boldsymbol{\xi}_j\right) 1_{g_{\text{SG}}(\boldsymbol{\xi}_j)=\boldsymbol{\xi}_i} \\
& - \beta_{\text{SG}}(\boldsymbol{\xi}_i) N(\boldsymbol{\xi}_i) + \sum_{j=1}^{n_{\text{p}}(P(\boldsymbol{\xi}_i))} \sum_{k=1}^{j-1} \beta_{\text{SC}}\left(p_j,p_k\right) 1_{g_{\text{SC}}(\boldsymbol{\xi}_j)=\boldsymbol{\xi}_i} - \beta_{\text{SC}}(\boldsymbol{\xi}_i) N(\boldsymbol{\xi}_i).
\end{aligned} \tag{3.122}$$

3.4 Methods

3.4.1 Solver implementation

The partial differential equations that are the governing equations are discretised using the finite volume method that is common in computational fluid dynamics. The PISO algorithm [148] is used to handle the pressure-velocity coupling. The details of the software, algorithm, and validation test cases are presented in the next sections.

Software

OpenFOAM [343] is an open source toolbox for solving continuum mechanics. The code is written in C++ with object-oriented programming and makes heavy use of templating to reduce code duplication. OpenFOAM provides many libraries for turbulence and thermochemical models in addition to prebuilt pre-processing, post-processing and physical solvers. If a model or algorithm is missing, the user can create their own versions of the executables or libraries to complete the missing functionality.

*k*inetics© [65] is a detailed chemical modelling suite that is able to solve a range of 0- and 1D problems in addition to flames, engines, and reactor networks. The 0D models can solve the detailed ordinary differential equations of coupled gas-phase chemistry and particle models. Detailed thermochemical and transport models are available through the software (as described in Section 3.2.1). Outside the range of solvers provided, a C/Fortran Application Programming Interface is available to use the numerical tools in custom executables.

It was found that the transport libraries provided with OpenFOAM were inadequate for laminar combustion; for example, the viscosity for a multicomponent mixture is calculated by a mass-weighted sum of individual components, and the diffusion coefficients were not mixture dependent. A custom solver was created to accomplish the following: (i) implement more physical transport models commonly used in combustion; (ii) replace the inbuilt OpenFOAM chemistry integrator with the chemistry tools provided through the *k*inetics© Application Programming Interface [65]; and (iii) solve a coupled population balance using the Method of Moments with Interpolative Closure [116].

Algorithm

The algorithm used in this work is rooted in the PISO algorithm [148] for handling the velocity-pressure coupling, with the addition of solving scalar fields for chemistry and particle fields. A weakly-incompressible (low Mach) version of a laminar transport solver was used due to the variable density. To maintain the ability to solve without moments, the algorithm contains

logical checks to skip sections of the code that would pertain to the moments. These are not shown for clarity.

Algorithm 1 presents the full time-marching loop and is visualised in Figure 3.5. The code initialises (Alg. 5) by creating all of the necessary OpenFOAM controls including the time directories, mesh, and solver controls. Switches are read in via an OpenFOAM dictionary that controls which equations are solved (such as whether to solve the species transport equations). The aim of these switches is to provide algorithmic control to overcome numerical stiffness and save computational cost. These switches are not shown in the algorithms for readability. Next, the *k*inetics API is initialised and the gas-phase chemistry models and particle models are read in. The number of species, moments, and unknowns are retrieved from the API to dynamically allocate local work arrays to be passed between the calling code and the API. Next, fields are created in this order: species, fluid properties, and moments (if required). Before advancing to the time-stepping routine, the transport properties are updated (Alg. 7).

For each time step, the following procedure is completed. The time step is set, whether fixed *a priori* or determined by limiting the Courant number, Co:

$$\mathrm{Co} = \frac{U\Delta t}{\Delta x}, \tag{3.123}$$

where Δx is the grid spacing. The chemistry (and particle) ODEs are then integrated as a closed batch reactor to solve for the species, temperature, and particle source terms. The species and moment source terms are calculated as the time averaged difference in concentration and the enthalpy source term is calculated as the sum of the species source term and its specific enthalpy. Species, enthalpy, and particle fluxes are calculated. Next, the velocity equation is solved. The species equations are solved for all active species except for an inert species (the carrier gas) which is solved as the balance. The enthalpy transport equation is then solved. The gas mole fraction, average molecular weight, and compressibility are updated before moving into the pressure-velocity coupling of the PISO algorithm. At the end of the time step, if the time step advanced to the next write step, the solution is saved and any post processing tools are also run.

Modern computational power allows for this computation to be run in parallel. The solver is parallelised using a domain decomposition method, where the domain is split into smaller domains for each processor to solve for. Adjacent domains are connected using halo cells.

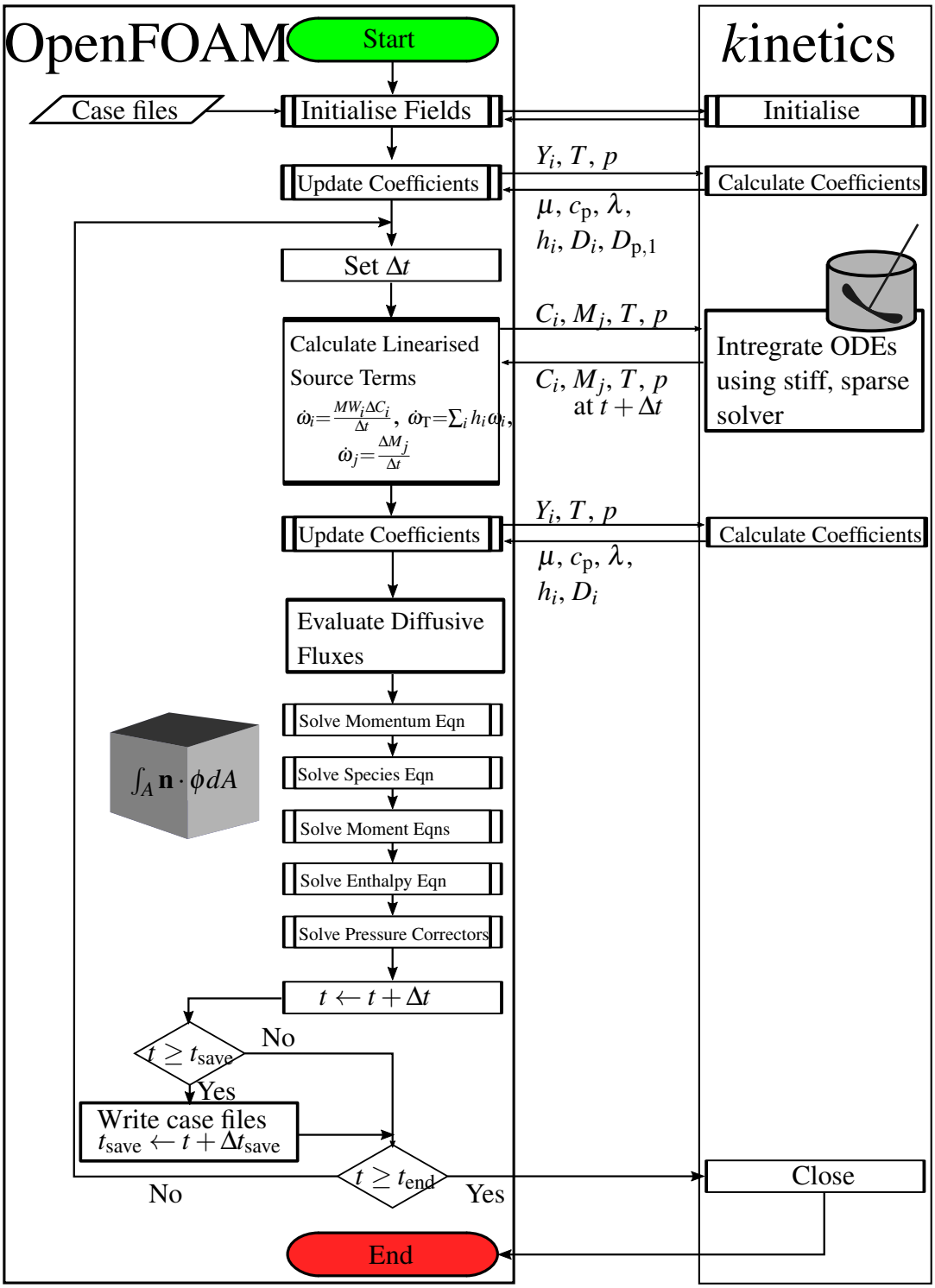

Fig. 3.5 A diagram of the implemented algorithm. The governing transport equations are solved using OpenFOAM [343] while detailed coefficients and source terms are calculated using *k*inetics [65].

Algorithm 1: Implemented PISO algorithm

Output : Solutions from t_{start} to t_{end} with spacing of t_{incr}
initialisation (Alg. 5)
update transport properties, (Alg. 7)
$t_{\text{write}} \leftarrow t_{\text{start}} + t_{\text{incr}}$
while $t < t_{\text{end}}$ **do**
  set Δt
  integrate chemistry, linearise source term ($\dot{\omega}_i$, $\dot{\omega}_{\text{T}}$, $\dot{\omega}_j$), (Alg. 2)
  update transport properties: μ (Eqn. 3.16), λ (Eqn. 3.25), c_{P} (Eqn. 3.7), D_i (Eqn. 3.27), D_{p_1} (Eqn. 3.29), V_{T} (Eqn. 3.32), (Alg. 7)
  calculate species and enthalpy diffusion flux, $\rho Y_i V_i^c$, $\rho \sum_{i=1}^{N} c_{\text{p}_i} Y_i V_i^c$ (Eqn. 3.28)
  solve velocity equation (Eqn. 3.2)
  foreach species **do**
    solve species mass fraction transport equation (Eqn. 3.3)
  end
  foreach moment **do**
    solve moment transport equation (Eqn. 3.5)
  end
  solve enthalpy transport equation (Eqn. 3.4)
  calculate mole fractions, X_i, and average molecular weight, W
  update $\psi = \frac{W}{\text{R}_{\text{g}} T}$
  `/* Pressure corrector loop */`
  $p_{\text{iter}} \leftarrow 0$
  while *not converged* **do**
    solve pressure coupling
    $p_{\text{iter}}++$
    if $p_{\text{iter}} \geq$ *max iterations* **then**
      break
    end
  end
  $t \leftarrow t + \Delta t$
  if $t \geq t_{\text{write}}$ **then**
    save solution
    $t_{\text{write}} \leftarrow t_{\text{write}} + t_{\text{incr}}$
    if $t_{\text{write}} \geq t_{\text{end}}$ **then**
      $t_{\text{write}} \leftarrow t_{\text{end}}$
    end
  end
end

Algorithm 2: Solve Chemistry

Input scalars : time step, Δt; lower bound for reactions, T_{L}; molecular weights (kg/mol), W_i

Input scalars fields : pressure, p; density, ρ; temperature, T; mass fractions, Y_i; moments, M_j

Output : source terms for chemistry, $\dot{\omega}_i$; enthalpy, $\dot{\omega}_{\mathrm{T}}$; and moments, $\dot{\omega}_j$

foreach *cell* **do**

  $T_{cell} \leftarrow T\,[cell]$

  $\rho_{cell} \leftarrow \rho\,[cell]$

  $p_{cell} \leftarrow p\,[cell]$

  if $T_{cell} > T_{\mathrm{L}}$ **then**

    /* Create array of variables (ϕ) to pass to *k*inetics API and store initial state (C^{I}, M^{I}) */

    for $i = 0; i < \mathrm{N_{sp}}; i++$ **do**

      $\phi[i], \mathrm{C}^{\mathrm{I}}[i] \leftarrow \rho_{cell} * Y_i[cell]/W_i$

    end

    $\phi[\mathrm{N_{sp}}] \leftarrow T_{cell}$

    for $j = 0; j < \mathrm{N_{mom}}; j++$ **do**

      $\phi[\mathrm{N_{sp}} + 1 + j], \mathrm{M}^{I}_{\mathrm{cell}}[j] \leftarrow \rho_{cell} * \hat{M}_j[cell]$

    end

    /* Get Species Specific Enthalpy at T_{cell} */

    $h \leftarrow$Get Specific Enthalpy(T_{cell})

    /* Integrate chemical ODEs in a batch reactor over Δt */

    $\phi \leftarrow$Integrate Chemistry$(\phi, p_{cell}, \Delta t)$

    /* Calculate averaged source terms */

    for $i = 0; i < \mathrm{N_{sp}}; i++$ **do**

      $\mathrm{C}^{\mathrm{F}}[i] \leftarrow \phi[i]$

      $\dot{\omega}_i\,[cell] \leftarrow \frac{\mathrm{C}^{\mathrm{F}}[i] - \mathrm{C}^{\mathrm{I}}[i]}{\Delta t} * W_i$

      $\dot{\omega}_{\mathrm{T}}\,[cell] \leftarrow \dot{\omega}_T\,[cell] + \dot{\omega}[i]\,[cell] * h[i]$

    end

    for $j = 0; j < \mathrm{N_{mom}}; j++$ **do**

      $\mathrm{M}^{F}_{\mathrm{cell}}[j] \leftarrow \phi[\mathrm{N}_{sp} + 1 + j]$

      $\dot{\omega}_j\,[cell] \leftarrow \frac{\mathrm{M}^{F}_{\mathrm{cell}}[j] - \mathrm{M}^{I}_{\mathrm{cell}}[j]}{\Delta t}$

    end

  else

    $\dot{\omega}_i\,[cell]\,, \dot{\omega}_{\mathrm{T}}\,[cell]\,, \dot{\omega}_j\,[cell] \leftarrow 0$

  end

end

3.4.2 Method of moments

The method of moments transforms the population balance equation from an infinite set of PDEs into a finite set of PDEs by solving for the moments of the size distribution, M_j. It is used here to solve the univariate population balance equation as presented in Section 3.3.1. For a population of particles of size k and number density $N(k)$, the moments of the size distribution are defined as

$$M_j = \sum_{k=1}^{\infty} k^j N(k). \tag{3.124}$$

In order to exactly reconstruct the PSD, the infinite set of moments must be known. An infinite set of moments is not solved for in practice, which makes reconstructing the PSD challenging. Even without full resolution of the PSD, some integral quantities of the distributions commonly of interest are attainable. These include total number density, area density, mass density, and average diameter:

$$\text{Number density} = M_0, \tag{3.125}$$

$$\text{Area density} = A_1 M_{2/3}, \tag{3.126}$$

$$\text{Mass density} = m_1 M_1, \text{ and} \tag{3.127}$$

$$\text{Average diameter} = d_1 \frac{M_{1/3}}{M_0}. \tag{3.128}$$

These population averaged properties are reliant on the spherical particle shape assumption and dependent on the monomer properties: A_1, the monomer surface area; m_1, the mass of a monomer; and d_1, the monomer diameter. Under the spherical particle assumption, A_1 and d_1 are calculated from m_1 using the density. In this work, the bulk density is taken to be that of rutile ($\rho_{\text{rutile}} = 4250$ kg m^{-3}).

When working with moments, it is common to use reduced moments, μ_j, that are defined as

$$\mu_j = \frac{M_j}{M_0}. \tag{3.129}$$

Interpolative closure

The method of moments equations are generally unclosed where fractional-order moments are required but not solved for. The fractional-order moments are obtained using Lagrangian interpolation (extrapolation in the case of negative order moments) using reduced, whole-

ordered moments, μ_j, as described by Frenklach [115]. L_q is the Lagrange operator with respect to q,

$$\log(\mu_q) \approx \sum_{i=0}^{n} \log(\mu_i) L_i^n(q), \tag{3.130}$$

where

$$n = \begin{cases} N_{\text{mom}} - 1, & p > 0, \\ 2, & p < 0. \end{cases} \tag{3.131}$$

Additionally, there are terms in the coagulation source term equations that are unclosed. The ${}^{\frac{1}{2}}f_{r,j-r}$ terms that appear in the coagulation source terms (Eqn. 3.52) are a subset of a more generic function:

$${}^{m}f_{x,y} = \sum_{k_1=k_{min}}^{\infty} \sum_{k_2=k_{min}}^{\infty} \frac{k_1^x k_2^y}{\sqrt{k_1 k_2}} (k_1 + k_2)^m \left(k_1^{\frac{1}{3}} + k_2^{\frac{1}{3}} \right)^2 \frac{N(k_1) N(k_2)}{M_0^2} \quad m \in \mathbb{R}. \tag{3.132}$$

This family of functions is only closed for natural numbers $m \in \mathbb{N}$. The $m = \frac{1}{2}$ terms can be obtained by logarithmic Lagrangian interpolation from the $m \in \mathbb{N}$ terms. These terms act as 'grid points' in Lagrange space and have the following form based on reduced moments:

$${}^{m}f_{x,y} = \sum_{r=0}^{j} \binom{j}{r} \left(\mu_{r+x+\frac{1}{6}} \mu_{j+y-r-\frac{1}{2}} + 2\mu_{r+x-\frac{1}{6}} \mu_{j+y-r-\frac{1}{6}} + \mu_{r+x-\frac{1}{2}} \mu_{j+y-r-\frac{1}{6}} \right) \quad m \in \mathbb{N}, \tag{3.133}$$

$$\log\left({}^{\frac{1}{2}}f_{x,y} \right) \approx \sum_{i=0}^{n} \log({}^{i}f_{x,y}) L_i^n\left(\frac{1}{2}\right), \tag{3.134}$$

where $L_i^n(m)$ is an i^{th} Lagrange polynomial of order n,

$$L_i^n(m) = \prod_{j=0, j\neq i}^{n} \frac{m-j}{i-j}, \tag{3.135}$$

and the order n is determined by

$$n = \min(3, \mathrm{N}_{\text{mom}} - 1 - \max(x, y)). \tag{3.136}$$

3.4.3 Direct simulation Monte Carlo Method

The evolution of particles described by the hybrid particle-number/detailed particle model (Section 3.3.3) was solved using a stochastic, direct simulation Monte Carlo (DSMC) method. This method simulates the evolution of an ensemble of representative stochastic particles using a direct simulation algorithm (Alg. 3). Stochastic particles are transformed by jump processes, which are comprised of a mathematical transformation and a process rate. The simulation progresses by randomly selecting a jump process and the necessary required stochastic particles, performing the jump process, and advancing the simulation by an exponentially distributed waiting time.

Several adjustments were made to improve the computational performance of the direct simulation algorithm. To decrease the cost of calculating the coagulation rate, a majorant kernel with fictitious jumps [95, 124, 272] was used. To more efficiently handle sintering and surface growth (also known as condensation), a linear process deferment algorithm [274] was used. The details of the algorithm and implementation can be found in references [39, 200].

The two particle models are implemented as follows. The particle-number model is efficiently stored as a list of size $\mathbb{R}^{N_{\text{thresh}}}$. Additional information is cached to further increase efficiency, such as total mass and a list of diameters. The detailed particle model is implemented in a binary tree structure [305, 311], where the leaves of the tree are primary particle nodes. The limitations (such as no ternary connections or closed loop structures) are discussed in Lindberg et al. [198]. The models and algorithms are implemented in a C++ library known as *MOpS Particle Simulator* [69].

Post-processing Lagrangian trajectories

Particle models can be used as a post-processing step [198]. In the first simulation, a representative particle model is used to simulate growth fully coupled to the gas-phase. Data from this simulation is extracted along Lagrangian trajectories and is used as the input for a second simulation with the detailed particle model. This data includes temperature, pressure, and species concentration. The trajectories should follow the particle path; the path is usually calculated from convective and thermophoretic velocities. In the second simulation, the PBE is spatially homogeneous, such that the ensemble of particles are travelling in a sample volume through the flame to the stagnation plate. The number densities of the particles evolve with the following governing equation:

$$\frac{\mathrm{d}N(\boldsymbol{\xi},t)}{\mathrm{d}\tau} = R(\boldsymbol{\xi}) - \Gamma N(\boldsymbol{\xi},t), \tag{3.137}$$

where N is the number density of particles of type $\boldsymbol{\xi}$, R is the rate of change due to particle processes, and Γ is the rate of gas-phase expansion.

The stochastic method approximates the true population by tracking an ensemble of computational particles in a sample volume of size V_{smp}. The expansion of the sample volume due to gas-phase expansion and contraction is:

$$\Gamma = \frac{1}{V_{\text{smp}}}\frac{\mathrm{d}V_{\text{smp}}}{\mathrm{d}\tau} = \frac{1}{\rho}\frac{\mathrm{d}\rho}{\mathrm{d}\tau}. \tag{3.138}$$

Thermophoresis is a significant driving factor near the stagnation surface in jet-wall stagnation flames. Therefore, a thermophoretic correction is needed when post-processing trajectories of jet-wall stagnation flames. The transport equation for particles of type $\boldsymbol{\xi}$ is a function of space $\boldsymbol{\zeta}$ and time t:

$$\frac{\partial\left(\rho\frac{N(\boldsymbol{\xi},t)}{\rho}\right)}{\partial t} + \nabla_{\boldsymbol{\zeta}}\cdot\left(\rho U\frac{N(\boldsymbol{\xi},t)}{\rho}\right) + \nabla_{\boldsymbol{\zeta}}\cdot\left(\rho V_{\mathrm{T}}\frac{N(\boldsymbol{\xi},t)}{\rho}\right) - \nabla_{\boldsymbol{\zeta}}\cdot\left(\rho D_{\boldsymbol{\xi}}\nabla_{\boldsymbol{\zeta}}\frac{N(\boldsymbol{\xi},t)}{\rho}\right) = R(\boldsymbol{\xi}). \tag{3.139}$$

When the post-processing is applied, the number density of particles, $N(\boldsymbol{\xi},t)$, is assumed to be a field at steady state (i.e. $\partial/\partial t = 0$). An additional assumption is applied: diffusive transport is small compared to convective and thermophoretic transport. This yields the following form:

$$\nabla_{\boldsymbol{\zeta}}\cdot((U+V_{\mathrm{T}})N(\boldsymbol{\xi},t)) = R(\boldsymbol{\xi}), \tag{3.140}$$

$$(U+V_{\mathrm{T}})\cdot\nabla_{\boldsymbol{\zeta}}N(\boldsymbol{\xi},t) + N(\boldsymbol{\xi},t)\left(\nabla_{\boldsymbol{\zeta}}\cdot(U) + \nabla_{\boldsymbol{\zeta}}\cdot(V_{\mathrm{T}})\right) = R(\boldsymbol{\xi}). \tag{3.141}$$

The following transformation, $\mathrm{d}\boldsymbol{\zeta} = (U+V_{\mathrm{T}})\mathrm{d}\tau$, can then be applied to move to an equation that is a function of residence time of a Lagrangian particle:

$$\frac{\mathrm{d}N(\boldsymbol{\xi},t)}{\mathrm{d}\tau} + \frac{1}{U+V_{\mathrm{T}}}\left(\frac{\mathrm{d}U}{\mathrm{d}\tau} + \frac{\mathrm{d}V_{\mathrm{T}}}{\mathrm{d}\tau}\right)n(\boldsymbol{\xi},t) = R(\boldsymbol{\xi}). \tag{3.142}$$

The derivative of convective velocity can be replaced using the continuity equation:

$$\frac{\mathrm{d}N(\boldsymbol{\xi},t)}{\mathrm{d}\tau} = R(\boldsymbol{\xi}) - \frac{1}{U+V_{\mathrm{T}}}\left(\frac{U}{\rho}\frac{\mathrm{d}\rho}{\mathrm{d}\tau} + \frac{\mathrm{d}V_{\mathrm{T}}}{\mathrm{d}\tau}\right)N(\boldsymbol{\xi},t). \tag{3.143}$$

Therefore, for a Lagrangian trajectory subject to thermophoretic velocity, the expansion rate of the sample volume is:

$$\Gamma = \frac{1}{U+V_{\mathrm{T}}}\left(\frac{U}{\rho}\frac{\mathrm{d}\rho}{\mathrm{d}\tau} + \frac{\mathrm{d}V_{\mathrm{T}}}{\mathrm{d}\tau}\right). \tag{3.144}$$

It is worth mentioning that this form retains the original form of the volumetric expansion when the thermophoretic velocity is zero.

Algorithm

The direct simulation Monte Carlo algorithm for the particle-number/particle model can be found in the following algorithms, with further algorithms specific to physical processes can be found in the Appendix B. The implementation of ballistic cluster-cluster aggregation with a random impact parameter (BCCA) described by Jullien [152] is shown in Algorithm 9. Particle rotations are performed using the method proposed by Arvo [13] and particle bounding spheres are calculated using the method proposed by Ritter [294].

A surface adjustment as a result of a condensation event is performed according to Algorithm 10. Note, it is assumed that a primary is composed solely of discrete units of TiO_2. Therefore, a redistribution of composition (mass) between primaries only takes place if the volume change of the neighbour is sufficiently large. This can lead to some deviation between the volume derived from the composition

$$v_i = \frac{\eta_{\mathrm{TiO_2},i} M_{\mathrm{TiO_2}}}{\rho_{\mathrm{TiO_2}} \mathrm{N_A}}, \tag{3.145}$$

and the volume derived from the primary geometry

$$v_i = \frac{4}{3}\pi r_i^3 - \frac{1}{3}\pi \sum_j (2r_i^3 + x_{ij}^3 - 3r_i^2 x_{ij}). \tag{3.146}$$

The system, however, is to some extent self-correcting due to two processes. First, the movement of a neck during a surface adjustment will to a certain degree be offset by an opposing change during a possible future surface adjustment to the other primary. Second, the need to redistribute mass is eliminated by the merger of the two primaries during a coalescence event. Furthermore, the likelihood of the primaries coalescing is increased with more surface growth of one primary at the expense of the other.

Sintering is performed on a particle P_q using Algorithm 11. Where two primaries, p_i and p_j, are in point contact (i.e. their neck area is $A_{\mathrm{n},ij} = 0$) the sintering rate is undefined. In this case, a neck radius of 1% of the smaller primary radius, $R_{ij} = \min(r_i, r_j)/100$, is assumed.

Neighbouring primaries p_i and p_j in a particle P_q are merged according to Algorithm 12, once the sintering level (Eq. 3.112) exceeds $s_{ij} \geq 0.95$. The sintering level is defined while the neck remains between the primary particle centres and the primaries are merged as the neck leaves this region.

Algorithm 3: Direct simulation Monte Carlo with particle-number/particle model

Input : $\mathbf{X}(t_0)$, $T(t_0)$, $z_{\mathbb{X}}(t_0)$, $z_{\mathbb{M}}(t_0)$, N_{thresh}, t_{split}
Output : $z_{\mathbb{X}}(t_f)$, $z_{\mathbb{M}}(t_f)$

Set $t \leftarrow t_0$, $\mathbf{X} \leftarrow \mathbf{X}(t_0)$, $T \leftarrow T(t_0)$, $z_{\mathbb{X}} \leftarrow z_{\mathbb{X}}(t_0)$, $z_{\mathbb{M}} \leftarrow z_{\mathbb{M}}(t_0)$

Calculate overall rates of non-deferred processes:

$$R_{\text{IN}} = I(\mathbf{X}, T); \qquad R_{\text{CG}} = \mathbb{K}\left((\mathbb{X} \cup \mathbb{M})^2\right); \qquad R_{\text{tot}} = R_{\text{IN}} + R_{\text{CG}}$$

Select a waiting time $\tau \sim \exp(R_{\text{total}})$

if $t + \tau < t_{split}$ **then**

Choose process $\in$ {IN, CG} using:

$$\mathbb{P}(\text{process}) = R_{\text{process}} \cdot {R_{\text{tot}}}^{-1}$$

if *process* = *IN* **then**

Update property sums for change in number of particles at index 2:

$$N_2 \leftarrow (N_2 + 1); \qquad N(z_{\mathbb{M}}) \leftarrow (N(z_{\mathbb{M}}) + 1)$$

Update gas phase $\mathbf{X}$, T

else if *process* = *CG* **then**

if $(N(z_{\mathbb{M}}) + N(z_{\mathbb{X}})) > 1$ **then**

Pick $(P_i, P_j) \in (\mathbb{X} \cup \mathbb{M})$ (Alg. 8) and allow coagulation with probability:

$$\mathbb{P}_{i,j} = \beta_{\text{tr}}(P_i, P_j) \cdot \hat{\beta}_{\text{tr}}(P_i, P_j)^{-1}$$

if *Coagulation allowed* **then**

Coagulation between P_i and P_j forms P_k

if $(P_k \in \mathbb{M}, k = \{i, j\})$ **then**

Update property sums for change in number of particles at index k

$$N_k \leftarrow (N_k - 1); \qquad N(z_{\mathbb{M}}) \leftarrow N(z_{\mathbb{M}}) - 1$$

if $(P_i \in \mathbb{M}, P_j \in \mathbb{M})$ **then**

Add P_i to ensemble:

$$z_{\mathbb{X}} \leftarrow \{z_{\mathbb{X}}, P_i\}; \qquad N(z_{\mathbb{X}}) \leftarrow (N(z_{\mathbb{X}}) + 1)$$

Perform coagulation $P_i \leftarrow (P_i + P_j)$

Set $t \leftarrow (t + \tau)$

else

Set $t \leftarrow (t + t_{\text{split}})$

Algorithm 4: Update particle-number lists

Input : $\mathbf{X}(t)$, $T(t)$, $z_{\mathbb{X}}(t)$, $z_{\mathbb{M}}(t)$, N_{thresh}, t_f, template particle of size d_{thresh}: $P_{\text{thresh}}^{\text{tmp}}$
Output : $\mathbf{X}(t_f)$, $T(t_f)$, $z_{\mathbb{M}}(t_f)$

Set $n_{\text{add,total}} \leftarrow 0$

Compute expected surface growth factor:

$$\tilde{\beta}_{\text{SG}} \leftarrow \tilde{\beta}_{\text{SG}}(\mathbf{X}, T)(t_f - t_0)$$

for $index = N_{thresh}, \ldots, 1$ **do**
  if $N_{index} > 0$ **then**
    Choose number of units to add from:

$$n_{\text{add,index}} \sim \text{Poisson}\left(\tilde{\beta} A(P_{\text{index}})\right)$$

    Set newIndex $\leftarrow$ (index $+ n_{\text{add,index}}$)
    if $newIndex > index$ **then**
      Update $n_{\text{add,total}} \leftarrow (n_{\text{add,total}} + n_{\text{add,index}})$
      if $newIndex \leq N_{thresh}$ **then**
        Update property sums for change in number at index, newIndex
        Set $N_{\text{newIndex}} \leftarrow (N_{\text{newIndex}} + N_{\text{index}})$
        Set $N_{\text{index}} \leftarrow 0$
      else
        Update property sums for change in number at index
        Update total particle number:

$$N(z_{\mathbb{M}}) \leftarrow (N(z_{\mathbb{M}}) - N_{\text{index}})$$

        Set $N_{\text{index}} \leftarrow 0$
        Copy template particle:

$$P_{\text{new}} \leftarrow P_{\text{thresh}}^{\text{tmp}}$$

        Add (newIndex $- N_{\text{thresh}}$) monomers to P_{new}
        for $j = 1, \ldots, N_{index}$ **do**
          Add particle to ensemble:

$$z_{\mathbb{X}} \leftarrow \{z_{\mathbb{X}}, P_{\text{new}}\}$$

Update $n_{\text{add,total}}$ surface growth events

3.4.4 Verification

The aim of this section is to show that the implementation of the governing equations is correctly solved using the finite volume method and detailed transport coefficients from the *k*inetics API. These governing equations are restated and marked to group specific terms of the conservation of mass, momentum, species, enthalpy and moments.

$$\underbrace{\frac{\partial \rho}{\partial t} + \nabla \cdot (\rho U) = 0}_{\text{I}}$$

$$\underbrace{\frac{\partial \rho U}{\partial t} + \nabla \cdot (\rho UU) = -\nabla p - \mu \left(\nabla U + (\nabla U)^T\right)}_{\text{I}}$$

$$\underbrace{\frac{\partial \rho Y_i}{\partial t} + \nabla \cdot (\rho U Y_i)}_{\text{I}} + \underbrace{\nabla \cdot (\rho V_i^c Y_i)}_{\text{III}} = \underbrace{\dot{\omega}_i}_{\text{V}}$$

$$\underbrace{c_p \frac{\partial \rho T}{\partial t} + c_p \nabla \cdot (\rho U T)}_{\text{I}} = \underbrace{\nabla \cdot (\lambda \nabla T)}_{\text{II}} - \underbrace{\left(\rho \sum_{j=1}^{N} c_{p_j} Y_j V_j^c\right) \cdot \nabla T}_{\text{IV}} + \underbrace{\dot{\omega}_\text{T}}_{\text{V}}$$

$$\underbrace{\frac{\partial \rho \hat{M}_j}{\partial t} + \nabla \cdot (\rho U \hat{M}_j)}_{\text{II}} + \underbrace{\nabla \cdot (\rho V_T \hat{M}_j)}_{\text{VII}} = \underbrace{\nabla \cdot \left(\rho D_{p_1} \nabla \hat{M}_{j-\frac{2}{3}}\right)}_{\text{VIII}} + \underbrace{\dot{\omega}_j}_{\text{VI}}$$

Table 3.1 lists the test cases used to verify the implementation of the new solver. The test cases were designed to introduce specific terms of the transport equations against a reference solution in a step-wise manner. This allowed for the contribution of the terms to the numerical solution to be tested individually. Several of these tests are redundant, such that they test the same terms of the governing equations with different levels of complexity. For example, the diffusion terms are tested in a binary and ternary case. The full set of test cases is listed in Table 3.1, but the results of some of the cases are presented in Appendix A for brevity.

Unless otherwise stated, the test cases are axisymmetric counterflow domains and compared against the 1D method. The 1D approximation is valid for infinitely wide nozzles, which is replicated in 2D with nozzle inlets that cover the entire radial domain, which make them a good point of comparison for non-analytically derivable problems.

Table 3.1 A summary of the verification test cases

		Left boundary (x = 0)			Right boundary (x = L)		
Case	Terms tested	Velocity m s^{-1}	Composition Mass fraction	Temperature K	Velocity m s^{-1}	Composition Mass fraction	Temperature K
Analytical diffusion[1]		0	1	-	0	0	-
Isothermal, flow	I, μ, c_p	0.2	$Y_{N_2} = 1$	450	-0.2	$Y_{N_2} = 1$	450
Nonisothermal, flow	II, λ	0.2	$Y_{N_2} = 1$	450	-0.2	$Y_{N_2} = 1$	450
Isothermal, binary diffusion constant specific enthalpy	III, μ, c_p	0.2	$Y_{N_2} = 0.5$ $Y_{H_2} = 0.5$	450	-0.2	$Y_{N_2} = 1$	450
Nonisothermal, binary diffusion constant specific enthalpy	II, III, λ	0.2	$Y_{N_2} = 1$ $Y_{H_2} = 0.5$	450	-0.2	$Y_{N_2} = 0.5$	450
Isothermal, binary diffusion[1]	III, μ, c_p	0.2	$Y_{N_2} = 0.5$ $Y_{H_2} = 0.5$	450	-0.2	$Y_{N_2} = 1$	450
Nonisothermal, binary diffusion	IV, λ	0.2	$Y_{N_2} = 1$ $Y_{H_2} = 0.5$	450	-0.2	$Y_{N_2} = 0.5$	2000
Isothermal, ternary diffusion[1] constant specific enthalpy	III, μ, c_p	0.2	$Y_{N_2} = 0.5$ $Y_{H_2} = 0.5$	450	-0.2	$Y_{N_2} = 0.5$ $Y_{O_2} = 0.5$	450

Continued on next page

[1]Presented in Appendix A

Table 3.1 – continued from previous page

Case	Terms tested	Left boundary (x = 0) Velocity m s^{-1}	Composition Mass fraction	Temperature K	Right boundary (x = L) Velocity m s^{-1}	Composition Mass fraction	Temperature K
Nonisothermal, ternary diffusion[1] constant specific enthalpy	III, λ	0.2	$Y_{N_2} = 0.5$ $Y_{H_2} = 0.5$	450	-0.2	$Y_{N_2} = 0.5$ $Y_{O_2} = 0.5$	2000
Isothermal, ternary diffusion[1]	III, μ, c_p	0.2	$Y_{N_2} = 0.5$ $Y_{H_2} = 0.5$	450	-0.2	$Y_{N_2} = 0.5$ $Y_{O_2} = 0.5$	450
Nonisothermal, ternary diffusion[1]	IV, λ	0.2	$Y_{N_2} = 0.5$ $Y_{H_2} = 0.5$	450	-0.2	$Y_{N_2} = 0.5$ $Y_{O_2} = 0.5$	2000
Single Reaction $2H_2 + O_2 = 2H_2O$	V, μ, c_p	0.2	$Y_{N_2} = 0.5$ $Y_{H_2} = 0.5$	450	-0.2	$Y_{N_2} = 0.5$ $Y_{O_2} = 0.5$	2000
Counterflow diffusion flame	I-V	0.2	$Y_{N_2} = 0.5$ $Y_{H_2} = 0.5$	450	-0.2	$Y_{N_2} = 0.5$ $Y_{O_2} = 0.5$	2000
Counterflow diffusion flame with particles	VII,VIII	0.2	$Y_{N_2} = 0.94$ $Y_{H_2} = 0.05$ $Y_{TTIP} = 0.01$	450	-0.2	$Y_{N_2} = 0.77$ $Y_{O_2} = 0.23$	2000
Batch Reactor with particle model	V,VI	-	$Y_{Ar} = 0.7681$ $Y_{H_2} = 0.0479$ $Y_{O_2} = 0.1761$ $Y_{TTIP} = 0.0079$	1000			

Isothermal, single species flow

Terms tested: I, μ, c_p

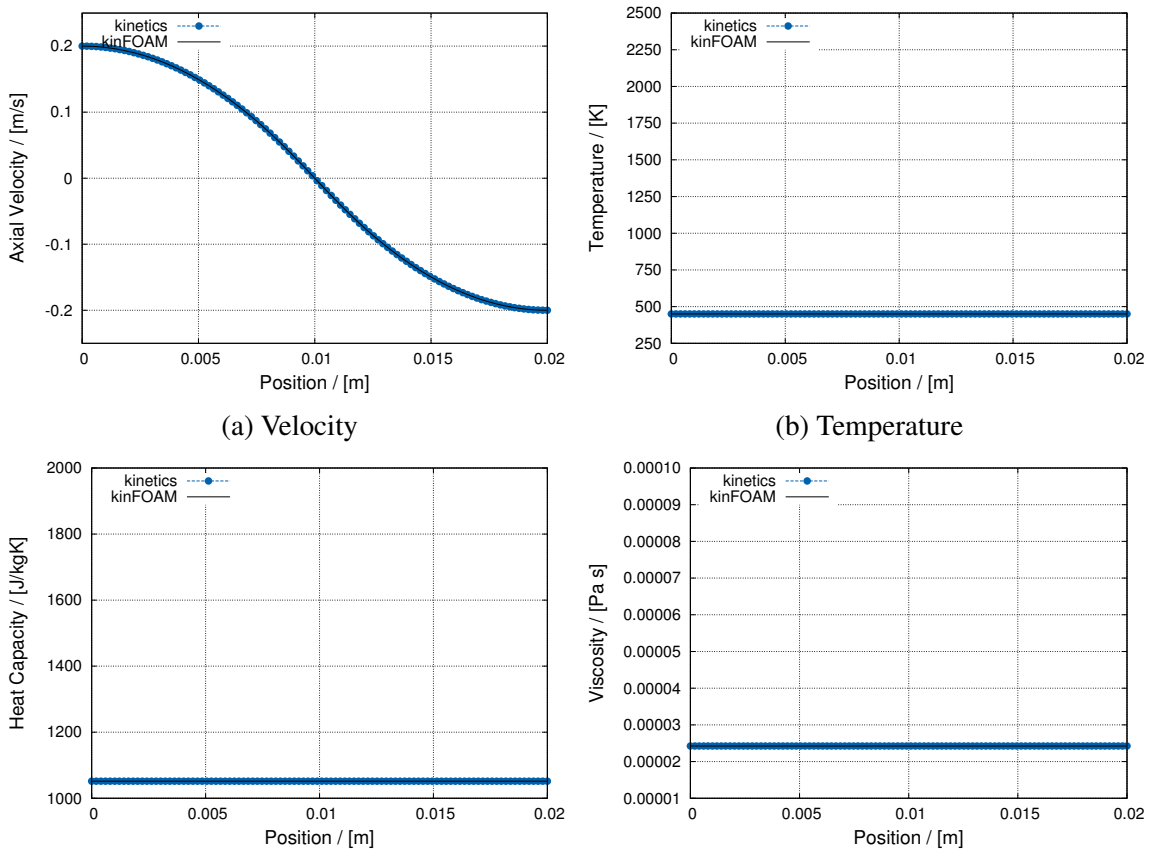

(a) Velocity

(b) Temperature

(c) Heat Capacity

(d) Viscosity

Fig. 3.6 Centreline comparison between *k*inetics and new solver for isothermal, inert flow test case (Table 3.1).

The centreline velocity profile is captured very well, as can be observed by the overlapping lines in Figure 3.6. The heat capacity and viscosity are also shown to be in agreement, verifying that the mapping of thermochemical properties is implemented correctly.

Nonisothermal, single species flow

Terms tested: II, λ

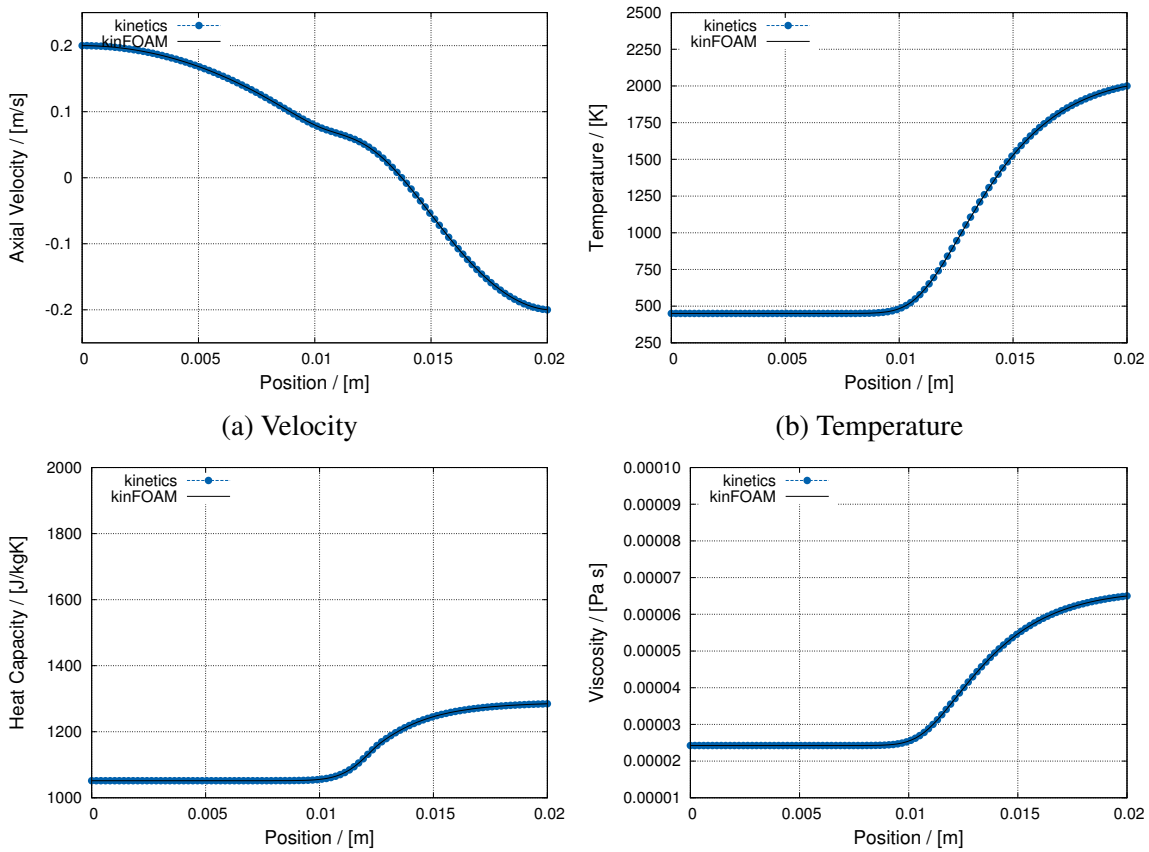

(a) Velocity

(b) Temperature

(c) Heat Capacity

(d) Viscosity

Fig. 3.7 Centreline comparison between *k*inetics and new solver for nonisothermal, inert flow test case (Table 3.1).

The centreline temperature profile is captured very well, as can be observed by the overlapping lines in Figure 3.7. The coupling between temperature and flow (through density) is captured well, as the velocity profile is also in good agreement. The heat capacity and viscosity are also shown to be in agreement, verifying that the mapping of thermochemical properties is implemented correctly.

Isothermal, binary diffusion with constant specific enthalpy

Terms tested: III, λ

Constant enthalpies removes term V from the enthalpy equation, retaining terms I – IV.

$$\left(\rho \sum_{j=1}^{N} c_{p_j} Y_j V_j^c\right) \nabla T = \underbrace{\left(\rho c_p \sum_{j=1}^{N} Y_j V_j^c\right)}_{\sum_j Y_j V_j^c = 0} \nabla T = 0$$

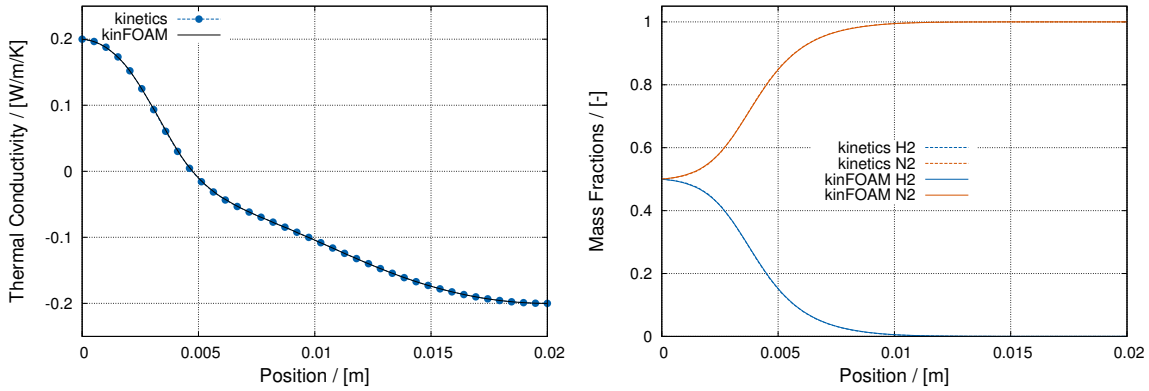

(a) Thermal Conductivity

(b) Mass Fractions

Fig. 3.8 Centreline comparison between *k*inetics and new solver for isothermal binary diffusion with constant specific enthalpy test case (Table 3.1).

Figure 3.8 shows the thermal conductivity and species mass fractions to be in good agreement with the reference solution provided by *k*inetics. Therefore, it is concluded that the diffusion of species is handled correctly in the binary case. Additionally, the multicomponent calculation of thermal conductivity is shown to be in agreement with the reference solution.

Nonisothermal, binary diffusion with constant specific enthalpy

This case is a more complex version of the previous one, as it releases the enforced isothermal condition; no new terms are tested.

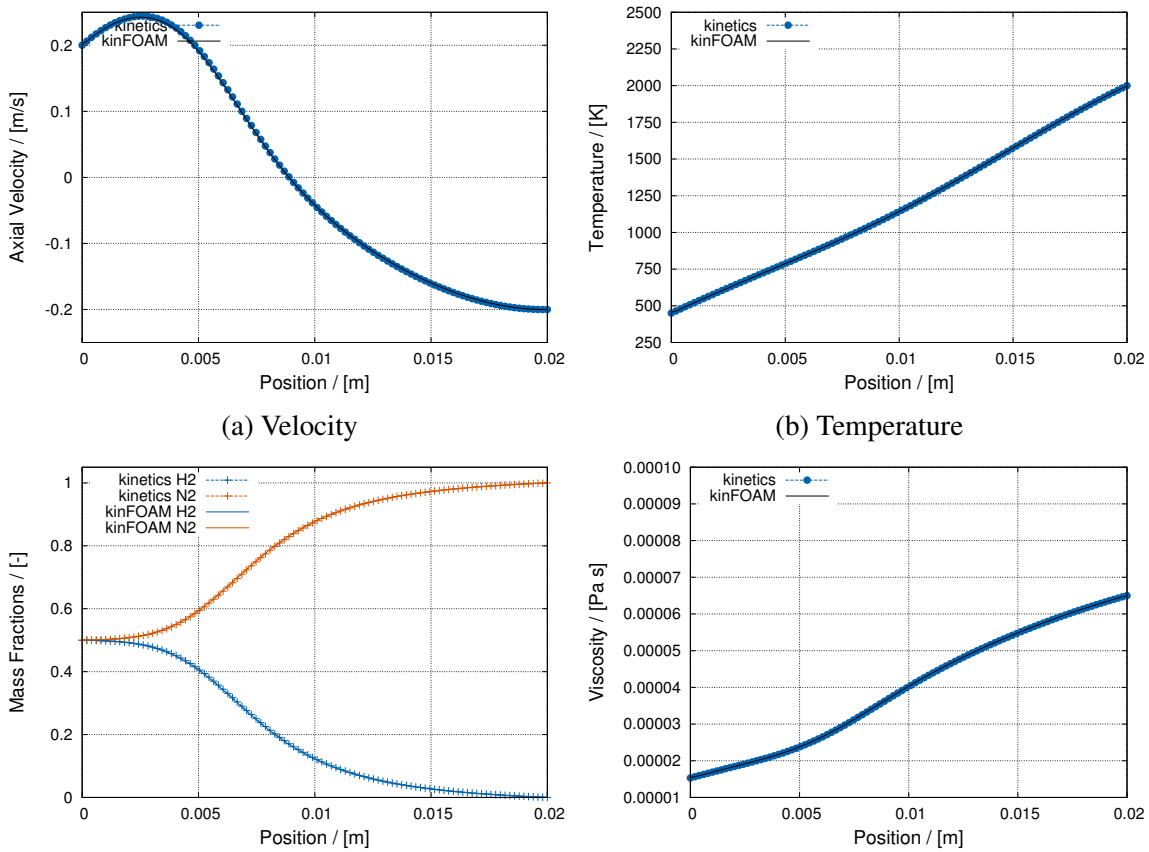

(a) Velocity

(b) Temperature

(c) Mass Fractions

(d) Viscosity

Fig. 3.9 Centreline comparison between *k*inetics and the new solver for nonisothermal, binary diffusion with constant specific enthalpy test case (Table 3.1).

Figure 3.9 shows that the diffusion of species is handled correctly under nonisothermal conditions.

Nonisothermal, binary diffusion

No new terms tested, more complex version of test above.

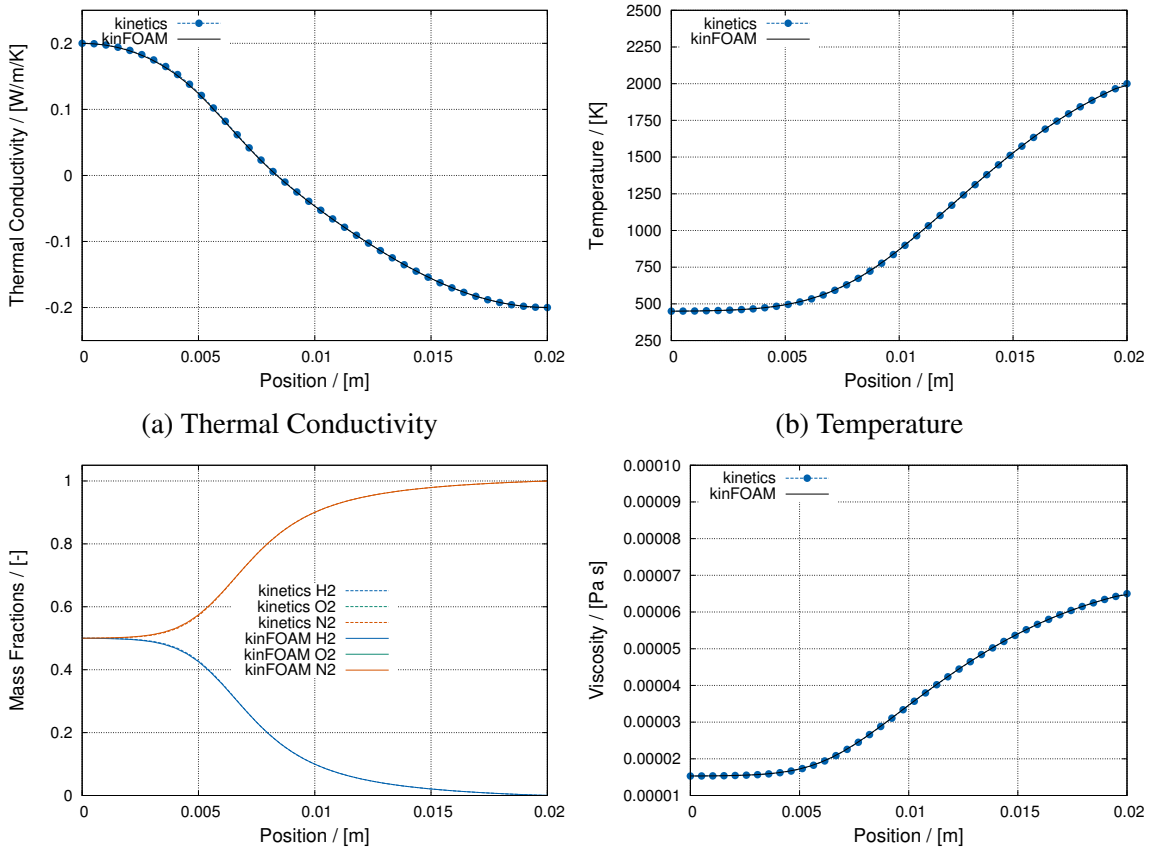

(a) Thermal Conductivity

(b) Temperature

(c) Mass Fractions

(d) Viscosity

Fig. 3.10 Centreline comparison between *k*inetics and the new solver for nonisothermal, binary diffusion test case (Table 3.1).

Single reaction

Terms tested: V

The reaction $2H_2 + O_2 = 2H_2O$ is used with the following kinetic parameters: $A = 1.915E14$ s and $E_a = 68784.96$ J mol^{-1}.

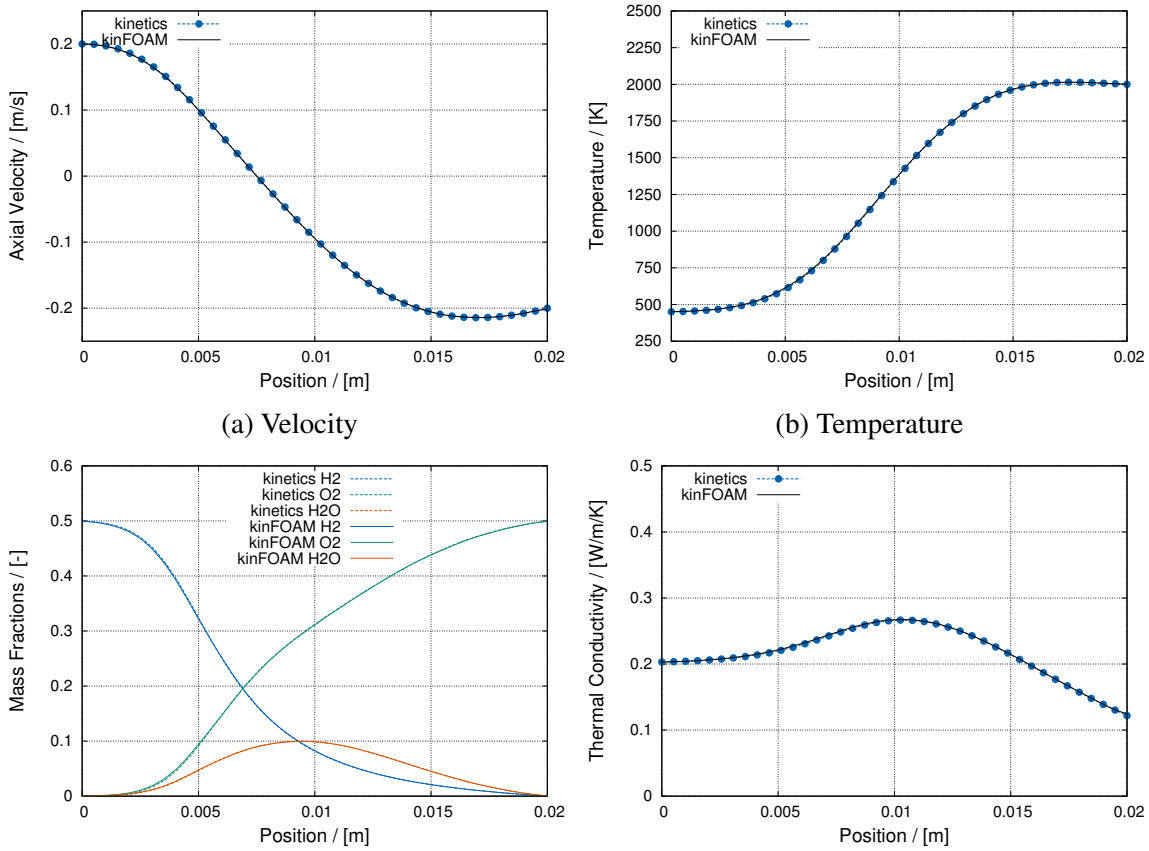

(a) Velocity

(b) Temperature

(c) Mass Fractions

(d) Thermal Conductivity

Fig. 3.11 Centreline comparison between *k*inetics and the new solver with a single global reaction test case (Table 3.1).

This test case introduces a single global reaction. Figure 3.11 shows the velocity, temperature, mass fraction and thermal conductivity of the test case. For all results shown, the results predicted by the new solver overlap with the reference solution provided by *k*inetics. As this test case builds off the previous cases, it can be concluded that the calculation of the gas-phase source terms, and therefore all terms that describe the gas phase, are implemented correctly.

Counterflow diffusion flame

Concurrently tests all terms in the mass, momentum, species, and enthalpy equations. The hydrogen combustion mechanism of Li et al. [189] was used.

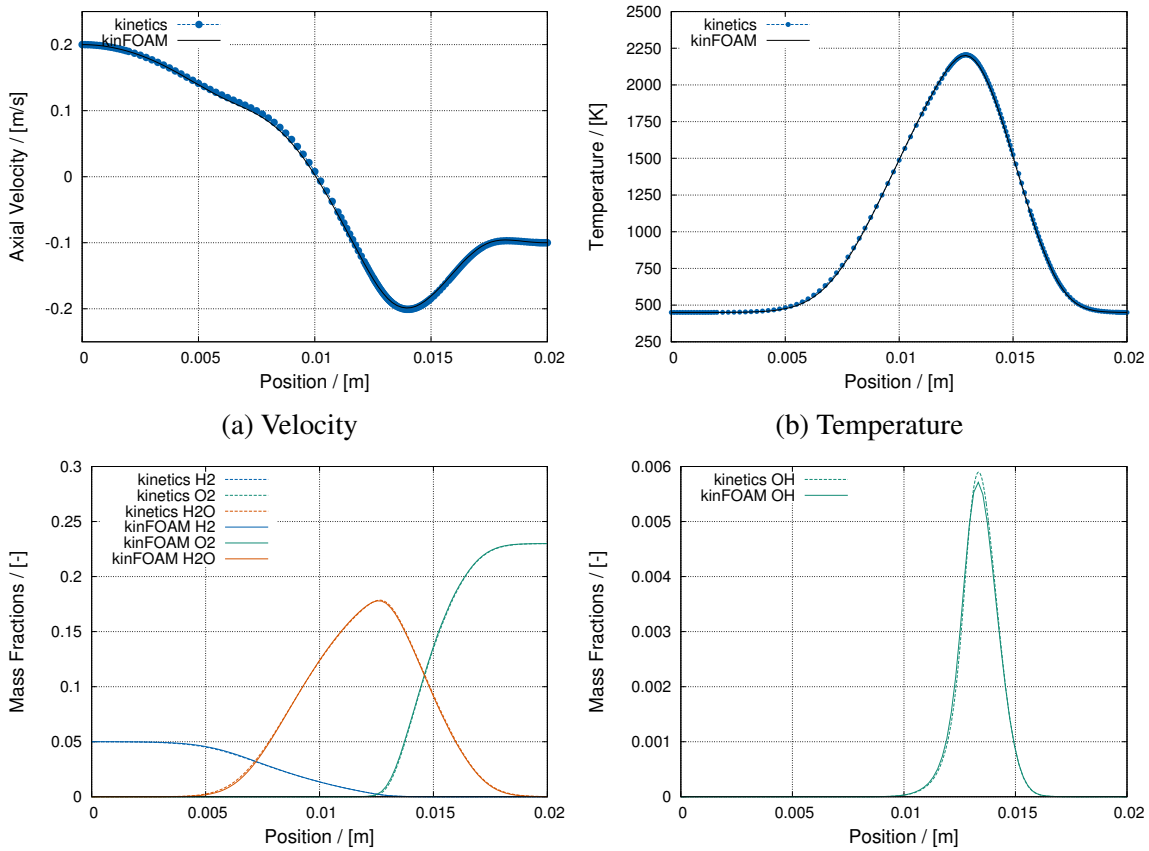

(a) Velocity

(b) Temperature

(c) H_2, O_2, and H_2O mass fractions

(d) OH mass fractions

Fig. 3.12 Centreline comparison between *k*inetics and the new solver for a counterflow diffusion flame with a detailed mechanism test case (Table 3.1).

A more complicated counterflow diffusion flame is predicted with a hydrogen reaction mechanism found in literature [189]. The results are found to be in very good agreement as seen by Figures 3.12 and 3.13. The prediction of the hydroxyl species (OH) is found to be in the same location with a maximum value that is very similar. The gas phase prediction of multicomponent combustion with detailed transport and thermodynamic variables has been shown to be in good agreement with the 1D opposed flow diffusion model (discussed in Section 2.3.2) as implemented in *k*inetics.

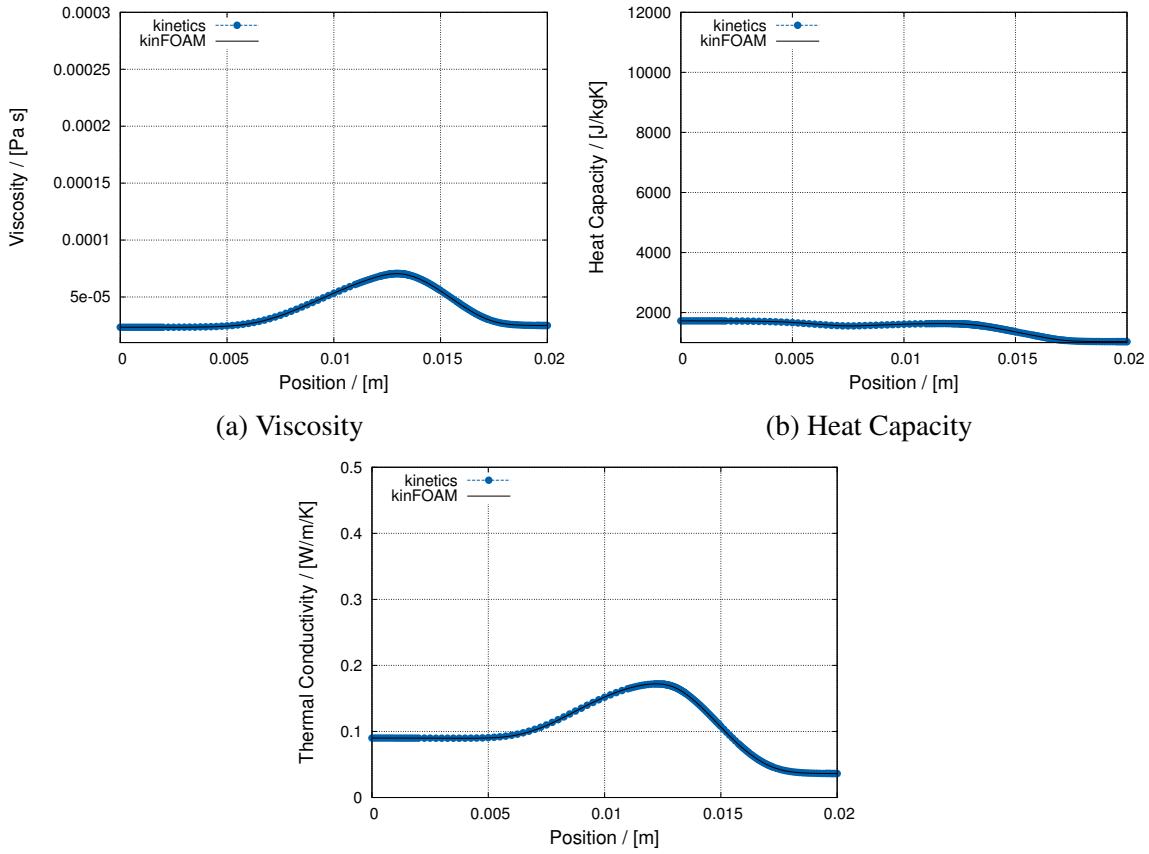

(a) Viscosity

(b) Heat Capacity

(c) Thermal Conductivity

Fig. 3.13 Centreline comparison of thermochemical properties between *k*inetics and the new solver for a counterflow diffusion flame with a detailed mechanism test case (Table 3.1).

Batch reactor with particle model

An ignition delay simulation of a H_2-O_2-Ar system is computed with *k*inetics and the OpenFOAM-API implementation. The hydrogen combustion mechanism of Li et al. [189] was used. The pressure in the batch reactor was held constant over the time. This tests the source terms of the species, temperature and moment equations to ensure the linearised source terms of Algorithm 2 agree with the detailed ODE solvers. The simplified particle model (described in Section 3.3.2) is used and has the special property that the gas phase composition of particle precursor, TTIP, is independent of the particle state. When the particle model is coupled with the H_2 mechanism, TTIP and C_3H_6 must be added to the mechanism. Further reactions of C_3H_6 were intionally ignored in these numerical tests. Consequently, the gas phase species C_3H_6 is a species whose only source term is the particle model and has no other sink terms, making it an excellent indicator of the gas-phase/particle coupling.

This test is also interesting because of the difference in formulation of the state space of each model. In the *k*inetics Driver, the batch reactor is solved as a closed system with constant mass. Pressure is held constant and the system is allowed to expand or contract as determined by the ideal gas law. The species are solved as extensive quantities. In contrast, the OpenFOAM-API implementation is solved on a fixed mesh and cannot expand or contract to maintain constant pressure. Instead, the total mass in the system will change as density changes according to the ideal gas law. The species are also represented as intensive mass fractions. The former leads to a more natural formulation when considering mass transfer between phases and is what is used when calculating the source terms for the later case. It is important to demonstrate that the formulation as intensive quantities does not introduce error in the calculations.

Figure 3.14 shows excellent agreement between the two solutions. This test case demonstrates that the linearisation of source terms in the moment equations is a good approximation of the internally time-step adjusted solution of the ODE solvers. This was achieved despite orders of magnitude differences in time steps. The formulation of intensive quantities does not lead to significant differences in the particle results.

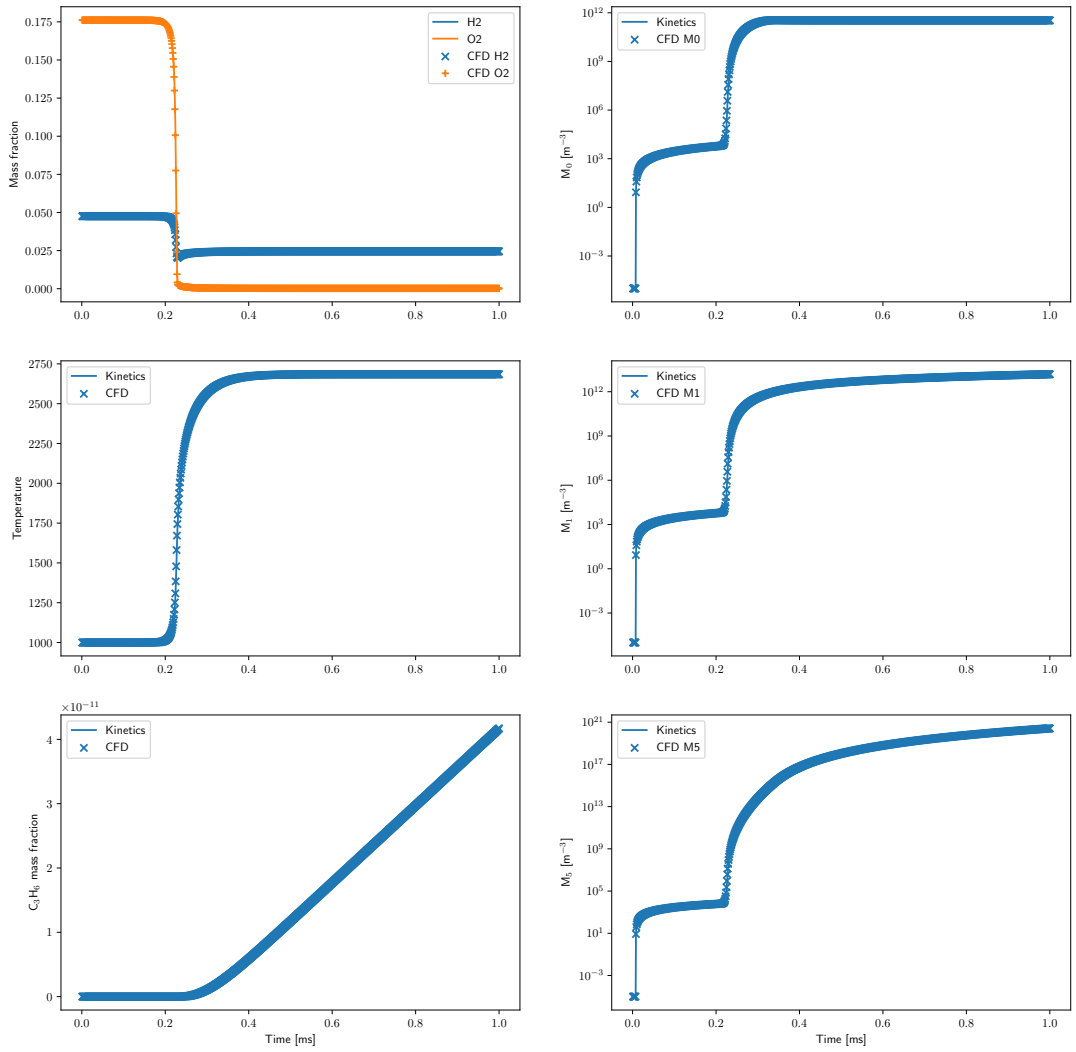

Fig. 3.14 Comparison between *k*inetics and the new solver for a reacting gas phase-particle system in a constant pressure batch reactor test case (Table 3.1).

Flame with particle model

This test case simultaneously tests all terms using a H_2 counterflow diffusion flame with TTIP particles. Further reactions of C_3H_6 are ignored in the numerical tests. Numerical difficulty

was experienced when solving the 1D reference case, as the 1D solution would not converge on a more refined grid. Thus, extra care is taken to ensure the solution is correct and sensible.

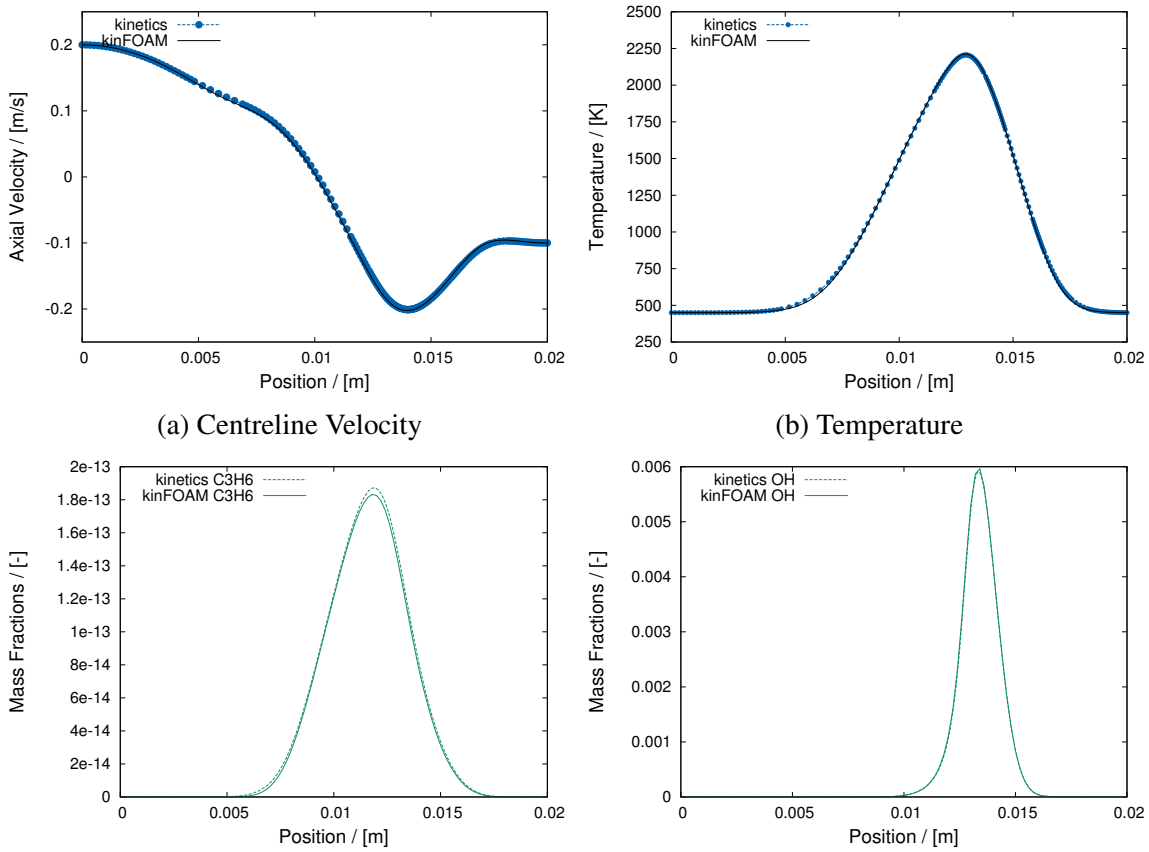

(a) Centreline Velocity

(b) Temperature

(c) Mass Fractions

(d) Mass Fractions

Fig. 3.15 Centreline comparison between *k*inetics and the new solver for a counterflow diffusion flame with TiO_2 nanoparticles test case (Table 3.1).

Significant differences exist between the 1D moment predictions and the new solver's moment predictions, specifically in the order of magnitude. Qualitatively, the shape of the distributions between the two methods are in agreement. The C_3H_6 mass fractions are in excellent agreement, differing in levels that are comparable to the absolute tolerances. The mass flux of TiO_2 through the domain outlet as calculated from the C_3H_6 mass flux and the M_1 flux was calculated. Both fluxes are orders of magnitude smaller than the total mass flux through the domain outlet. The two predicted mass fluxes of TiO_2 are on the same order of magnitude and well within solver tolerances, so it is not believed that there are any significant inconsistencies between the 2D C_3H_6 solution and particle moment solutions, though significant differences exist as compared to the 1D solution.

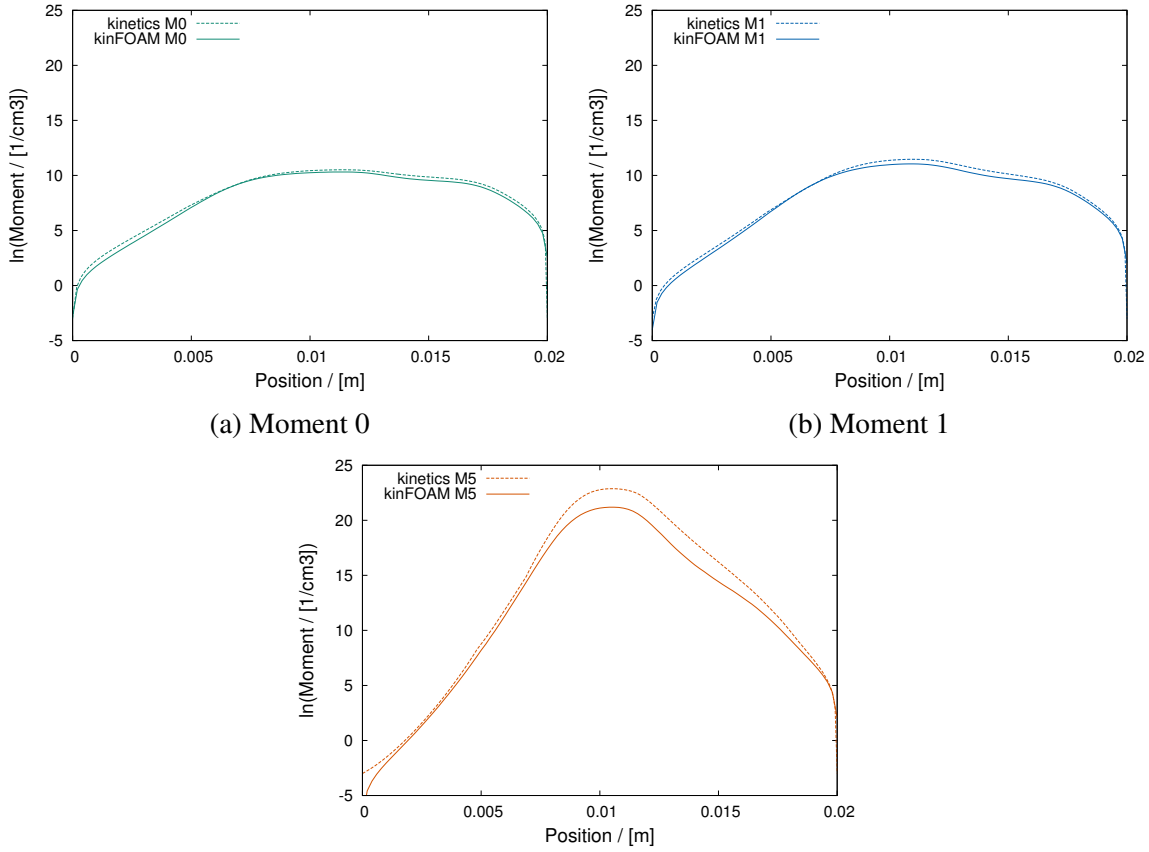

(a) Moment 0

(b) Moment 1

(c) Moment 5

Fig. 3.16 Centreline comparison of moment profiles between *k*inetics and the new solver test case (Table 3.1).

Chapter 4

Gas phase predictions of premixed, jet-wall stagnation flames

This chapter demonstrates the predictions of the new solver by studying four premixed ethylene, jet-wall stagnation flames. Key results are compared to experimental measurements. The flames differ by varying experimental design parameters that are commonly changed: inlet velocity, gas composition, and nozzle-plate separation distances. The flame position is non-invasively determined from CH chemiluminescence images. The flame temperature profile is measured in 2D using thin filament pyrometry. The 2D method is able to easily describe the experimental flames and has well defined boundary conditions, whereas the 1D model can only describe the centreline and the determination of the boundary conditions is non-trivial. The second dimension allows for the curvature of the flame to be explored, as well as additional temperature-residence profiles to be extracted.*

4.1 Acknowledgement

The author would like to acknowledge that the work of this chapter was published under: Jochen A.H. Dreyer, **Eric J. Bringley**, Manoel Y. Manuputty, Jethro Akroyd and Markus Kraft (2021). Temperature and CH* Measurements and Simulations of Laminar Premixed Ethylene Jet-Wall Stagnation Flames. *Proceedings of the Combustion Institute*, 38(2):2083-2091. doi:10.1016/j.proci.2020.06.106. Additionally, the author would like to note that the experimental work was completed by Jochen A.H. Dreyer and Manoel Y. Manuputty. The fitting of the 1D model boundary conditions to experimental flame locations was also completed

by Manoel Y. Manuputty. The manuscript was written by the author of this thesis and feedback was provided by other authors.

4.2 Introduction

One type of laminar flame that has gained recent interest in both fundamental combustion research [27, 374] as well as material synthesis applications [215, 345] are premixed, jet-wall stagnation flames. One advantage of premixed, jet-wall stagnation flames is that the stagnation plane is well defined; the heat loss to the stagnation surface has been shown to have little effect on the laminar flame speeds at low strain rates and low stagnation surface temperatures [94]. They are also "approximately flat" and axially symmetric, thus facilitating modelling efforts. The most widely used approach to simulate such flames is to use a 1D model based on the stream function assumption [164]. This approach is computationally efficient, but is limited to idealised flows with constant radial pressure gradients and radially uniform profiles [29, 43, 119, 246]. An alternate approach is to solve the full set of Navier-Stokes and conservation equations for chemically reacting flow, while making use of symmetry to reduce the problem from 3D to 2D.

The applicability of 1D models has been the subject of many studies for counterflow [246, 151] and jet-wall stagnation flames [26, 43, 327]. Discrepancies between 1D and 2D models have largely been attributed to differences in the non-uniform pressure curvature [246, 327, 43]. Bergthorson and co-workers [29, 27, 30] have shown that the assumptions made in the 1D model are satisfied if the boundary conditions are specified appropriately after the free-jet region. Bouvet et al. [43] studied a jet-wall, stagnation flame confined by a cooling jacket and found the 1D simulation was unable to simulate the free-jet due to the non-uniform pressure curvature. Johnson et al. [151] showed that the 1D approach is applicable for counterflow streams from contoured nozzles of greater than 12 mm diameter because of the negligible contribution of radial terms on the momentum and energy equations.

Most applications of 2D simulations have focused on either coflow diffusion flames [324] or non-premixed counterflow flames [262]. Only a few works have considered 2D simulations of premixed, jet-wall flames [327, 43]. Sone [327] performed 2D simulations of premixed stagnation flames but focused on analysis of centreline profiles, making only one comparison against 2D CH planar laser induced fluorescence data. With the exception of velocity profiles [43, 10], very few works compare 2D simulations of premixed, jet-wall stagnation flames to 2D experimental data. Such comparisons would be useful when using premixed, jet-wall flames for material synthesis applications.

The purpose of this chapter is to experimentally characterise and model premixed, jet-wall stagnation flames in two dimensions. The flame position, shape, and temperature are measured experimentally as 2D fields through CH* chemiluminescence and thin filament pyrometry. It is evaluated whether 1D and 2D models can reproduce the experimental observations when the nozzle-stagnation surface distance, burner exit velocity and ethylene-air equivalence ratio are varied. Information from the 2D simulations is extracted along streamlines and compared to assess the uniformity of the temperature-residence times.

4.3 Experimental

4.3.1 Flame conditions

Four flame conditions, summarised in Table 4.1, were studied. All of the gas flows were controlled with Bronkhorst mass flow controllers. The nitrogen flow rate was set such that the flow velocity was 150 cm s^{-1} for all experiments. The other conditions were chosen to study the effect of flow velocity at the nozzle exit v, equivalence ratio ϕ, and ratio between the nozzle-stagnation plate distance L to nozzle diameter d.

Table 4.1 Flame conditions for the four flames studied. ϕ is the equivalence ratio, v is the burner exit velocity, L/d is the ratio between the burner-surface separation to nozzle diameter, T_{stag} is the measured temperature of the stagnation surface and G_0 is the strain used for the boundary conditions in the 1D simulations. The nitrogen flow velocity was 150 cm s^{-1} for all experiments.

Flame	ϕ -	v cm s^{-1}	L/d -	G_0 s^{-1}	T_{stag} K
1	0.7	200	1	27.5	497
2	0.8	200	1	46.5	522
3	0.7	300	1	22.0	524
4	0.7	200	0.6	163.3	513

4.3.2 Premixed stagnation flame apparatus

A burner was used to study premixed hydrocarbon flames stabilised on a water-cooled stagnation surface (Fig. 4.1a). An ethylene/air mixture is introduced at the bottom of the burner. The premixed gas is expanded in a central cylinder with a diameter of 50 mm filled with glass beads to homogenise the flow. The flow then passes through a porous ceramic plug to remove remaining fluctuations, before the gas is accelerated in a contoured nozzle. The inner shape

results in a plug flow at the nozzle exit (diameter d = 14 mm) and facilitates the stabilisation of a flat flame. More information about the shape of the nozzle and its design procedure can be found in Appendix C.

Nitrogen is used as a sheath gas and is introduced through three ports at the bottom of the burner. It is distributed and stabilised with the aid of glass beads and a porous aluminium foam. The nitrogen is accelerated in a contoured nozzle and exits around the central nozzle to shield the flame from ambient air.

A water cooled, stainless steel plate was used as the stagnation surface. The cooling water enters close to the centre of the plate, flows through a spiral shaped channel and exits on the outer edge of the plate. A cylindrical plug is placed in the centre of the plate to accommodate a thermocouple. The thermocouple tip is flush with the stagnation plate and measures the temperature at the stagnation point, T_{stag}.

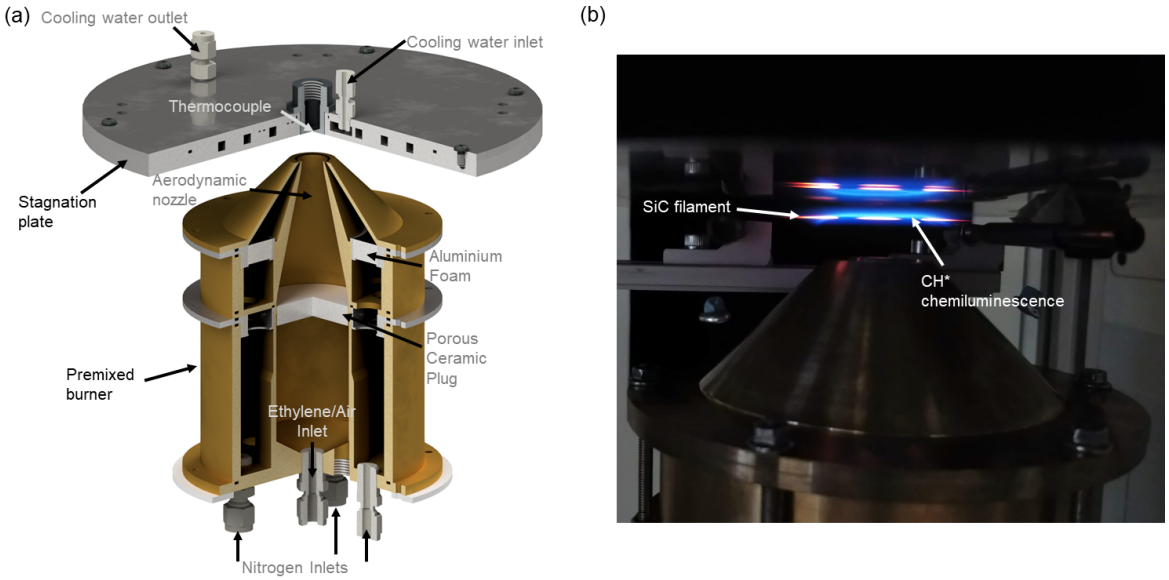

Fig. 4.1 (a) Rendered CAD drawing of the in-house developed premixed burner and water cooled stagnation surface. (b) Photograph of the SiC filament inside the premixed stagnation stabilised flat flame.

4.3.3 CH* chemiluminescence measurements

The chemiluminescence of CH* was recorded with a Blackfly S camera equipped with a MVL25M23 lens from Thorlabs with an aperture set to f/1.4 and a focal length of 25 mm. A 430 nm bandpass filter (Thorlabs, FWHM 10 nm) was used to image the light emitted during the $A^2\Delta \rightarrow X^2\Pi$ relaxation of the thermally excited CH radicals. The 2D projection recorded by

the camera was transformed into a 2D cross section by making use of the flame symmetry and applying an inverse Abel transform using the basis-set expansion (BASEX) method [11, 84]. The Abel transform used time-averaged images to ensure that the symmetry was not broken by the oscillations in the wings of the flame (see Fig. D.1 in Appendix D). All results were normalised by the highest CH* emission recorded, which was the peak emission from Flame 2 in this study.

4.3.4 Thin filament pyrometry

The flame temperatures were measured using SiC thin filament pyrometry (TFP) [179, 226, 37]. A brief summary is given here with full details in Appendix E. The light emission from a SiC filament placed into the flame is used to infer the temperature of the surrounding gas. The approach applied here infers the filament temperature, T_{SiC}, by comparing the ratio of observed intensities of colour channels to a previously generated temperature look-up table [208]. Three replicate measurements were taken of each flame. T_{SiC} was converted to gas temperature using an energy balance of radiation and forced convection over an inclined cylinder. In line with previous reports, conduction along the filament was neglected due to its small diameter (14 µm) and low thermal conductivity (2.2 W $\mathrm{m}^{-1}\mathrm{K}^{-1}$) [179, 226]. This work improves upon past methods by using multicomponent gas phase properties and 2D flow fields from 2D simulations to assess convective heat transfer. The equations, S-type thermocouple calibration procedure, and further details regarding the calculation of the temperature look-up table are fully described in literature [179, 207, 83]. Additional details regarding this method, the image processing, and the equipment used can be found in Appendix E.

4.4 Simulation

The description of the 2D simulation method can be found in Section 3.4.1. Figure 4.2 depicts the mesh of the 2D simulations. The simulated domain starts upstream of the nozzle inside the burner and extends radially outward from the burner to capture the full flow field over the stagnation plate. Mass flux boundary conditions were specified to match the experimental conditions upstream of the nozzle. Isothermal and no-slip conditions were specified at walls and ambient pressure outlets at the radial simulation boundary.

The equations for the 1D simulation of jet-wall stagnation flames [206] can be found in Section 2.3.2. The boundary conditions to the system of ODEs are as follows: at the upstream

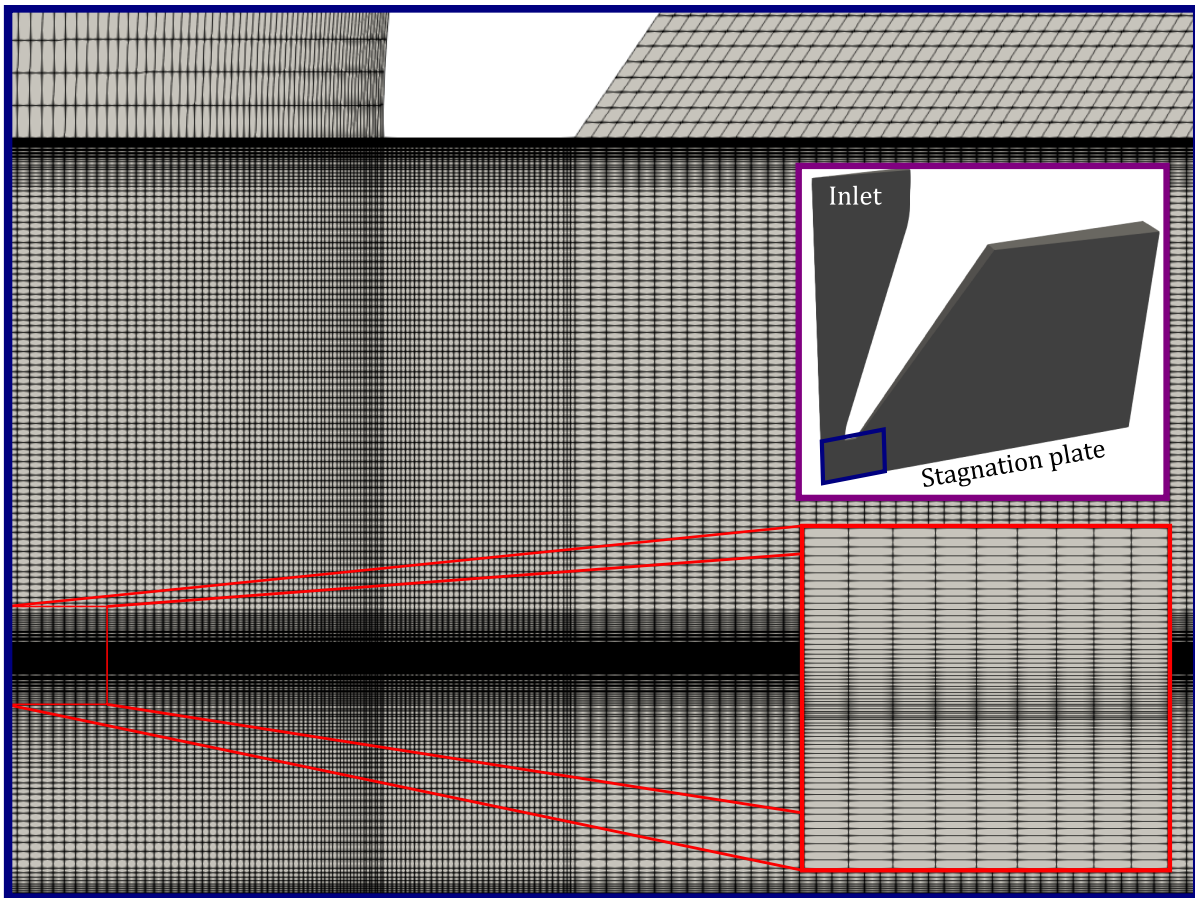

Fig. 4.2 Example Mesh for Flame 1. The full mesh is shown in the inset purple figure where the nozzle inlet and stagnation plate are labelled. The region between the nozzle outlet and the stagnation plate is marked in blue and shown in the main figure. The inset figure, outlined in red, shows the refinement near the flame front.

boundary, $z = z_{\text{end}}$,

$$\begin{aligned} F(z_{\text{end}}) &= \frac{\rho(z_{\text{end}})v}{2} \\ G(z_{\text{end}}) &= G_0 \\ T(z_{\text{end}}) &= T_{\text{inlet}} \\ \rho(z_{\text{end}})Y_i(z_{\text{end}})V_i^c(z_{\text{end}}) &= \rho(z_{\text{end}})v(Y_{i,0} - Y_i(z_{\text{end}})) \quad \text{for } i = 1,\ldots,\text{N}_{\text{sp}}, \end{aligned} \tag{4.1}$$

where v is fixed axial velocity, G_0 is the radial strain, T_{inlet} is the unburned gas temperature, and $Y_{i,0}$ is the fixed upstream gas composition; at the inert stagnation plate, $z = 0$,

$$\begin{aligned} F(0) &= 0 \\ G(0) &= 0 \\ T(0) &= T_{\text{wall}} \\ \rho(0)Y_i(0)V_i^c(0) &= 0 \qquad\qquad \text{for } i = 1,\ldots,\text{N}_{\text{sp}}, \end{aligned} \tag{4.2}$$

where T_{wall} is the stagnation plate temperature.

The chemical mechanism used in the 1D and 2D models in this study was the San Diego Mechanism [354], which was chosen because of its past application to ethylene stagnation flames [26, 27] and its ability to predict the flame location [25]. Further work has examined and sought to optimise the prediction of the flame location [362]. Full coupling of sub-mechanisms for CH* was previously shown to have negligible effects on the flame characteristics due to its orders of magnitude difference in concentration [261, 367]. Therefore, CH* species profiles are calculated as a post-process assuming it is in quasi-steady state. Production of CH* from C_2H and O or O_2 and quenching from spontaneous emission (described by the Einstein coefficient) and reactions with H_2O, CO_2, CO, H_2, O_2, CH_4, and N_2 were considered; all rates and Einstein coefficients used for this work are reported in Table 4.2.

4.5 Flame position and shape

The flame positions and shapes from the 2D simulations and experiments were assessed by comparing the normalised 2D profiles of CH* (Fig. 4.3). The chemiluminescence was non-invasively measured and can be compared without concerns about flame disturbance. Overall, the agreement between the simulations and experiments is very good. All of the flame positions and major trends with changing flame parameters are captured by the 2D simulations. Oscillations are observed at the flame edge ($r > 11$ mm) in both simulations and experiments (Fig. 4.3), but repeated experimental measurements lead to time-averaged results. Because the

Table 4.2 Chemiluminescence reaction mechanism used to model CH* formation in flames, modified from Table 2.2 in [261]. Rate coefficients are expressed as $k = AT^b \exp(-E_a/RT)$, where E_a has units of cal mol^{-1}, T has units K, and A has units of cm^3 mol^{-1} s^{-1}.

Index	**Reaction**	A	b	E_a	**Ref.**
1	$C_2 + OH \longleftrightarrow CH^* + CO$	2×10^{14}	0	0	[132]
2	$C_2H + O \longleftrightarrow CH^* + CO$	$1.08(\pm 0.4) \times 10^{13}$	0	0	[76]
3	$C_2H + O_2 \longleftrightarrow CH^* + CO_2$	$2.17(\pm 0.8) \times 10^{10}$	0	0	[76]
4	$CH^* + H_2O \longleftrightarrow CH + H_2O$	5.3×10^{13}	0	0	[341]
5	$CH^* + CO_2 \longleftrightarrow CH + CO_2$	2.41×10^{-1}	4.3	-1695	[341]
6	$CH^* + CO \longleftrightarrow CH + CO$	2.44×10^{12}	0.5	0	[341]
7	$CH^* + H_2 \longleftrightarrow CH + H_2$	1.47×10^{14}	0	1361	[341]
8	$CH^* + O_2 \longleftrightarrow CH + O_2$	2.48×10^{6}	2.14	-1720	[341]
9	$CH^* + N_2 \longleftrightarrow CH + N_2$	3.03×10^{2}	3.4	-381	[341]
10	$CH^* + CH_4 \longleftrightarrow CH + CH_4$	1.73×10^{13}	0	167	[341]
11	Einstein Emission	1.85×10^{6} s^{-1}	0	0	[341]

oscillations are outside the region of interest ($r < 11$ mm), instantaneous simulation results are compared to the experimental results.

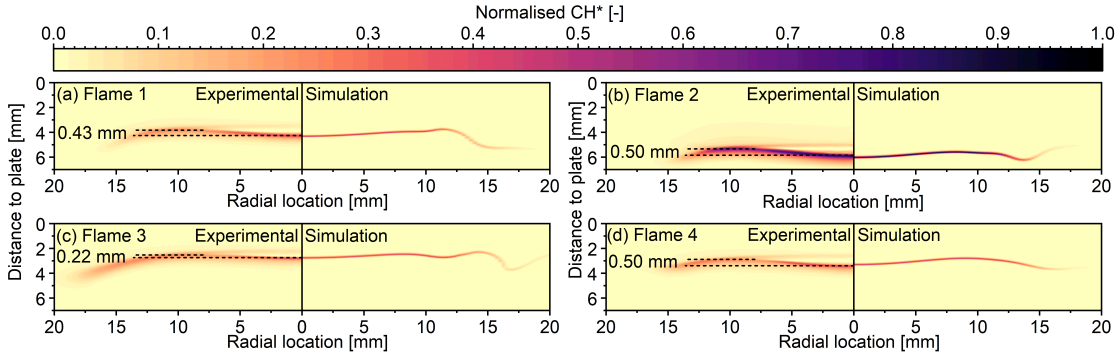

Fig. 4.3 Normalised CH* profiles obtained from experiments by recording the CH* chemiluminescence (left-hand panes) and the 2D simulations (right-hand panes). The dotted lines mark the points used to calculate the difference in vertical position, ε.

Flame 1 is located 4.3 mm from the plate, with its centre slightly curved towards the burner nozzle (Fig. 4.3a). The extent to which the flame was curved was quantified by calculating the difference between the vertical position of the flame centre and the position where the flame wing was closest to the plate, ε (analogous to the amplitude of a transverse wave, $\varepsilon = 0.43$ mm for Flame 1; see Fig. 4.3), and by calculating the arc-chord ratio, γ, (1.0178 for Flame 1) over the same region. Increasing the equivalence ratio in the experiments from $\phi = 0.7$ to $\phi = 0.8$ causes the flame to move closer towards the nozzle (5.8 mm from the plate) and to become

more curved (Fig. 4.3b; $\varepsilon = 0.50$ mm; $\gamma = 1.0312$). Simultaneously, the normalised CH* signal more than doubles as seen from the colour scale in Fig. 4.3 as well as extracted line plots shown in Fig. 4.4. The simulation predicts a flame location of 6.0 mm, captures the change in shape, and also predicts a twofold increase in CH*. The reason that the flame front shifts towards the burner is that the laminar flame speed is increased when the equivalence ratio is increased from $\phi = 0.7$ to $\phi = 0.8$. The increased CH* amount can be explained by the larger relative concentration of ethylene and the increase in temperature. Flames have been shown to curve as they move closer to the burner because the centreline flow is decelerated due to a build up in stagnation pressure [359].

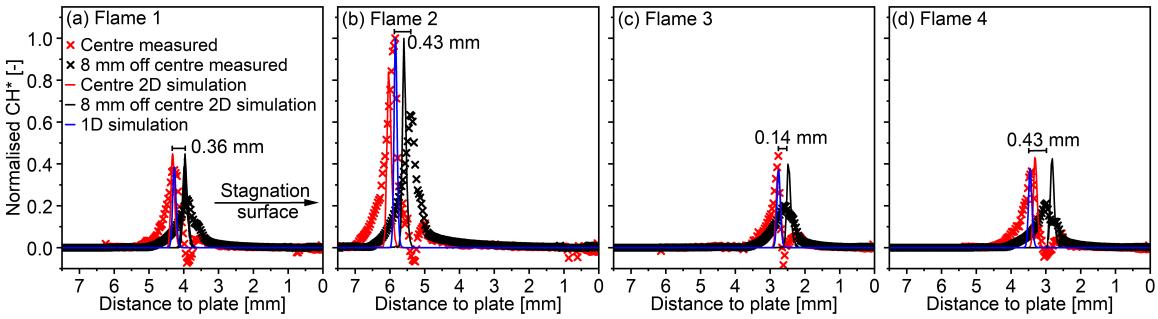

Fig. 4.4 Centre line and 8 mm off centre normalised CH* axial profiles with the addition of 1D simulation results.

When the experimental burner exit velocity was increased from 200 cm s^{-1} to 300 cm s^{-1}, the flame moved closer to the plate (2.8 mm) and became less curved (Fig. 4.3c; $\varepsilon = 0.22$ mm; $\gamma = 1.0093$). This is expected because the cold gas velocity has increased while the laminar flame speed remains unchanged. Similar observations have been made by other researchers [94, 359]. The 2D simulations capture both the shift of the flame towards the stagnation plate (2.8 mm) as well as the flattening of the flame shape.

Moving the burner nozzle closer to the stagnation plate shifts the flame closer to the plate and significantly curves the flame (Fig. 4.3d; $\varepsilon = 0.50$ mm; $\gamma = 1.0199$). This trend can be seen in both the experimental as well as the simulated CH* profiles. Flame 4 is more curved than Flame 1 because the stagnation pressure propagates into the nozzle for small separation distances [29]. This leads to an increased centreline deceleration and more curved flames [359].

4.5.1 Flame temperature

The 2D temperature profiles and selected line profiles are shown in Fig. 4.5 and Fig. 4.6, respectively. Because the flame was shown to attach to the filament when positioned upstream of the flame front (Section E.1.1), only temperature downstream of the flame front is shown.

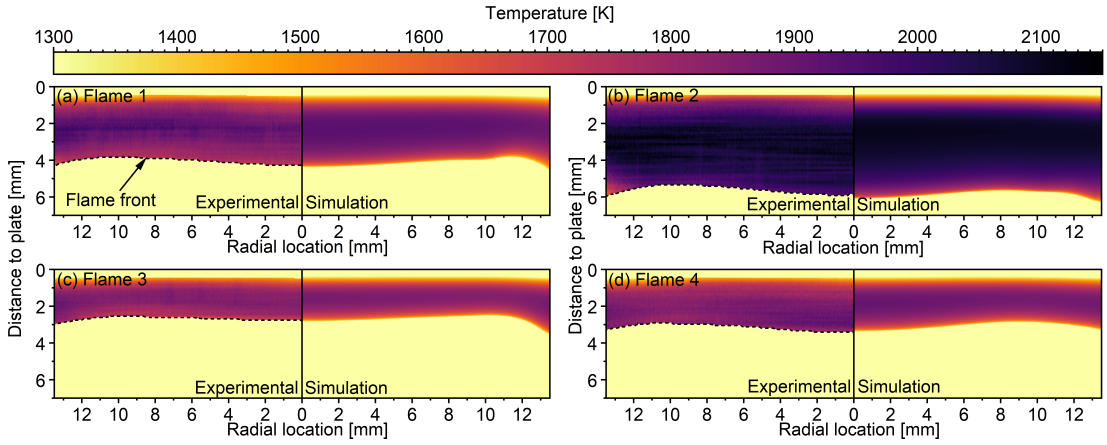

Fig. 4.5 Cross sections of temperature profiles from thin filament pyrometry experiments (left-hand panes) and 2D simulations (right-hand panes). The average of three repeat measurements are reported.

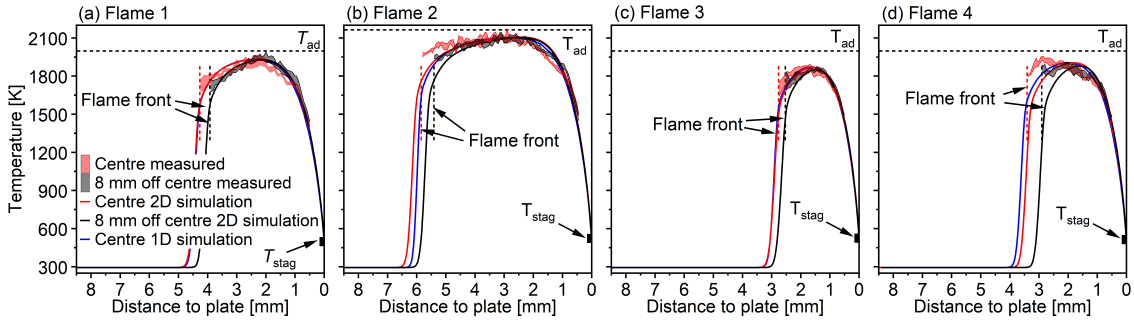

Fig. 4.6 Extracted temperature profiles along $r = 0$ mm and $r = 8$ mm for experiments and 2D simulation and 1D simulation of centreline values. Three repetitions were measured. The standard deviation of the temperature measurements is shown as a shaded area with the average being in the centre.

For the purpose of these figures, the flame front was defined as the maximum in CH* chemiluminescence recorded from the undisturbed flame. Nevertheless, a slightly higher temperature can be observed in the pre-heat zone of the experimental results, most likely due to the flame attachment and accompanied shift in the high-temperature region.

The absolute temperatures and trends with changing flame parameters are in excellent agreement between the experiments and 2D simulations (Fig. 4.5). Increasing the equivalence ratio from $\phi = 0.7$ to $\phi = 0.8$ increases the flame temperature by about 170 K. The reason for this is the increase in the adiabatic flame temperature from $T_{ad} = 2001$ K to 2165 K (calculated using *k*inetics™ [65]). When the flame was closer to the plate, the heat loss to the water-cooled stagnation surface increases and thus cools the flame slightly (∼60 K from Flame 1 to 3 and ∼30 K from Flame 1 to 4). The increased heat loss can also be seen in the increase in the stagnation plate temperature T_{stag} reported in Table 4.1.

Temperatures obtained from the 1D simulations are also shown in Fig. 4.6. They are essentially identical to the centreline temperatures obtained from the 2D simulations. The only noticeable difference is that the onset of the temperature rise is slightly shifted for Flames 2 and 4. The reason for this is that the boundary conditions for the 1D simulations were chosen such that the CH* peak matches the experiments exactly (see Fig. 4.4) while the 2D simulations predict the flame positions based on the experimental parameters. Thus the 1D simulations require some kind of experimental characterisation of the flame (CH* profiles as in this study or velocity fields as in [27, 374]) while the 2D simulations are predictive.

4.5.2 Temperature-residence time profiles

The 2D simulations can be used to extract a number of quantities of interest. Given that premixed stagnation flames are increasingly used for nanoparticle synthesis [345, 216], one quantity that might be of particular interest is time-temperature curves along streamlines. These could be used to assess the temperature history that nanoparticles experience during synthesis and serve as input to models that resolve the evolution of a population of particles with a given chemical environment [199].

Velocity profiles of Flame 1 superimposed with vector fields and calculated streamlines are shown in Fig. 4.7a (see Fig. 4.8 for other flames). The temperatures as a function of residence

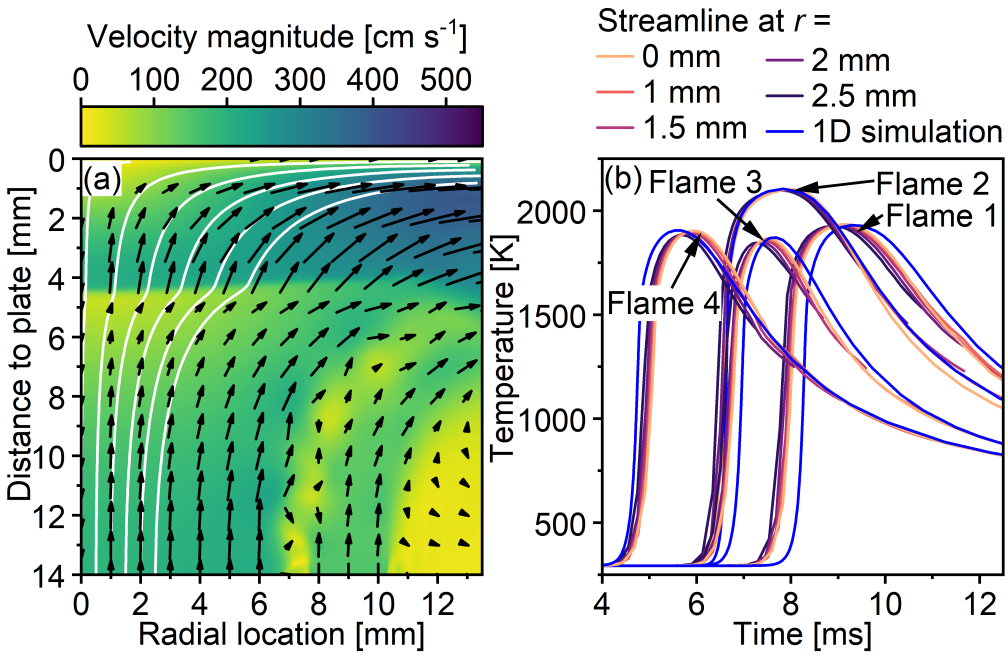

Fig. 4.7 (a) 2D velocity-streamline plot for Flame 1 and (b) temperature-residence time plot for all flames. The abrupt change in the streamlines occurs at the flame front (left panel).

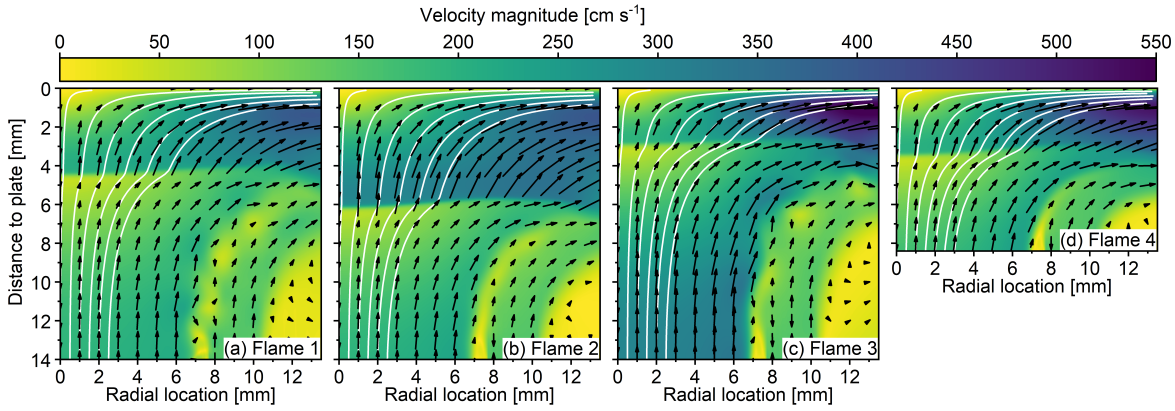

Fig. 4.8 Simulated 2D velocity fields of the four flames studied. Details regarding the flame parameters can be found in Table 4.1. The abrupt change in the streamlines occurs at the flame front.

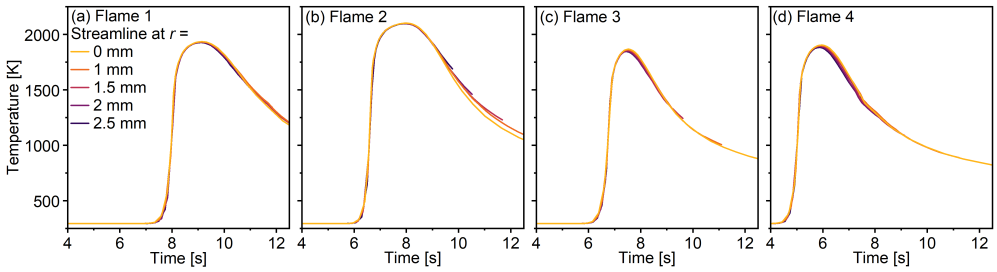

Fig. 4.9 Time-temperature profiles of the streamlines shown in Fig. 4.8. Except for the streamline at $r = 0$ mm, the curves were shifted on the abscissa such that the time at which they reach 1500 K is identical to the streamline at $r = 0$ mm.

time along these streamlines are plotted in Fig. 4.7b. The time-temperature curves of the 1D model agree reasonably well with the results at $r = 0$ from the 2D simulations. The onset in temperature rise seems to be shifted slightly which might be due to the differences in flame positions (see Fig. 4.4) or the boundary conditions imposed in the 1D model (see Section 4.5.1). Comparing the streamlines at different radial positions reveals that they do differ slightly for some flames, such as the peak temperatures experienced in Flame 3 and 4. The differences in streamline profiles are consequences of intricately linked reasons, such as a shift in flame front towards the burner close to the axis of symmetry for the highly curved flames. However, even after shifting the profiles such that the pre-heat zone overlaps at all radial positions, a slight spread of the profiles can be observed (Fig. 4.9). To what extent this influences particle properties during material synthesis is suggested as future work. It is interesting to note, however, that the streamline profiles appear to overlap most for Flame 2 even though it showed

the highest tortuosity of all flames (Fig. 4.3). Thus, optical inspection of the flame shape seems to be insufficient to assess how similar the streamlines at different radial positions will be.

4.6 Comparison between 1D and 2D simulations

Table 4.3 shows values of the axial velocity and strain extracted 1–2 mm upstream of the flame front from the 1D and 2D simulations reported in the main text. The values are in good agreement with those fit to experimental flame position. The values of the axial velocity and strain extracted from the 2D flame were subsequently imposed as boundary conditions in a new set of 1D simulations. Figure 4.10 compares the temperature, CH mass fraction and axial velocity from the new 1D simulations with the 2D simulations. The flow, temperature profiles and the prediction of CH location are in agreement for Flames 1 and 3. However, the results for Flames 2 and 4 differ between the 1D and 2D simulations. Flame 2 differs in the flame location as described by CH as well as in the axial velocity and temperature profiles. Smaller differences can be observed in Flame 4. Flame 2 and Flame 4 are both systems where the flame-nozzle separation is decreased. This is because of an increased laminar flame speed in Flame 2, and decreased nozzle-plate separation in Flame 4. In these situations, the constant pressure gradient assumption in the 1D model may not be adequate.

Table 4.3 Comparison between 1D boundary conditions extracted from the 2D simulations and boundary conditions fit to an observed experimental location used in this chapter.

		2D Simulations		1D Simulation	
Flame	x_{pos} mm	Axial Velocity cm s^{-1}	Strain s^{-1}	Axial Velocity cm s^{-1}	Strain s^{-1}
1	6.0	79.8	141	77.1	126
2	8.0	97.1	133	99.9	121
3	4.0	77.0	213	77.7	200
4	4.0	53.4	195	48.4	184

Another important point to consider is whether uncertainty in the boundary conditions may disguise deficiencies in the mechanism. The 2D simulations have well defined boundary conditions upstream of the nozzle, which makes identifying appropriate boundary conditions relatively simple. On the other hand, the 1D simulations require a radial strain profile to be specified as a boundary condition. It is non-trivial to identify the correct value for this boundary condition. In absence of *a priori* information, it must be guessed, for example by adjusting the strain boundary condition until the desired flame position is observed. There is an inherent assumption that the choice of mechanism leads to the proper prediction of the flame front,

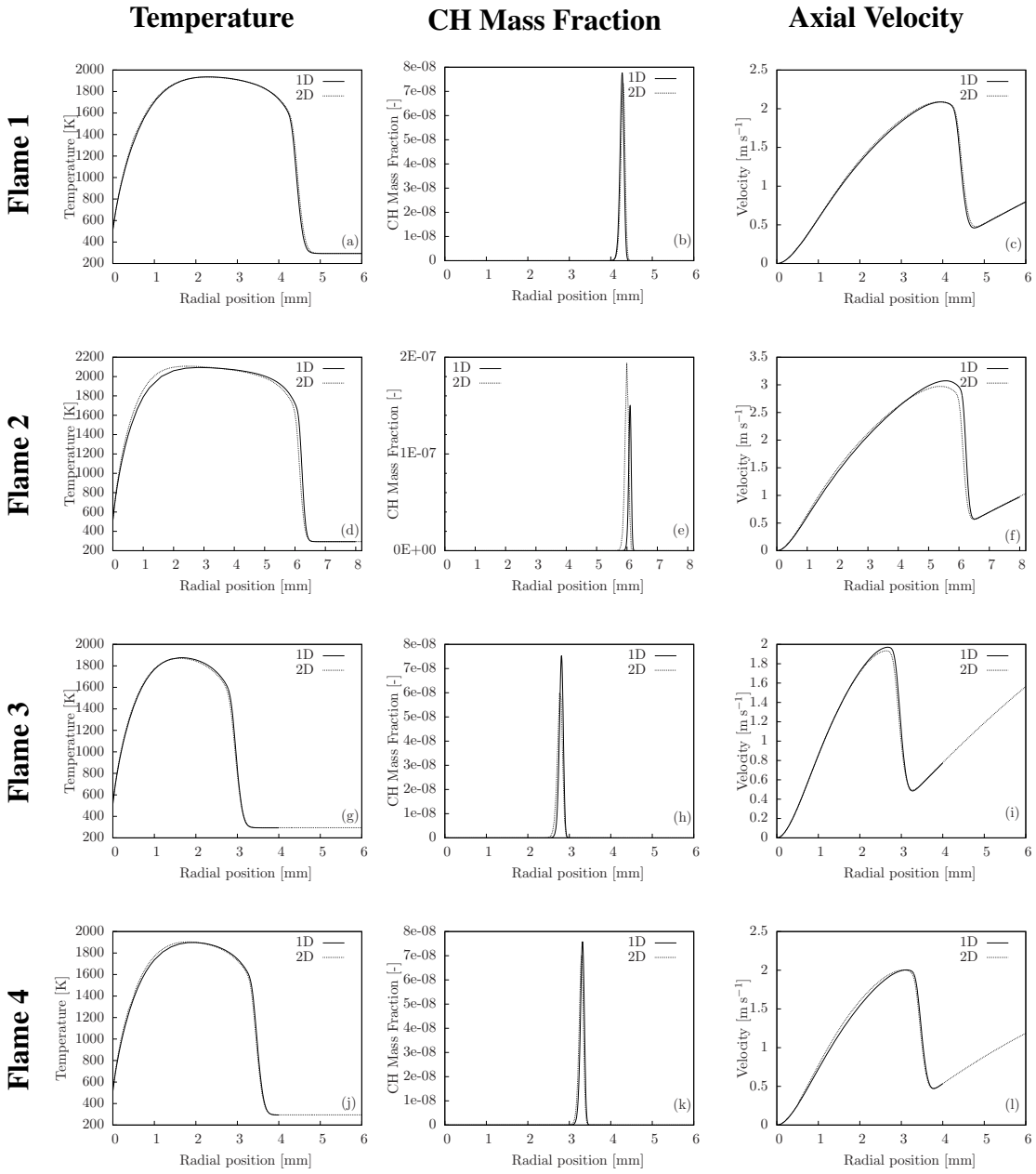

Fig. 4.10 Comparison between 1D and 2D simulations using boundary conditions extracted from the 2D simulations.

which is not always the case. This can be observed by running 1D simulations and observing the change in the predicted flame front location when using different mechanisms with a given set of boundary conditions, such as in the work of Watson [373]. If not careful, such adjustment of the strain boundary condition can 'compensate' for errors in the prediction of the flame front location, leading to unfair comparisons between experiments and simulations. In the 2D

simulations, the choice of mechanism will still lead to different predictions of the flame front, but the modeller has more confidence in the choice of boundary conditions.

4.7 Conclusions

The flame location, shape, and temperature were characterised as 2D fields using CH* chemiluminescence and thin filament pyrometry to capture the changes in a premixed, jet-wall stagnation flame when varying the equivalence ratio, exit gas velocity, and burner-plate separation distance. Information from 2D simulations allows for TFP measurements to infer the gas temperature by performing a heat balance over the filament.

The new experimental data will provide a new point of comparison for future experiments and simulations. The flame temperature, location, and shape are reported, which are key markers for assessing how well a simulation reproduces experimental observations. The spatial uncertainty in the temperature data is significantly less than previously reported in literature due to the small diameter of the filament compared to thermocouples.

The new experimental data is compared to 1D and 2D simulations. The computed temperature profiles are in excellent agreement with the experimentally-observed temperature. However, the 2D simulations only require trivial boundary conditions (such as mass flux) to predict the flame properties while additional full specification of the strain rate boundary condition are required for the 1D simulation. The additional radial information provided by the 2D simulations allows for streamline profiles to be extracted off the centreline. The temperature-residence time distributions of each flame were found to be approximately uniform, however, the uniformity was not found to correlate with the flatness of the flame.

Chapter 5

Radial dependence of properties of flame synthesised TiO_2 nanoparticle

The implemented 2D method has now been shown to reliably predict the flame structure when compared to experiments. A spherical particle model is added to study the growth of nanoparticles in jet-wall stagnation flames. Titania is used as the synthesised material to demonstrate the ability to simulate nanoparticle growth with different precursor loadings. Particle trajectories from different radial locations are extracted from the 2D simulations and the residence time distributions are examined. The trajectories are post-processed using a detailed particle model to examine the differences in titania nanoparticle growth along different streamlines. The particle size distributions are found to be statistically different beyond a critical radius.

5.1 Acknowledgement

This work is in preparation for submission: **Eric J. Bringley**, Manoel Y. Manuputty, Casper S. Lindberg, Gustavo Leon, Jethro Akroyd and Markus Kraft. Simulations of TiO_2 nanoparticle synthesised off-centreline in jet-wall stagnation flames. *In Preparation*. The co-authors contributed to the experimental design, to the interpretation and presentation of the results, and to the revision of the manuscript.

5.2 Introduction

Jet-wall stagnation flames have several advantages when employed to study the fundamental physics of nanoparticle synthesis. First, they are a laminar and stable system with a well-defined stagnation plane. This makes them easy to model, simulate, and study experimentally. Second, the temperature-residence time is well controlled along the centreline of jet-wall stagnation flames. This facilitates narrow nanoparticle size distributions and thermophoretic deposition. Third, changing experimental parameters have been shown to produce nanoparticle with different properties, such as average particle size [202], crystalline phase [202, 215, 218], and oxygen-vacancies [394]. This provides a simple route to produce and test particles with specific properties.

There are two ways to control the temperature residence time in jet-wall stagnation flames. First, the premixed gas can be varied by changing its composition (e.g. fuel; equivalence ratio, ϕ; and dilution) or total flow rate [218]. Second, the ability to cool the stagnation surface [345, 217] creates large temperature gradients that drive thermophoretic deposition of nanoparticles. The stagnation surface is cooled through one of two ways: air-cooling or water-cooling. In the air-cooled systems, the stagnation surface is rotated such that it is cooled by forced convection. This system is known as a flame stabilised on a rotating surface (FSRS) system [345, 239, 393, 215]. Alternatively, a water-cooled stagnation surface with sampling orifices can be used [217, 82].

Works that model nanoparticle synthesis in jet-wall stagnation flames [345, 239, 216, 198, 199, 175, 218] frequently describe the flame environment using the pseudo 1D model [164]. Although the 1D model provides a computationally efficient approach, the model only resolves centreline information, leaving radial information unresolved. Simulations of jet-wall stagnation flames with a stationary and rotating surface in 3D [145] showed that the total residence time and deposition temperature vary along different particle trajectories depending on their starting inlet radius. How this impacts nanoparticle growth is missing in the literature and cannot be addressed using the 1D model. Therefore, alternative approaches that solve the full set of Navier-Stokes conservation equations are needed to explore the physics off-centreline.

In order to examine the effect of the variation of residence time, a population balance equation (PBE) needs to be solved to describe the evolution of nanoparticles. Depending on the particle model, different levels of details about particles can be obtained. A two-step methodology has previously been developed to resolve detailed particle information in jet-wall stagnation flames [198]. A spherical particle model is coupled to the psuedo 1D model to account for the TiO_2 nanoparticle growth in the 1D simulation. The Lagrangian streamline along the centreline is then post-processed using a detailed particle model to resolve information such as the particle size distribution [199] or crystal phase [218]. Because the Lagrangian

streamline is applied as a post-process, it can be applied to any Lagrangian streamline, such as those calculated by multidimensional solvers.

The **purpose of this chapter** is to explore the properties of TiO_2 particles synthesised along different radial trajectories in a laminar, jet-wall stagnation flame. A spherical particle model was fully coupled to the governing reacting flow equations and solved in 2D to resolve average details of TiO_2 particles. Particle trajectories extracted from the 2D simulations were post-processed with a detailed particle model to resolve particle properties, such as the size distributions, primary particle sizes, and particle morphology.

5.3 Burner geometry and boundary conditions

Figure 5.1 presents the premixed, jet-wall stagnation burner that was simulated in this work. The setup is similar to those used in previous studies of synthesis of titania from titanium(IV) tetraisopropoxide (TTIP) [216–218, 417] as well as in experiments measuring temperature in 2D by thin-filament pyrometry as seen in the previous chapter (Chapter 4).

The burner consists of a nozzle with two concentric outlets and a water-cooled stagnation surface. The central outlet consists of an aerodynamic nozzle used to accelerate the gases, while the annular outlet provides a sheath flow of nitrogen to separate the premixed gases from the ambient atmosphere. The burner is open to the atmosphere and at ambient pressure (101.325 kPa). The burner and stagnation surface are separated by 14 mm, corresponding to a unity ratio between nozzle-surface separation distance and nozzle diameter as is frequently used when characterising jet-wall stagnation experiments [27].

The gases used for the simulations in this work were mixtures of ethylene-oxygen-argon at two different equivalence ratios as motivated by past experimental work: a lean flame with an equivalence ratio of $\phi = 0.35$ and a stoichiometric flame with an equivalence ratio of $\phi = 1.0$. For the purpose of this study, the two equivalence ratios provide two different backgrounds for TiO_2 synthesis. A premixed gas flow rate of 28 slpm was used for both equivalence ratios; this corresponds to an exit velocity of 436 cm/s. The sheath flow rate of 13.6 slpm of nitrogen was kept constant for all conditions studied; this produces a velocity of 150 cm/s. Two TTIP loadings were studied in this work: 280 and 560 ppm of TTIP. Argon was assumed to be displaced by the presence of TTIP, which changes the mass fraction of argon by less than 0.5%. The full list of mass fractions at the inlet boundary are tabulated in Table 5.1. The boundary conditions for other species mass fractions at the inlets were fixed at 0. All other species boundary conditions were specified as zero-gradient.

The remaining boundary conditions used are as follows: The inlet gas temperature was specified as 423 K for both the gas and sheath flow, to replicate the experimental preheating

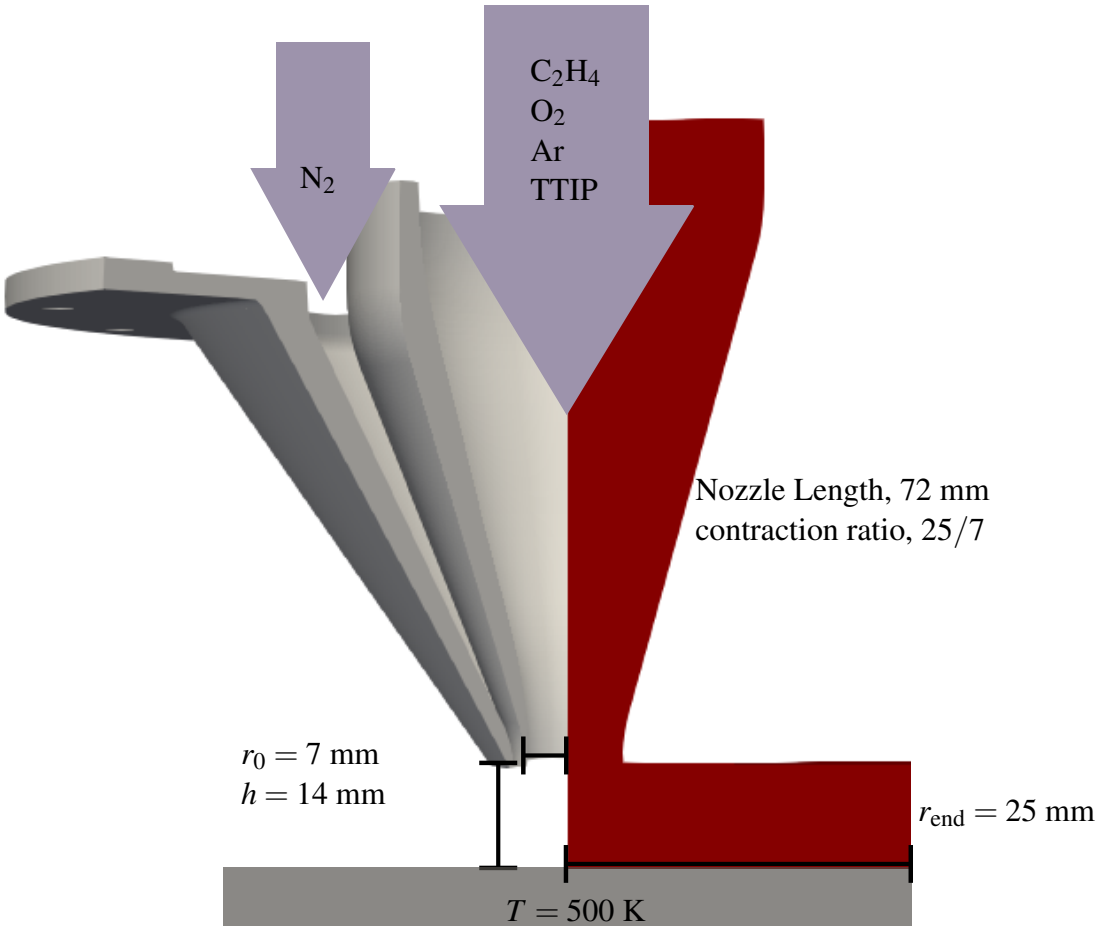

Fig. 5.1 Burner geometry and computational domain (red) for the premixed, jet-wall stagnation flame modelled in this chapter.

Table 5.1 Mass fraction boundary conditions.

	Mass Fractions (%)			
ϕ (-)	C_2H_4	O_2	Ar	TTIP
0.35	2.27	25.94	71.79	0
	2.27	25.94	71.58	0.21
	2.27	25.94	71.36	0.43
1.0	3.45	11.79	84.56	0
	3.45	11.79	84.35	0.21
	3.45	11.79	84.13	0.43

that was used to avoid TTIP condensation. The gas and sheath flow inlet velocities were fixed to match the volumetric flow rates assuming uniform velocity profiles. Zero gradient pressure boundary conditions were assigned to the inlets while ambient pressure outlets were specified at the boundaries open to the atmosphere (fixed 101.325 kPa). Isothermal and no-slip boundary

conditions were specified at walls. The temperature of the burner walls was assumed to be equal to that of the inlet gas ($T = 423$ K), while the stagnation surface was assumed to have a uniform temperature of 500 K, which was previously experimentally measured at the stagnation point of a water-cooled stagnation surface (see Chapter 4). The inlet boundary condition of the particle fields corresponded to no particles; for all other particulate field boundaries, a zero gradient boundary condition was used.

5.4 Models

The model equations for the laminar flame and spherical particle model for the 2D flow simulations were described in Sections 3.2 and 3.3.1 respectively. In short, the governing equations include the convective-diffusive-reactive equations for the gas and particle phases (mass, momentum, enthalpy, species mass fraction, and moments). Thermodynamic properties are described by JANAF polynomials [126]. The viscosity is defined by a semi-empirical formula [386, 33]. Species diffusion is modelled with the mixture-averaged approach [139]. The ideal gas law is used to close the equation of state.

The gas phase combustion mechanism used in this study was the San Diego Mechanism [354]. The full mechanism of the decomposition of TTIP [47, 48] is too large to be included in fully coupled 2D simulations. Therefore, a reduced mechanism for the decomposition of TTIP [199] is used with the combustion mechanism. It captures the decomposition of TTIP via C_3H_6 abstraction and CH_3/H abstractions to form $Ti(OH)_4$.

The model equations for the hybrid particle-number/detailed particle model used to post-process particle trajectories were described in Section 3.3.3. The particle-number threshold, N_{thresh} was set to 100, corresponding to a diameter of $d(N_{\text{thresh}}) = 1.8$ nm. Sintering parameters suggested by Lindberg et al. [199] are used and reported in Table 5.2.

5.5 Methods

The methods used to solve the model equations for the laminar flame, spherical particle model, and hybrid particle-number/detailed particle model are presented in Sections 3.4.1, 3.4.2 and 3.4.3, respectively. In summary, the governing equations were solved by the finite volume method, the spherical particle model was solved using the Method of Moments with Interpolative Closure [116, 115], and the hybrid particle-number/detailed particle model was solved using a direct simulation, Monte Carlo method.

To facilitate visualisation of the particle size distributions, kernel density estimates (KDE) were calculated using Gaussian kernels (bandwidth of 0.3 nm) to produce a continuous estimate

Table 5.2 Model Parameters

Parameter	Value	Notes
	Gas-phase model	
Mechanism		UCSD mechanism [354]
		Reduced mechanism TTIP decomposition [199]
c_p, h		JANAF polynomials (Eqns. 3.7 and 3.9) [126]
μ		Semi-empirical formula (Eqn. 3.16) [386, 34]
λ		Eqn. 3.25 [277, 225]
D_i		Mixture-averaged diffusion (Eqn. 3.27) [138]
	Spherical particle model	
ε	2.64	Collision enhancement factor
$d_{c,Ti(OH)_4}$	5.128×10^{-10} m	Collision diameter of $Ti(OH)_4$ [47]
$m_{Ti(OH)_4}$	115.93 kg kmol^{-1}	Mass of $Ti(OH)_4$
α_T	1	Thermal accommodation factor
γ_{IN}	1	Inception efficiency
γ_{SG}	1	Surface growth efficiency
ρ_{TiO_2}	4.25 kg m^{-3}	Density of rutile
	Hybrid particle-number/detailed particle model	
N_{thresh}	100	$d(N_{thresh}) = 1.8$ nm
α_{crit}	3	Critical sintering exponent [199]
$d_{p,crit}$	4 nm	Critical sintering diameter [199]
$E_{a,sintering}$	31030 K	Grain boundary diffusion activation energy
$A_{sintering}$	2.278×10^{17} s m^{-4} K^{-1}	Sintering frequency factor
ε	2.64	Collision enhancement factor
γ_{IN}	1	Inception efficiency
γ_{SG}	1	Surface growth efficiency
ρ_{TiO_2}	3.84 kg m^{-3}	Density of anatase

of the PSD using the Sci-kit Learn package [275]. To assess the similarity between distributions, binary comparisons of PSDs were made using a two sample, non-parametric Kolmogorov-Smirnov (KS) test [223, 141] as implemented in the Sci-Py numerical computing package [365]. For the KS tests, the null hypothesis, H_0, is that the two underlying distributions from which the samples are taken are equal. The confidence threshold used in this work is $\alpha = 0.01$.

5.6 Results and discussion

5.6.1 Thermochemical environment

Figure 5.2 presents the thermochemical environments in each flame for the two different TTIP loadings, 280 and 560 ppm. The centreline profiles of temperature and $Ti(OH)_4$, the gas phase species involved in inception and surface growth reactions, are shown at the bottom of the figure. For comparison, the thermochemical environment for the two equivalence ratio flames without TTIP can be found in the appendix (Fig. F.1).

It can be observed that the shapes of all the flames are very similar: the flames contain a flat central region with up-turned wings at $r/r_0 \approx 1.5$ (1 cm). The TTIP loading affected the location of the flame front of the lean flame as determined by the peak CH mass fraction (Fig. 5.2a). This can also be seen in Fig. 5.2d, where the flame front of the lean flame was located at $h = 1.7$ mm (dotted line) without TTIP. The addition of TTIP shifted the flame front closer to the burner. The flame was found to rest at $h = 1.9$ mm (solid line) above the stagnation surface for the 280 ppm loading and $h = 2.2$ mm (dashed line) for the 560 ppm loading. The lean flame location is predicted to be closer to the surface than past experiments which reported the flame front around 3 mm above the stagnation plate [216, 199]. In the stoichiometric flame, the flame front remained located at $h = 4.5$ mm for both loadings (Fig. 5.2d). This is in good agreement with measurements reported in literature: a stoichiometric flame was found to rest 3.5 mm from the stagnation surface [215] when the nozzle-surface separation was smaller than in this work. This will create a higher strain rate at the flame front and push the flame closer to the surface. The 1 mm difference in flame position is consistent with the change seen in previous work when changing the nozzle-surface ratio (see Chapter 4).

Figure 5.2 also shows the temperature (Fig. 5.2b) and the mass fraction of $Ti(OH)_4$ (Fig. 5.2c), the gas phase species involved in inception and surface growth reactions. The addition of TTIP to the flame contributed extra hydrocarbons which release extra enthalpy. However, the TTIP loading affected the lean and stoichiometric flames differently. The $\phi = 0.35$ flame had a peak temperature around 1840 K for 580 ppm TTIP, which was 160 K higher than without TTIP (1680 K, Fig. 5.2d). For 280 ppm TTIP in the lean flame, the peak temperature was 1760 K, which was 90 K higher than without TTIP. The $\phi = 1.0$ flame had a peak temperature around 2340 K for 560 ppm TTIP, which was 20 K higher than without TTIP. The two flames show very different $Ti(OH)_4$ fields. In the lean flame (Fig. 5.2c left column), $Ti(OH)_4$ was present downstream of the flame front with two peaks (Fig. 5.2e). This is consistent with centreline profiles predicted by the reduced mechanism in 1D simulations in the work of Lindberg et al. [199]. In contrast, $Ti(OH)_4$ was produced and consumed at the flame front of the stoichiometric flame (Fig. 5.2e).

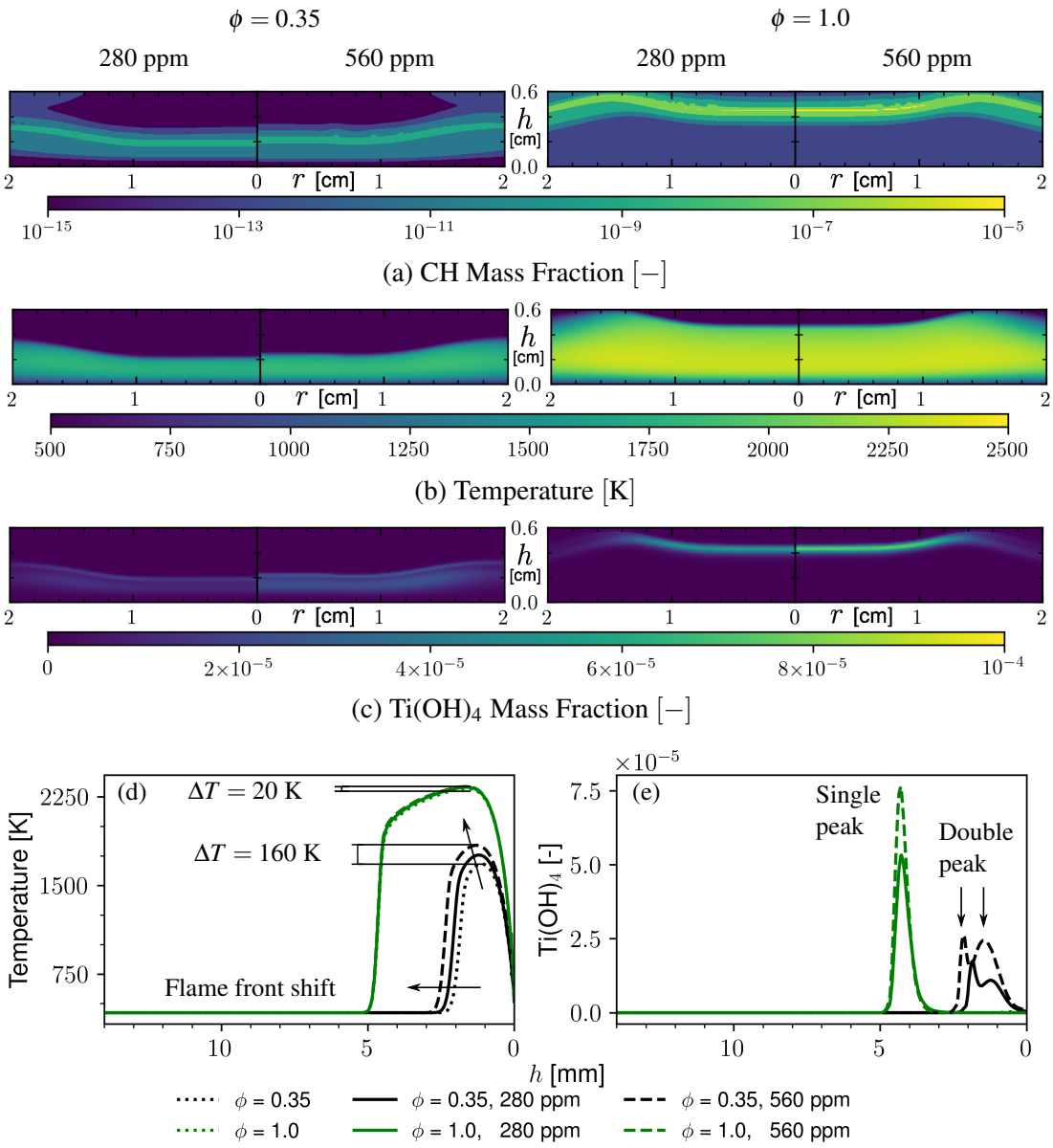

Fig. 5.2 2D mass fraction and temperature fields for the 280 ppm (left sub-panel) and 560 ppm (right sub-panel) TTIP loadings in the $\phi = 0.35$ (left) and $\phi = 1.0$ (right) flames. The centreline (d) temperature and (e) $Ti(OH)_4$ mass fraction are plotted to assist visual clarity.

5.6.2 Spherical particle model

Figure 5.3 shows fields for TiO_2 nanoparticles as predicted by the spherical model in the 2D simulations. The quantities in the figure are integral quantities of the distribution calculated from the moments.

The particle number density field (Fig. 5.3a) mirrors that of the precursor, $Ti(OH)_4$ (Fig. 5.2c). In the $\phi = 0.35$ flame (left column), the number density has two peaks, indicating that the rate of inception downstream of the flame front is competitive with that of coagulation. The $\phi = 1.0$ flame, in contrast, has a well defined peak in the number density at the flame front. The number density decreases moving downstream of the flame front, indicating that the rate of coagulation far exceeds the rate of inception downstream of the flame front.

Figure 5.3b shows the particle mass density field. There was a significantly slower transfer of mass from the gas phase to the particle phase in the $\phi = 0.35$ flame than in the $\phi = 1.0$ flame. In the lean flames, the particle mass density was very low at the flame front and peaked ≈ 1 mm above the stagnation surface. In the stoichiometric flames, the particle mass density rapidly approached its peak value at the flame front (≈ 4 mm above the surface); downstream of the flame front, the particle density changed with temperature due to thermal expansion and contraction of the gas (see temperature change downstream of flame front in Fig. 5.2d).

The average particle diameter (Fig. 5.3c) shows two different trends as a function of equivalence ratio. In the lean flames, the particles remain small (≈ 1 nm) until they approach the surface (Fig. 5.3c left column). In the 280 ppm case, the average diameter on the surface was 3 nm. In the 560 ppm case, it was 10 nm. In the stoichiometric flames, the particles have an average diameter of approximately 3 nm near the flame front and continue to grow until they reach the stagnation surface. In the 280 ppm case, the average diameter on the surface was 5 nm. In the 560 ppm case, it was 8 nm.

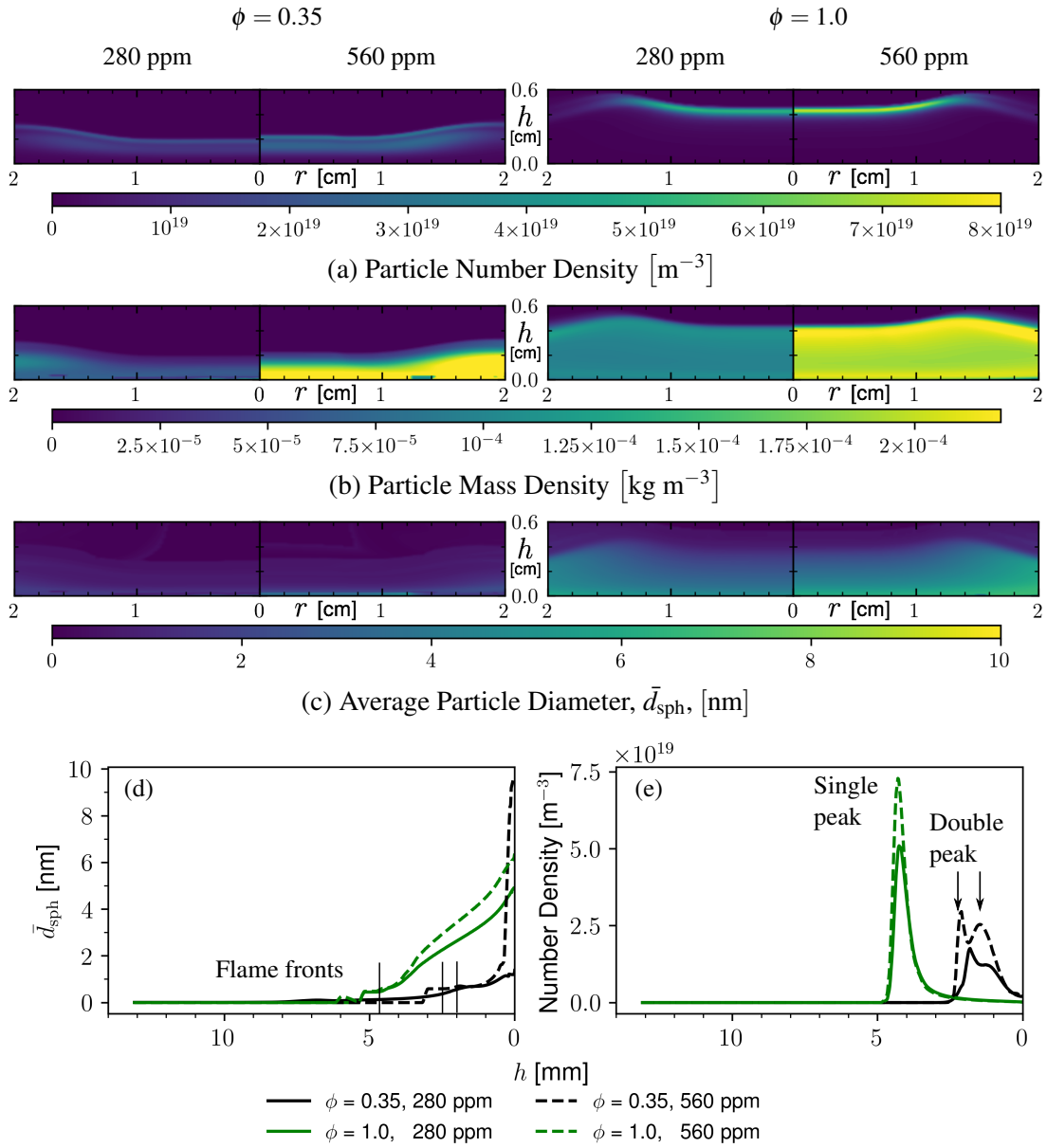

Fig. 5.3 2D particle fields for the 280 ppm (left sub-panel) and 560 ppm (right sub-panel) TTIP loadings in the $\phi = 0.35$ (left) and $\phi = 1.0$ (right) flames. The centreline (d) average particle diameter and (e) number density are plotted to assist visual clarity.

5.6.3 Residence time distributions

Figure 5.4 shows the total residence time and deposition radius of the trajectories sampled from the 2D simulations as a function of the radial starting point of each trajectory. The trajectories were calculated considering both convective and thermophoretic transport. Without the thermophoretic transport, the trajectories would not impinge (see Fig. 5.5). The total residence time is approximately constant up to an inlet radius of $r/r_0 = 1/7$ (1 mm), after which it begins to grow, leading to more time for particles to evolve. The deposition radius is approximately linearly dependent on the initial radius. Additionally, it can be observed that the 560 ppm TTIP loading results in a residence time that is 0.5 ms shorter than the 280 ppm TTIP loading in the $\phi = 0.35$ flame. The TTIP loading did not affect the residence time distributions in the $\phi = 1.0$ flame because the predicted temperature profiles were almost the same.

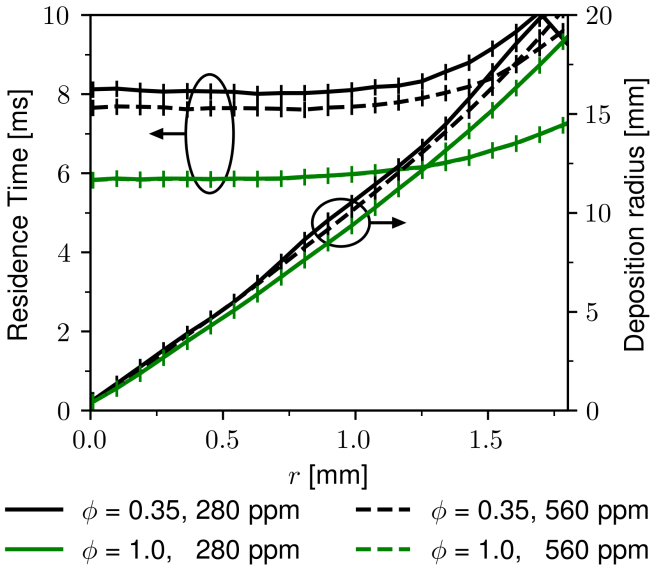

Fig. 5.4 Total residence time (left) and deposition radius (right) as a function of starting radial point, r. The total nozzle outlet radius is $r_0 = 7$ mm. The markers indicate the starting radii of the sampled trajectories used in the subsequent analysis.

Figure 5.6 shows the temperature as a function of residence time along different particle trajectories. The profiles are very similar at the flame fronts, but trajectories originating from larger starting radii spend more time at higher temperatures, with some trajectories leaving the computational domain before depositing on the stagnation surface. This produces different rates of cooling as the particles move from the flame front to the stagnation surface. Figure 5.7 shows the mole fraction of $Ti(OH)_4$, the particle precursor, as a function of residence time. In the $\phi = 0.35$ flames, $Ti(OH)_4$ was present downstream of the flame front. This leads to increased inception and surface growth rates in the lean flames. In contrast, the $\phi = 1.0$ flames

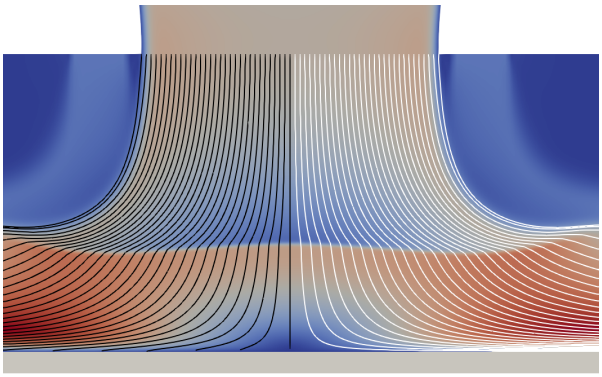

Fig. 5.5 Trajectories with (left) and without (right) thermophoretic drift. The trajectories that include thermophoretic drift impinge on the stagnation plate whereas trajectories without it do not.

have a delta-like profile at the flame front. The terminal values of the trajectories approached zero, indicating that $Ti(OH)_4$ was consumed through mass transfer to the particle phase. This is also the reason why the trajectories that leave the computational domain observed in Fig. 5.6 are not visible in Fig. 5.7.

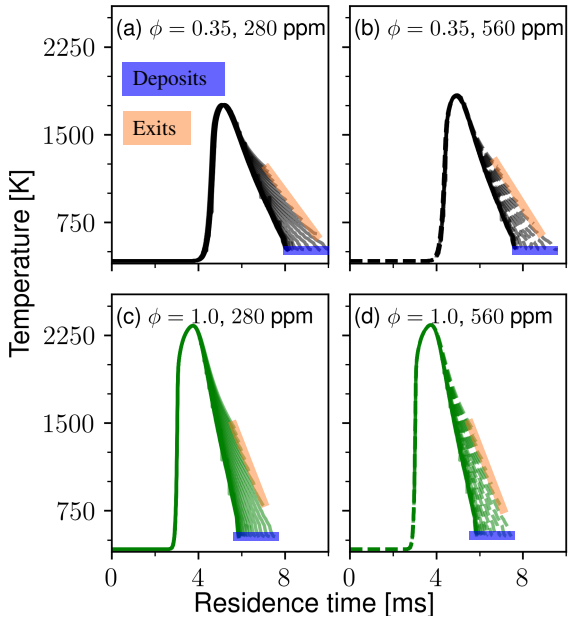

Fig. 5.6 Temperature as a function of residence time along particle trajectories at different starting radii (solid to transparent moving outwards). The ends of the trajectories are marked with bars indicating that the trajectories deposited on the stagnation surface (blue) or exit the simulation domain (orange).

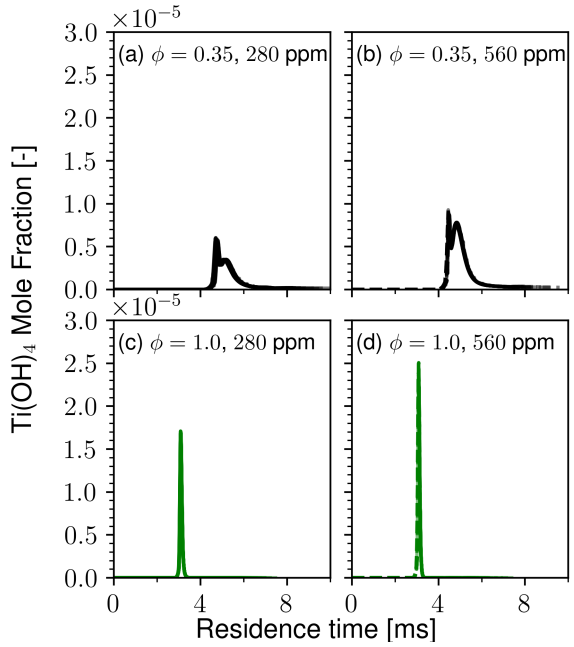

Fig. 5.7 $Ti(OH)_4$ as a function of residence time along particle trajectories at different starting radii (solid to transparent moving outwards). The profiles are found to be very similar and are seen to overlap.

Figure 5.7 shows that the $Ti(OH)_4$ mole fraction does not significantly change with the increased residence time of the trajectories that impinged on the stagnation surface. A similar trend was observed for other species (not shown). However, it is worth noting that trajectories originating from an inlet radius of $r/r_0 > 1/2$ (3.5 mm) begin to experience dilution from diffusion of the sheath flow. This changes the local thermochemical environment in these trajectories. These trajectories do not impinge on the stagnation surface due to the flow divergence at large radii and are not considered further in this study. However, these trajectories may be important if large flow re-circulation is experienced.

5.6.4 Detailed particle model

Particle size distributions

Figures 5.8 and 5.9 show the predicted mean aggregate diameter and mean number of primaries along different trajectories as a function of residence time. Like the chemical environment, the particle size distributions at the flame front were nearly identical. Differences begin to occur near the end of the trajectories, and are most easily seen by examining the particles that impinge on the stagnation surface. Therefore, the ends of the trajectories are examined further.

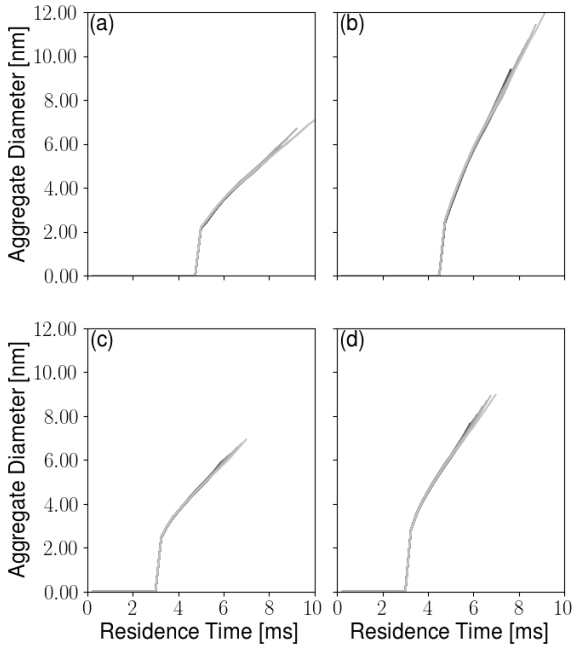

Fig. 5.8 Mean aggregate diameter as as a function of residence time along different trajectories (dark to light moving radially outwards from the centre of the flame) in (a) $\phi = 0.35$, 280 ppm flame, (b) $\phi = 0.35$, 560 ppm flame, (c) $\phi = 1.0$, 280 ppm flame, and (d) $\phi = 1.0$, 560 ppm flame. The inception mode is excluded in this figure.

Figure 5.10 shows the size distributions of the particles that impinge on the stagnation surface for each trajectory of each flame. The sphere-equivalent diameter is used to characterise particle size, which has shown to be comparable to mobility sizes measurements when the particles are nearly spherical [217], as is the case here. Note that Fig. 5.10 includes all particles tracked by the hybrid model, some of which are smaller than what may be experimentally observed.

The two equivalence ratios present different particle size distributions. In the lean flames (top row), the particle size distributions are bimodal with an inception mode and a coagulation mode. In the stoichiometric flames (bottom row), the particle size distributions are monomodal. The monomodal distributions are approximately log-normal. The lean flames produce larger particles due to the longer residence times (Fig. 5.4).

Table 5.3 shows the centreline values of the median diameter and geometric standard deviation for the primary particles and aggregates, alongside comparable experimental data from the literature. The primary particle sizes are determined experimentally by transmission electron microscopy (TEM), whereas aggregate particle sizes are determined from mobility size measurements. A small level of aggregation in the simulated particles can be inferred in

the cases where the median aggregate diameter is observed to be larger than the median primary particle diameter, though this comparison is not conclusive.

Table 5.3 A comparison between experimentally determined primary and aggregate particle sizes in the literature and sizes predicted by the simulations in this work at similar TTIP loadings.

			Primary Particle		Aggregate Particle	
Reference	ϕ	TTIP ppm	Median nm	GSD -	Median nm	GSD -
This work	0.35	280	6.1	1.34	6.0	1.44
		560	7.8	1.24	9.0	1.44
	1.0	280	6.0	1.40	5.9	1.45
		560	7.5	1.35	7.7	1.45
Manuputty et al. [217]	0.35	190	5.7	1.50	5.7	1.34
		580	9.7	1.62	10.4	1.44
	1.67	190	7.1	1.52	7.1	1.40
		580	9.8	1.63	9.9	1.40
Manuputty et al. [218]	1.0	365	-	-	8.0	1.5
Tolmachoff et al. [345]	0.45	300	5.8	1.31	8.9	1.34

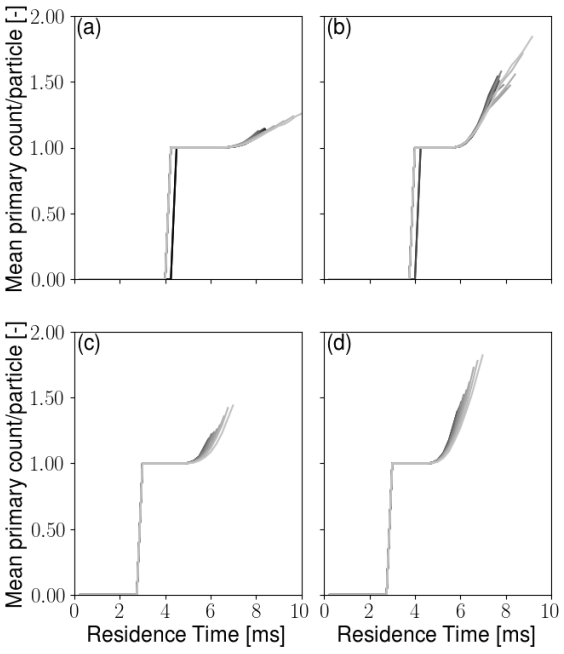

Fig. 5.9 Mean number of primaries per aggregate as a function of residence time along different trajectories (dark to light moving radially outwards from the centre of the flame) in (a) $\phi = 0.35$, 280 ppm flame, (b) $\phi = 0.35$, 560 ppm flame, (c) $\phi = 1.0$, 280 ppm flame, and (d) $\phi = 1.0$, 560 ppm flame.

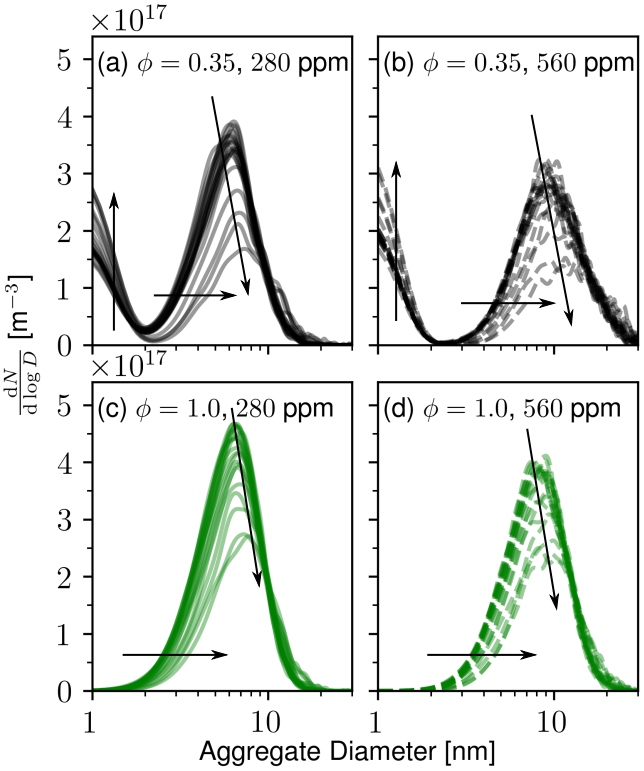

Fig. 5.10 Particle size distribution at the end of trajectories (solid to transparent moving radially outwards from the centre of the flame) that deposit on the stagnation surface. The arrows mark the trend moving radially outwards. The equivalent spherical diameter is used to characterise the particle size.

The quantities predicted by the simulations are in reasonable agreement with the experimental data. In the simulation of the lean flame, the median aggregate particle sizes were found to be 6.0 nm and 9.0 nm for 280 ppm and 560 ppm TTIP respectively. These values compare well with the median particle sizes of 5.7 nm and 10.4 nm measured by Manuputty et al. [217] in $\phi = 0.35$ flames with 190 ppm and 580 ppm TTIP.

In the work of Tolmachoff et al. [345], the primary and aggregate particle properties were measured with stagnation surfaces at difference temperatures. This was originally thought to be responsible for the difference between the primary and aggregate sizes [345]. It has since been shown that the difference in surface temperature does not explain the difference between the primary and aggregate sizes [216] and there is experimental evidence to suggest that the difference is due to a small degree of aggregation [217, 198].

A less direct comparison can be made for the stoichiometric flame simulated in this work. An aggregate particle size of 8.0 nm was measured by Manuputty et al. [218] for a TTIP loading of 365 ppm. This loading falls in between the values studied in the simulations in this work, which predicted aggregate particle sizes of 5.9 nm and 7.7 nm at 280 ppm and

560 ppm TTIP respectively. The results of this work appear to slightly under-predict the experimental aggregate sizes of Manuputty et al. [218], but are nevertheless in the right range and are considered to be physically reasonable.

The following sections examines similarity between the particle size distribution and the particle morphology. The radial dependency of the particle properties is discussed in Section 5.6.4.

Assessment of particle size distribution similarity

The similarity of the PSDs are assessed using the two sample Kolmogorov-Smirnov (KS) test [223, 141, 365] for each distribution pair. The null hypothesis, H_0, was that the two underlying distributions from which the samples were taken are equal.

Figure 5.11 presents the results of the two sample KS tests as reject (blue) or fail-to-reject (yellow) the null hypothesis of equivalent distributions. Similar trends are observed in all four cases. The PSDs of trajectories are mostly similar up to a critical radius beyond which the distributions become statistically different. In the lean flame, the critical radius was $r/r_0 \approx 1$ (0.7 cm) for the 280 ppm loading and $r/r_0 \approx 1.5$ (1.1 cm) for the 560 ppm loading. In the stoichiometric flame, the critical radius was $r/r_0 \approx 1$ (0.7 cm) for both TTIP loadings.

Particle morphology

Particle morphology is important for many applications. In the analyses that follow, particles from the particle-number model ($d(\mathrm{N}_{\mathrm{thresh}}) < 2$ nm) are excluded because they are smaller than the lower limit of the experimental TEM measurements (3 nm) [217]. In addition, the model parameters are such that rapid sintering causes small primaries ($d < 4$ nm) to coalesce with their larger neighbours. This makes the analysis consistent with experimental measurements of primary particle size by TEM.

Figure 5.12 shows the size distributions of the primary particles that impinge on the stagnation surface for each trajectory of each flame. As the particle trajectories move radially outwards, the frequency of the primary particles at 4 nm (the sintering limit) decreases, and the number of large primaries grow. This is most apparent in the flames with 280 ppm TTIP (left column). In the stoichiometric flames (bottom row), the distribution moves to the right. This is explained by coagulation and sintering of small primaries.

The median and geometric standard deviation of the primary particle sizes are tabulated in Table 5.3. The lean and stoichiometric flames have a median primary particle size of 6.1 nm and 6.0 nm at 280 ppm TTIP respectively. This is in good agreement with the available experimental data, which reports values of 5.69 nm [217] and 5.8 nm [345] in lean flames.

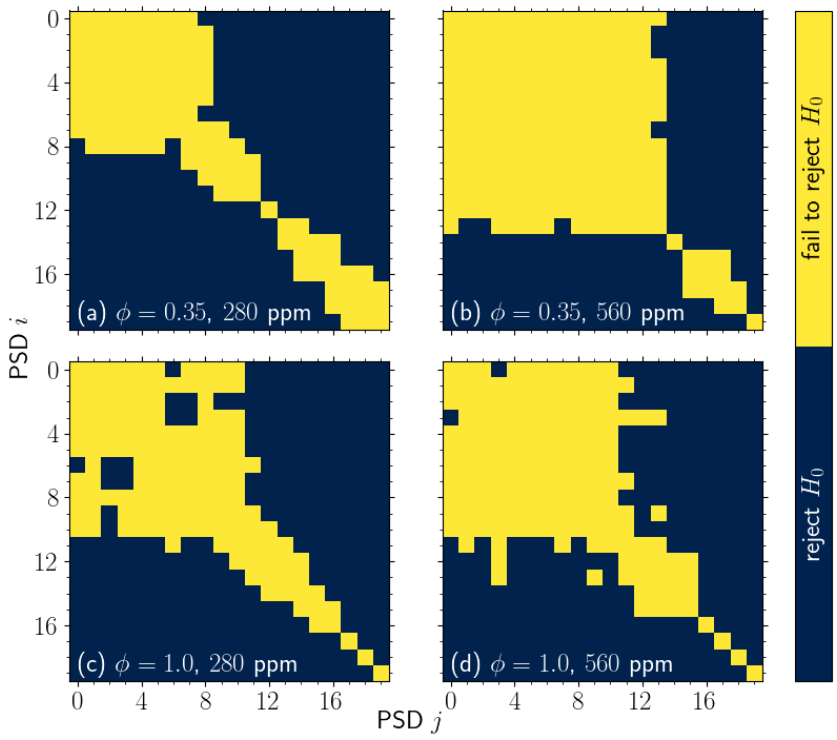

Fig. 5.11 Results of two sample Kolmogorov-Smirnov test between particle ensembles from different trajectories. The null hypothesis, H_0, was that the two underlying distributions from which the samples were taken are equal. Results marked with yellow fail to reject H_0: the two distributions are equal at the $\alpha = 0.01$ confidence level; results marked with blue provide evidence to reject H_0 ($p < 0.005$).

Figure 5.13 shows joint distributions of aggregate collision diameter and average primary diameter, number of primaries, and average sintering level for three different trajectories for the lean flame with 560 ppm TTIP. The sintering level is defined as the ratio of the 'neck' radius and the radius of the smaller primary [200]. The averages are calculated as the arithmetic mean of the corresponding quantities for the primaries within each aggregate. The trajectories are selected to represent the centreline, an off-centreline trajectory that shows similar trends to the centreline, and an off-centreline trajectory that shows significant differences. The black dotted lines in the figure show the corresponding values for values spherical particles. The fraction of spherical particles is reported for each trajectory. Results for the other flames showed similar trends and can be found in the supplementary material (Fig. F.2).

Figure 5.13 shows that aggregates are comprised of larger primary particles that are near the median size. Additionally, that the number of primaries in point contact grows as the deposition radius increases (moving left to right). This is most strongly affected by the TTIP loading

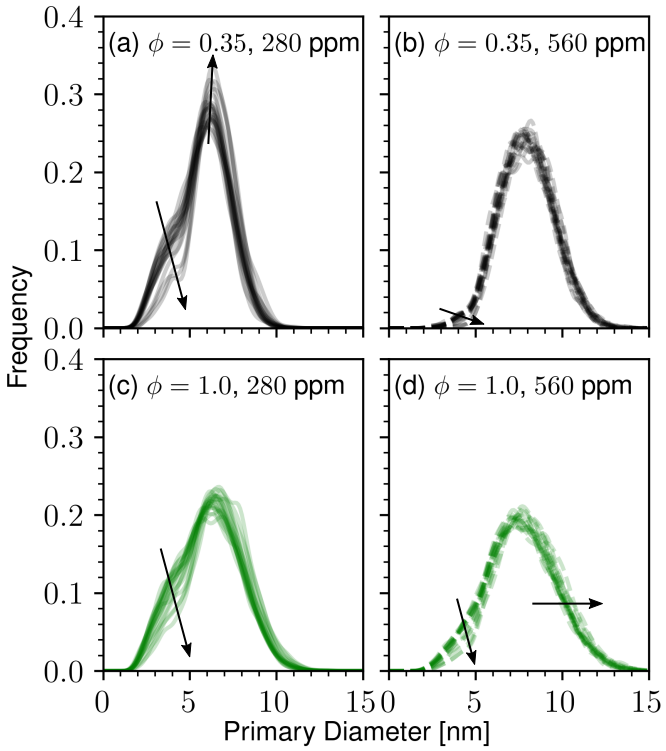

Fig. 5.12 Primary particle size distributions at the end of trajectories (solid to transparent moving radially outwards from the centre of the flame) that deposited on the stagnation surface. The arrows mark the trend moving radially outwards.

(Fig. F.2) as higher TTIP loadings results in more aggregated particles. These particles are not strongly sintered, suggesting that they coagulate at the end of the trajectories and do not have time to fully coalesce when above the sintering critical diameter. This is further supported by the observation that the average number of primaries remains small until larger residence times (Fig. 5.9).

While the previous analysis has considered joint distributions between the properties of the primary particles and the aggregates, the shape information provided by the detailed particle model allows for individual particles to be analysed. Figure 5.14 shows simulated TEM-style images for the stoichiometric flame with 560 ppm of TTIP for trajectories with three deposition radii, chosen to show the centreline trajectory, an off-centreline trajectory with similar PSD, and an off-centreline trajectory with a different PSD. For each trajectory, the simulated TEMs are produced for particles with collision diameters in the range: 3 nm $< d_c \leq$ 10 nm, 10 nm $< d_c \leq$ 20 nm, and 20 nm $< d_c$ to aid visual clarity. The relative frequencies between particles of different sizes are not preserved in Fig. 5.14. Particles with small collision diameters are observed to be largely spherical with very few aggregates. Between 10 and 20 nm, there is a

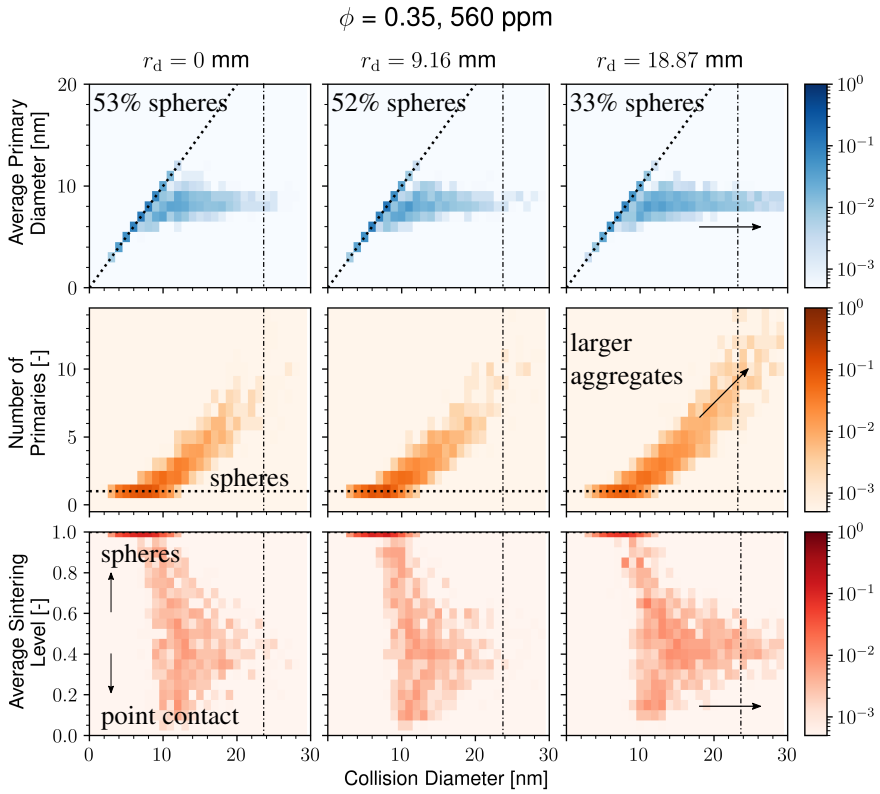

Fig. 5.13 Joint distributions of average primary diameter, number of primaries, and average sintering level with collision diameter at different deposition radii, r_d, for the lean flame with 560 ppm TTIP. The averages are arithmetic means are taken over the primary particles within each aggregate. The fraction of particles that are spherical are reported as a percentage. The dotted black line corresponds to spherical particles, while the dot-dash lines (column 3) mark the collision diameter of large aggregates that form at large deposition radii.

mix of spherical particles ($n_p = 1$) and aggregates. Above 20 nm, the particles are aggregates with the constituent primaries mostly in point contact or weakly sintered. The frequency of nanoparticles with collision diameters above 20 nm is higher in the outer trajectory. The nanoparticles produced along the centreline agree well with the experimentally produced particles seen in TEM images found the work of Manuputty et al. [217] who sampled particles from the centreline and shown in Fig. 5.15. Similar trends were observed for the other flames (not shown).

Radial dependency of the particle properties

Statistics of the aggregate and primary particles are compared as a function of the deposition radius to examine the effect of different trajectories on nanoparticle formation.

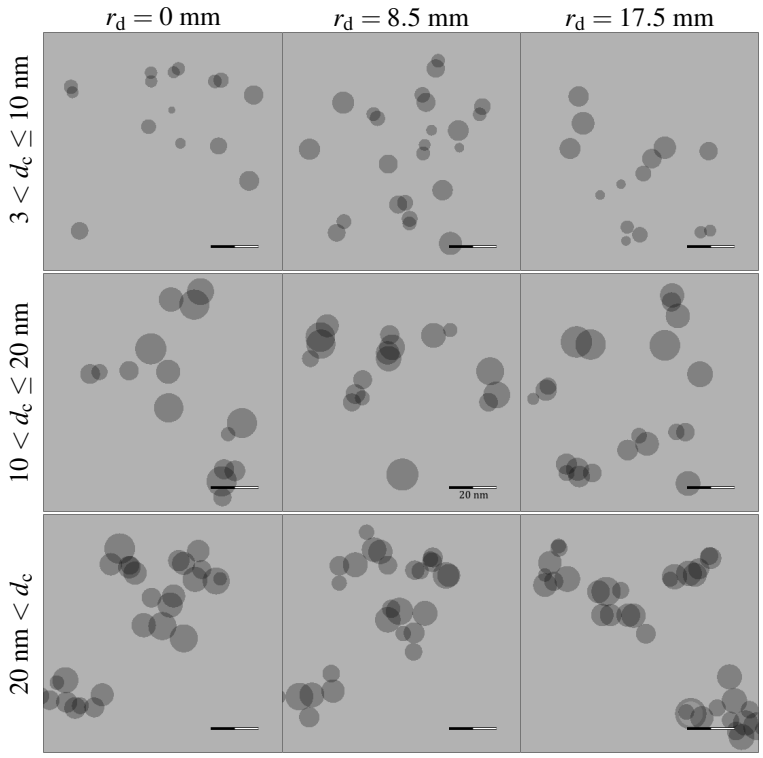

Fig. 5.14 Simulated TEM images of particles with different collision diameters, d_c at different deposition radii, r_d, in the stoichiometric flame with 560 ppm TTIP. The scale bar is 20 nm in width. The TEM images are 'supervised' such that the particles do not overlap. The largest particles are aggregates composed of primary particles that are in similar in size to the primary particles seen in the smaller particles.

Figure 5.16 shows the median sphere-equivalent diameter, $\langle d_{sph} \rangle$, and geometric standard deviation, GSD, of the terminal particle size distribution of the aggregates as a function of deposition radius. The trend observed in the median particle size is analogous to that seen in the

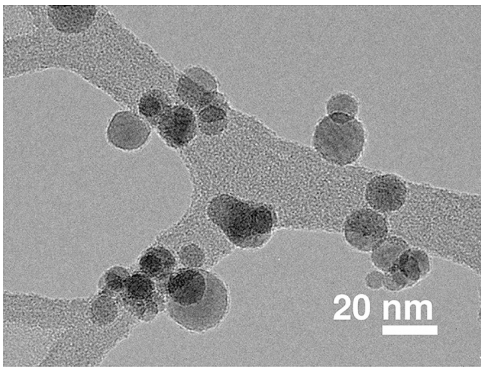

Fig. 5.15 Experimental TEM image adapted from Manuputty et al. [217] with permission from Elsevier.

total residence time (Fig. 5.4): the median particle size is approximately constant over a central region before growing with deposition radius. The radius at which the distributions begin to differ from the centreline ($r_d = 0$ mm) was determined using a two-sample Kolmogorov-Smirnov test (confidence threshold $\alpha = 0.01$, see 5.6.4 in the supplementary material for details), and is marked by the width of the shaded bar on Fig. 5.16a. For the lean flames (black), the distributions begin to differ at a deposition radius of 7.5 mm and 12 mm for 280 ppm and 560 ppm, respectively. For the stoichiometric flames (green), the distributions begin to differ at a deposition radius of 8.5 mm and 9.3 mm for 280 ppm and 560 ppm, respectively. The geometric standard deviation of the particle size distribution was between 1.4 and 1.47 for all deposition radii and all flames, which is very close to the self-preserving size distribution value of 1.45 (Fig. 5.16b). The observation that the distributions achieve a GSD close to that of the self-preserving size distribution is consistent with empirical rules for the time required for an ensemble of particles undergoing coagulation to reach the self-preserving distribution [360]. This indicates that the distributions are coagulation driven as the particles approach the stagnation surface.

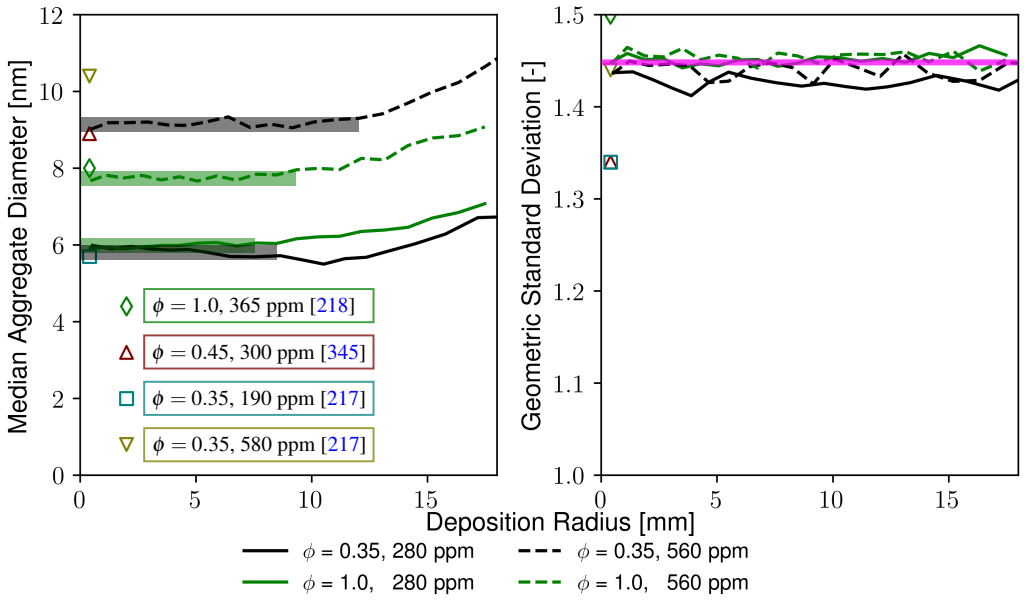

Fig. 5.16 The (a) median aggregate diameter, $\langle d_{sph} \rangle$ and (b) geometric standard deviation (GSD) as a function of deposition radius, r_d. The median aggregate diameters at $r_d = 0$ mm are marked by semi-transparent bars; the horizontal extent of the bars shows where the size distributions begin to deviate from the distribution observed at $r_d = 0$ mm as determined by a two-sample Kolmogorov-Smirnov test (confidence threshold $\alpha = 0.01$). The GSD of a self-preserving size distribution is marked in pink.

Figure 5.17 shows the median primary diameter and (arithmetic) average number of primaries per particle as a function of deposition radius. The width of the semi-transparent bars in Fig. 5.17 indicate the range of deposition radii where the aggregate particle size distribution was determined to be similar (see Section 5.6.4). The median primary diameter remains constant across the trajectories studied, consistent with the observations made during the analysis of Fig. 5.13. The particles were found to aggregate more as the deposition radius increases (Fig. 5.17b). This is due to the increased residence time of trajectories originating from larger radii (Fig. 5.4). In the stoichiometric flames and lean flame with 280 ppm TTIP, the average number of primaries ranges between 1.1 and 1.5, indicating some aggregation. In the lean flame with 560 ppm TTIP, the mean number of primaries per particle is between 1.7 and 2.6, indicating a higher level of aggregation.

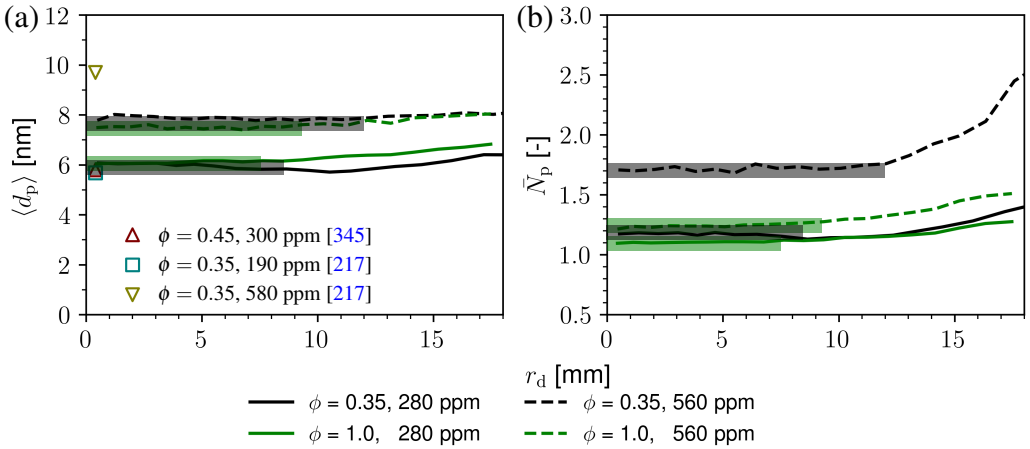

Fig. 5.17 The (a) median primary diameter, $\langle d_p \rangle$ and (b) average number of primaries per aggregate, $\bar{N}_p$, as a function of deposition radius, r_d. The values at $r = 0$ mm are marked by semi-transparent bars; the bars terminate at the radius where the size distribution of the aggregates begins to change from the distribution observed at $r_d = 0$ as determined by a two-sample Kolmogorov-Smirnov test (confidence threshold $\alpha = 0.01$).

The small increase in residence time experienced by trajectories originating from larger radii is the key factor driving the differences observed in this work. Coagulation has been shown to be the main process responsible for the radial differences in the particles, with the most pronounced difference being the increase in aggregation at larger radii. The observation that the particles deposited at different radii on the stagnation surface are different has implications for the experimental synthesis of materials in jet-wall stagnation flames. As particle size is an important parameter for the application of materials, it is important to understand the extent of the region in which the particles are expected to be uniform ($r/r_0 < 1.5$, $r \lesssim 1$ cm in this case). Experimentally, this may be overly restrictive. Nonetheless, it is worth considering the impact of the radial dependence of the particle properties on the suitability of the particles for a

given application. Further, the disruption of the temperature-residence time profiles in flame configurations with rotating stagnation surfaces should be considered in the context of particle synthesis. As it has been shown that the increase in residence time produces differences in the size distribution, it is possible that disruption to the particle trajectories from a rotating surface could interfere with this effect. This combination of effects warrants further study to ensure that particles collected at different deposition radii do indeed have sufficiently similar properties.

5.7 Conclusions

The synthesis of TiO_2 nanoparticles in jet-wall stagnation flames was studied to explore the radial dependence of the particle properties. The 2D structure of the flame was resolved with the particles described by a spherical particle model; the moments of the population balance describing the particles were transported in 2D space. The results were post-processed using a detailed particle model solved using a direct simulation Monte Carlo method. Two flames, a lean flame (equivalence ratio, $\phi = 0.35$) and a stoichiometric flame ($\phi = 1.0$), were studied to explore the particle formation under two different, but experimentally relevant, thermochemical environments. The addition of TTIP contributed extra hydrocarbons which releases extra enthalpy which significantly affected the lean flame while leaving the stoichiometric flame unaffected.

Integral properties of the particle population were shown to vary between the two flames. In the $\phi = 0.35$ flame, the $Ti(OH)_4$ particle precursor was observed downstream of the flame front, which was consistent with previous work [198]. In the $\phi = 1.0$ flame, the precursor was generated and consumed near the flame front. Particle number density profiles mirror those of the precursor. In the $\phi = 0.35$ flame, high number densities were observed downstream of the flame front, whereas the number density peaked at the flame front in the $\phi = 1.0$ flame. The average particle diameters show similar trends to previous studies [198]. In the lean flame, the particle diameter remained constant at the flame front before growing as the particles approached the stagnation surface to reach a final average size of 3 to 10 nm. In the stoichiometric flame, the particles rapidly grew to 3 mm at the flame front and continued to grow throughout the flame to reach a final average size of between 5 and 8 mm.

Trajectories originating from different initial radial positions at the burner outlet (radius, $r_0 = 7$ mm) were examined. Trajectories that originated from $r/r_0 \leq 1/7$ had similar residence times for both flames and deposited particles at radii up to $r_d/r_0 \lesssim 1.5$ (≈ 1 cm). Trajectories that originated from $1/7 < r/r_0 \leq 1/2$ spent more time at elevated temperatures due to flow divergence, but experienced similar chemical environments. Trajectories that originated from

$r/r_0 > 1/2$ experienced significant changes in their chemical environment due to the dilution from the sheath flow, but did not deposit on the stagnation surface.

The trajectories were post-processed to study TiO_2 nanoparticle growth using a hybrid particle-number/detailed particle model solved using a direct simulation Monte Carlo method. The detailed particle model resolves details about the aggregate size distribution, morphology and composition. The aggregates were predicted to have collision diameters between 6 and 12 nm, whereas the spherical model predicted (spherical) diameters between 3 and 10 nm. This is in close agreement with experimental values of 5 to 10 nm measured at the centreline [217, 345]. The differences in the thermochemical environments between the flames led to different processes influencing the particle growth. In the lean flame, the simulated temperatures were lower and the particle precursor persisted further into the flame, leading to higher rates of inception and surface growth compared to the stoichiometric flame. This resulted in bimodal PSDs with a large inception mode at small diameters (< 2 nm). In the stoichiometric flame, the size distributions were found to be approximately log-normal and had GSDs of approximately 1.45, consistent with the particles reaching a self-preserving distribution. Experiments have reported that the particle size distribution produced in jet-wall stagnation flames is narrow, but the simulations suggest that the narrowness is a consequence of the small size of the particles.

The particle size distributions were shown to vary as a function of deposition radius. For the cases studied, differences in the observed particle size distribution began to occur at a deposition radius of $r/r_0 \approx 1.5$ ($\approx$ 1 cm). The differences were due to an increase in aggregation resulting from an increase in residence time at larger radii. Moving forward, it is suggested that applications that use stagnation flames for nanoparticle synthesis should consider any radial variation in the performance of the particles for the intended application.

Chapter 6

Conclusions and suggestions for future work

The conclusions of the thesis are presented, along with a discussion of future work.

6.1 Conclusions

In this work, nanoparticle synthesis in jet-wall stagnation flames is studied in multiple spatial dimensions to explore the coupling between flow and particle synthesis. Flame synthesised titanium dioxide (TiO_2) is used as the test case. To accomplish this goal, a new solver for simulating the growth of a particulate phase coupled to the Navier-Stokes equations in two spatial dimensions was developed. The gas phase is described by a multicomponent mixture with detailed transport properties and chemical source terms. The PDEs are discretised using the finite volume method to produce a system of linear equations that are solved using OpenFOAM [343]. The chemical source terms, transport coefficients, and thermodynamic coefficients are calculated by the *k*inetics© Application Programming Interface [65] (API). The PDEs for the dilute particle phase are transformed using the method of moments, which allows the moments of the distribution to be transported in the new solver. The source terms of the moment PDEs are calculated by the *k*inetics© API. The implementation of the solver was verified through a series of comparisons against tests cases that included analytical diffusion, batch reactor, and counterflow diffusion flames. These test cases were selected to increase complexity of the test cases one step at a time, creating a term-by-term verification.

The new solver was applied to study jet-wall stagnation flames when varying the equivalence ratio, exit gas velocity, and burner-plate separation distance. The results of 2D simulations were compared to 1D simulations, which were in good agreement. The 1D simulation boundary

conditions require the strain rate to be supplied as a boundary condition. The strain rate of flames is not commonly provided when listing experimental parameters in literature or when performing a new experiment (i.e. total flow rate is directly controlled, not strain rate). This leads users of the 1D model to arbitrarily vary the strain rate boundary condition to 'match' an experimentally observed flame front. The boundary conditions of the 2D simulations, in contrast, are well described by reported design parameters such as total flow rate.

The predictions of jet-wall stagnation flames under the varied experimental parameters were compared to experimental observations. The flame shape was measured from CH* chemiluminescence and compared to chemiluminescence predicted from the simulations under a quasi-steady state assumption. The 2D simulations were in good agreement with the experimental measurements and captured the experimentally observed responses to changing the experimental parameters. The temperature was measured by thin filament pyrometry. The energy balance to calculate gas phase temperature from filament temperature relied on velocity and thermochemical properties from the 2D simulations to include heat transfer over an inclined cylinder. The additional radial information provided by the 2D simulations allows for streamline profiles to be extracted off-centreline. The temperature-residence time distributions of each flame was found to be approximately uniform, however, the uniformity was not found to correlate with the flatness of the flame.

The solver was then applied to study TiO_2 nanoparticle synthesis in jet-wall stagnation flames. Two different TTIP loadings (280 and 560 ppm) were studied in two flames, a lean flame (equivalence ratio, $\phi = 0.35$) and a stoichiometric flame ($\phi = 1.0$). The particles were simulated using a two-step methodology: first, a spherical particle model is coupled to the flow solver to resolve field-level information regarding particle synthesis; second, Lagrangian trajectories are post-processed using a hybrid particle-number/detailed particle model to resolve detailed particle properties. The thermochemical environments of the fields as well as Lagrangian particle trajectories were examined. The introduction of TTIP affected the flame location in the lean flame, whereas it did not significantly affect the stoichiometric flame.

The average diameter of the particles in the four cases studied showed trends similar to previous studies [198]. In the lean flame, the particle diameter remained constant at the flame front before growing as the particles approached the plate. In the stoichiometric flame, the particles rapidly grew to 3 mm at the flame front and grew throughout the flame to reach a final average size between 5 and 8 mm. The particle size distributions were shown to vary as a function of deposition radius. For the cases studied, differences in the observed particle size distribution begin to occur around a deposition radius of $r/r_0 \approx 1.5$ ($\approx$ 1 cm). This could have significant effects on experiments that collect particles at different particle radii, such as in the FSRS experiments. Experimentalists may find that this observation provides an overly

restrictive limitation, as a small fraction ($\approx 10\%$) of the total Ti mass will be deposited over this area.

This work provides evidence that challenges the assumption that nanoparticles synthesised in a jet-wall stagnation flame have uniform particle properties at all deposition radii. The particle models that were previously used to study the synthesis of TiO_2 nanoparticles along the centreline were applied to off-centreline particle trajectories. The predictions indicate that the threshold for uniformity of the PSD was $r/r_0 \approx 1.5$ ($\approx$ 1 cm), which may be lower than experimentalists previously assumed.

The consequences of this observation should be considered appropriately. First, it is warranted to ask how accurately the simulations captured observed physical phenomena. More experimental evidence is needed to support or rebuke this theoretical prediction. The model may be found to be overly sensitive to some parameters or may be neglecting other important physics. For example, this work assumes that particles deposited on the cool stagnation plate do not undergo further changes in shape or size, but recent work regarding oxygen vacancies and deposition times [394] provides evidence that this may be an important phenomenon to include. This is an important aspect to relating the results of the simulations to experiments.

Second, the experimental significance of the difference is dependent on the application in question. While this analysis used particle diameter as the discriminating property for assessing uniformity, other properties may be more important. For example, the photocatalytic activity of TiO_2 is known to be dependent on crystal phase [423] and this may prove to be a more important criterion for assessing "uniformity" than the particle size distribution. From an experimental point of view, these results suggest that it is worth investing time to critically assess how radially uniform flame synthesised particles are for the chosen application. From a modelling point of view, the models need to capture the phenomena important to the intended application for assessment of "uniformity".

It is hoped that the methods developed in this thesis will continue to complement experiments towards studying the fundamental physics of nanoparticle synthesis for novel materials.

6.2 Suggestions for future work

There are several aspects where the work could continue: application to new systems, further model development, improvement of the numerical method, and further assessment of the numerical performance.

6.2.1 Application to new systems

The application to new systems is a wide open field. The solver allows for study of any gas phase/dilute particulate phase model in multiple spatial dimensions.

The first application that must be mentioned is studying the impact of the rotating surface on nanoparticle synthesis in the FSRS system. In this system, a jet-wall stagnation flame is situated above a rotating surface at a fixed, but non-zero radius. Due to the loss of symmetry in such a system, this system would be very computationally expensive to model. The domain would need to be large enough to capture the boundary layer of the surface, which would result in a volume that is several orders of magnitude larger than what is studied in this work. The first attempts at modelling this work by Hu et al. [145] modelled the domain with a total volume of 2,500 cm^3 and 1M cells using a one-step chemistry model. Including a gas-phase precursor decomposition and particulate model in a domain of this size would lead to intractably large computational times.

An alternative system to study would be a 2D slot burner above a moving surface. This would provide a more simple geometry that would be computationally more tractable while still providing insight into the influence of the boundary layer of the moving surface. Additionally, slot-burners would provide an experimental application for synthesis of large sheets with deposited materials, so it would provide a system that could be industrially relevant. The work of Rott [300] towards boundary layer solutions of stagnation point flow, Libby [193], and Wang [366] may be useful towards this endeavour.

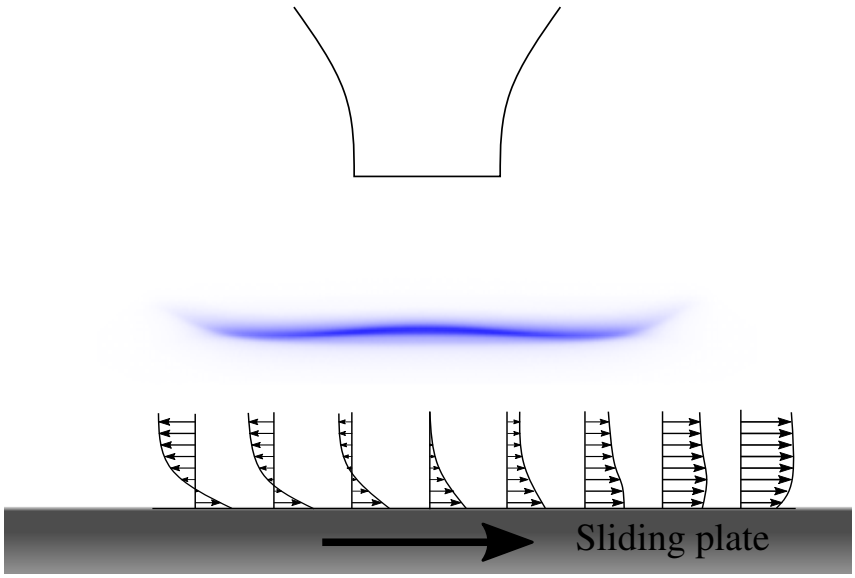

Fig. 6.1 Example of slot burner geometry proposed for future work. Representative boundary layer velocity profiles from analysis by Rott [300] are shown (spatial location arbitrary).

One important point to note is the ability to re-use the flow simulations to study a wide array of particle physics. When using the two-step methodology, the predictions of the first step can be reused for a single experimental setup without costly flow simulations. For an accurate representation of the source terms to be shared across the simulations, the representation of the mass transfer between gas and particle phases must be consistent, despite the difference in the model representation of particles. Specifically, this means the models for inception and surface growth (condensation) must be consistent such as using the same models and assumptions. For this work, $Ti(OH)_4$ was assumed to be the species involved in mass transfer and the rate was assumed to be collision limited with the rate calculated by the free-molecular collision kernel. With these criteria satisfied, the thermochemical environment from the flow step can be re-used in subsequent post-processing steps with different detailed particle models that contain different levels of detail. For example, in this work, the composition of the detailed particle model was tracked by counting TiO_2 monomers. If a researcher sought to learn about the crystal phase produced in this experiment and test different models of phase change, a detailed particle model that tracks crystal phase [218] can be used with the same gas-phase input.

6.2.2 Model development

There are several interesting model components that can be expanded upon. First, a model for deposition of particles could be included. Currently the stagnation plate is treated with a zero flux boundary condition on particulate fields. This is not physically accurate as there is significant thermophoretic deposition of particles

Second, the heat transfer to the stagnation plate is left unresolved in the current study and the plate is assumed to be a uniform temperature. This assumption is a good enough approximation directly under the flame, but it relies on experimental measurements and the assumption begins to break down as one moves further away from the flame centreline. Heat transfer characteristics of flames on surfaces is a common research question [57]. Releasing the uniform stagnation surface approximation would allow for a non-uniform temperature gradient to be resolved. This could yield important insight into the radial deposition characteristics of particles.

Another area for improvement is the detailed particle models. These models provide a means to test the interplay between complex processes. Recently, these models have been used to study crystal phase [218], but further work could be expanded to study other properties. One such example would be the recent observations that oxygen vacancies of flame synthesised TiO_2 were found to depend on the deposition time [394].

6.2.3 Method development

Another area for improvement is the numerical methods applied in this thesis. Simulating flames in 2D is computationally expensive, which was one of the major limitations in this work. The thesis establishes a baseline of what is possible with the method in its current state. There is room for improvement and several areas are discussed below.

Calculating detailed chemical source terms for stiff combustion chemistry is a highly researched topic. There are several methods in literature that aim to reduce the total computational cost. One such method that has been developed is *in situ* adaptive tabulation (ISAT) developed by Pope and co-workers [282], where solutions of chemical source terms are stored for reuse later.

The second area that was computationally expensive is the calculation of multicomponent mixture properties. This is because many of the formulations scale with $\mathcal{O}(N_{sp}^2)$ or greater. There are two suggested solutions: reduce the number of species used to calculate thermochemical properties or pre-tabulate the coefficients.

Many of the species introduced by detailed chemical mechanisms are present in trace levels. While they may be of critical importance to the flame properties (such as laminar flame speed, ignition delay, or nanoparticle formation), they contribute to the multicomponent mixture properties proportional to their concentration. Due to the high uncertainty in these properties, a possible route to reduce computational effort is to eliminate the trace species from the multicomponent mixture calculations.

The second way to reduce computational effort is to avoid repeated calculations of mixture properties. For example, consider the region inside the burner. This region will contain nearly identical composition and temperature, while the flow is accelerated in this area. The calculation of viscosity and thermal conductivity is repeated for each cell at each time step despite this identical composition and temperature. Having this calculation pre-tabulated and called via a lookup table would be advantageous, especially due to the transient algorithm currently employed. This idea is analogous to that of *in situ* adaptive tabulation (ISAT) [282] for chemical source terms.

6.2.4 Performance benchmarking

The solver developed in this work was motivated by unsatisfactory performance of the implemented libraries in OpenFOAM [343] to solve stiff combustion chemistry with detailed transport. This complaint is widely discussed and attributed to the poor chemical source terms [64] and lack of detailed mixture properties. The method validation presented in this work sought to incrementally test individual terms of the Navier-Stokes equations, leading

up to a final comparison of a counterflow H_2 diffusion flame doped with a small amount of TTIP. There are several other systems that could be of interest to demonstrate the capability and accuracies of the method in the work. These systems include premixed flames and coflow diffusion flames. There are two other solvers which it would be suggested to compare to: laminarSMOKE [71] and reactingFOAM-SCI [404]. Both of these solvers are also based in OpenFOAM [343], making it relatively simple to compare the performance of each on the same mesh. The differences between the solvers are the libraries that calculate the detailed chemical properties and ODE solvers, as well as the operator splitting schemes. A comparison between the computational performance in terms of accuracy and computational effort would be highly valuable towards knowing which solver would reduce overall computational effort moving forward. Another point of comparison that would be valuable is comparing particle model performance against a quadrature based moment method. A significant amount of work has gone towards implementing quadrature based methods in OpenFOAM by Passalacqua and co-workers [269] and implementeing a nodal approach in OpenFOAM by Boise and co-workers [389].

It is hoped that these suggestions will lead to the development of more robust, efficient, and detailed models for nanoparticle synthesis in flames that can further support experimental work.

References

[1] M. Abbaszadeh and M. Dehghan. Reduced order modeling of time-dependent incompressible Navier–Stokes equation with variable density based on a local radial basis functions-finite difference (LRBF-FD) technique and the POD/DEIM method. *Computer Methods in Applied Mechanics and Engineering*, 364:112914, 2020. doi:10.1016/j.cma.2020.112914.

[2] A. Abdali, M. Fikri, H. Orthner, H. Wiggers, and C. Schulz. Ignition delay times of shock-heated tetraethoxysilane, hexamethyldisiloxane, and titanium tetraisopropoxide. *Chemical Physics Letters*, 601:54–58, 2014. doi:10.1016/j.cplett.2014.03.079.

[3] K. M. Akhtar, S. E. Pratsinis, and S. V. Mastrangelo. Vapor phase synthesis of Al-doped titania powders. *Journal of Materials Research*, 9(5):1241–1249, 1994. doi:10.1557/JMR.1994.1241.

[4] M. K. Akhtar, Y. Xiong, and S. E. Pratsinis. Vapor synthesis of titania powder by titanium tetrachloride oxidation. *AIChE Journal*, 37(10):1561–1570, 1991. doi:10.1002/aic.690371013.

[5] J. Akroyd, A. J. Smith, R. Shirley, L. R. McGlashan, and M. Kraft. A coupled CFD-population balance approach for nanoparticle synthesis in turbulent reacting flows. *Chemical Engineering Science*, 66(17):3792–3805, 2011. doi:10.1016/j.ces.2011.05.006.

[6] S. Alzyod and S. Charton. A meshless Radial Basis Method (RBM) for solving the detailed population balance equation. *Chemical Engineering Science*, page 115973, 2020. doi:10.1016/j.ces.2020.115973.

[7] S. Alzyod, M. Attarakih, and H.-J. Bart. The Sectional Quadrature Method of Moments (SQMOM): An extension to nonhomogeneous bivariate population balances. *Chemical Engineering Research and Design*, 115:195–203, 2016. doi:10.1016/j.cherd.2016.09.024.

[8] C. R. Anderson. Vorticity boundary conditions and boundary vorticity generation for two-dimensional viscous incompressible flows. *Journal of Computational Physics*, 80 (1):72–97, 1989. doi:10.1016/0021-9991(89)90091-0.

[9] H. U. Anderson. Initial Sintering of Rutile. *Journal of the American Ceramic Society*, 50(5):235–238, 1967. doi:10.1111/j.1151-2916.1967.tb15094.x.

[10] A. Ansari and F. N. Egolfopoulos. Flame ignition in the counterflow configuration: Reassessing the experimental assumptions. *Combustion and Flame*, 174:37 – 49, 2016. doi:10.1016/j.combustflame.2016.09.021.

[11] M. Apostolopoulos, M. Taroudakis, and D. Papazoglou. Application of inverse abel techniques in in-line holographic microscopy. *Optics Communications*, 296:25 – 34, 2013. doi:10.1016/j.optcom.2013.01.053.

[12] O. I. Arabi–Katbi, S. E. Pratsinis, P. W. Morrison, and C. M. Megaridis. Monitoring the flame synthesis of TiO_2 particles by in-situ FTIR spectroscopy and thermophoretic sampling. *Combustion and Flame*, 124(4):560–572, 2001. doi:10.1016/S0010-2180(00)00227-3.

[13] J. Arvo. Fast random rotation matrices. In D. Kirk, editor, *Graphics Gems III*, pages 117–120. Academic Press, 1992.

[14] M. Ashna, M. H. Rahimian, and A. Fakhari. Extended lattice Boltzmann scheme for droplet combustion. *Physical Review E*, 95(5):053301, 2017. doi:10.1103/PhysRevE.95.053301.

[15] G. Athanassoulis and P. Gavriliadis. The truncated Hausdorff moment problem solved by using kernel density functions. *Probabilistic Engineering Mechanics*, 17(3):273–291, 2002. doi:10.1016/S0266-8920(02)00012-7.

[16] P. Atkins. *Physical Chemistry*. W. H. Freeman, 2006. ISBN 0716787598.

[17] M. Attarakih. Integral formulation of the population balance equation: Application to particulate systems with particle growth. *Computers and Chemical Engineering*, 48: 1–13, 2013. doi:10.1016/j.compchemeng.2012.08.001.

[18] M. M. Attarakih, C. Drumm, and H.-J. Bart. Solution of the population balance equation using the sectional quadrature method of moments (SQMOM). *Chemical Engineering Science*, 64(4):742–752, 2009. doi:10.1016/j.ces.2008.05.006.

[19] J. Bai, R. Geeson, F. Farazi, S. Mosbach, J. Akroyd, E. J. Bringley, and M. Kraft. Automated calibration of a poly(oxymethylene) dimethyl ether oxidation mechanism using knowledge-graph technology. *Journal of Chemical Information and Modeling*, Under Review.

[20] J. Barrett and N. Webb. A comparison of some approximate methods for solving the aerosol general dynamic equation. *Journal of Aerosol Science*, 29(1–2):31–39, 1998. doi:10.1016/S0021-8502(97)00455-2.

[21] G. A. Battiston, R. Gerbasi, M. Porchia, and A. Gasparotto. Metal Organic CVD of Nanostructured Composite TiO_2-Pt Thin Films: A Kinetic Approach. *Chemical Vapor Deposition*, 5(1):13–20, 1999. doi:10.1002/(SICI)1521-3862(199901)5:1%3C13::AID-CVDE13%3E3.0.CO;2-%23.

[22] V. Bayona, M. Sánchez-Sanz, E. Fernández-Tarrazo, and M. Kindelan. Micro-combustion modelling with RBF-FD: A high-order meshfree method for reactive flows in complex geometries. *Applied Mathematical Modelling*, 94:635–655, 2021. doi:10.1016/j.apm.2021.01.032.

[23] R. Becker, M. Braack, and R. Rannacher. Numerical simulation of laminar flames at low Mach number by adaptive finite elements. *Combustion Theory and Modelling*, 3(3): 503–534, 1999. doi:10.1088/1364-7830/3/3/305.

[24] J. H. Bell and R. D. Mehta. Contraction Design for Small Low-Speed Wind Tunnels. Technical Report April, NASA, 1988.

[25] L. Benezech. *Premixed Hydrocarbon Stagnation Flames: Experiments and Simulations to Validate Combustion Chemical-Kinetic Models*. Engineer's thesis, California Institute of Technology, Pasadena, CA, June 2008.

[26] J. M. Bergthorson. *Experiments and modeling of impinging jets and premixed hydrocarbon stagnation flames*. PhD thesis, California Institute of Technology, Pasadena, CA, May 2005.

[27] J. M. Bergthorson and P. E. Dimotakis. Premixed laminar C_1-C_2 stagnation flames: Experiments and simulations with detailed thermochemistry models. *Proceedings of the Combustion Institute*, 31(1):1139 – 1147, 2007. doi:10.1016/j.proci.2006.07.110.

[28] J. M. Bergthorson, K. Sone, T. W. Mattner, P. E. Dimotakis, D. G. Goodwin, and D. I. Meir. Advances and challenges in laminar flame experiments and implications for combustion chemistry. *Physical Review E*, 72:066307, 2005. doi:10.1103/PhysRevE.72.066307.

[29] J. M. Bergthorson, K. Sone, T. W. Mattner, P. E. Dimotakis, D. G. Goodwin, and D. I. Meiron. Impinging laminar jets at moderate Reynolds numbers and separation distances. *Physical Review E*, 72:066307, 2005. doi:10.1103/PhysRevE.72.066307.

[30] J. M. Bergthorson, S. D. Salusbury, and P. E. Dimotakis. Experiments and modelling of premixed laminar stagnation flame hydrodynamics. *Journal of Fluid Mechanics*, 681: 340–369, 2011. doi:10.1017/jfm.2011.203.

[31] S. Bhoi and D. Sarkar. Hybrid Finite Volume and Monte Carlo Method for Solving Multi-dimensional Population Balance Equations in Crystallization Processes. *Chemical Engineering Science*, page 115511, 2020. doi:10.1016/j.ces.2020.115511.

[32] P. Bianchi Neto, F. Meierhofer, H. F. Meier, U. Fritsching, and D. Noriler. Modelling polydisperse nanoparticle size distributions as produced via flame spray pyrolysis. *Powder Technology*, 370:116–128, 2020. doi:10.1016/j.powtec.2020.05.019.

[33] G. A. Bird. Approach to Translational Equilibrium in a Rigid Sphere Gas. *The Physics of Fluids*, 6(10):1518–1519, 1963. doi:10.1063/1.1710976.

[34] R. B. Bird, W. E. Stewart, and E. N. Lightfoot. *Transport Phenomena*. John Wiley & Sons, 2nd edition, 2001.

[35] P. Biswas, Y. Wang, and M. Attoui. Sub-2 nm particle measurement in high-temperature aerosol reactors: A review. *Current Opinion in Chemical Engineering*, 21:60–66, 2018. doi:10.1016/j.coche.2018.03.004.

[36] B. J. Blackburn, C. Drosos, D. B. Brett, M. A. Parkes, C. J. Carmalt, and I. P. Parkin. In situ mass spectrometry analysis of chemical vapour deposition of TiO_2 thin films to study gas phase mechanisms. *RSC Advances*, 6(113):111797–111805, 2016. doi:10.1039/C6RA22801A.

[37] L. G. Blevins, M. W. Renfro, K. H. Lyle, N. M. Laurendeau, and J. P. Gore. Experimental study of temperature and CH radical location in partially premixed CH_4/air coflow flames. *Combustion and Flame*, 118(4):684 – 696, 1999. doi:10.1016/S0010-2180(99)00023-1.

[38] A. L. Bodor, B. Franzelli, T. Faravelli, and A. Cuoci. A post processing technique to predict primary particle size of sooting flames based on a chemical discrete sectional model: Application to diluted coflow flames. *Combustion and Flame*, 208:122–138, 2019. doi:10.1016/j.combustflame.2019.06.008.

[39] A. Boje, J. Akroyd, and M. Kraft. A hybrid particle-number and particle model for efficient solution of population balance equations. *Journal of Computational Physics*, 389:189–218, 2019. doi:10.1016/j.jcp.2019.03.033.

[40] T. Boningari, S. N. R. Inturi, M. Suidan, and P. G. Smirniotis. Novel continuous single-step synthesis of nitrogen-modified TiO_2 by flame spray pyrolysis for photocatalytic degradation of phenol in visible light. *Journal of Materials Science and Technology*, 34 (9):1494–1502, 2018. doi:10.1016/j.jmst.2018.04.014.

[41] R. Botet and R. Jullien. Intrinsic anisotropy of clusters in cluster-cluster aggregation. *Journal of Physics A*, 19(15):L907–L912, 1986. doi:10.1088/0305-4470/19/15/008.

[42] A. Bouaniche, L. Vervisch, and P. Domingo. A hybrid stochastic/fixed-sectional method for solving the population balance equation. *Chemical Engineering Science*, 209:115198, 2019. doi:10.1016/j.ces.2019.115198.

[43] N. Bouvet, D. Davidenko, C. Chauveau, L. Pillier, and Y. Yoon. On the simulation of laminar strained flames in stagnation flows: 1D and 2D approaches versus experiments. *Combustion and Flame*, 161(2):438 – 452, 2014. doi:10.1016/j.combustflame.2013.09.010.

[44] D. Brassard and M. Ferchichi. Transformation of a Polynomial for a Contraction Wall Profile. *Journal of Fluids Engineering*, 127(1):183, 2005. doi:10.1115/1.1852492.

[45] C. A. Brau and R. M. Jonkman. Classical theory of rotational relaxation in diatomic gases. *The Journal of Chemical Physics*, 52(2):477–484, 1970. doi:10.1063/1.1673010.

[46] K. Brezinsky. Gas-phase combustion synthesis of materials. *Symposium (International) on Combustion*, 26(2):1805–1816, 1996. doi:10.1016/S0082-0784(96)80001-4.

[47] P. Buerger, D. Nurkowski, J. Akroyd, S. Mosbach, and M. Kraft. First-Principles Thermochemistry for the Thermal Decomposition of Titanium Tetraisopropoxide. *The Journal of Physical Chemistry A*, 119(30):8376–8387, 2015. doi:10.1021/acs.jpca.5b01721.

[48] P. Buerger, D. Nurkowski, J. Akroyd, and M. Kraft. A kinetic mechanism for the thermal decomposition of titanium tetraisopropoxide. *Proceedings of the Combustion Institute*, 36(1):1019–1027, 2017. doi:10.1016/j.proci.2016.08.062.

[49] P. Buerger, J. Akroyd, and M. Kraft. Extended first-principles thermochemistry for the oxidation of titanium tetrachloride. *Combustion and Flame*, 199:441–450, 2019. doi:10.1016/j.combustflame.2018.07.021.

[50] B. Buesser, A. J. Gröhn, and S. E. Pratsinis. Sintering Rate and Mechanism of TiO_2 Nanoparticles by Molecular Dynamics. *The Journal of Physical Chemistry C*, 115(22): 11030–11035, 2011. doi:10.1021/jp2032302.

[51] M. D. Buhmann. Radial basis functions. *Acta Numerica*, 9:1–38, 2000. doi:10.1017/S0962492900000015.

[52] S. P. Burke and T. E. W. Shumann. Diffusion flames. *Industrial and Engineering Chemistry Research*, 1928.

[53] C. A. Bustamante, H. Power, and W. F. Florez. A global meshless collocation particular solution method for solving the two-dimensional Navier–Stokes system of equations. *Computers and Mathematics with Applications*, 65(12):1939–1955, 2013. doi:10.1016/j.camwa.2013.04.014.

[54] J. Cai, N. Lu, and C. M. Sorensen. Analysis of Fractal Cluster Morphology Paramters: Structural Coefficient and Density Autocorrelation Function Cutoff. *Journal of Colloid and Interface Science*, 171(2):470–473, 1995. doi:10.1006/jcis.1995.1204.

[55] F. Carbone, K. Gleason, and A. Gomez. Probing gas-to-particle transition in a moderately sooting atmospheric pressure ethylene/air laminar premixed flame. Part I: Gas phase and soot ensemble characterization. *Combustion and Flame*, 181:315–328, 2017. doi:10.1016/j.combustflame.2017.01.029.

[56] P. Chan and B. Dahneke. Free-molecule drag on straight chains of uniform spheres. *Journal of Applied Physics*, 52(5):3106–3110, 1981. doi:10.1063/1.329173.

[57] S. Chander and A. Ray. Flame impingement heat transfer: A review. *Energy Conversion and Management*, 46(18):2803–2837, 2005. doi:10.1016/j.enconman.2005.01.011.

[58] S. Chapman, T. G. Cowling, and D. Burnett. *The Mathematical Theory of Non-Uniform Gases: An Account of the Kinetic Theory of Viscosity, Thermal Conduction and Diffusion in Gases*. Cambridge University Press, 1990. ISBN 978-0-521-40844-8.

[59] D. Chen, Z. Zainuddin, E. Yapp, J. Akroyd, S. Mosbach, and M. Kraft. A fully coupled simulation of PAH and soot growth with a population balance model. *Proceedings of the Combustion Institute*, 34(1):1827–1835, 2013. doi:10.1016/j.proci.2012.06.089.

[60] P. P. Chinchapatnam, K. Djidjeli, and P. B. Nair. Radial basis function meshless method for the steady incompressible Navier–Stokes equations. *International Journal of Computer Mathematics*, 84(10):1509–1521, 2007. doi:10.1080/00207160701308309.

[61] K. Cho and P. Biswas. Sintering Rates for Pristine and Doped Titanium Dioxide Determined Using a Tandem Differential Mobility Analyzer System. *Aerosol Science and Technology*, 40(5):309–319, 2006. doi:10.1080/02786820600599424.

[62] S. U. Choi and J. A. Eastman. Enhancing thermal conductivity of fluids with nanoparticles. Technical report, 10 1995.

[63] S.-L. Chung and J. L. Katz. The counterflow diffusion flame burner: A new tool for the study of the nucleation of refractory compounds. *Combustion and Flame*, 61(3): 271–284, 1985. doi:10.1016/0010-2180(85)90108-7.

[64] C. T. Cloney, R. C. Ripley, M. J. Pegg, and P. R. Amyotte. Laminar burning velocity and structure of coal dust flames using a unity Lewis number CFD model. *Combustion and Flame*, 190:87–102, 2018. doi:10.1016/j.combustflame.2017.11.010.

[65] CMCL Innovations, UK. *k*inetics® and SRM Engine Suite, v9.1.1, 2019.

[66] W. S. Coblenz, J. M. Dynys, R. M. Cannon, and R. L. Coble. Initial Stage Solid State Sintering Models: A Critical Analysis and Assessment. In *Sintering Processes*, volume 13 of *Materials Science Research*, pages 141–157. Plenum Press, New York, 1980.

[67] E. R. Cohen and E. U. Vaughan. Approximate solution of the equations for aerosol agglomeration. *Journal of Colloid and Interface Science*, 35(4):612–623, 1971. doi:10.1016/0021-9797(71)90219-0.

[68] D. R. Collins, W. Smith, N. M. Harrison, and T. R. Forester. Molecular dynamics study of the high temperature fusion of TiO_2 nanoclusters. *Journal of Materials Chemistry*, 7 (12):2543–2546, 1997. doi:10.1039/A704673A.

[69] Computational Modelling Group, Department of Chemical Engineering and Biotechnology, University of Cambridge. MOpS Particle Simulator. https://github.com/ucam-ceb-como/MOpS, 2021. Commit: 404e1504c65bfb0a3f02d238bfac8be728073233.

[70] E. Cunningham and J. Larmor. On the velocity of steady fall of spherical particles through fluid medium. *Proceedings of the Royal Society A*, 83(563):357–365, 1910. doi:10.1098/rspa.1910.0024.

[71] A. Cuoci, A. Frassoldati, T. Faravelli, and E. Ranzi. Numerical Modeling of Laminar Flames with Detailed Kinetics Based on the Operator-Splitting Method. *Energy and Fuels*, 27(12):7730–7753, 2013. doi:10.1021/ef4016334.

[72] F. A. da Cunha and C. A. G. Veras. Modelling laminar diffusion flames using a fast convergence three-dimensional CVFEM code. *Combustion Theory and Modelling*, 0(0): 1–28, 2021. doi:10.1080/13647830.2021.1889682.

[73] M. S. Day and J. B. Bell. Numerical simulation of laminar reacting flows with complex chemistry. *Combustion Theory and Modelling*, 4(4):535–556, 2000. doi:10.1088/1364-7830/4/4/309.

[74] G. De Falco, R. Ciardiello, M. Commodo, P. Del Gaudio, P. Minutolo, A. Porta, and A. D'Anna. TiO_2 nanoparticle coatings with advanced antibacterial and hydrophilic properties prepared by flame aerosol synthesis and thermophoretic deposition. *Surface and Coatings Technology*, 349:830–837, 2018. doi:10.1016/j.surfcoat.2018.06.083.

[75] L. G. M. de Souza, G. Janiga, V. John, and D. Thévenin. Reconstruction of a distribution from a finite number of moments with an adaptive spline-based algorithm. *Chemical Engineering Science*, 65(9):2741–2750, 2010. doi:10.1016/j.ces.2010.01.007.

[76] K. Devriendt, H. Van Look, B. Ceursters, and J. Peeters. Kinetics of formation of chemiluminescent CH($A^2\Delta$) by the elementary reactions of $C_2H(X^2\Sigma^+)$ with $O(^3P)$ and $O_2(X^3\Sigma_g^-)$: A pulse laser photolysis study. *Chemical Physics Letters*, 261(4):450–456, 1996. doi:10.1016/0009-2614(96)01023-8.

[77] G. Dixon-Lewis. Flame structure and flame reaction kinetics II. transport phenomena in multicomponent systems. *Proceedings of the Royal Society A*, 307(1488):111–135, 1968. doi:10.1098/rspa.1968.0178.

[78] G. Dixon-Lewis. Flame structure and flame reaction kinetics. V. investigation of reaction mechanism in a rich hydrogen + nitrogen + oxygen flame by solution of conservation equations. *Proceedings of the Royal Society A*, 317(1529):235–263, 1970. doi:10.1098/rspa.1970.0114.

[79] R. Djenadic and M. Winterer. Control of nanoparticle agglomeration through variation of the time-temperature profile in chemical vapor synthesis. *Journal of Nanoparticle Research*, 19(2):28, 2017. doi:10.1007/s11051-016-3714-5.

[80] C. J. Doolan. Numerical Evaluation of Contemporary Low-Speed Wind Tunnel Contraction Designs. *Journal of Fluids Engineering*, 129(9):1241–1244, 2007. doi:10.1115/1.2771578.

[81] D. R. Dowling. *Mixing in Gas Phase Turbulent Jets*. PhD thesis, California Institute of Technology, Pasadena, CA, USA, April 1988.

[82] J. A. Dreyer, E. J. Bringley, M. Y. Manuputty, J. Akroyd, and M. Kraft. Temperature and CH* measurements and simulations of laminar premixed ethylene jet-wall stagnation flames. *Proceedings of the Combustion Institute*, pages 2083–2091, 2020. doi:https://doi.org/10.1016/j.proci.2020.06.106.

[83] J. A. H. Dreyer, R. I. Slavchov, E. J. Rees, J. Akroyd, M. Salamanca, S. Mosbach, and M. Kraft. Improved methodology for performing the inverse abel transform of flame images for color ratio pyrometry. *Applied Optics*, 58(10):2662–2670, 2019. doi:10.1364/AO.58.002662.

[84] V. Dribinski, A. Ossadtchi, V. A. Mandelshtam, and H. Reisler. Reconstruction of Abel-transformable images: The Gaussian basis-set expansion Abel transform method. *Review of Scientific Instruments*, 73(7):2634–2642, 2002. doi:10.1063/1.1482156.

[85] S. Dworkin, B. Bennett, and M. Smooke. A mass-conserving vorticity–velocity formulation with application to nonreacting and reacting flows. *Journal of Computational Physics*, 215(2):430–447, 2006. doi:10.1016/j.jcp.2005.11.002.

[86] N. A. Eaves, Q. Zhang, F. Liu, H. Guo, S. B. Dworkin, and M. J. Thomson. CoFlame: A refined and validated numerical algorithm for modeling sooting laminar coflow diffusion flames. *Computer Physics Communications*, 207:464–477, 2016. doi:10.1016/j.cpc.2016.06.016.

[87] C. Edusi, G. Hyett, G. Sankar, and I. P. Parkin. Aerosol-Assisted CVD of Titanium Dioxide Thin Films from Methanolic Solutions of Titanium Tetraisopropoxide; Substrate and Aerosol-Selective Deposition of Rutile or Anatase. *Chemical Vapor Deposition*, 17 (1–3):30–36, 2011. doi:10.1002/cvde.201006872.

[88] M. L. Eggersdorfer. *Nanoparticle Agglomerates and Aggregates in Aerosols by Coagulation and Sintering*. PhD thesis, ETH Zurich, 2012.

[89] M. L. Eggersdorfer and S. E. Pratsinis. The Structure of Agglomerates Consisting of Polydisperse Particles. *Aerosol Science and Technology*, 46(3):347–353, 2012. doi:10.1080/02786826.2011.631956.

[90] M. L. Eggersdorfer and S. E. Pratsinis. Agglomerates and aggregates of nanoparticles made in the gas phase. *Advanced Powder Technology*, 25(1):71–90, 2014. doi:10.1016/j.apt.2013.10.010.

[91] M. L. Eggersdorfer, D. Kadau, H. J. Herrmann, and S. E. Pratsinis. Multiparticle Sintering Dynamics: From Fractal-Like Aggregates to Compact Structures. *Langmuir*, 27(10):6358–6367, 2011. doi:10.1021/la200546g.

[92] M. L. Eggersdorfer, D. Kadau, H. J. Herrmann, and S. E. Pratsinis. Aggregate morphology evolution by sintering: Number and diameter of primary particles. *Journal of Aerosol Science*, 46:7–19, 2012. doi:10.1016/j.jaerosci.2011.11.005.

[93] F. Egolfopoulos, D. Zhu, and C. Law. Experimental and numerical determination of laminar flame speeds: Mixtures of C_2-hydrocarbons with oxygen and nitrogen. *Proceedings of the Combustion Institute*, 23(1):471–478, 1991. doi:10.1016/S0082-0784(06)80293-6.

[94] F. Egolfopoulos, H. Zhang, and Z. Zhang. Wall effects on the propagation and extinction of steady, strained, laminar premixed flames. *Combustion and Flame*, 109(1–2):237–252, 1997. doi:10.1016/S0010-2180(96)00152-6.

[95] A. Eibeck and W. Wagner. An Efficient Stochastic Algorithm for Studying Coagulation Dynamics and Gelation Phenomena. *SIAM Journal on Scientific Computing*, 22(3): 802–821, 2000. doi:10.1137/S1064827599353488.

[96] A. Eibeck and W. Wagner. Stochastic Particle Approximations for Smoluchoski's Coagulation Equation. *The Annals of Applied Probability*, 11(4):1137–1165, 2001.

[97] B. Endrődi, E. Kecsenovity, K. Rajeshwar, and C. Janáky. One-Step Electrodeposition of Nanocrystalline TiO_2 Films with Enhanced Photoelectrochemical Performance and Charge Storage. *ACS Applied Energy Materials*, 1(2):851–858, 2018. doi:10.1021/acsaem.7b00289.

[98] A. Ern and M. D. Smooke. Vorticity-Velocity Formulation for Three-Dimensional Steady Compressible Flows. *Journal of Computational Physics*, 105(1):58–71, 1993. doi:10.1006/jcph.1993.1053.

[99] A. Ern, C. C. Douglas, and M. D. Smooke. Detailed chemistry modeling of laminar diffusion flames on parallel computers. *The International Journal of Supercomputer Applications and High Performance Computing*, 9(3):167–186, 1995. doi:10.1177/109434209500900301.

[100] K. S. Ershov, S. A. Kochubei, V. G. Kiselev, and A. V. Baklanov. Decomposition Pathways of Titanium Isopropoxide $Ti(O^iPr)_4$: New Insights from UV-Photodissociation Experiments and Quantum Chemical Calculations. *The Journal of Physical Chemistry A*, 122(4):1064–1070, 2018. doi:10.1021/acs.jpca.7b10396.

[101] F. Family, T. Vicsek, and P. Meakin. Are Random Fractal Clusters Isotropic? *Physical Review Letters*, 55(7):641–644, 1985. doi:10.1103/PhysRevLett.55.641.

[102] J. Fang, Y. Wang, J. Kangasluoma, M. Attoui, H. Junninen, M. Kulmala, T. Petäjä, and P. Biswas. Cluster formation mechanisms of titanium dioxide during combustion synthesis: Observation with an APi-TOF. *Aerosol Science and Technology*, 51(9): 1071–1081, 2017. doi:10.1080/02786826.2017.1331028.

[103] J. H. Ferziger and M. Perić. *Computational Methods for Fluid Dynamics*. Springer, Berlin, 3rd, rev. ed edition, 2002. ISBN 978-3-540-42074-3.

[104] C. P. Fictorie, J. F. Evans, and W. L. Gladfelter. Kinetic and mechanistic study of the chemical vapor deposition of titanium dioxide thin films using tetrakis-(isopropoxo)-titanium(IV). *Journal of Vacuum Science and Technology A*, 12(4):1108–1113, 1994. doi:10.1116/1.579173.

[105] K. Fikret and K. Hiroshi. Low Temperature Synthesis of TiO_2 by Vapor-Phase Hydrolysis of Titanium Isopropoxide. *Chemistry Letters*, 17(5):791–794, 1988. doi:10.1246/cl.1988.791.

[106] A. V. Filippov, M. Zurita, and D. E. Rosner. Fractal-like aggregates: Relation between morphology and physical properties. *Journal of Colloid and Interface Science*, 229: 261–273, 2000. doi:10.1006/jcis.2000.7027.

[107] O. Filippova and D. Hänel. Lattice-BGK Model for Low Mach Number Combustion. *International Journal of Modern Physics C*, 09(08):1439–1445, 1998. doi:10.1142/S0129183198001308.

[108] O. Filippova and D. Hänel. A Novel Lattice BGK Approach for Low Mach Number Combustion. *Journal of Computational Physics*, 158(2):139–160, 2000. doi:10.1006/jcph.1999.6405.

[109] O. Filippova, D. Hänel, and I. Wlokas. Two approaches for reactive flow at low Mach number. In C.-H. Bruneau, editor, *Sixteenth International Conference on Numerical Methods in Fluid Dynamics*, pages 476–481, Berlin, Heidelberg, 1998. Springer Berlin Heidelberg. ISBN 978-3-540-49540-6.

[110] L. Forestier-Coste and S. Mancini. A finite volume preserving scheme on nonuniform meshes and for multidimensional coalescence. *SIAM Journal on Scientific Computing*, 34(6):B840–B860, 2012. doi:10.1137/110847998.

[111] M. Formenti, F. Juillet, P. Meriaudeau, S. Teichner, and P. Vergnon. Preparation in a hydrogen-oxygen flame of ultrafine metal oxide particles. oxidative properties toward hydrocarbons in the presence of ultraviolet radiation. *Journal of Colloid and Interface Science*, 39(1):79–89, 1972. doi:10.1016/0021-9797(72)90144-0.

[112] B. Fornberg and N. Flyer. *A primer on radial basis functions with applications to the geosciences*. SIAM, 2015.

[113] S. R. Forrest and T. A. Witten. Long-range correlations in smoke-particle aggregates. *Journal of Physics A*, 12(5):L109–L117, 1979. doi:10.1088/0305-4470/12/5/008.

[114] R. O. Fox. Bivariate direct quadrature method of moments for coagulation and sintering of particle populations. *Journal of Aerosol Science*, 37(11):1562–1580, 2006. doi:10.1016/j.jaerosci.2006.03.005.

[115] M. Frenklach. Method of moments with interpolative closure. *Chemical Engineering Science*, 57(12):2229–2239, 2002. doi:10.1016/S0009-2509(02)00113-6.

[116] M. Frenklach and S. J. Harris. Aerosol dynamics modeling using the method of moments. *Journal of Colloid and Interface Science*, 118(1):252–261, 1987. doi:10.1016/0021-9797(87)90454-1.

[117] U. Frey, M. Graf, S. Taschini, K.-U. Kirstein, and A. Hierlemann. A Digital CMOS Architecture for a Micro-Hotplate Array. *IEEE Journal of Solid-State Circuits*, 42(2): 441–450, 2007. doi:10.1109/JSSC.2006.889367.

[118] S. K. Friedlander. *Smoke, Dust and Haze*. Oxford University Press, Oxford, second edition, 2000.

[119] C. Frouzakis, J. Lee, A. Tomboulides, and K. Boulouchos. Two-dimensional direct numerical simulation of opposed-jet hydrogen-air diffusion flame. *Proceedings of the Combustion Institute*, 27(1):571 – 577, 1998. doi:10.1016/S0082-0784(98)80448-7.

[120] D. Fry, A. Mohammad, A. Chakrabarti, and C. M. Sorensen. Cluster Shape Anisotropy in Irreversibly Aggregating Particulate Systems. *Langmuir*, 20(18):7871–7879, 2004. doi:10.1021/la0494369.

[121] M. J. Gázquez, J. P. Bolívar, R. Garcia-Tenorio, and F. Vaca. A Review of the Production Cycle of Titanium Dioxide Pigment. *Materials Sciences and Applications*, 05(07): 441–458, 2014. doi:10.4236/msa.2014.57048.

[122] R. N. Ghoshtagore. Mechanism of Heterogeneous Deposition of Thin Film Rutile. *Journal of the Electrochemical Society*, 117(4):529, 1970. doi:10.1149/1.2407561.

[123] M. Gonchikzhapov and T. Kasper. Decomposition Reactions of $Fe(CO)_5$, $Fe(C_5H_5)_2$, and TTIP as Precursors for the Spray-Flame Synthesis of Nanoparticles in Partial Spray Evaporation at Low Temperatures. *Industrial and Engineering Chemistry Research*, 59 (18):8551–8561, 2020. doi:10.1021/acs.iecr.9b06667.

[124] M. Goodson and M. Kraft. An Efficient Stochastic Algorithm for Simulating Nano-particle Dynamics. *Journal of Computational Physics*, 183(1):210–232, 2002. doi:10.1006/jcph.2002.7192.

[125] D. G. Goodwin, R. L. Speth, H. K. Moffat, and B. W. Weber. Cantera: An object-oriented software toolkit for chemical kinetics, thermodynamics, and transport processes. https://www.cantera.org, 2018. Version 2.4.0.

[126] S. Gordon and B. J. McBride. Computer program for calculation of complex chemical equilibrium compositions, rocket performance, incident and reflected shocks and chapman-jouguet detonations. Technical Report NASA Report SP-273, National Aeronautics and Space Administration, Washington, DC, United States, March 1976. https://ntrs.nasa.gov/archive/nasa/casi.ntrs.nasa.gov/19780009781.pdf.

[127] J. F. Grcar. The Twopnt Program for Boundary Value Problems. Technical Report SAND-91-8230, Sandia National Labs., Livermore, CA (United States), 1992.

[128] J. F. Grcar, R. J. Kee, M. D. Smooke, and J. A. Miller. A hybrid Newton/time-integration procedure for the solution of steady, laminar, one-dimensional, premixed flames. *Symposium (International) on Combustion*, 21(1):1773–1782, 1988. doi:10.1016/S0082-0784(88)80411-9.

[129] I. E. Grey, C. Li, I. C. Madsen, and G. Braunshausen. TiO_2-II. Ambient pressure preparation and structure refinement. *Materials Research Bulletin*, 23(5):743–753, 1988. doi:10.1016/0025-5408(88)90040-2.

[130] A. A. Gribb and J. F. Banfield. Particle size effects on transformation kinetics and phase stability in nanocrystalline TiO_2. *American Mineralogist*, 82:717–728, 1997. doi:10.2138/am-1997-7-809.

[131] S. M. Gupta and M. Tripathi. A review on the synthesis of TiO_2 nanoparticles by solution route. *Central European Journal of Chemistry*, 10(2):279–294, 2012. doi:10.2478/s11532-011-0155-y.

[132] J. Hall, J. de Vries, A. Amadio, and E. Petersen. Towards a Kinetics Model of CH Chemiluminescence. In *43rd AIAA Aerospace Sciences Meeting and Exhibit*, Reno, Nevada, Jan. 2005. American Institute of Aeronautics and Astronautics. ISBN 978-1-62410-064-2. doi:10.2514/6.2005-1318.

[133] D. Hänel, U. Lantermann, R. Kaiser, and I. Wlokas. Generalized lattice-BGK concept for thermal and chemically reacting flows at low Mach numbers. *International Journal for Numerical Methods in Fluids*, 51(4):351–369, 2006. doi:10.1002/fld.982.

[134] X. Hao, H. Zhao, Z. Xu, and C. Zheng. Population Balance-Monte Carlo Simulation for Gas-to-Particle Synthesis of Nanoparticles. *Aerosol Science and Technology*, 47(10): 1125–1133, 2013. doi:10.1080/02786826.2013.823642.

[135] M. C. Heine and S. E. Pratsinis. Polydispersity of primary particles in agglomerates made by coagulation and sintering. *Journal of Aerosol Science*, 38(1):17–38, 2007. doi:10.1016/j.jaerosci.2006.09.005.

[136] W. R. Heinson, C. M. Sorensen, and A. Chakrabarti. Does Shape Anisotropy Control the Fractal Dimension in Diffusion-Limited Cluster-Cluster Aggregation? *Aerosol Science and Technology*, 44(12):i–iv, 2010. doi:10.1080/02786826.2010.516032.

[137] Y. Hiram and A. Nir. A simulation of surface tension driven coalescence. *Journal of Colloid and Interface Science*, 95(2):462–470, 1983. doi:10.1016/0021-9797(83)90206-0.

[138] J. O. Hirschfelder and C. F. Curtiss. The Theory of Flame Propagation. *The Journal of Chemical Physics*, 17(11):1076–1081, 1949. doi:10.1063/1.1747115.

[139] J. O. Hirschfelder, C. F. Curtiss, and D. E. Campbell. The theory of flame propagation. iv. *The Journal of Physical Chemistry*, 57(4):403–414, 1953. doi:10.1021/j150505a004.

[140] J. O. Hirschfelder, C. F. Curtiss, and R. B. Bird. *Molecular Theory of Gases and Liquids*. John Wiley & Sons, 2nd edition, 1954.

[141] J. L. Hodges. The Significance Probability of the Smirnov Two-Sample Test. *Arkiv för Matematik*, 3(5):469–486, 1958. doi:10.1007/BF02589501.

[142] S. A. Hosseini, H. Safari, N. Darabiha, D. Thévenin, and M. Krafczyk. Hybrid Lattice Boltzmann-finite difference model for low mach number combustion simulation. *Combustion and Flame*, 209:394–404, 2019. doi:10.1016/j.combustflame.2019.07.041.

[143] S. A. Hosseini, A. Abdelsamie, N. Darabiha, and D. Thévenin. Low-Mach hybrid lattice Boltzmann-finite difference solver for combustion in complex flows. *The Physics of Fluids*, 32(7):077105, 2020. doi:10.1063/5.0015034.

[144] D. Hou, C. S. Lindberg, M. Y. Manuputty, X. You, and M. Kraft. Modelling soot formation in a benchmark ethylene stagnation flame with a new detailed population balance model. *Combustion and Flame*, 203:56–71, 2019. doi:10.1016/j.combustflame.2019.01.035.

[145] L. Hu, Z. Miao, Y. Zhang, H. Zhang, and H. Yang. Numerical assessment on rotation effect of the stagnation surface on nanoparticle deposition in flame synthesis. *Materials*, 12(9), 2019. doi:10.3390/ma12091361.

[146] H. M. Hulburt and S. Katz. Some problems in particle technology: A statistical mechanical formulation. *Chemical Engineering Science*, 19(8):555–574, 1964. doi:10.1016/0009-2509(64)85047-8.

[147] C.-H. Hung and J. L. Katz. Formation of mixed oxide powders in flames: Part I. TiO_2-SiO_2. *Journal of Materials Research*, 7(7):9, 1992. doi:10.1557/JMR.1992.1861.

[148] R. Issa. Solution of the implicitly discretised fluid flow equations by operator-splitting. *Journal of Computational Physics*, 62(1):40 – 65, 1986. doi:10.1016/0021-9991(86)90099-9.

[149] V. John, I. Angelov, A. Öncül, and D. Thévenin. Techniques for the reconstruction of a distribution from a finite number of its moments. *Chemical Engineering Science*, 62 (11):2890–2904, 2007. doi:10.1016/j.ces.2007.02.041.

[150] M. V. Johnson, S. S. Goldsborough, Z. Serinyel, P. O'Toole, E. Larkin, G. O'Malley, and H. J. Curran. A Shock Tube Study of *n*- and *iso*-Propanol Ignition. *Energy and Fuels*, 23(12):5886–5898, 2009. doi:10.1021/ef900726j.

[151] R. Johnson, A. VanDine, G. Esposito, and H. Chelliah. On the axisymmetric counterflow flame simulations: is there an optimal nozzle diameter and separation distance to apply quasi one-dimensional theory? *Combustion Science and Technology*, 187(1–2):37–59, 2015. doi:10.1080/00102202.2014.972503.

[152] R. Jullien. Transparency effects in cluster-cluster aggregation with linear trajectories. *Journal of Physics A*, 17(14):L771–L776, 1984. doi:10.1088/0305-4470/17/14/009.

[153] R. Jullien and R. Botet. Aggregation and fractal aggregates. *Annals of Telecommunications*, 41:343 (short version). 120 p, 1987. https://cds.cern.ch/record/205985.

[154] R. Jullien and P. Meakin. Simple models for the restructuring of three-dimensional ballistic aggregates. *Journal of Colloid and Interface Science*, 127(1):265–272, 1989. doi:10.1016/0021-9797(89)90027-1.

[155] V. I. Kalikmanov. Classical Nucleation Theory. *Nucleation Theory*, pages 17–41, 2013. doi:10.1007/978-90-481-3643-8_3.

[156] H. K. Kammler, S. E. Pratsinis, P. W. Morrison, and B. Hemmerling. Flame temperature measurements during electrically assisted aerosol synthesis of nanoparticles. *Combustion and Flame*, 128(4):369–381, 2002. doi:10.1016/S0010-2180(01)00357-1.

[157] T. Kanai, H. Komiyama, and H. Inoue. TiO_2 Particles By Chemical Vapor-Deposition-Particle Formation Mechanism And Chemical-Kinetics. *Kagaku Kogaku Ronbunshu*, 11 (3):317–323, 1985.

[158] J. F. Kanney, C. T. Miller, and C. T. Kelley. Convergence of iterative split-operator approaches for approximating nonlinear reactive transport problems. *Advances in Water Resources*, 26(3):247–261, 2003. doi:10.1016/S0309-1708(02)00162-8.

[159] Y. Karakaya, J. Sellmann, I. Wlokas, and T. Kasper. Influence of the sampling probe on flame temperature, species, residence times and on the interpretation of ion signals of methane/oxygen flames in molecular beam mass spectrometry measurements. *Combustion and Flame*, 229:111388, 2021. doi:10.1016/j.combustflame.2021.02.034.

[160] J. L. Katz and C.-H. Hung. Ultrafine Refractory Particle Formation in Counterflow Diffusion Flames. *Combustion Science and Technology*, 82(1–6):169–183, 1992. doi:10.1080/00102209208951818.

[161] M. Katzer, A. P. Weber, and G. Kasper. The effects of electrical fields on growth of titania particles formed in a CH_4-O_2 diffusion flame. *Journal of Aerosol Science*, 32(9): 23, 2001. doi:10.1016/S0021-8502(01)00041-6.

[162] A. Kazakov and M. Frenklach. Dynamic Modeling of Soot Particle Coagulation and Aggregation: Implementation With the Method of Moments and Application to High-Pressure Laminar Premixed Flames. *Combustion and Flame*, 114(3–4):484–501, 1998. doi:10.1016/S0010-2180(97)00322-2.

[163] R. Kee, J. Grcar, M. Smooke, and J. Miller. A fortran program for modeling steady laminar one-dimensional premixed flames, report no. *SAND85-8240, Sandia National Laboratories*, 1985.

[164] R. J. Kee, J. A. Miller, G. H. Evans, and G. Dixon-Lewis. A computational model of the structure and extinction of strained, opposed flow, premixed methane-air flames. *Proceedings of the Combustion Institute*, 22(1):1479 – 1494, 1989. doi:10.1016/S0082-0784(89)80158-4.

[165] R. J. Kee, M. E. Coltrin, and P. Glarborg. *Chemically Reacting Flow: Theory and Practice*. Wiley-Interscience, Hoboken, N.J, 2003. ISBN 978-0-471-26179-7.

[166] M. Kindelan and V. Bayona. Application of the RBF meshless method to laminar flame propagation. *Engineering Analysis with Boundary Elements*, 37(12):1617–1624, 2013. doi:10.1016/j.enganabound.2013.09.004.

[167] A. Kobata, K. Kusakabe, and S. Morooka. Growth and transformation of TiO_2 crystallites in aerosol reactor. *AIChE Journal*, 37(3):347–359, 1991. doi:10.1002/aic.690370305.

[168] W. Koch and S. K. Friedlander. The effect of particle coalescence on the surface area of a coagulating aerosol. *Journal of Colloid and Interface Science*, 140(2):419–427, 1990. doi:10.1016/0021-9797(90)90362-R.

[169] M. Kolb and H. J. Herrmann. Surface fractals in irreversible aggregation. *Physical Review Letters*, 59(4):454–457, 1987. doi:10.1103/PhysRevLett.59.454.

[170] M. Kolb, R. Botet, and R. Jullien. Scaling of kinetically growing clusters. *Physical Review Letters*, 51(13):1123–1126, 1983. doi:10.1103/PhysRevLett.51.1123.

[171] A. Konnov, I. Dyakov, and J. De Ruyck. The effects of composition on the burning velocity and NO formation in premixed flames of $C_2H_4 + O_2 + N_2$. *Experimental Thermal and Fluid Science*, 32(7):1412–1420, 2008. doi:10.1016/J.EXPTHERMFLUSCI.2007.11.017.

[172] A. A. Konnov, R. Riemeijer, V. N. Kornilov, and L. P. H. de Goey. 2D effects in laminar premixed flames stabilized on a flat flame burner. *Experimental Thermal and Fluid Science*, 47:213–223, 2013. doi:10.1016/j.expthermflusci.2013.02.002.

[173] A. A. Konnov, A. Mohammad, V. R. Kishore, N. I. Kim, C. Prathap, and S. Kumar. A comprehensive review of measurements and data analysis of laminar burning velocities for various fuel+air mixtures. *Progress in Energy and Combustion Science*, 68:197 – 267, 2018. doi:10.1016/j.pecs.2018.05.003.

[174] V. N. Koparde and P. T. Cummings. Molecular Dynamics Simulation of Titanium Dioxide Nanoparticle Sintering. *The Journal of Physical Chemistry B*, 109(51):24280–24287, 2005. doi:10.1021/jp054667p.

[175] O. P. Korobeinichev, A. Shmakov, R. A. Maksyutov, A. G. Tereshchenko, D. A. Knyazkov, T. A. Bolshova, M. L. Kosinova, V. S. Sulyaeva, and J.-S. Wu. Synthesis of mesoporous nanocrystalline TiO_2 films in a premixed H_2/O_2/Ar flame. *Combustion, Explosion, and Shock Waves*, 48:49–56, 2012. doi:10.1134/S0010508212010078.

[176] M. Kraft. Modelling of Particulate Processes. *KONA Powder and Particle Journal*, 23: 18–35, 2005. doi:10.14356/kona.2005007.

[177] T. Krüger, H. Kusumaatmaja, A. Kuzmin, O. Shardt, G. Silva, and E. M. Viggen. *The Lattice Boltzmann Method: Principles and Practice*. Graduate Texts in Physics. Springer International Publishing, Cham, 2017. ISBN 978-3-319-44647-9 978-3-319-44649-3. doi:10.1007/978-3-319-44649-3.

[178] F. E. Kruis, K. A. Kusters, S. E. Pratsinis, and B. Scarlett. A Simple Model for the Evolution of the Characteristics of Aggregate Particles Undergoing Coagulation and Sintering. *Aerosol Science and Technology*, 19(4):514–526, 1993. doi:10.1080/02786829308959656.

[179] P. B. Kuhn, B. Ma, B. C. Connelly, M. D. Smooke, and M. B. Long. Soot and thin-filament pyrometry using a color digital camera. *Proceedings of the Combustion Institute*, 33(1):743 – 750, 2011. doi:10.1016/j.proci.2010.05.006.

[180] J. Kumar, M. Peglow, G. Warnecke, and S. Heinrich. The cell average technique for solving multi-dimensional aggregation population balance equations. *Computers and Chemical Engineering*, 32(8):1810–1830, 2008. doi:10.1016/j.compchemeng.2007.10.001.

[181] J. Kumar, M. Peglow, G. Warnecke, S. Heinrich, E. Tsotsas, L. Mörl, M. Hounslow, and G. Reynolds. Numerical Methods on Population Balances. In *Modern Drying Technology*, chapter 6, pages 209–260. John Wiley & Sons, Ltd, 2014. ISBN 978-3-527-63172-8. doi:10.1002/9783527631728.ch6.

[182] S. Kumar and D. Ramkrishna. On the solution of population balance equations by discretization—I. A fixed pivot technique. *Chemical Engineering Science*, 51(8):1311–1332, 1996. doi:10.1016/0009-2509(96)88489-2.

[183] S. Lapointe, R. A. Whitesides, and M. J. McNenly. Sparse, iterative simulation methods for one-dimensional laminar flames. *Combustion and Flame*, 204:23–32, 2019. doi:10.1016/j.combustflame.2019.02.030.

[184] S. Lapointe, Y. Xuan, H. Kwon, R. A. Whitesides, and M. J. McNenly. A computationally-efficient method for flamelet calculations. *Combustion and Flame*, 221:94–102, 2020. doi:10.1016/j.combustflame.2020.07.035.

[185] M. Lapuerta, R. Ballesteros, and F. J. Martos. A method to determine the fractal dimension of diesel soot agglomerates. *Journal of Colloid and Interface Science*, 303: 149–158, 2006. doi:10.1016/j.jcis.2006.07.066.

[186] M. Lattuada, H. Wu, and M. Morbidelli. Hydrodynamic radius of fractal clusters. *Journal of Colloid and Interface Science*, 268(1):96–105, 2003. doi:10.1016/j.jcis.2003.07.028.

[187] T. Lei, Z. Wang, and K. H. Luo. Study of pore-scale coke combustion in porous media using lattice Boltzmann method. *Combustion and Flame*, 225:104–119, 2021. doi:10.1016/j.combustflame.2020.10.036.

[188] C. Li, L. Shi, D. Xie, and H. Du. Morphology and crystal structure of A1-doped TiO_2 nanoparticles synthesized by vapor phase oxidation of titanium tetrachloride. *Journal of Non-Crystalline Solids*, 352(38–39):4128–4135, 2006. doi:10.1016/j.jnoncrysol.2006.06.036.

[189] J. Li, Z. Zhao, A. Kazakov, and F. L. Dryer. An updated comprehensive kinetic model of hydrogen combustion. *International Journal of Chemical Kinetics*, 36(10):566–575, 2004. doi:10.1002/kin.20026.

[190] S. Li, Y. Ren, P. Biswas, and S. D. Tse. Flame aerosol synthesis of nanostructured materials and functional devices: Processing, modeling, and diagnostics. *Progress in Energy and Combustion Science*, 55:1–59, 2016. doi:10.1016/j.pecs.2016.04.002.

[191] Y. Li and T. Ishigaki. Thermodynamic analysis of nucleation of anatase and rutile from TiO_2 melt. *Journal of Crystal Growth*, 242(3):511–516, 2002. doi:10.1016/S0022-0248(02)01438-0.

[192] G. Li Puma, A. Bono, D. Krishnaiah, and J. G. Collin. Preparation of titanium dioxide photocatalyst loaded onto activated carbon support using chemical vapor deposition: A review paper. *Journal of Hazardous Materials*, 157(2):209–219, 2008. doi:10.1016/j.jhazmat.2008.01.040.

[193] P. A. Libby. Wall Shear at a Three-Dimensional Stagnation Point with a Moving Wall. *AIAA Journal*, 12(3):408–409, 1974. doi:10.2514/3.49255.

[194] P. A. Libby and F. A. Williams. Strained Premixed Laminar Flames Under Nonadiabatic Conditions. *Combustion Science and Technology*, 31(1–2):1–42, 1983. doi:10.1080/00102208308923629.

[195] H. W. Liepmann. Investigations on laminar boundary-layer stability and transition on curved boundaries. Technical Report ACR No. 3H30, NACA Wartime Report W-107, 1943.

[196] K. Liffman. A direct simulation Monte-Carlo method for cluster coagulation. *Journal of Computational Physics*, 100(1):116–127, 1992. doi:10.1016/0021-9991(92)90314-O.

[197] K. C. Lin, C.-T. Chiu, H. Tao, and Y.-C. Liao. Formation of unsaturated hydrocarbons, carbonyl compounds and PAHs in a non-premixed methane/air flame doped with methyl butanoate: CFD modeling and comparison with experimental data. *Fuel*, 182:487–493, 2016. doi:10.1016/j.fuel.2016.06.003.

[198] C. S. Lindberg, M. Y. Manuputty, J. Akroyd, and M. Kraft. A two-step simulation methodology for modelling stagnation flame synthesised aggregate nanoparticles. *Combustion and Flame*, 202:143 – 153, 2019. doi:10.1016/j.combustflame.2019.01.010.

[199] C. S. Lindberg, M. Y. Manuputty, P. Buerger, J. Akroyd, and M. Kraft. Numerical simulation and parametric sensitivity study of titanium dioxide particles synthesised in a stagnation flame. *Journal of Aerosol Science*, 138:105451, 2019. doi:10.1016/j.jaerosci.2019.105451.

[200] C. S. Lindberg, M. Y. Manuputty, E. K. Yapp, J. Akroyd, R. Xu, and M. Kraft. A detailed particle model for polydisperse titanium dioxide aggregate particles. *Journal of Computational Physics*, 397:108799, 2019. doi:10.1016/j.jcp.2019.06.074.

[201] H. M. Lindsay, R. Klein, D. A. Weitz, M. Y. Lin, and P. Meakin. Structure and anisotropy of colloid aggregates. *Physical Review A*, 39:3112–3119, 1989. doi:10.1103/PhysRevA.39.3112.

[202] C. Liu, J. Camacho, and H. Wang. Phase Equilibrium of TiO_2 Nanocrystals in Flame-Assisted Chemical Vapor Deposition. *ChemPhysChem*, 19(2):180–186, 2018. doi:10.1002/cphc.201700962.

[203] A. E. Long, R. L. Speth, and W. H. Green. Ember: An open-source, transient solver for 1D reacting flow using large kinetic models, applied to strained extinction. *Combustion and Flame*, 195:105–116, 2018. doi:10.1016/j.combustflame.2018.05.001.

[204] L. Lovachev and Z. Kaganova. Calculation of hydrogen bromide flame characteristics. *DOKLADY AKADEMII NAUK SSSR*, 188(5):1087, 1969.

[205] Z. Lu, H. Zhou, S. Li, Z. Ren, T. Lu, and C. K. Law. Analysis of operator splitting errors for near-limit flame simulations. *Journal of Computational Physics*, 335:578–591, 2017. doi:10.1016/j.jcp.2017.01.044.

[206] A. E. Lutz, R. J. Kee, J. F. Grcar, and F. M. Rupley. OPPDIF: A Fortran Program for Computing Opposed-Flow Diffusion Flames. Technical Report SAND96-8243, Sandia National Laboratories, Livermore, CA 94551-0969, 1997.

[207] B. Ma and M. B. Long. Absolute light calibration using S-type thermocouples. *Proceedings of the Combustion Institute*, 34(2):3531 – 3539, 2013. doi:10.1016/j.proci.2012.05.030.

[208] B. Ma, G. Wang, G. Magnotti, R. S. Barlow, and M. B. Long. Intensity-ratio and color-ratio thin-filament pyrometry: Uncertainties and accuracy. *Combustion and Flame*, 161(4):908 – 916, 2014. doi:10.1016/j.combustflame.2013.10.014.

[209] L. Ma, K.-P. Cheong, H. Ning, and W. Ren. An improved study of the uniformity of laminar premixed flames using laser absorption spectroscopy and CFD simulation. *Experimental Thermal and Fluid Science*, 112:110013, 2020. doi:10.1016/j.expthermflusci.2019.110013.

[210] D. P. Macwan, P. N. Dave, and S. Chaturvedi. A review on nano-TiO_2 sol–gel type syntheses and its applications. *Journal of Materials Science*, 46(11):3669–3686, 2011. doi:10.1007/s10853-011-5378-y.

[211] E. Madadi-Kandjani and A. Passalacqua. An extended quadrature-based moment method with log-normal kernel density functions. *Chemical Engineering Science*, 131:323–339, 2015. doi:10.1016/j.ces.2015.04.005.

[212] P. Maghsoudi, H. Lakzayi, and M. Bidabadi. Analytical investigation of magnesium aerosol combustion based on the asymptotic model of flame structure. *Sustainable Energy Technologies and Assessments*, 43:100914, 2021. doi:10.1016/j.seta.2020.100914.

[213] A. Maisels, F. Einar Kruis, and H. Fissan. Direct simulation Monte Carlo for simultaneous nucleation, coagulation, and surface growth in dispersed systems. *Chemical Engineering Science*, 59(11):2231–2239, 2004. doi:10.1016/j.ces.2004.02.015.

[214] B. B. Mandelbrot. *The Fractal Geometry of Nature*. W. H. Freeman, San Francisco, 1982.

[215] M. Manuputty, J. Dreyer, Y. Sheng, E. J. Bringley, M. Botero, J. Akroyd, and M. Kraft. Polymorphism of nanocrystalline TiO_2 prepared in a stagnation flame: formation of the TiO_2-II phase. *Chemical Science*, 10:1342–1350, 2019. doi:10.1016/j.combustflame.2006.12.001.

[216] M. Y. Manuputty, J. Akroyd, S. Mosbach, and M. Kraft. Modelling TiO_2 formation in a stagnation flame using method of moments with interpolative closure. *Combustion and Flame*, 178:135 – 147, 2017. doi:10.1016/j.combustflame.2017.01.005.

[217] M. Y. Manuputty, C. S. Lindberg, M. L. Botero, J. Akroyd, and M. Kraft. Detailed characterisation of TiO_2 nano-aggregate morphology using TEM image analysis. *Journal of Aerosol Science*, 133:96–112, 2019. doi:10.1016/j.jaerosci.2019.04.012.

[218] M. Y. Manuputty, C. S. Lindberg, J. A. H. Dreyer, J. Akroyd, J. Edwards, and M. Kraft. Understanding the anatase-rutile stability in flame-made TiO_2. *Combustion and Flame*, 226:347–361, 2021. doi:10.1016/j.combustflame.2020.12.017.

[219] Q. Mao, Y. Ren, K. H. Luo, and S. Li. Sintering-Induced Phase Transformation of Nanoparticles: A Molecular Dynamics Study. *The Journal of Physical Chemistry C*, 119(51):28631–28639, 2015. doi:10.1021/acs.jpcc.5b08625.

[220] D. Marchisio. *Computational models for polydisperse particulate and multiphase systems*. Cambridge University Press, Cambridge, 2013. ISBN 978-0-521-85848-9.

[221] D. L. Marchisio and R. O. Fox. Solution of population balance equations using the direct quadrature method of moments. *Journal of Aerosol Science*, 36(1):43–73, 2005. doi:10.1016/j.jaerosci.2004.07.009.

[222] D. L. Marchisio, R. D. Vigil, and R. O. Fox. Implementation of the quadrature method of moments in CFD codes for aggregation–breakage problems. *Chemical Engineering Science*, 58(15):3337–3351, 2003. doi:10.1016/S0009-2509(03)00211-2.

[223] F. J. Massey. The Kolmogorov-Smirnov Test for Goodness of Fit. *Journal of the American Statistical Association*, 46(253):68–78, 1951. doi:10.1080/01621459.1951.10500769.

[224] M. Massot, F. Laurent, D. Kah, and S. de Chaisemartin. A Robust Moment Method for Evaluation of the Disappearance Rate of Evaporating Sprays. *SIAM Journal on Applied Mathematics*, 70(8):3203–3234, 2010. doi:10.1137/080740027.

[225] S. Mathur, P. Tondon, and S. Saxena. Thermal conductivity of binary, ternary and quaternary mixtures of rare gases. *Molecular Physics*, 12(6):569–579, 1967. doi:10.1080/00268976700100731.

[226] J. D. Maun, P. B. Sunderland, and D. L. Urban. Thin-filament pyrometry with a digital still camera. *Applied Optics*, 46(4):483–488, 2007. doi:10.1364/AO.46.000483.

[227] M. T. McDowell, S. W. Lee, W. D. Nix, and Y. Cui. 25th Anniversary Article: Understanding the Lithiation of Silicon and Other Alloying Anodes for Lithium-Ion Batteries. *Advanced Materials*, 25(36):4966–4985, 2013. doi:10.1002/adma.201301795.

[228] R. McGraw. Description of Aerosol Dynamics by the Quadrature Method of Moments. *Aerosol Science and Technology*, 27(2):255–265, 1997. doi:10.1080/02786829708965471.

[229] A. D. McGuire, S. Mosbach, G. K. Reynolds, R. I. Patterson, E. Bringley, N. Eaves, J. A. Dreyer, and M. Kraft. Analysing the effect of screw configuration using a stochastic twin-screw granulation model. *Chemical Engineering Science*, 203:358 – 379, 2019. doi:https://doi.org/10.1016/j.ces.2019.03.078.

[230] M. J. McNenly, R. A. Whitesides, and D. L. Flowers. Faster solvers for large kinetic mechanisms using adaptive preconditioners. *Proceedings of the Combustion Institute*, 35(1):581–587, 2015. doi:10.1016/j.proci.2014.05.113.

[231] L. R. Mead and N. Papanicolaou. Maximum entropy in the problem of moments. *Journal of Mathematical Physics*, 25(8):2404–2417, 1984. doi:10.1063/1.526446.

[232] P. Meakin. Formation of fractal clusters and networks by irreversible diffusion-limited aggregation. *Physical Review Letters*, 51(13):1119–1122, 1983. doi:10.1103/PhysRevLett.51.1119.

[233] P. Meakin. A Historical Introduction to Computer Models for Fractal Aggregates. *Journal of Sol-Gel Science and Technology*, 15:97–117, 1999. doi:10.1023/A:1008731904082.

[234] P. Meakin and R. Jullien. The effects of restructuring on the geometry of clusters formed by diffusion-limited, ballistic, and reaction-limited cluster–cluster aggregation. *The Journal of Chemical Physics*, 89(1):246–250, 1988. doi:10.1063/1.455517.

[235] M. Mehta, Y. Sung, V. Raman, and R. O. Fox. Multiscale Modeling of TiO $_2$ Nanoparticle Production in Flame Reactors: Effect of Chemical Mechanism. *Industrial and Engineering Chemistry Research*, 49(21):10663–10673, 2010. doi:10.1021/ie100560h.

[236] M. Mehta, R. O. Fox, and P. Pepiot. Reduced Chemical Kinetics for the Modeling of TiO_2 Nanoparticle Synthesis in Flame Reactors. *Industrial and Engineering Chemistry Research*, 54(20):5407–5415, 2015. doi:10.1021/acs.iecr.5b00130.

[237] R. D. Mehta. Turbulent boundary layer perturbed by a screen. *AIAA Journal*, 23(9): 1335–1342, 1985. doi:10.2514/3.9089.

[238] A. Meister. Asymptotic Single and Multiple Scale Expansions in the Low Mach Number Limit. *SIAM Journal on Applied Mathematics*, 60(1):256–271, 1999. doi:10.1137/S0036139998343198.

[239] S. Memarzadeh, E. D. Tolmachoff, D. J. Phares, and H. Wang. Properties of nanocrystalline TiO_2 synthesized in premixed flames stabilized on a rotating surface. *Proceedings of the Combustion Institute*, 33(2):1917 –1924, 2011. doi:10.1016/j.proci.2010.05.065.

[240] W. Merchan-Merchan, W. Cuello Jimenez, O. Rodriguez Coria, and C. Wallis. Chapter 7 - Flame Synthesis of Nanostructured Transition Metal Oxides: Trends, Developments, and Recent Advances. In Y. Beeran Pottathara, S. Thomas, N. Kalarikkal, Y. Grohens, and V. Kokol, editors, *Nanomaterials Synthesis*, Micro and Nano Technologies. Elsevier, 2019. ISBN 978-0-12-815751-0. doi:10.1016/B978-0-12-815751-0.00007-9.

[241] B. Michaelis and B. Rogg. FEM-simulation of laminar flame propagation. I: Two-dimensional flames. *Journal of Computational Physics*, 196(2):417–447, 2004. doi:10.1016/j.jcp.2003.10.033.

[242] B. Michaelis and B. Rogg. FEM-Simulation of Laminar Flame Propagation II: Twin and Triple Flames in Counterflow. *Combustion Science and Technology*, 177(5–6):955–978, 2005. doi:10.1080/00102200590926941.

[243] F. Migliorini, S. De Iuliis, F. Cignoli, and G. Zizak. How "flat" is the rich premixed flame produced by your McKenna burner? *Combustion and Flame*, 153(3):384–393, 2008. doi:10.1016/j.combustflame.2008.01.007.

[244] J. A. Miller and R. J. Kee. Chemical nonequilibrium effects in hydrogen-air laminar jet diffusion flames. *The Journal of Physical Chemistry*, 81(25):2534–2542, 1977. doi:10.1021/j100540a035.

[245] D. Mitrakos, E. Hinis, and C. Housiadas. Sectional Modeling of Aerosol Dynamics in Multi-Dimensional Flows. *Aerosol Science and Technology*, 41(12):1076–1088, 2007. doi:10.1080/02786820701697804.

[246] V. Mittal, H. Pitsch, and F. Egolfopoulos. Assessment of counterflow to measure laminar burning velocities using direct numerical simulations. *Combustion Theory and Modelling*, 16(3):419–433, 2012. doi:10.1080/13647830.2011.631033.

[247] L. Monchick and E. A. Mason. Transport Properties of Polar Gases. *The Journal of Chemical Physics*, 35(5):1676–1697, 1961. doi:10.1063/1.1732130.

[248] V. T. Morgan. The overall convective heat transfer from smooth circular cylinders. *Advances in Heat Transfer*, 11:199 – 264, 1975. doi:10.1016/S0065-2717(08)70075-3.

[249] S. Mosbach and M. Kraft. An explicit numerical scheme for homogeneous gas-phase high-temperature combustion systems. *Combustion Theory and Modelling*, 10(1):171–182, 2006. doi:10.1080/13647830500352465.

[250] F. Moukalled, L. Mangani, and M. Darwish. *The Finite Volume Method in Computational Fluid Dynamics*, volume 113 of *Fluid Mechanics and Its Applications*. Springer, Cham, 2016. ISBN 978-3-319-16873-9. doi:10.1007/978-3-319-16874-6.

[251] R. D. Mountain, G. W. Mulholland, and H. Baum. Simulation of Aerosol Agglomeration in the Free Molecular and Continuum Flow Regimes. *Journal of Colloid and Interface Science*, 114(1):15, 1986. doi:10.1016/0021-9797(86)90241-9.

[252] M. Mueller, G. Blanquart, and H. Pitsch. Hybrid Method of Moments for modeling soot formation and growth. *Combustion and Flame*, 156(6):1143–1155, 2009. doi:10.1016/j.combustflame.2009.01.025.

[253] R. Mueller, L. Mädler, and S. E. Pratsinis. Nanoparticle synthesis at high production rates by flame spray pyrolysis. *Chemical Engineering Science*, 58(10):1969–1976, 2003. doi:10.1016/S0009-2509(03)00022-8.

[254] S. Murshed, K. Leong, and C. Yang. Enhanced thermal conductivity of TiO_2-water based nanofluids. *International Journal of Thermal Sciences*, 44(4):367–373, 2005. doi:10.1016/j.ijthermalsci.2004.12.005.

[255] K. Nakaso, T. Fujimoto, T. Seto, M. Shimada, K. Okuyama, and M. M. Lunden. Size Distribution Change of Titania Nano-Particle Agglomerates Generated by Gas Phase Reaction, Agglomeration, and Sintering. *Aerosol Science and Technology*, 35(5):929–947, 2001. doi:10.1080/02786820126857.

[256] A. Navrotsky. Nanoscale Effects on Thermodynamics and Phase Equilibria in Oxide Systems. *ChemPhysChem*, 12(12):2207–2215, 2011. doi:10.1002/cphc.201100129.

[257] S. Nikraz and H. Wang. Dye sensitized solar cells prepared by flames stabilized on a rotating surface. *Proceedings of the Combustion Institute*, 34(2):2171–2178, 2013. doi:10.1016/J.PROCI.2012.06.069.

[258] S. Nikraz, D. J. Phares, and H. Wang. Mesoporous Titania Films Prepared by Flame Stabilized on a Rotating Surface: Application in Dye Sensitized Solar Cells. *The Journal of Physical Chemistry C*, 116(9):5342–5351, 2012. doi:10.1021/jp2095533.

[259] M. Nitta, S. Kanefusa, and M. Haradome. Propane Gas Detector Using SnO_2 Doped with Nb, V, Ti, or Mo. *Journal of the Electrochemical Society*, 125(10):5, 1978. doi:10.1149/1.2131271.

[260] A. Nonaka, M. S. Day, and J. B. Bell. A conservative, thermodynamically consistent numerical approach for low Mach number combustion. Part I: Single-level integration. *Combustion Theory and Modelling*, 22(1):156–184, 2018. doi:10.1080/13647830.2017.1390610.

[261] V. N. Nori. *Modeling and Analysis of Chemiluminescence sensing for syngas, methane, and Jet-A Combustion*. PhD thesis, Georgia Institute of Technology, Atlanta, GA, August 2008.

[262] C. B. Oh, A. Hamins, M. Bundy, and J. Park. The two-dimensional structure of low strain rate counterflow nonpremixed-methane flames in normal and microgravity. *Combustion Theory and Modelling*, 12(2):283–302, 2008. doi:10.1080/13647830701642201.

[263] H. Oh, H. Park, and S. Kim. Effects of Particle Shape on the Unipolar Diffusion Charging of Nonspherical Particles. *Aerosol Science and Technology*, 38(11):1045–1053, 2004. doi:10.1080/027868290883324.

[264] H. Okamoto. O-Ti (Oxygen-Titanium). *Journal of Phase Equilibria and Diffusion*, 32 (5):473–474, 2011. doi:10.1007/s11669-011-9935-5.

[265] K. Okuyama, R. Ushio, Y. Kousaka, R. C. Flagan, and J. H. Seinfeld. Particle generation in a chemical vapor deposition process with seed particles. *AIChE Journal*, 36(3): 409–419, 1990. doi:10.1002/aic.690360310.

[266] N.-E. Olofsson, H. Bladh, A. Bohlin, J. Johnsson, and P.-E. Bengtsson. Are Sooting Premixed Porous-Plug Burner Flames One-Dimensional? A Laser-Based Experimental Investigation. *Combustion Science and Technology*, 185(2):293–309, 2013. doi:10.1080/00102202.2012.718006.

[267] H. M. Omar and S. Rohani. Crystal Population Balance Formulation and Solution Methods: A Review. *Crystal Growth & Design*, 17(7):4028–4041, 2017. doi:10.1021/acs.cgd.7b00645.

[268] J. G. Parker. Rotational and vibrational relaxation in diatomic gases. *The Physics of Fluids*, 2(4):449–462, 1959. doi:10.1063/1.1724417.

[269] A. Passalacqua, F. Laurent, E. Madadi-Kandjani, J. Heylmun, and R. Fox. An open-source quadrature-based population balance solver for OpenFOAM. *Chemical Engineering Science*, 176:306–318, 2018. doi:10.1016/j.ces.2017.10.043.

[270] S. Patankar. *Numerical Heat Transfer and Fluid Flow*. Series on Computational Methods in Mechanics and Thermal Science. Hemisphere Publishing Corporation (CRC Press, Taylor & Francis Group), 1980. ISBN 978-0891165224.

[271] S. Patankar and D. Spalding. A calculation procedure for heat, mass and momentum transfer in three-dimensional parabolic flows. *International Journal of Heat and Mass Transfer*, 15(10):1787 – 1806, 1972. doi:10.1016/0017-9310(72)90054-3.

[272] R. I. Patterson, J. Singh, M. Balthasar, M. Kraft, and W. Wagner. Extending stochastic soot simulation to higher pressures. *Combustion and Flame*, 145(3):638–642, 2006. doi:10.1016/j.combustflame.2006.02.005.

[273] R. I. Patterson, W. Wagner, and M. Kraft. Stochastic weighted particle methods for population balance equations. *Journal of Computational Physics*, 230(19):7456–7472, 2011. doi:10.1016/j.jcp.2011.06.011.

[274] R. I. A. Patterson, J. Singh, M. Balthasar, M. Kraft, and J. R. Norris. The Linear Process Deferment Algorithm: A new technique for solving population balance equations. *SIAM Journal on Scientific Computing*, 28(1):303–320, 2006. doi:10.1137/040618953.

[275] F. Pedregosa, G. Varoquaux, A. Gramfort, V. Michel, B. Thirion, O. Grisel, M. Blondel, P. Prettenhofer, R. Weiss, V. Dubourg, J. Vanderplas, A. Passos, D. Cournapeau, M. Brucher, M. Perrot, and É. Duchesnay. Scikit-learn: Machine learning in python. *Journal of Machine Learning Research*, 12(85):2825–2830, 2011.

[276] W. Pejpichestakul, E. Ranzi, M. Pelucchi, A. Frassoldati, A. Cuoci, A. Parente, and T. Faravelli. Examination of a soot model in premixed laminar flames at fuel-rich conditions. *Proceedings of the Combustion Institute*, 37(1):1013–1021, 2019. doi:10.1016/j.proci.2018.06.104.

[277] N. Peters and J. Warnatz, editors. *Discussion of Test Problem B*, chapter J. Warnatz, pages 49–64. Vieweg+Teubner Verlag, Wiesbaden, 1982. doi:10.1007/978-3-663-14006-1_5.

[278] F. Pierce, C. M. Sorensen, and A. Chakrabarti. Computer simulation of diffusion-limited cluster-cluster aggregation with an epstein drag force. *Physical Review E*, 74:021411, 2006. doi:10.1103/PhysRevE.74.021411.

[279] M. Pigou, J. Morchain, P. Fede, M.-I. Penet, and G. Laronze. New developments of the Extended Quadrature Method of Moments to solve Population Balance Equations. *Journal of Computational Physics*, 365:243–268, 2018. doi:10.1016/j.jcp.2018.03.027.

[280] H. Pitsch, E. Riesmeier, and N. Peters. Unsteady Flamelet Modeling of Soot Formation in Turbulent Diffusion Flames. *Combustion Science and Technology*, 158(1):389–406, 2000. doi:10.1080/00102200008947342.

[281] T. Poinsot and D. Veynante. *Theoretical and Numerical Combustion*. by the authors, third edition, 2012.

[282] S. Pope. Computationally efficient implementation of combustion chemistry using in situ adaptive tabulation. *Combustion Theory and Modelling*, 1(1):41–63, 1997. doi:10.1080/713665229.

[283] S. E. Pratsinis. Simultaneous nucleation, condensation, and coagulation in aerosol reactors. *Journal of Colloid and Interface Science*, 124(2):416–427, 1988. doi:10.1016/0021-9797(88)90180-4.

[284] S. E. Pratsinis. Flame Aerosol Synthesis of Ceramic Powders. *Progress in Energy and Combustion Science*, 24:197–219, 1998.

[285] S. E. Pratsinis. Aerosol-based technologies in nanoscale manufacturing: From functional materials to devices through core chemical engineering. *AIChE Journal*, 56(12):3028–3035, 2010. doi:10.1002/aic.12478.

[286] S. E. Pratsinis and P. T. Spicer. Competition between gas phase and surface oxidation of $TiCl_4$ during synthesis of TiO_2 particles. *Chemical Engineering Science*, 53(10): 1861–1868, 1998. doi:10.1016/S0009-2509(98)00026-8.

[287] S. E. Pratsinis, H. Bai, P. Biswas, M. Frenklach, and S. V. R. Mastrangelo. Kinetics of Titanium(IV) Chloride Oxidation. *Journal of the American Ceramic Society*, 73(7): 2158–2162, 1990. doi:10.1111/j.1151-2916.1990.tb05295.x.

[288] Y. H. Qian, D. D'Humières, and P. Lallemand. Lattice BGK Models for Navier-Stokes Equation. *Europhysics Letters*, 17(6):479–484, 1992. doi:10.1209/0295-5075/17/6/001.

[289] L. Quartapelle. Vorticity conditioning in the computation of two-dimensional viscous flows. *Journal of Computational Physics*, 40(2):453–477, 1981. doi:10.1016/0021-9991(81)90222-9.

[290] D. Ramkrishna and M. R. Singh. Population Balance Modeling: Current Status and Future Prospects. *Annual Review of Chemical and Biomolecular Engineering*, 5:123–146, 2014. doi:10.1146/annurev-chembioeng-060713-040241.

[291] M. R. Ranade, A. Navrotsky, H. Z. Zhang, J. F. Banfield, S. H. Elder, A. Zaban, P. H. Borse, S. K. Kulkarni, G. S. Doran, and H. J. Whitfield. Energetics of nanocrystalline TiO_2. *Proceedings of the National Academy of Sciences*, 99(Supplement 2):6476–6481, 2002. doi:10.1073/pnas.251534898.

[292] Reaction Design. *Theory Manual*. Chemkin, 2004.

[293] Y. Ren, J. Wei, and S. Li. In-situ laser diagnostic of nanoparticle formation and transport behavior in flame aerosol deposition. *Proceedings of the Combustion Institute*, 37(1): 935–942, 2019. doi:10.1016/j.proci.2018.06.015.

[294] J. Ritter. An efficient bounding sphere. In A. S. Glassner, editor, *Graphics Gems*, pages 301–303. Academic Press, 1990.

[295] P. J. Roache. Quantification of Uncertainty in Computational Fluid Dynamics. *Annual Review of Fluid Mechanics*, 29(1):123–160, 1997. doi:10.1146/annurev.fluid.29.1.123.

[296] S. N. Rogak, R. C. Flagan, and H. V. Nguyen. The Mobility and Structure of Aerosol Agglomerates. *Aerosol Science and Technology*, 18(1):25–47, 1993. doi:10.1080/02786829308959582.

[297] W. M. Rohsenow, J. P. Hartnett, Y. I. Cho, et al. *Handbook of Heat Transfer*. McGraw-Hill, 3 edition, 1998.

[298] P. Romppainen and V. Lantto. The effect of microstructure on the height of potential energy barriers in porous tin dioxide gas sensors. *Journal of Applied Physics*, 63(10): 5159–5165, 1988. doi:10.1063/1.340419.

[299] A. Rothschild and Y. Komem. The effect of grain size on the sensitivity of nanocrystalline metal-oxide gas sensors. *Journal of Applied Physics*, 95(11):6374–6380, 2004. doi:10.1063/1.1728314.

[300] N. Rott. Unsteady viscous flow in the vicinity of a stagnation point. *Quarterly of Applied Mathematics*, 13(4):444–451, 1956. doi:10.1090/qam/74194.

[301] A. J. Rulison, P. F. Miquel, and J. L. Katz. Titania and silica powders produced in a counterflow diffusion flame. *Journal of Materials Research*, 11(12):3083–3089, 1996. doi:10.1557/JMR.1996.0392.

[302] C. Saggese, A. Cuoci, A. Frassoldati, S. Ferrario, J. Camacho, H. Wang, and T. Faravelli. Probe effects in soot sampling from a burner-stabilized stagnation flame. *Combustion and Flame*, 167:184–197, 2016. doi:10.1016/j.combustflame.2016.02.013.

[303] S. Salenbauch, A. Cuoci, A. Frassoldati, C. Saggese, T. Faravelli, and C. Hasse. Modeling soot formation in premixed flames using an Extended Conditional Quadrature Method of Moments. *Combustion and Flame*, 162(6):2529–2543, 2015. doi:10.1016/j.combustflame.2015.03.002.

[304] S. Salenbauch, C. Hasse, M. Vanni, and D. L. Marchisio. A numerically robust method of moments with number density function reconstruction and its application to soot formation, growth and oxidation. *Journal of Aerosol Science*, 128:34–49, 2019. doi:10.1016/j.jaerosci.2018.11.009.

[305] M. Sander, R. H. West, M. S. Celnik, and M. Kraft. A Detailed Model for the Sintering of Polydispersed Nanoparticle Agglomerates. *Aerosol Science and Technology*, 43(10): 978–989, 2009. doi:10.1080/02786820903092416.

[306] W. S. Saric. Görtler Vortices. *Annual Review of Fluid Mechanics*, 26(1):379–409, 1994. doi:10.1146/annurev.fl.26.010194.002115.

[307] H. Sato, S. Endo, M. Sugiyama, T. Kikegawa, O. Shimomura, and K. Kusaba. Baddeleyite-Type High-Pressure Phase of TiO_2. *Science*, 251(4995):786–788, 1991. doi:10.1126/science.251.4995.786.

[308] N. Sawant, B. Dorschner, and I. V. Karlin. Consistent lattice Boltzmann model for multicomponent mixtures. *Journal of Fluid Mechanics*, 909, 2021. doi:10.1017/jfm.2020.853.

[309] T. Seto, M. Shimada, and K. Okuyama. Evaluation of Sintering of Nanometer-Sized Titania Using Aerosol Method. *Aerosol Science and Technology*, 23(2):183–200, 1995. doi:10.1080/02786829508965303.

[310] T. Seto, A. Hirota, T. Fujimoto, M. Shimada, and K. Okuyama. Sintering of Polydisperse Nanometer-Sized Agglomerates. *Aerosol Science and Technology*, 27(3):422–438, 1997. doi:10.1080/02786829708965482.

[311] S. Shekar, W. J. Menz, A. J. Smith, M. Kraft, and W. Wagner. On a multivariate population balance model to describe the structure and composition of silica nanoparticles. *Computers and Chemical Engineering*, 43:130–147, 2012. doi:10.1016/j.compchemeng.2012.04.010.

[312] J. Shen, M. Yu, and J. Lin. Description of Atmospheric Aerosol Dynamics Using an Inverse Gaussian Distributed Method of Moments. *Journal of the Atmospheric Sciences*, 77(9):3011–3031, 2020. doi:10.1175/JAS-D-20-0077.1.

[313] M. Shiea, A. Buffo, M. Vanni, and D. Marchisio. Numerical Methods for the Solution of Population Balance Equations Coupled with Computational Fluid Dynamics. *Annual Review of Chemical and Biomolecular Engineering*, 11(1):339–366, 2020. doi:10.1146/annurev-chembioeng-092319-075814.

[314] R. Shirley, Y. Liu, T. S. Totton, R. H. West, and M. Kraft. First-principles thermochemistry for the combustion of a $ticl_4$ and $alcl_3$ mixture. *The Journal of Physical Chemistry A*, 113(49):13790–13796, 2009. doi:10.1021/jp905244w.

[315] R. Shirley, J. Akroyd, L. A. Miller, O. R. Inderwildi, U. Riedel, and M. Kraft. Theoretical insights into the surface growth of rutile TiO_2. *Combustion and Flame*, 158(10):1868–1876, 2011. doi:10.1016/j.combustflame.2011.06.007.

[316] A. Shmakov, O. Korobeinichev, D. Knyazkov, A. Paletsky, R. Maksutov, I. Gerasimov, T. Bolshova, V. Kiselev, and N. Gritsan. Combustion chemistry of $Ti(OC_3H_7)_4$ in premixed flat burner-stabilized H_2/O_2/Ar flame at 1atm. *Proceedings of the Combustion Institute*, 34(1):1143–1149, 2013. doi:10.1016/j.proci.2012.05.081.

[317] C. Shu, H. Ding, and K. S. Yeo. Local radial basis function-based differential quadrature method and its application to solve two-dimensional incompressible Navier–Stokes equations. *Computer Methods in Applied Mechanics and Engineering*, 192(7):941–954, 2003. doi:10.1016/S0045-7825(02)00618-7.

[318] S. Shu and N. Yang. GPU-accelerated large eddy simulation of stirred tanks. *Chemical Engineering Science*, 181:132–145, 2018. doi:10.1016/j.ces.2018.02.011.

[319] M. Singh, J. Kumar, A. Bück, and E. Tsotsas. An improved and efficient finite volume scheme for bivariate aggregation population balance equation. *Journal of Computational and Applied Mathematics*, 308:83–97, 2016. doi:10.1016/j.cam.2016.04.037.

[320] M. Singh, G. Kaur, T. De Beer, and I. Nopens. Solution of bivariate aggregation population balance equation: A comparative study. *Reaction Kinetics, Mechanisms and Catalysis*, 123(2):385–401, 2018. doi:10.1007/s11144-018-1345-9.

[321] M. Smith and T. Matsoukas. Constant-number Monte Carlo simulation of population balances. *Chemical Engineering Science*, 53(9):1777–1786, 1998. doi:10.1016/S0009-2509(98)00045-1.

[322] M. Smoluchowski. Versuch einer mathematischen Theorie der Koagulationskinetik kolloider Lösungen [An attempt for a mathematical theory of coagulation kinetics of colloidal solutions]. *Zeitschrift für Physikalische Chemie*, 92(1):129–168, 1917.

[323] M. Smooke, Y. Xu, R. Zurn, P. Lin, J. Frank, and M. Long. Computational and experimental study of OH and CH radicals in axisymmetric laminar diffusion flames. *Symposium (International) on Combustion*, 24(1):813–821, 1992. doi:10.1016/S0082-0784(06)80099-8.

[324] M. Smooke, C. McEnally, L. Pfefferle, R. Hall, and M. Colket. Computational and experimental study of soot formation in a coflow, laminar diffusion flame. *Combustion and Flame*, 117(1):117 – 139, 1999. doi:10.1016/S0010-2180(98)00096-0.

[325] M. D. Smooke. The computation of laminar flames. *Proceedings of the Combustion Institute*, 34(1):65–98, 2013. doi:10.1016/j.proci.2012.09.005.

[326] M. D. Smooke, R. E. Mitchell, and D. E. Keyes. Numerical Solution of Two-Dimensional Axisymmetric Laminar Diffusion Flames. *Combustion Science and Technology*, 67(4–6): 85–122, 1989. doi:10.1080/00102208908924063.

[327] K. Sone. *Modeling and simulation of axisymmetric stagnation flames*. PhD thesis, California Institute of Technology, Pasadena, CA, May 2007.

[328] C. Sorensen and C. Oh. Divine proportion shape preservation and the fractal nature of cluster-cluster aggregates. *Physical Review E*, 58(6):7545, 1998. doi:10.1103/PhysRevE.58.7545.

[329] C. M. Sorensen. The Mobility of Fractal Aggregates: A Review. *Aerosol Science and Technology*, 45(7):765–779, 2011. doi:10.1080/02786826.2011.560909.

[330] C. M. Sorensen and G. C. Roberts. The Prefactor of Fractal Aggregates. *Journal of Colloid and Interface Science*, 186(2):447–452, 1997. doi:10.1006/jcis.1996.4664.

[331] D. Spalding. Theoretical aspects of flame stabilization: An approximate graphical method for the flame speed of mixed gases. *Aircraft Engineering and Aerospace Technology*, 25(9):264–276, 1953. doi:10.1108/eb032332.

[332] D. Spalding. *GENMIX; a general computer program for two-dimensional parabolic phenomena*. Pergamon Press, Oxford, 1977.

[333] D. Spalding, P. Stephenson, and R. Taylor. A calculation procedure for the prediction of laminar flame speeds. *Combustion and Flame*, 17(1):55 – 64, 1971. doi:10.1016/S0010-2180(71)80138-4.

[334] D. B. Spalding. The theory of flame phenomena with a chain reaction. *Philosophical Transactions of the Royal Society A*, 249(957):1–25, 1956. doi:10.1098/rsta.1956.0013.

[335] R. Speth, W. H. Green, S. Macnamara, and G. Strang. Balanced splitting and rebalanced splitting. *SIAM Journal on Numerical Analysis*, 51, 2013. doi:10.1137/120878641.

[336] B. Sportisse. An Analysis of Operator Splitting Techniques in the Stiff Case. *Journal of Computational Physics*, 161(1):140–168, 2000. doi:10.1006/jcph.2000.6495.

[337] G. Strang. On the Construction and Comparison of Difference Schemes. *SIAM Journal on Numerical Analysis*, 5(3):506–517, 1968. doi:10.1137/0705041.

[338] Y. Sung, V. Raman, and R. O. Fox. Large-eddy-simulation-based multiscale modeling of TiO_2 nanoparticle synthesis in a turbulent flame reactor using detailed nucleation chemistry. *Chemical Engineering Science*, 66(19):4370–4381, 2011. doi:10.1016/j.ces.2011.04.024.

[339] W. Sutherland. The viscosity of gases and molecular force. *The London, Edinburgh, and Dublin Philosophical Magazine and Journal of Science*, 36(223):507–531, 1893. doi:10.1080/14786449308620508.

[340] A. Tagliani. Hausdorff moment problem and maximum entropy: A unifed approach. *Applied Mathematical Computing*, 105((2-3)):291–305, 1999. doi:10.1016/S0096-3003(98)10084-X.

[341] M. Tamura, P. A. Berg, J. E. Harrington, J. Luque, J. B. Jeffries, G. P. Smith, and D. R. Crosley. Collisional Quenching of CH(A), OH(A), and NO(A) in Low Pressure Hydrocarbon Flames. *Combustion and Flame*, 114(3):502 – 514, 1998. doi:10.1016/S0010-2180(97)00324-6.

[342] W. Y. Teoh, R. Amal, and L. Mädler. Flame spray pyrolysis: An enabling technology for nanoparticles design and fabrication. *Nanoscale*, 2(8):1324–1347, 2010. doi:10.1039/C0NR00017E.

[343] The OpenFOAM Foundation Ltd. OpenFOAM v5, 2017.

[344] M. Tiemann. Porous Metal Oxides as Gas Sensors. *Chemistry A European Journal*, 13 (30):8376–8388, 2007. doi:10.1002/chem.200700927.

[345] E. D. Tolmachoff, A. D. Abid, D. J. Phares, C. S. Campbell, and H. Wang. Synthesis of nano-phase TiO_2 crystalline films over premixed stagnation flames. *Proceedings of the Combustion Institute*, 32(2):1839 – 1845, 2009. doi:10.1016/j.proci.2008.06.052.

[346] T. S. Totton, R. Shirley, and M. Kraft. First-principles thermochemistry for the combustion of $TiCl_4$ in a methane flame. *Proceedings of the Combustion Institute*, 33(1): 493–500, 2011. doi:10.1016/j.proci.2010.05.011.

[347] M. Tournoux, R. Marchand, and L. Brohan. Layered $K_2Ti_4O_9$ and the open metastable TiO_2(B) structure. *Progress in Solid State Chemistry*, 17(1):33–52, 1986. doi:10.1016/0079-6786(86)90003-8.

[348] D. Trees, K. Seshadri, G. Balakrishnan, T. Brown, R. Pitz, S. Nandula, M. Smooke, and V. Giovangigli. The structure of nonpremixed hydrogen-air flames. *Combustion Science and Technology*, 104(4–6):427–439, 1995. doi:10.1080/00102209508907731.

[349] A. Tricoli, M. Graf, and S. E. Pratsinis. Optimal Doping for Enhanced SnO_2 Sensitivity and Thermal Stability. *Advanced Functional Materials*, 18(13):1969–1976, 2008. doi:10.1002/adfm.200700784.

[350] S. Tsantilis and S. E. Pratsinis. Narrowing the size distribution of aerosol-made titania by surface growth and coagulation. *Journal of Aerosol Science*, 35(3):405–420, 2004. doi:10.1016/j.jaerosci.2003.09.006.

[351] S. Tsantilis, H. Briesen, and S. E. Pratsinis. Sintering Time for Silica Particle Growth. *Aerosol Science and Technology*, 34(3):237–246, 2001. doi:10.1080/02786820119149.

[352] S. Tsantilis, H. K. Kammler, and S. E. Pratsinis. Population balance modeling of flame synthesis of titania nanoparticles. *Chemical Engineering Science*, 57(12):18, 2002. doi:10.1016/S0009-2509(02)00107-0.

[353] H. Tsuji. Counterflow diffusion flames. *Progress in Energy and Combustion Science*, 8: 93–119, 1982.

[354] UCSD. Chemical-kinetic mechanisms for combustion applications, 2005. San Diego Mechanism web page, Mechanical and Aerospace Engineering (Combustion Research), University of California at San Diego http://combustion.ucsd.edu/ (2005).

[355] G. Ulrich. Special report. *Chemical and Engineering News Archive*, 62:22–29, 1984. doi:10.1021/cen-v062n032.p022.

[356] G. D. Ulrich. Theory of particle formation and growth in oxide synthesis flames. *Combustion Science and Technology*, 4(1):47–57, 1971. doi:10.1080/00102207108952471.

[357] G. D. Ulrich and N. S. Subramanian. III. Coalescence as a Rate-Controlling Process. *Combustion Science and Technology*, 17(3–4):119–126, 1977. doi:10.1080/00102207708946822.

[358] G. D. Ulrich, B. A. Milnes, and N. S. Subramanian. Particle Growth in Flames. II: Experimental Results for Silica Particles. *Combustion Science and Technology*, 14(4–6): 243–249, 1976. doi:10.1080/00102207608547532.

[359] C. M. Vagelopoulos and F. N. Egolfopoulos. Direct experimental determination of laminar flame speeds. *Proceedings of the Combustion Institute*, 27(1):513 – 519, 1998. doi:10.1016/S0082-0784(98)80441-4.

[360] S. Vemury, K. A. Kusters, and S. E. Pratsinis. Time-Lag for Attainment of the Self-Preserving Particle Size Distribution by Coagulation. *Journal of Colloid and Interface Science*, 165(1):53–59, 1994. doi:10.1006/jcis.1994.1204.

[361] P. Versailles and J. M. Bergthorson. Optimized Laminar Axisymmetrical Nozzle Design Using a Numerically Validated Thwaites Method. *Journal of Fluids Engineering*, 134 (10):101203, 2012. doi:10.1115/1.4007155.

[362] P. Versailles, G. M. Watson, A. C. Lipardi, and J. M. Bergthorson. Quantitative CH measurements in atmospheric-pressure, premixed flames of C_1-C_4 alkanes. *Combustion and Flame*, 165:109–124, 2016. doi:10.1016/j.combustflame.2015.11.001.

[363] H. K. Versteeg and W. Malalasekera. *An Introduction to Computational Fluid Dynamics: The Finite Volume Method*. Pearson Education Ltd, Harlow, England, 2 edition, 2007. ISBN 978-0-13-127498-3.

[364] V. Vikas, Z. Wang, A. Passalacqua, and R. Fox. Realizable high-order finite-volume schemes for quadrature-based moment methods. *Journal of Computational Physics*, 230 (13):5328–5352, 2011. doi:10.1016/j.jcp.2011.03.038.

[365] P. Virtanen, R. Gommers, T. E. Oliphant, M. Haberland, T. Reddy, D. Cournapeau, E. Burovski, P. Peterson, W. Weckesser, J. Bright, S. J. van der Walt, M. Brett, J. Wilson, K. Jarrod Millman, N. Mayorov, A. R. J. Nelson, E. Jones, R. Kern, E. Larson, C. Carey, İ. Polat, Y. Feng, E. W. Moore, J. Vand erPlas, D. Laxalde, J. Perktold, R. Cimrman, I. Henriksen, E. A. Quintero, C. R. Harris, A. M. Archibald, A. H. Ribeiro, F. Pedregosa, P. van Mulbregt, and Contributors. SciPy 1.0: Fundamental Algorithms for Scientific Computing in Python. *Nature Methods*, 17:261–272, 2020. doi:10.1038/s41592-019-0686-2.

[366] C. Y. Wang. Stagnation slip flow and heat transfer on a moving plate. *Chemical Engineering Science*, 61(23):7668–7672, 2006. doi:10.1016/j.ces.2006.09.003.

[367] K. Wang, F. Li, Y. Wu, and X. Yu. Quantitative measurements of chemiluminescence in a laminar methane-air premixed flame and comparison to numerical methods. *Energy and Fuels*, 32(4):5536–5543, 2018. doi:10.1021/acs.energyfuels.7b03484.

[368] K. Wang, S. Yu, and W. Peng. A new method for solving population balance equations using a radial basis function network. *Aerosol Science and Technology*, 54(6):644–655, 2020. doi:10.1080/02786826.2019.1711358.

[369] S. Wang, Z. Wang, A. M. Elbaz, X. Han, Y. He, M. Costa, A. A. Konnov, and W. L. Roberts. Experimental study and kinetic analysis of the laminar burning velocity of NH_3/syngas/air, NH_3/CO/air and NH_3/H_2/air premixed flames at elevated pressures. *Combustion and Flame*, 221, 2020. doi:10.1016/j.combustflame.2020.08.004.

[370] Y. Wang, P. Liu, J. Fang, W.-N. Wang, and P. Biswas. Kinetics of sub-2 nm TiO_2 particle formation in an aerosol reactor during thermal decomposition of titanium tetraisopropoxide. *Journal of Nanoparticle Research*, 17(3):147, 2015. doi:10.1007/s11051-015-2964-y.

[371] Y. Wang, J. Kangasluoma, M. Attoui, J. Fang, H. Junninen, M. Kulmala, T. Petäjä, and P. Biswas. Observation of incipient particle formation during flame synthesis by tandem differential mobility analysis-mass spectrometry (DMA-MS). *Proceedings of the Combustion Institute*, 36(1):745–752, 2017. doi:10.1016/j.proci.2016.07.005.

[372] Y. Wang, G. Sharma, C. Koh, V. Kumar, R. Chakrabarty, and P. Biswas. Influence of flame-generated ions on the simultaneous charging and coagulation of nanoparticles during combustion. *Aerosol Science and Technology*, 51(7):833–844, 2017. doi:10.1080/02786826.2017.1304635.

[373] G. M. Watson, P. Versailles, and J. M. Bergthorson. NO formation in premixed flames of C_1-C_3 alkanes and alcohols. *Combustion and Flame*, 169:242 – 260, 2016. doi:https://doi.org/10.1016/j.combustflame.2016.04.015.

[374] G. M. Watson, P. Versailles, and J. M. Bergthorson. NO formation in rich premixed flames of C_1-C_4 alkanes and alcohols. *Proceedings of the Combustion Institute*, 36(1): 627 – 635, 2017. doi:10.1016/j.proci.2016.06.108.

[375] C. A. G. Webster. A note on the sensitivity to yaw of a hot-wire anemometer. *Journal of Fluid Mechanics*, 13(2):307–312, 1962. doi:10.1017/S0022112062000695.

[376] J. Wei, Y. Ren, Y. Zhang, B. Shi, and S. Li. Effects of temperature-time history on the flame synthesis of nanoparticles in a swirl-stabilized tubular burner with two feeding modes. *Journal of Aerosol Science*, 133:72–82, 2019. doi:10.1016/j.jaerosci.2019.04.002.

[377] J. Z. Wen, M. J. Thomson, M. F. Lightstone, S. H. Park, and S. N. Rogak. An Improved Moving Sectional Aerosol Model of Soot Formation in a Plug Flow Reactor. *Combustion Science and Technology*, 178(5):921–951, 2006. doi:10.1080/00102200500270007.

[378] R. H. West, G. J. O. Beran, W. H. Green, and M. Kraft. First-Principles Thermochemistry for the Production of TiO_2 from $TiCl_4$. *The Journal of Physical Chemistry A*, 111(18): 3560–3565, 2007. doi:10.1021/jp0661950.

[379] R. H. West, M. S. Celnik, O. R. Inderwildi, M. Kraft, G. J. O. Beran, and W. H. Green. Toward a Comprehensive Model of the Synthesis of TiO_2 Particles from $TiCl_4$. *Industrial and Engineering Chemistry Research*, 46(19):6147–6156, 2007. doi:10.1021/ie0706414.

[380] R. H. West, R. A. Shirley, M. Kraft, C. F. Goldsmith, and W. H. Green. A detailed kinetic model for combustion synthesis of titania from $TiCl_4$. *Combustion and Flame*, 156(9):1764–1770, 2009. doi:10.1016/j.combustflame.2009.04.011.

[381] C. K. Westbrook and F. L. Dryer. Simplified Reaction Mechanisms for the Oxidation of Hydrocarbon Fuels in Flames. *Combustion Science and Technology*, 21:31–43, 1981. doi:10.1080/00102208108946970.

[382] F. White. *Turbulent Flows*. Cambridge University Press, Cambridge, 2000.

[383] F. M. White. *Fluid Mechanics*. McGraw-Hill, seventh edition, 2011. ISBN 978-0-07-352934-9.

[384] A. Wick, A. Attili, F. Bisetti, and H. Pitsch. DNS-driven analysis of the Flamelet/Progress Variable model assumptions on soot inception, growth, and oxidation in turbulent flames. *Combustion and Flame*, 214:437–449, 2020. doi:10.1016/j.combustflame.2020.01.012.

[385] A. Wick, M. Frenklach, and H. Pitsch. Systematic assessment of the Method of Moments with Interpolative Closure and guidelines for its application to soot particle dynamics in laminar and turbulent flames. *Combustion and Flame*, 214:450–463, 2020. doi:10.1016/j.combustflame.2020.01.007.

[386] C. Wilke. A viscosity equation for gas mixtures. *The Journal of Chemical Physics*, 18 (4):517–519, 1950. doi:10.1063/1.1747673.

[387] F. A. Williams. *Combustion theory : the fundamental theory of chemically reacting flow systems*. Addison/Wesley Pub. Co, Redwood City, Calif, 1985. ISBN 9780201407778.

[388] T. A. Witten and L. M. Sander. Diffusion-Limited Aggregation, a Kinetic Critical Phenomenon. *Physical Review Letters*, 47(19):1400–1403, 1981. doi:10.1103/PhysRevLett.47.1400.

[389] M. Woo, R. T. Nishida, M. A. Schriefl, M. E. J. Stettler, and A. M. Boies. Open-source modelling of aerosol dynamics and computational fluid dynamics: Nodal method for nucleation, coagulation, and surface growth. *Computer Physics Communications*, 261: 107765, 2021. doi:10.1016/j.cpc.2020.107765.

[390] D. L. Wright. Numerical advection of moments of the particle size distribution in Eulerian models. *Journal of Aerosol Science*, 38(3):352–369, 2007. doi:10.1016/j.jaerosci.2006.11.011.

[391] D. L. Wright, R. McGraw, and D. E. Rosner. Bivariate Extension of the Quadrature Method of Moments for Modeling Simultaneous Coagulation and Sintering of Particle Populations. *Journal of Colloid and Interface Science*, 236(2):242–251, 2001. doi:10.1006/jcis.2000.7409.

[392] S. Wu and W. Yang. Comparisons of methods for reconstructing particle size distribution from its moments. *Fuel*, 252:325–338, 2019. doi:10.1016/j.fuel.2019.04.124.

[393] S. Wu, W. Wang, W. Tu, S. Yin, Y. Sheng, M. Y. Manuputty, M. Kraft, and R. Xu. Premixed Stagnation Flame Synthesized TiO_2 Nanoparticles with Mixed Phases for Efficient Photocatalytic Hydrogen Generation. *ACS Sustainable Chemistry and Engineering*, 6(11):14470–14479, 2018. doi:10.1021/acssuschemeng.8b03142.

[394] S. Wu, M. Y. Manuputty, Y. Sheng, H. Wang, Y. Yan, M. Kraft, and R. Xu. Flame Synthesized Blue TiO_2-x with Tunable Oxygen Vacancies from Surface to Grain Boundary to Bulk. *Small Methods*, page 2000928, 2020. doi:10.1002/smtd.202000928.

[395] L. Xie, Q. Liu, and Z.-H. Luo. A multiscale CFD-PBM coupled model for the kinetics and liquid–liquid dispersion behavior in a suspension polymerization stirred tank. *Chemical Engineering Research and Design*, 130:1–17, 2018. doi:10.1016/j.cherd.2017.11.045.

[396] Y. Xing, D. E. Rosner, Ü. Ö. Köylü, and P. Tandon. Morphological evolution of nanoparticles in diffusion flames: Measurements and modeling. *AIChE Journal*, 43 (S11):2641–2649, 1997. doi:10.1002/aic.690431307.

[397] Y. Xing, U. O. Koylu, and D. E. Rosner. In situ light-scattering measurements of morphologically evolving flame-synthesized oxide nanoaggregates. *Applied Optics*, 38 (12):2686–2697, 1999. doi:10.1364/AO.38.002686.

[398] Y. Xiong and S. E. Pratsinis. Formation of agglomerate particles by coagulation and sintering—Part I. A two-dimensional solution of the population balance equation. *Journal of Aerosol Science*, 24(3):283–300, 1993. doi:10.1016/0021-8502(93)90003-R.

[399] Y. Xu and M. D. Smooke. Application of a Primitive Variable Newton's Method for the Calculation of an Axisymmetric Laminar Diffusion Flame. *Journal of Computational Physics*, 104(1):99–109, 1993. doi:10.1006/jcph.1993.1012.

[400] Z. Xu, H. Zhao, and C. Zheng. Accelerating population balance-Monte Carlo simulation for coagulation dynamics from the Markov jump model, stochastic algorithm and GPU parallel computing. *Journal of Computational Physics*, 281:844–863, 2015. doi:10.1016/j.jcp.2014.10.055.

[401] Z. Xu, H. Zhao, and H. Zhao. CFD-population balance Monte Carlo simulation and numerical optimization for flame synthesis of TiO_2 nanoparticles. *Proceedings of the Combustion Institute*, 36(1):1099–1108, 2017. doi:10.1016/j.proci.2016.07.008.

[402] Y. Xuan and G. Blanquart. Two-dimensional flow effects on soot formation in laminar premixed flames. *Combustion and Flame*, 166:113 – 124, 2016. doi:10.1016/j.combustflame.2016.01.007.

[403] G. Yang, H. Zhuang, and P. Biswas. Characterization and sinterability of nanophase titania particles processed in flame reactors. *Nanostructured Materials*, 7(6):675–689, 1996. doi:10.1016/0965-9773(96)00033-5.

[404] Q. Yang, P. Zhao, and H. Ge. reactingFoam-SCI: An open source CFD platform for reacting flow simulation. *Computers and Fluids*, 190:114–127, 2019. doi:10.1016/j.compfluid.2019.06.008.

[405] E. K. Y. Yapp, D. Chen, J. Akroyd, S. Mosbach, M. Kraft, J. Camacho, and H. Wang. Numerical simulation and parametric sensitivity study of particle size distributions in a burner-stabilised stagnation flame. *Combustion and Flame*, 162(6):2569–2581, 2015. doi:10.1016/j.combustflame.2015.03.006.

[406] M. Yu and J. Lin. New scheme for implementing the method of moments with interpolative closure. *Aerosol Science and Technology*, 51(8):956–971, 2017. doi:10.1080/02786826.2017.1319566.

[407] M.-Z. Yu, J.-Z. Lin, and T.-L. Chan. Effect of precursor loading on non-spherical TiO_2 nanoparticle synthesis in a diffusion flame reactor. *Chemical Engineering Science*, 63 (9):2317–2329, 2008. doi:10.1016/j.ces.2007.11.008.

[408] C. Yuan and R. Fox. Conditional quadrature method of moments for kinetic equations. *Journal of Computational Physics*, 230(22):8216–8246, 2011. doi:10.1016/j.jcp.2011.07.020.

[409] C. Yuan, F. Laurent, and R. Fox. An extended quadrature method of moments for population balance equations. *Journal of Aerosol Science*, 51:1–23, 2012. doi:10.1016/j.jaerosci.2012.04.003.

[410] Y. Zeldovich. On the theory of combustion of initially unmixed gases. Technical Report NACA-TM-1296, National Advisory Committee for Aeronautics; Washington, DC, United States, 1951. https://ntrs.nasa.gov/archive/nasa/casi.ntrs.nasa.gov/19930093934.pdf.

[411] Y. Zeldovich and G. Barenblatt. Theory of flame propagation. *Combustion and Flame*, 3:61 – 74, 1959. doi:10.1016/0010-2180(59)90007-0.

[412] H. Zhang and J. F. Banfield. Thermodynamic analysis of phase stability of nanocrystalline titania. *Journal of Materials Chemistry*, 8(9):2073–2076, 1998. doi:10.1039/a802619j.

[413] H. Zhang and J. F. Banfield. Understanding Polymorphic Phase Transformation Behavior during Growth of Nanocrystalline Aggregates: Insights from TiO_2. *The Journal of Physical Chemistry B*, 104(15):3481–3487, 2000. doi:10.1021/jp000499j.

[414] H. Zhang and J. F. Banfield. Structural Characteristics and Mechanical and Thermodynamic Properties of Nanocrystalline TiO_2. *Chemical Reviews*, 114(19):9613–9644, 2014. doi:10.1021/cr500072j.

[415] Y. Zhang, S. Li, W. Yan, Q. Yao, and S. D. Tse. Role of dipole–dipole interaction on enhancing Brownian coagulation of charge-neutral nanoparticles in the free molecular regime. *The Journal of Chemical Physics*, 134(8):084501, 2011. doi:10.1063/1.3555633.

[416] B. Zhao, Z. Yang, M. V. Johnston, H. Wang, A. S. Wexler, M. Balthasar, and M. Kraft. Measurement and numerical simulation of soot particle size distribution functions in a laminar premixed ethylene-oxygen-argon flame. *Combustion and Flame*, 133(1–2): 173–188, 2003. doi:10.1016/S0010-2180(02)00574-6.

[417] B. Zhao, K. Uchikawa, J. R. McCormick, C. Y. Ni, J. G. Chen, and H. Wang. Ultrafine anatase TiO_2 nanoparticles produced in premixed ethylene stagnation flame at 1 atm. *Proceedings of the Combustion Institute*, 30(2):2569–2576, 2005. doi:10.1016/j.proci.2004.08.146.

[418] B. Zhao, K. Uchikawa, and H. Wang. A comparative study of nanoparticles in premixed flames by scanning mobility particle sizer, small angle neutron scattering, and transmission electron microscopy. *Proceedings of the Combustion Institute*, 31(1):851–860, 2007. doi:10.1016/j.proci.2006.08.064.

[419] H. Zhao and C. Zheng. A population balance-Monte Carlo method for particle coagulation in spatially inhomogeneous systems. *Computers and Fluids*, 71:196–207, 2013. doi:10.1016/j.compfluid.2012.09.025.

[420] H. Zhao, F. E. Kruis, and C. Zheng. Reducing Statistical Noise and Extending the Size Spectrum by Applying Weighted Simulation Particles in Monte Carlo Simulation of Coagulation. *Aerosol Science and Technology*, 43(8):781–793, 2009. ISSN 0278-6826, 1521-7388. doi:10.1080/02786820902939708.

[421] H. Zhao, X. Liu, and S. D. Tse. Effects of pressure and precursor loading in the flame synthesis of titania nanoparticles. *Journal of Aerosol Science*, 40(11):919–937, 2009. doi:10.1016/j.jaerosci.2009.07.004.

[422] H. Zhao, F. E. Kruis, and C. Zheng. A differentially weighted Monte Carlo method for two-component coagulation. *Journal of Computational Physics*, 229(19):6931–6945, 2010. doi:10.1016/j.jcp.2010.05.031.

[423] W.-N. Zhao, S.-C. Zhu, Y.-F. Li, and Z.-P. Liu. Three-phase junction for modulating electron–hole migration in anatase–rutile photocatalysts. *Chemical Science*, 6(6):3483–3494, 2015. doi:10.1039/C5SC00621J.

[424] W. Zhu and S. E. Pratsinis. Flame Synthesis of Nanosize Powders: Effect of Flame Configuration and Oxidant Composition. In G.-M. Chow and K. E. Gonsalves, editors, *Nanotechnology*, volume 622, pages 64–78. American Chemical Society, Washington, DC, Mar. 1996. ISBN 978-0-8412-3392-8 978-0-8412-1566-5. doi:10.1021/bk-1996-0622.ch004.

Appendix A

Additional verification cases

Analytical diffusion

This system considers a diffusion only system:

$$\frac{\partial \rho Y}{\partial t} = \nabla \cdot (\rho D \nabla Y)\,. \tag{A.1}$$

For an incompressible, 1D system with a constant diffusion coefficient, the equation reduces to:

$$\frac{\partial Y}{\partial t} = D\frac{\partial^2 Y}{\partial x^2}. \tag{A.2}$$

A 1D rod of length L has boundary and initial conditions of:

$$\begin{aligned} &Y(0,t) = 1, \\ &Y(L,t) = 0, \quad \text{and} \\ &Y(x,0) = 0. \end{aligned} \tag{A.3}$$

This problem has an analytical solution:

$$Y(x,t) = 1 - \frac{x}{L} - \frac{2}{\pi}\sum_{n=1}^{\infty}\frac{1}{n}\exp\left(-D\frac{n^2\pi^2}{L^2}t\right)\sin(\frac{n\pi x}{L}). \tag{A.4}$$

Figure A.1 shows this analytical solution compared to the implemented model. The results of the simulation agree very well with the analytical solution.

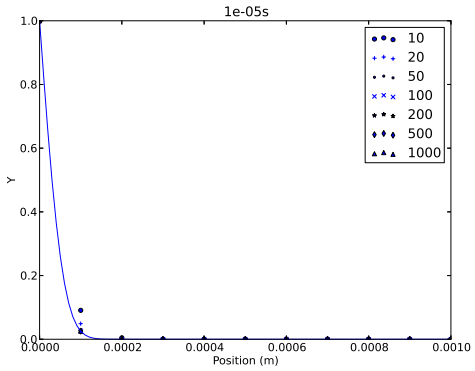

(a) Solution at $1E-5$ s

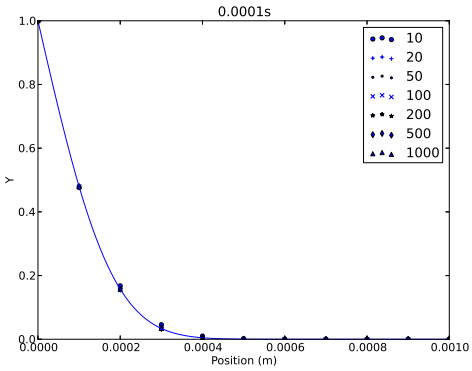

(b) Solution at $1E-4$ s

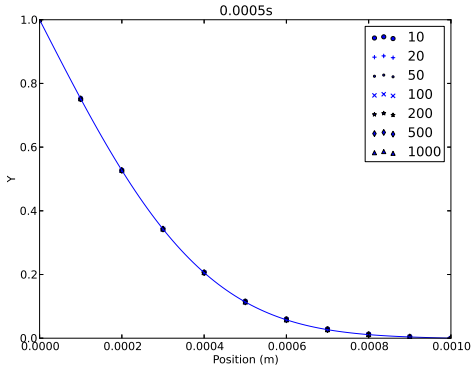

(c) Solution at $5E-4$ s

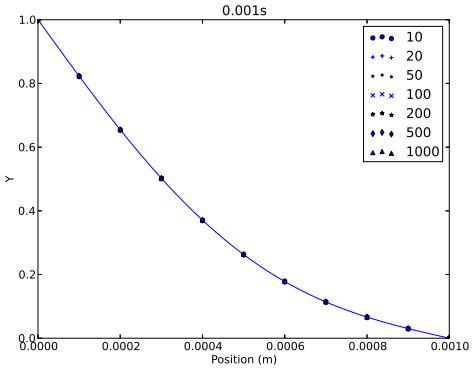

(d) Solution at $1E-3$ s

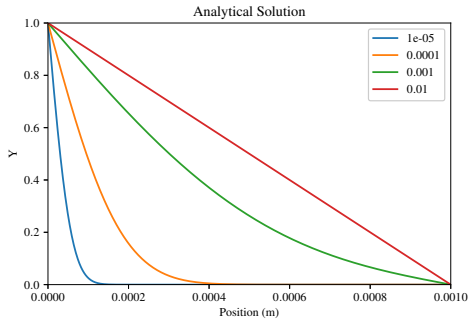

(e) The analytical solution at different times for $D = 0.0001$ and $L = 0.001$.

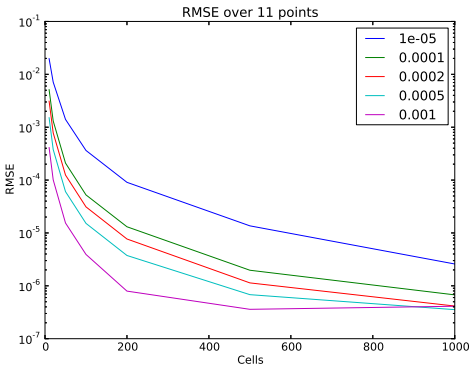

(f) The Root Mean Square Error of different times as a function of number of cells.

Fig. A.1 Diffusion test case compared to the analytical solution.

Isothermal, binary diffusion

This test case is a more complex version of the test case titled “isothermal binary diffusion with constant specific enthalpy” presented in Section 3.4.4.

Terms tested: III, λ

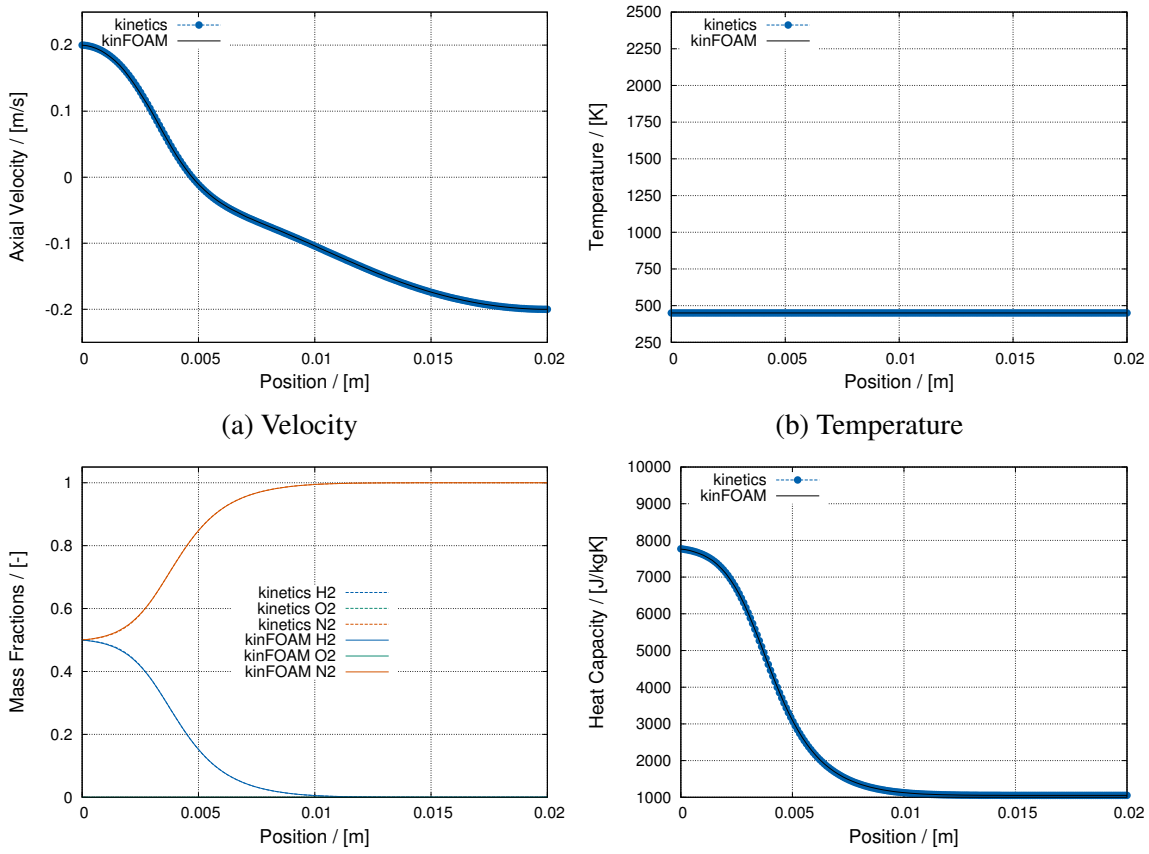

(a) Velocity

(b) Temperature

(c) Mass Fractions

(d) Heat Capacity

Fig. A.2 Centreline comparison between kinetics and ther new solver for isothermal, binary diffusion.

Isothermal, ternary diffusion with constant specific enthalpy

Terms tested: III, λ

Constant enthalpies removes term V from the enthalpy equation, retaining terms I – IV.

$$\left(\rho \sum_{j=1}^{N} c_{p_j} Y_j V_j^c\right) \nabla T = \underbrace{\left(\rho c_p \sum_{j=1}^{N} Y_j V_j^c\right)}_{\sum_j Y_j V_j^c = 0} \nabla T = 0$$

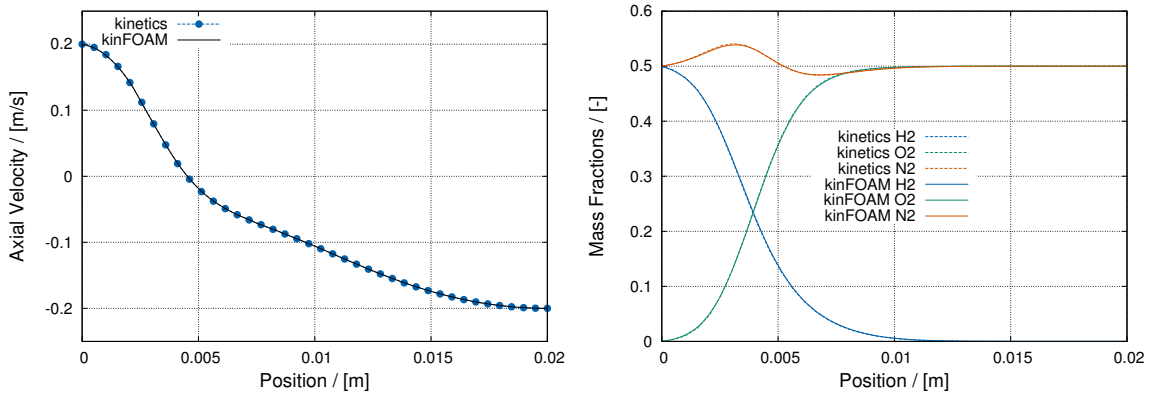

(a) Velocity (b) Mass Fractions

Fig. A.3 Centreline comparison between kinetics and the new solver for isothermal ternary diffusion with constant specific enthalpy.

Nonisothermal, ternary diffusion with constant specific enthalpy

No new terms tested, more complex version of test above.

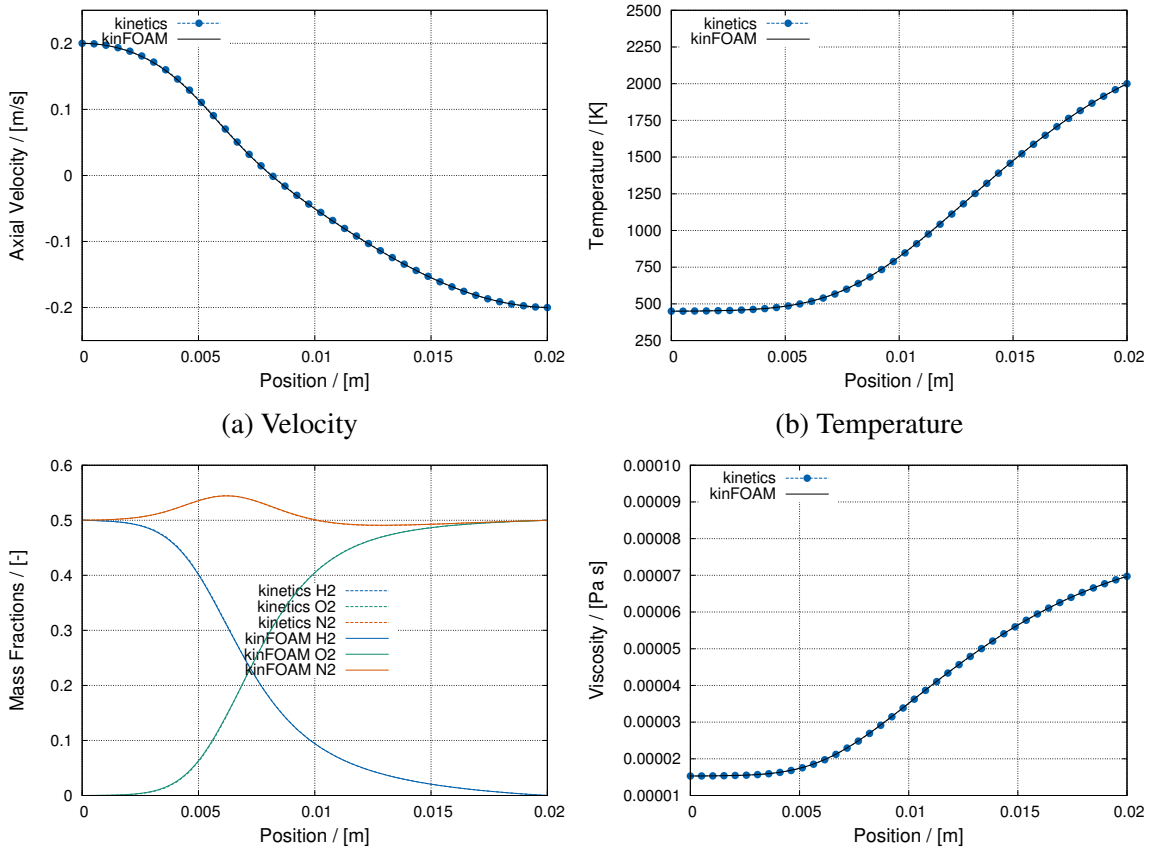

(a) Velocity

(b) Temperature

(c) Mass Fractions

(d) Viscosity

Fig. A.4 Centreline comparison between kinetics and the new solver for nonisothermal ternary diffusion with constant specific enthalpy.

Isothermal, ternary diffusion

Terms tested: III, λ

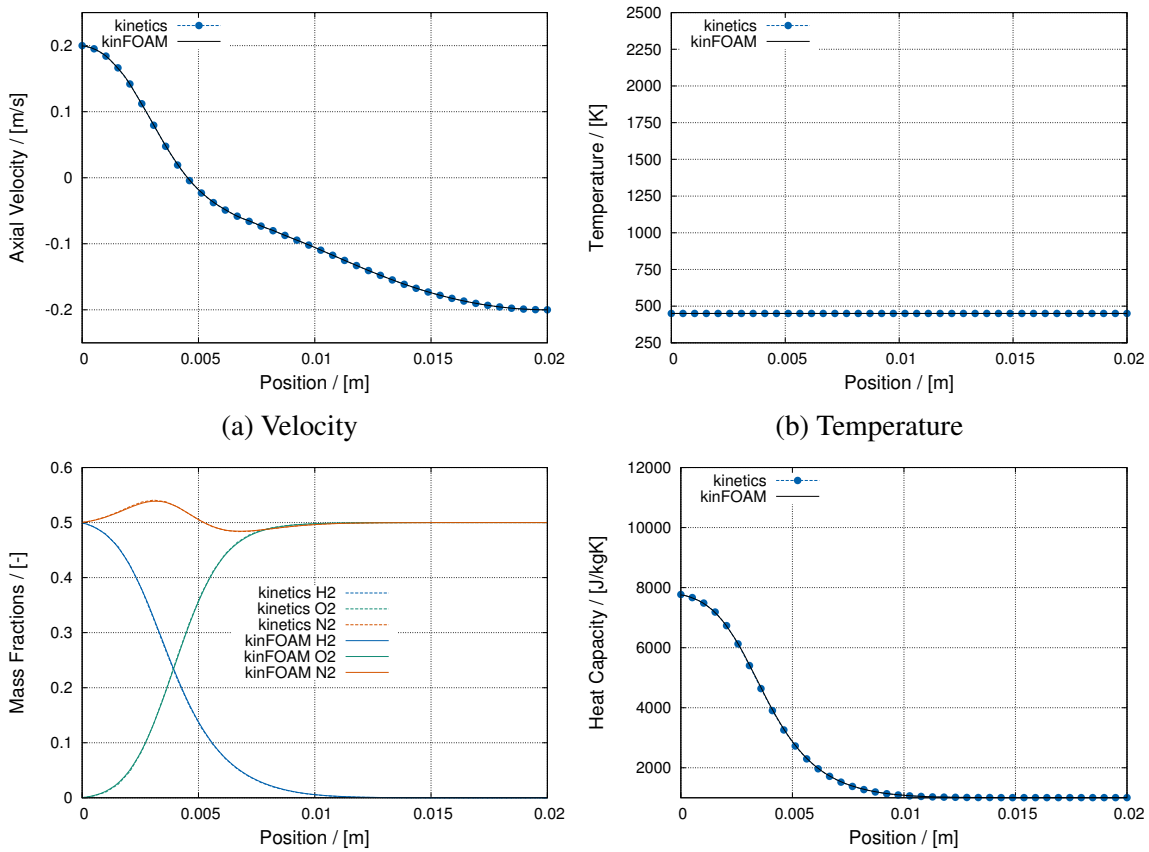

(a) Velocity

(b) Temperature

(c) Mass Fractions

(d) Heat Capacity

Fig. A.5 Centreline comparison between kinetics and the new solver for isothermal ternary diffusion.

Nonisothermal, ternary diffusion

No new terms tested, more complex version of test above.

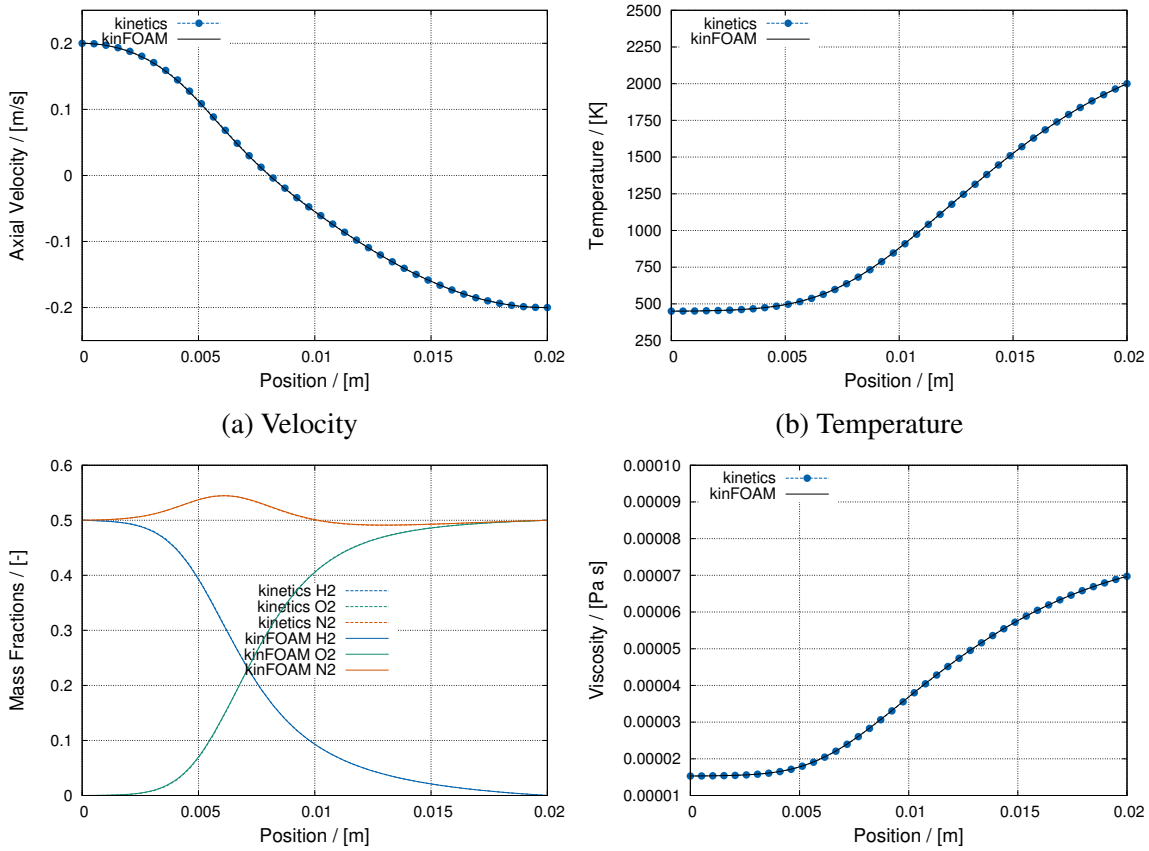

(a) Velocity

(b) Temperature

(c) Mass Fractions

(d) Viscosity

Fig. A.6 Centreline comparison between kinetics and the new solver for nonisothermal ternary diffusion.

Appendix B

Additional algorithms details

The following algorithms provide extra details to the abstraction in Algorithms 1 to 4.

Algorithm 5: Initialisation

Input : *k*inetics input file: `InputParams.xml`
mechanism file, thermodynamic file and transport file
OpenFOAM mesh files: boundary, faces, neighbour, owner and points
OpenFOAM dictionaries: controlDict, fvSchemes, fvSolution, flameDict
OpenFOAM time directory containing field values and boundary conditions

Result: Instances of the fields and chemical mechanism to be used by solver

`/* Initalise OpenFOAM mesh, time control, and solver instances by standard OpenFOAM macros */`

`InitialiseFOAM ()`

`/* Read in algorithm controls in flameDict: */`

`Read Algorithm Switches ()`

`/* Initialise kinetics */`

`InitialiseKinetics ()`

`/* Create instances of field variables: */`

create pointer lists of fields for mass fractions, Y_i; mole fractions, X_i; diffusion coefficients, D_i, diffusion velocities, YV_i; source terms, $\dot{\omega}_i$; and heat capacities, $c_{\mathrm{p},i}$

foreach species i **do**
  allocate or read from file Y_i, X_i, D_i, YV_i, $\dot{\omega}_i$, $c_{\mathrm{p},i}$
end

calculate average molecular weight, W

`/* Read in flow variables */`

read pressure field, p; temperature field, T; and velocity flow field, U

calculate density field, ρ, from W, p, and T using ideal gas law

create compressibility field, $\psi = \rho/p$

create diffusion correction velocity field, V_c, and particle thermophoretic field, V_T

create enthalpy flux field

create advective flux surface field, ϕ

create or read thermophysical fields: μ, λ, c_p, $\dot{\omega}_\mathrm{T}$

if $\mathrm{N}_{\mathrm{mom}} > 0$ **then**
  create pointer lists of fields for moments, M_j; specific moments, $\hat{M}_j$; $j-\frac{2}{3}$ moment fields, $\hat{M}_{j-\frac{2}{3}}$; source term field, $\dot{\omega}_j$.
  foreach moment j **do**
    allocate or read from file M_j, $\hat{M}_j$, $\hat{M}_{j-\frac{2}{3}}$, $\dot{\omega}_j$
  end
end

update mole fraction fields

Algorithm 6: Initialisation Cont.

```
/* Create instances of OpenFOAM classes and solvers                    */
Function InitialiseFOAM ()
    #include "setRootCase.H";
    #include "createTime.H";
    #include "createMesh.H";
    #include "createControl.H";
    #include "createTimeControls.H";
    #include "initContinuityErrs.H";
/* Read switches of algorithm control and inert species                */
Function Read Algorithm Switches ()
    read in switches: solveFlow, solveTemperature, solveSpecies, solveMoments
    read in switches: holdTransportConstant, integrateChemistry, solveChemistryOnce
    read in scalar: Temperature lower bound for reactions to occur, T_L
    read in word: InertSpecies
/* Launch kinetics API                                                 */
Function InitialiseKinetics ()
    initialise kinetics API (gas phase mechanism and PBE model)
    retrieve N_sp; N_mom; and number of unknowns, N_unknown = N_sp + N_mom + 1
    initialise constants: R_g, k_B, N_A
    retrieve species names (in order)
    retrieve species molecular weights
```

Algorithm 7: Update Transport

Input scalars fields : pressure, p; temperature, T; mole fractions fields, X_i; average molecular weight, W; moments, M_j; and $j-\frac{2}{3}$ moments, .

Output : updated transport property fields

`/* Update Internal Field Values */`

foreach *cell* **do**

$T_{cell} \leftarrow T[cell]$ $\rho_{cell} \leftarrow \rho[cell]$ $p_{cell} \leftarrow p[cell]$ $W_{cell} \leftarrow W[cell]$

foreach species i **do**

$\phi[i] \leftarrow X_i[cell]$

end

foreach moment j **do**

$\phi_{\mathrm{M}}[j] \leftarrow M_j[cell]$

end

$\mu[cell] \leftarrow$Get Viscosity$(\phi_{\mathrm{X}}, T_{cell})$

$\lambda[cell] \leftarrow$Get Thermal Conductivity(ϕ_{X}, T_k)

$C_{\mathrm{p}}[cell] \leftarrow$Get Heat Capacity$(\phi_{\mathrm{X}}, T_k)$

$D_{\mathrm{mix}} \leftarrow$ Get Mixture Averaged Diffusion Coeff $(\phi_{\mathrm{X}}, T_k, p_k)$

`/* Map values to fields: */`

foreach species i **do**

$D_i[cell] \leftarrow D_{mix}[i]$

end

`/* Interpolate moment fields: */`

$moments_{j-\frac{2}{3}} \leftarrow$Get Interpolated Moments (ϕ_{M})

foreach moment j **do**

$\hat{M}_{j-\frac{2}{3}}[cell] \leftarrow moments_{j-\frac{2}{3}}/rho_{cell}$

end

end

repeat the above process for the boundary faces

calculate thermophoretic velocity, V_{T} (Eqn. 3.32)

calculate particle diffusion coefficient, $D_{\mathrm{p_1}}$ (Eqn. 3.29)

Algorithm 8: Particle selection algorithm with particle-number/particle model

Input : $z_{\mathbb{X}}(t)$, $z_{\mathbb{M}}(t)$, selection criterion 'choose according to property σ'
Output : Selected particle P_i

Define the sums of properties in each space (note these properties are cached):

$$\Sigma_{\mathbb{M}} \leftarrow \sum_{i=1}^{N_{\text{thresh}}} N_i \sigma_i; \qquad \Sigma_{\mathbb{X}} \leftarrow \sum_{i=1}^{N(t)} \sigma(P_i); \qquad \Sigma_{\text{total}} \leftarrow \Sigma_{\mathbb{M}} + \Sigma_{\mathbb{X}}$$

Choose a uniform random number: $\alpha \sim \mathrm{U}(0,1)$
Set $\gamma \leftarrow \alpha \Sigma_{\text{total}}$
if $\gamma \leq \Sigma_{\mathbb{M}}$ **then**
    `/* Select index` i `from particle-number list` $z_{\mathbb{M}}$ `*/`
    $j \leftarrow 1$
    while $j \leq N_{thresh}$ **do**
        if $\gamma \leq (N_j \sigma_j)$ **then**
            $i \leftarrow j$
        else
            $\gamma \leftarrow (\gamma - N_j \sigma_j)$
            $j \leftarrow (j+1)$
    Create the new particle P_i (Clone the particle with index i from reference particles)
else
    `/* Select particle` P_i `from particle ensemble` $z_{\mathbb{X}}$ `*/`
    $\gamma \leftarrow \alpha \Sigma_{\text{total}} - \Sigma_{\mathbb{M}}$
    $j \leftarrow 1$
    while $j \leq N(t)$ **do**
        if $\gamma \leq \sigma(P_j)$ **then**
            $i \leftarrow j$
        else
            $\gamma \leftarrow (\gamma - \sigma(P_j))$
            $j \leftarrow (j+1)$
    Use the ensemble particle P_i

Algorithm 9: Ballistic cluster-cluster algorithm with a random impact parameter

Input: Particles $P_q, P_r \in (\mathbb{M} \cup \mathbb{X})$ and chosen for coagulation.
Output: Daughter particle $P_s \in \mathbb{X}$.

begin
- Randomly rotate P_q and P_r around their centres of mass (using Ref. [13])
- Calculate the bounding spheres $r_\mathrm{b}(P_q)$ and $r_\mathrm{b}(P_r)$ (using Ref. [294])
- Centre the bounding spheres
- **repeat**
  - `/* Determine random trajectory */`
  - Uniformly select a point $H_1(\theta, \phi)$ on a unit sphere:

$$\phi = 2\pi U \quad \text{and} \quad \theta = \arccos(2U - 1),$$

    where U is a uniformly distributed random variable;
  - Construct a rotation matrix $\mathbf{R}$ that rotates the vector $(0,0,-1)$ to the point H_1;
  - `/* Determine random impact parameter */`
  - Uniformly select a point:

$$H_2 = (R\sqrt{r}\cos\theta, R\sqrt{r}\sin\theta, -R),$$

    on a disk of radius $R = r_\mathrm{b}(P_q) + r_\mathrm{b}(P_r)$ centred on $(0,0,-R)$ in the $z = -R$ plane with $r = U$, and $\theta = 2\pi U$, where U is a uniformly distributed random variable;
  - `/* Set initial positions */`
  - Apply the rotation to H_2 giving a new point $G = \mathbf{R}H_2$;
  - Place particle P_r at point G;
  - Place particle P_q at $O = (0,0,0)$;
  - `/* Perform the collision */`
  - **while** *No point of contact* **do**
    - Translate P_r along a vector parallel to H_1O by distance $R/100$;
    - Check for contact;
    - **if** *P_r has passed through the bounding sphere of P_q* **then**
      - `/* This is an unsuccessful collision */`
      - Break;
  - **if** *Single point of contact* **then**
    - `/* This is a successful collision */`
    - New particle P_s created by connecting the binary trees of P_q and P_r at a new head node;
    - Contacting primaries p_i and p_j connected at the new head node;
    - **return** *New particle P_s*
- **until** *Successful collision*

Algorithm 10: Surface growth

Input: Particle $P_q \in \mathbb{X}$; Number of units of TiO_2 added n
Output: Particle $P_q \in \mathbb{X}$
begin

Select a primary p_i in particle P_q with probability

$$P(p_i) = \frac{A_i}{\sum_{j=1}^{n_\mathrm{p}(P_q)} A_j};$$

Save old volume and radius: $v_{i,\mathrm{old}} \leftarrow v_i$ and $r_{i,\mathrm{old}} \leftarrow r_i$;
Update primary composition: $\eta_i \leftarrow \eta_i + n$;
Calculate new volume, v_i;
while $v_{i,\mathrm{old}} < v_i$ **do**
`/* Primary radius increased in 1% increments */`
$\Delta r \leftarrow r_i/100$;
$\Delta v \leftarrow A_i \Delta r$;
if $v_{i,old} + \Delta v > v_i$ **then**

$$\Delta r \leftarrow \frac{(v_i - v_{i,\mathrm{old}})}{\Delta v} \Delta r;$$

Increase radius: $r_i \leftarrow r_i + \Delta r$;
Update free surface area, A_i;
$v_{i,\mathrm{old}} \leftarrow v_{i,\mathrm{old}} + \Delta v$;
`/* Redistribution of composition between neighbours */`
foreach Neighbour p_j of p_i **do**
Estimate change in volume of p_j:

$$\Delta v_j \leftarrow -A_{\mathrm{n},ij} \frac{r_{i,\mathrm{old}}}{d_{ij}} \left(r_i - r_{i,\mathrm{old}}\right);$$

Calculate (integer) change in composition of p_j:

$$\Delta \eta_j \leftarrow \frac{\Delta v_j}{M_{\mathrm{TiO_2}} / \left(\rho_{\mathrm{TiO_2}} N_\mathrm{A}\right)},$$

rounded down to the nearest integer;
if $|\Delta \eta_j| > 0$ **then**
Update the composition of p_j: $\eta_j \leftarrow \eta_j + \Delta \eta_j$;
Update the composition of p_i: $\eta_i \leftarrow \eta_i - \Delta \eta_j$;
return P_q

Algorithm 11: Sintering

Input: Particle $P_q \in \mathbb{X}$; Time to sinter particle t_{sint}
Output: Particle $P_q \in \mathbb{X}$

begin

foreach *Neck between two primaries* p_i *and* p_j *in particle* P_q **do**

$\Delta d_{ij,\max} \leftarrow d_{ij}/100$;

$t \leftarrow 0$;

while $t < t_{\text{sint}}$ **do**

Calculate sintering rate: $\frac{\mathrm{d}d_{ij}}{\mathrm{d}t}$ (Eq. 3.106);

Calculate time step:

$$\Delta t \leftarrow \frac{\Delta d_{ij,\max}}{\frac{\mathrm{d}d_{ij}}{\mathrm{d}t}};$$

if $t_{\text{sint}} > t + \Delta t$ **then**

$$\mu \leftarrow 100;$$

else

$$\mu \leftarrow 100\frac{(t_{\text{sint}} - t)}{\Delta d_{ij,\max}}\frac{\mathrm{d}d_{ij}}{\mathrm{d}t};$$

Generate a Poisson random variate X with mean μ;

Calculate change in separation:

$$\Delta d_{ij} = -\frac{X}{100}\Delta d_{ij,\max};$$
$$\Delta \mathbf{d}_{ij} = -\Delta d_{ij}\frac{\mathbf{x}_j - \mathbf{x}_i}{|\mathbf{x}_j - \mathbf{x}_i|};$$

Adjust centre to centre separation: $d_{ij} \leftarrow d_{ij} + \Delta d_{ij}$;

`/* Only need to adjust the coordinates of primaries on one side of the neck, in this case` p_i`. */`

Translate primary p_i: $\mathbf{x}_i \leftarrow \mathbf{x}_i + \Delta \mathbf{d}_{ij}$;

`Translate neighbours` (p_i; p_j; $\Delta \mathbf{d}_{ij}$);

Compute change in radii using Eq. (3.108): Δr_i and Δr_j;

`Adjust connectivity` (p_i; p_j; Δr_i);

`Adjust connectivity` (p_j; p_i; Δr_j);

Update primary radii:

$$r_i \leftarrow r_i + \Delta r_i$$
$$r_j \leftarrow r_j + \Delta r_j$$

Update properties of primaries p_i and p_j;

$t \leftarrow t + \Delta t$;

if *Coalescence condition is met* **then**

Merge primaries p_i and p_j;

Break;

Algorithm 11: Sintering Cont.

`/* Translates all the neighbours of a primary` p_i `by` $\Delta \mathrm{d}_{ij}$`, except for neighbour` p_j `*/`

Function `Translate neighbours` (Primary p_i; Neighbour p_j; Translation $\Delta\mathbf{d}$)

  foreach *Neighbour* p_k *of* p_i*, except for primary* p_j **do**

    Translate p_k by $\Delta\mathbf{d}$;

$$\mathbf{x}_k \leftarrow \mathbf{x}_k + \Delta\mathbf{d};$$

    `/* Recursively translate the neighbours of` p_k`, except for primary` p_i `*/`

    `Translate neighbours` (Primary p_k; Neighbour p_i; Translation $\Delta\mathbf{d}$);

`/* Update centre to centre separations and coordinates of neighbours` p_k `of primary` p_i `except for neighbour` p_j `*/`

Function `Adjust connectivity` (Primary p_i; Neighbour p_j; Δr_i)

  foreach *Neck between primary* p_i *and neighbour* p_k*, except for primary* p_j **do**

    Calculate change in separation (Eq. 3.109):

$$\Delta d_{ik} = \frac{r_i}{x_{ik}} \Delta r_i;$$

$$\Delta\mathbf{d}_{ik} = \Delta d_{ik} \frac{\mathbf{x}_k - \mathbf{x}_i}{|\mathbf{x}_k - \mathbf{x}_i|};$$

    Translate neighbour to update centre to centre separation:

$$d_{ik} \leftarrow d_{ik} + \Delta d_{ik};$$

$$\mathbf{x}_k \leftarrow \mathbf{x}_k + \Delta\mathbf{d}_{ik};$$

    `Translate neighbours` (Primary p_k; Neighbour p_i; Translation $\Delta\mathbf{d}_{ik}$);

Algorithm 12: Coalescence

Input: Particle $P_q \in \mathbb{X}$; Primaries p_i and p_j to merge
Output: Particle $P_q \in \mathbb{X}$ with merged primary $p_{i,\text{new}}$
`/* Assume that` p_i `is the larger primary:` $r_i > r_j$ `*/`
begin

Solve Eq. 3.114 for the new merge primary radius of $r_{i,\text{new}}$;
Update the composition of p_i: $\eta_{i,\text{new}} = \eta_i + \eta_j$;
foreach *Neck between* p_i *and neighbour* p_k *except* p_j **do**

$$x_{ki} = \frac{d_{ik}^2 - r_i^2 + r_k^2}{2d_{ik}};$$
$$\Delta d_{ik} = \max\left(x_{ki} \pm \sqrt{x_{ki}^2 - r_k^2 + r_{i,\text{new}}}\right) - d_{ik};$$
$$\Delta \mathbf{d}_{ik} = \Delta d_{ik} \frac{\mathbf{x}_k - \mathbf{x}_i}{|\mathbf{x}_k - \mathbf{x}_i|};$$

Translate neighbour p_k:

$$d_{ik} \leftarrow d_{ik} + \Delta d_{ik};$$
$$\mathbf{x}_k \leftarrow \mathbf{x}_k + \Delta \mathbf{d}_{ik};$$

`Translate neighbours` (Primary p_k; Neighbour p_i; Translation $\Delta \mathbf{d}_{ik}$);
`/* The function Translate neighbours is defined in Algorithm 11 */`

foreach *Neck between* p_j *and neighbour* p_l *except* p_i **do**

$$x_{lj} = \frac{d_{jl}^2 - r_j^2 + r_k^2}{2d_{jl}};$$
$$\Delta d_{il} = \max\left(x_{lj} \pm \sqrt{x_{lj}^2 - r_l^2 + r_{i,\text{new}}}\right) - d_{il};$$
$$\Delta \mathbf{d}_{il} = \Delta d_{il} \frac{\mathbf{x}_l - \mathbf{x}_i}{|\mathbf{x}_l - \mathbf{x}_i|};$$

Translate neighbour p_l:

$$d_{il} \leftarrow d_{il} + \Delta d_{il};$$
$$\mathbf{x}_l \leftarrow \mathbf{x}_l + \Delta \mathbf{d}_{il};$$

`Translate neighbours` (Primary p_l; Neighbour p_j; Translation $\Delta \mathbf{d}_{il}$);

$r_i \leftarrow r_{i,\text{new}}$;
Remove primary p_j and restructure binary tree
Update particle properties
return P_q

Algorithm 13: TEM images

Input: Ensemble Q; Frame size $2a \times 2b$; Particles per frame N; Number of images n
Output: n TEM images
begin
    for *n frames* **do**
        for *N particles* **do**
            Uniformly select a particle P_q from ensemble Q;
            Randomly rotate P_q around its centres of mass using the method descibed by Arvo [13];
            Generate (x, y) coordinates uniformly in the image plane with $-a \leq x \leq a$ and $-b \leq y \leq b$;
            Position P_q in the image plane with its centre of mass at (x, y);
            Project P_q into the image plane;
            Remove P_q from the ensemble;

Appendix C

Nozzle design

C.1 Introduction

Nozzles are responsible for delivering premixed reactants to a flame in various burner configurations for various fundamental studies of flame chemistry [353], carbonaceous soot growth [416], and inorganic nanoparticle synthesis [216] . For both experimental and computational studies, it is important to have stable and well characterised flows at the nozzle outlets. Therefore, the design of the nozzle contraction profile needs to be such that it will not cause flow instabilities, such as flow separation or Görtler vorticies [306], and should aim to minimise the boundary layer at the nozzle outlet to create the most uniform flow profile over the outlet area. Commonly, designs are analyzed using theory on boundary layer stability and approximations of Thwaites' method [382], and can be most closely seen in wind tunnel design [24] and a handful of nozzle designs for flame applications [81, 26, 361]. A brief introduction to Thwaites' method and a summary of literature follows.

Thwaites' boundary layer approximations are a one-parameter integral method based on a momentum-integral relation of which derivations exist for both plane flow and axisymmetric flow [382]. The approach of T. von Karman was used to reach the so-called Karman momentum integral relation [382]. Thwaites multiplied the equation by a Reynolds number based on the boundary layer thickness and parameterised by a single parameter, the Holstein-Bohlen parameter λ. The single parameter relationships can be used to find boundary layer thickness, displacement thickness to within 5% error.

Design of low speed, laminar wind tunnels share the same objectives as nozzle design: stable and uniform flow profiles. For many years, these designs were empirical and by-eye, relying on heuristics, and rely on upstream meshes for turbulence management with low pressure drop. Two design methods exist and differ by what you prescribe. The nozzle shape can be found by prescribing the axial velocity distribution and solving the stream function equation, taking a

streamline of choice to be the nozzle shape. Alternatively, you can assign inlet and outlet radius along with an outlet velocity and parametrise the contraction with various functions. The shapes of the contractions traditionally fall into one of four families parameterised by scaled lengths: matched cubic polynomials, a third, fifth, or seventh order polynomial [24]. These shapes were compared using a potential flow code coupled to Thwaites' method for boundary layer analysis and the fifth order polynomial was found to give the best results without experiencing flow separation [24]. Due to the complexity of the fifth order polynomial, a transformation was proposed for use in design optimization [44]. The transformation allows you to change the shape using an arbitrary continuous function over the range of 0 to 1 while still maintaining zero values of the first and second derivative at the inlet and outlet. This transformation was used in a potential flow with Thwaites' method solver (similar to [24]) with a variety of arbitrary functions ranging from a constant to a cubic function and it was found that there were no significant advances over the polynomial [80].

Optimizing subsonic nozzles has been performed in literature for turbulent flame studies [81], laminar impinging flames [29, 26], and high pressure, laminar flames [361]. These works solve for the nozzle shape by fixing the boundary conditions and varying the remaining degrees of freedom to change the nozzle shape. Thwaites' method is used to solve for the boundary layer thickness and flow profiles. To extend the method to high pressure gradient flows, a piecewise function is used to make use of work that extended the shape factor relationship to highly favorable pressure gradients, thus introducing an additional term into the momentum thickness relationship[361]. Several criterion are considered to determine a superior design with different emphasis on each criterion used in each work. The first criterion is to minimise the Görtler instabilities for flow over concave surfaces by ensuring the Görtler parameter is below its transition value of 53 [306]. A second criterion is to ensure the displacement-thickness-based Reynolds number is below its critical value along the length of the nozzle [361]. A third criterion is that the shear stress must be monotonically increasing along the length of the nozzle [81].

In this thesis, a seventh order polynomial is used to describe the nozzle as a function of length for a given nozzle length and diameters. Thwaites' method is used to predict boundary layer thickness and displacement thickness of the resulting boundary layer. The Görtler parameter is minimised along the boundary layer by varying the two degrees of freedom and is kept below the critical value of 53. The displacement-thickness-based Reynolds number is kept below the critical value along the length of the nozzle. An alternative design that consists of two arcs connected by a straight line is proposed as it can be produced in-house. Two different lengths and outlet diameters are tested for a set inlet diameter. Inert and reactive computational

fluid dynamic simulations of impinging flows are used to explore the designs. The alternative designs are found to perform equally as well as the optimised designs for the conditions studied.

C.2 Nozzle design

C.2.1 Design method

The interior shape of the nozzle must be designed to minimise hydrodynamic instabilities, namely the Taylor-Görtler vortices in the concave region of the nozzle. The transition for these vortices occur when the Görtler parameter, Equation C.1, exceeds 53 [195]. G is the Görtler parameter, Re_θ is the Reynolds number based on the boundary layer thickness, θ, and r'' is the second derivative of the nozzle shape. The boundary layer thickness is approximated using a one-parameter integral method based on a momentum-integral relation, Thwaites' method for axisymmetric flows [382]:

$$G = -Re_\theta^2 \theta r'' . \tag{C.1}$$

The nozzle shape was described by a 7^{th} order polynomial with the following six boundary conditions (Equation C.2), leaving two degrees of freedom, following the work in Bergthorson [26] and Versailles and Bergthorson [361]. The inlet radius, r_0, was constant due to the upstream system. The nozzle exit length, x_e, and exit radius, r_e, are design constants.

$$\begin{aligned} r(0) &= r_0 & r(x_e) &= r_e \\ r'(0) &= 0 & r'(x_e) &= 0 \\ r''(0) &= 0 & r''(x_e) &= 0 \end{aligned} \tag{C.2}$$

The two degrees of freedom can be described using two fixed points (Equation C.3), or a fixed inflection point at a fixed height (Equation C.4). In this work, Equation C.3 was used as the two degrees of freedom.

$$r(x_1) = r_1, \quad r(x_2) = r_2 \tag{C.3}$$

$$r(x_1) = r_1, \quad r''(x_1) = 0 \tag{C.4}$$

The system of linear equations is solved to find the coefficients of the nozzle polynomial. The contour is used to approximate the boundary layer thickness, θ, using Thwaites'

method [382]. An iterative optimiser was used to pick a contour that minimised G across the nozzle.

Four nozzle designs were chosen to be considered and optimised for $r_0 = 2.5$ cm and a desired outlet velocity of 3 m/s:

- Design A: x_e = 10cm, r_e = 0.5 cm
- Design B: x_e = 7.2cm, r_e = 0.5 cm
- Design C: x_e = 10cm, r_e = 0.7 cm
- Design D: x_e = 7.2cm, r_e = 0.7 cm

These designs correspond to contraction ratios of 25 and 12.76 and length ratios ($x_e/2 * r_0$) of 1.44 and 2, falling within wind tunnel heuristics [24]. All four designs did not get close to reaching the transition threshold of $G = 53$, indicating that Görtler vortices are not a significant concern at these flow rates.

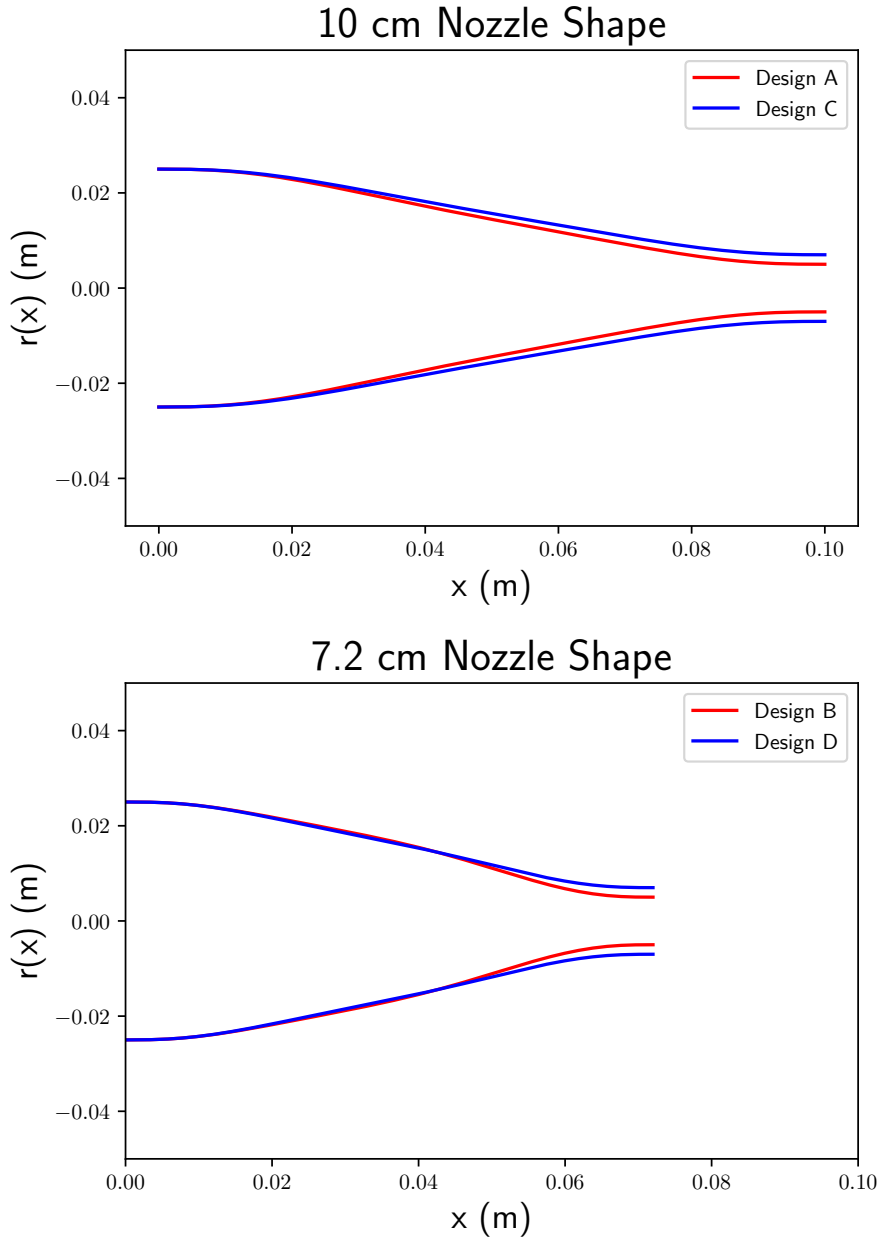

Fig. C.1 A comparison between different nozzle designs for two different exit radii and lengths.

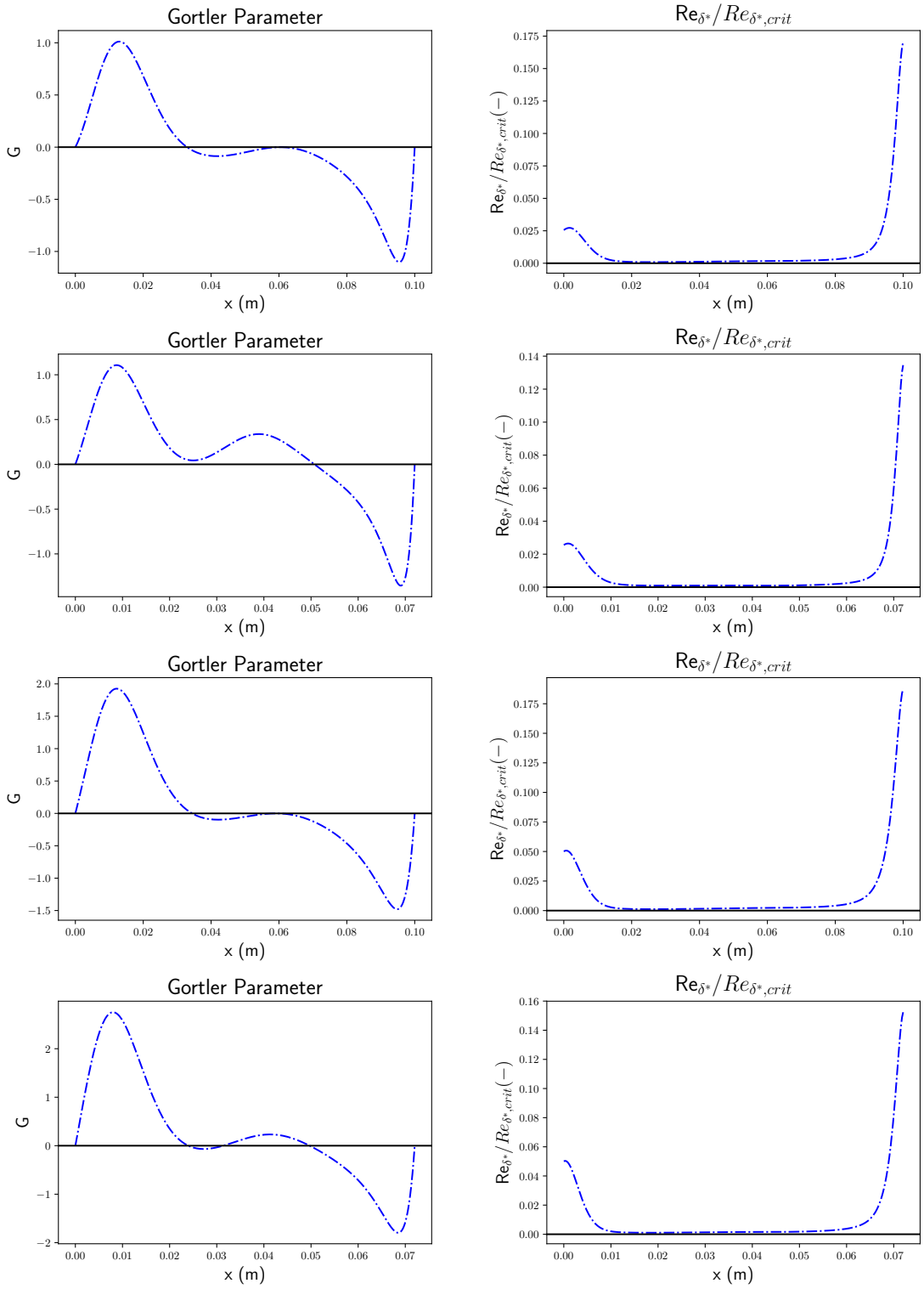

Fig. C.2 A comparison of Görtler parameters and the ratio of displacement-thickness based Reynolds number with its critical value for different nozzle designs.

C.2.2 Simplified design

A *simplified* design can be considered instead of a complex polynomial: a piecewise function of a straight line nozzle smoothed by two arcs connected by continuous first derivatives. For a given R_{inlet} and R_{outlet}, the design can be varied by changing the slope of the straight region, described by the angle between it and the horizontal entrance region walls, α, and the two radii of curvature of the arcs, R_1 and R_2. The nozzle length is determined as a consequence of these parameters. The primary advantage of such a design is its simplicity, specifically from a manufacturing and cost perspective, as the simple geometry is less complicated to produce.

Four designs are considered to predict the effect of such simplification that match the R_{inlet} and R_{outlet} of the detailed designs above: with $R_1 = R_2 = R_{inlet}$, α is varied to match the nozzle lengths.

- 1cm Diameter Outlet
  - $\alpha = 17.2475°$, $R_{\text{arc},1} = R_{\text{arc},2} = R_{\text{inlet}}$ for 7.2 cm nozzle
  - $\alpha = 11.915°$, $R_{\text{arc},1} = R_{\text{arc},2} = R_{\text{inlet}}$ for 10 cm nozzle
- 1.4cm Diameter Outlet
  - $\alpha = 15.425°$, $R_{\text{arc},1} = R_{\text{arc},2} = R_{\text{inlet}}$ for 7.2 cm nozzle
  - $\alpha = 10.69°$, $R_{\text{arc},1} = R_{\text{arc},2} = R_{\text{inlet}}$ for 10 cm nozzle

C.2.3 Improvements

Two possible points of improvement for future work could be to address the following:

Polynomial Shape Design An improvement would be to use Brassard and Ferchichi's transformation [44] to use the fifth order polynomial, which was shown to have better performance and less risk of separation for wind tunnels [237].

Objective Function Optimise by minimising the boundary layer thickness at the exit.

C.3 Cold Flow Calculations

The four designs in Section C.2 were modelled in an incompressible solver with the PISO-SIMPLE algorithm in OpenFOAM [343]. The axisymmetric system contained a region upstream of the nozzle, the optimised nozzle wall, a coflow jet, a stagnation surface, an open entrained boundary and a pressure outlet.

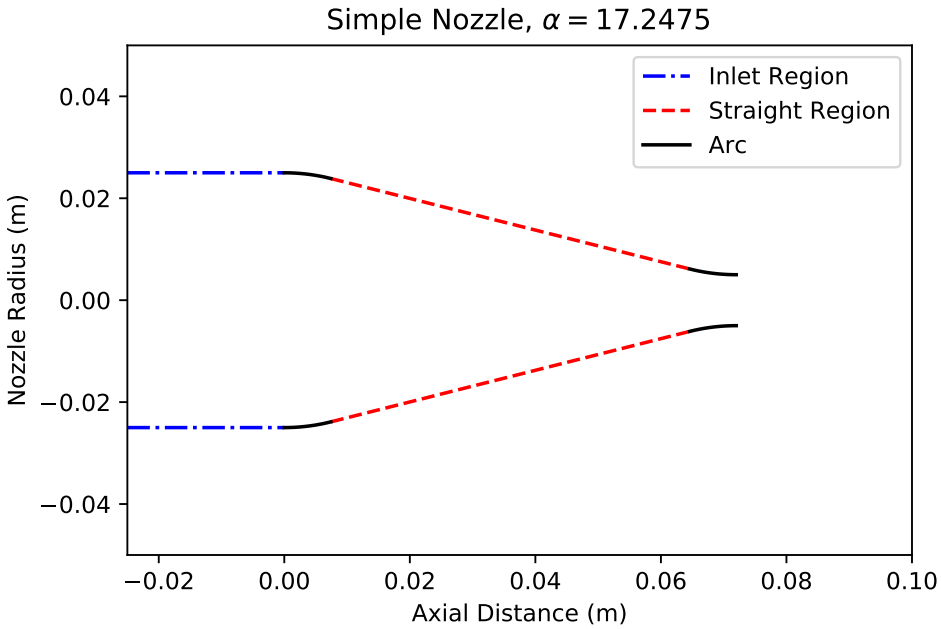

Fig. C.3 An example of a simple nozzle design ($\alpha = 17.2475°$, $R_{arc,1} = R_{arc,2} = R_{inlet}$) of arcs and a straight line.

Table C.1 Number of cells used in each mesh for nozzle design studies.

Level	Simple	Polynomial
0	24350	25975
1	65275	56950
2	87300	177900
3	261100	571800

Three mass flow rates were simulated at two temperatures, 398K and 423K; and three nozzle-to-plate separation distances, H, as a proportion of nozzle diameter, D, at $0.7D$, D, and $1.5D$. These bound common experimental conditions and correspond to the transition from free jet ($H \geq 1.5D$) to the stagnation pressure propagating up the nozzle ($H \leq 0.7D$) [29].

C.3.1 Grid independence

The level of refinement was studied to ensure a grid independent solution. Four levels were studied and the axial velocity distribution is compared in Figure C.4. No significant improvements are seen beyond level 1, and thus level 1 is used for simulations.

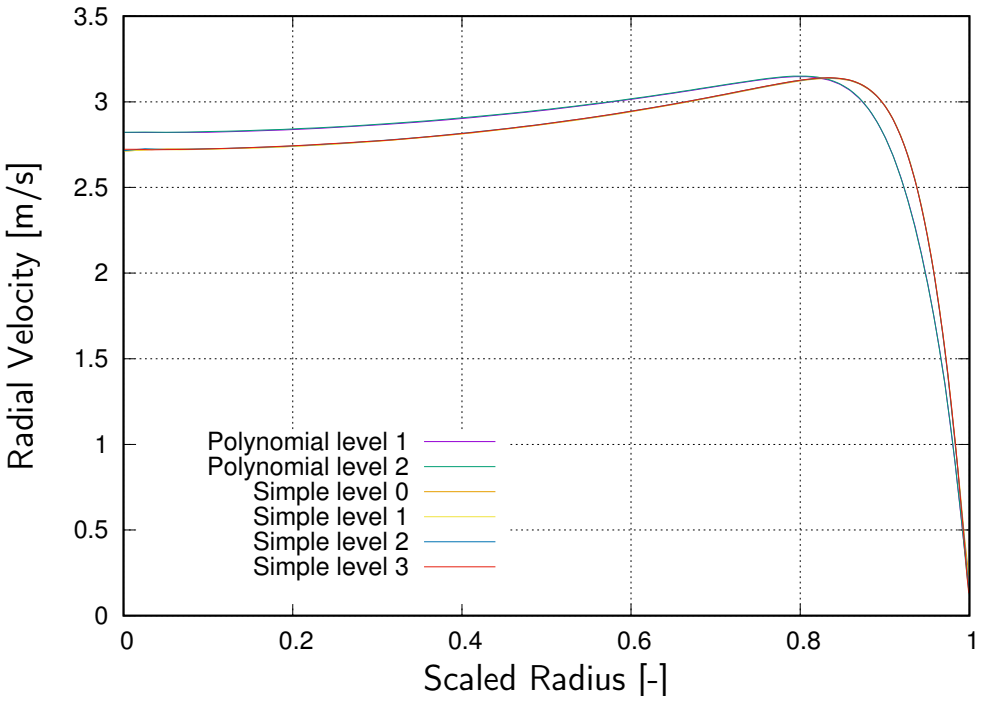

Fig. C.4 Additional grid refinement showed negligable difference in solution.

C.3.2 Polynomial design results

The results of the simulations can be summarised in Figure C.5. The uniformity of the profile at the nozzle exit is hindered by the boundary layer thickness and the stagnation pressure. The boundary layer thickness increases with nozzle length (x_e), but decreases with Reynolds number and when $H/D < 1$. The stagnation pressure begins to propagate into the nozzle exit at $H = D$ as seen in Figure C.8. This observation of the stagnation pressure propagating into the nozzle is consistent with literature [29].

C.3.3 Simplified design results

Simplified designs were considered to assess the significance of the optimised designs on the results. Four designs were proposed with the same R_{inlet} and R_{outlet} to match the detailed designs: with $R_1 = R_2 = R_{inlet}$, α is varied to match the nozzle lengths.

The results of the cold flow CFD calculations suggest that the nozzle design is of little significance at the flow rates considered for experimental use. There are no significant differences at the nozzle exit or in the impinging regions.

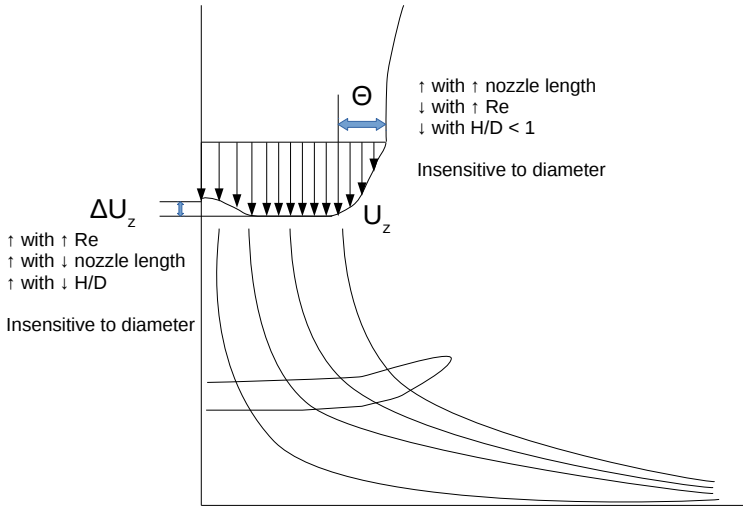

Fig. C.5 Summary of design parameter influences on cold flow.

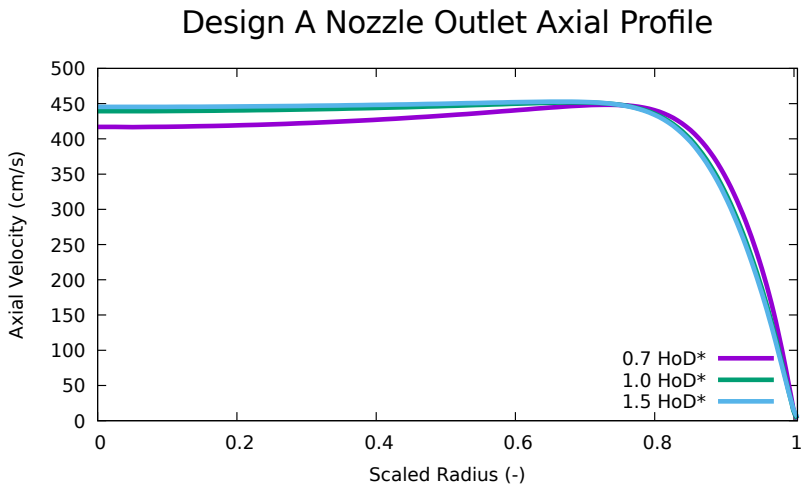

Fig. C.6 Influence of H/D ratio on axial profile on the outlet.

A further simplified nozzle of a straight-line is also considered with a uniform pressure outlet against a polynomial design and only shows a small increase in the radial velocity towards the centreline, but does not change the uniformity of the exit profile.

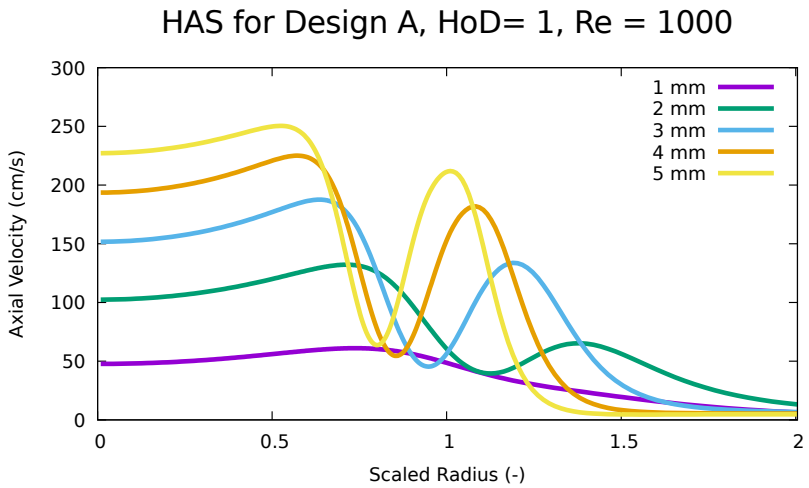

Fig. C.7 Axial velocity profiles for different height above stagnation surface (HAS) for Design A at $Re = 1000$.

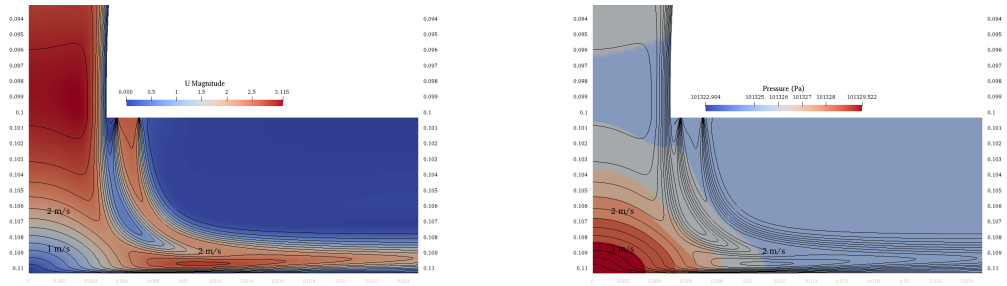

Fig. C.8 Velocity Magnitude contour for Design A at $Re = 1000$, $H/D = 1.0$, $T = 398$K.

C.4 Conclusions and suggestions

For the cold flow rates being considered for experimental studies, the detailed design does not provide significant improvements in the flow. The flowrates are well within the laminar regime.

The upstream boundary condition is assumed to be (a) laminar and stable and (b) somewhere between uniform (plug) and fully developed (parabolic). It is important that the upstream flow has time to fully develop and be passed through some form of a turbulence reduction (e.g. screen/mesh) to satisfy these assumptions.

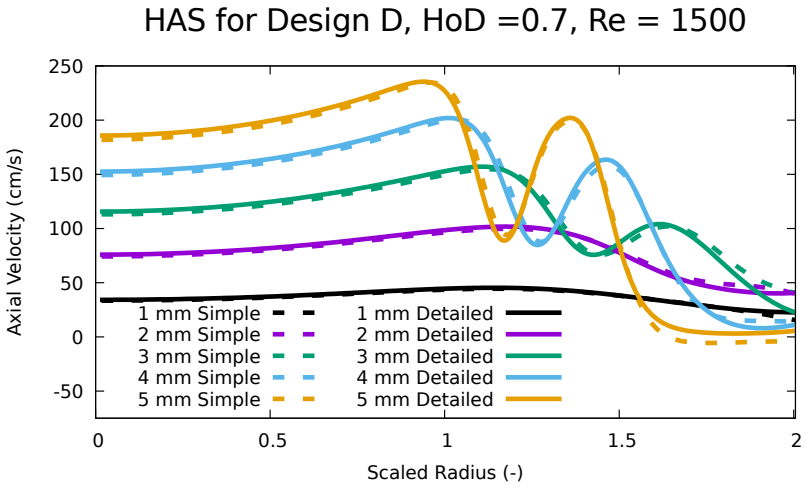

Fig. C.9 Axial velocity profiles for the same mass flow rates are compared for different H/D ratios for detailed and simplified designs.

Appendix D

CH* chemiluminescence

Measurements of CH* chemiluminescence were used to study premixed ethylene-oxygen-argon, jet-wall stagnation flames in Chapter 4. A 430 nm bandpass filter (Thorlabs, FWHM 10 nm) was used to image the light emitted during the $A^2\Delta \rightarrow X^2\Pi$ relaxation of the thermally excited CH radicals which emits at 431 nm. The chemiluminescence of CH* was recorded with a Blackfly S camera equipped with a MVL25M23 lens from Thorlabs with an aperture set to f/1.4 and a focal length of 25 mm.

The 2D projection recorded by the camera was transformed into a 2D cross section by making use of the flame symmetry and applying an inverse Abel transform using the basis-set expansion (BASEX) method [11, 84]. The Abel transform used time-averaged images to ensure that the symmetry was not broken by the oscillations in the wings of the flame (see Fig. D.1).

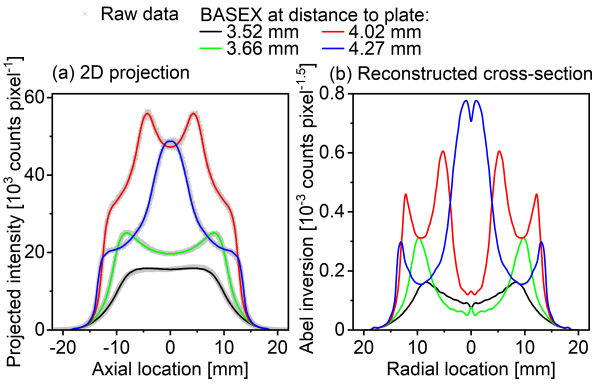

Fig. D.1 (a) Line intensity profiles at different distances from the plate recorded for the imaging of Flame 1 and the corresponding filtered/smoothed BASEX results. (b) Inverse Abel transform of the profiles shown in (a).

Appendix E

Thin filament pyrometry

E.1 Experimental method

This section describes the experimental method used to measure temperature in premixed, jet-wall stagnation flames reported in Section 4.5.1.

The light emission from a SiC filament placed into the flame is used to infer the temperature of the surrounding gas. The approach applied here infers the filament temperature, T_{SiC}, by comparing the ratio of observed intensities of colour channels to a previously generated temperature look-up table [208]. T_{SiC} was converted to gas temperature using an energy balance of radiation and forced convection over an inclined cylinder.

In line with previous reports, conduction along the filament was neglected due to its small diameter (14 µm) and low thermal conductivity (2.2 W $\mathrm{m}^{-1}\mathrm{K}^{-1}$) [179, 226]. This work improves upon past methods by using multicomponent gas phase properties and 2D flow fields from 2D simulations to assess convective heat transfer. The equations, S-type thermocouple calibration procedure, and further details regarding the calculation of the temperature look-up table are fully described in the literature [179, 207, 83].

The SiC filament temperature, T_{SiC}, was calculated from its colour. The ratio of the colour channels recorded by a camera hereby depend on T_{SiC} and emissivity ε of the imaged material [207, 179, 208]:

$$\frac{R_i}{R_j} = \frac{\int_0^\infty \eta_i(\lambda)\frac{\varepsilon}{\lambda^5}[\exp(hc/\lambda\sigma T_{\mathrm{SiC}})-1]^{-1}\mathrm{d}\lambda}{\int_0^\infty \eta_j(\lambda)\frac{\varepsilon}{\lambda^5}[\exp(hc/\lambda\sigma T_{\mathrm{SiC}})-1]^{-1}\mathrm{d}\lambda}, \tag{E.1}$$

where R_i and η_i are the light intensity and wavelength-dependent camera response of colour channel i, λ is the wavelength, σ is the Boltzmann constant, h is the Planck constant, and c is

the speed of light. The shape of the η_i curves was obtained using the quantum efficiency of the camera and wavelength-dependent filter and lens transmission data provided by the respective manufacturers. Following the procedure of Ma and Long [207], a hot S-type thermocouple was imaged at different temperatures for calibration of the optical system. Subsequently, Eq. E.1 was used to create a look-up table relating the recorded colour ratio to the SiC temperature [179, 208].

The SiC filaments used here (Ceramics Grade Nicalon, COI Ceramics Inc.) were reported to be mechanically and optically stable while having a diameter of only 14 µm, making them ideal for TFP measurements [208]. It was reported that their emissivity can be assumed to be wavelength independent and that their optical properties remain constant for 60 min [208]. Consequently, the SiC filaments used in this study were replaced after each experiment or after 60 minutes at the latest.

During the experiments, the filament was placed over two metal rods (Fig. 4.1b). Small weights were mounted on each end of the filament to keep it in place and maintain a small tension to minimise curving and vibration of the filament induced by the flow. The filament was imaged with a Blackfly S (BFS-U3-32S4C-C, FLIR Integrated Imaging Solutions, Inc.) having a 1/1.8" Sony IMX252 CMOS sensor with 2048×1536 pixels (pixel size 3.45 µm). The camera lens was a MVL50M23 with an aperture set to f/2.0 and a focal length of 35 mm. The distance between the camera and the filament was 25 cm, resulting in a pixel width corresponding to 1/73 mm in the focal plane through the centre of the flame where the filament was positioned. A BG-7 filter (Thorlabs) was used to balance the intensity ratios of the three colour channels and to block infrared light. The filament was moved in steps of 0.1 mm in the vertical direction through the flame using a manual translation stage (M-423, Newport) and a SM-25 Vernier Micrometer (Newport) with a 1.0 µm sensitivity and 10 µm graduations. At each step the camera exposure time was adjusted to maximise the signal from the SiC filament without saturating any of the three colour channels and 50 frames were recorded.

The images were analysed using an in-house developed Python code. The code searches for the SiC filament in the image and calculates its position. Note that due to the high flow velocities, the filament can be slightly curved. In the case of high background light intensities (i.e., high camera exposure and emission from CH*), a spline was used to subtract the background from the SiC signal. The colour ratio at each horizontal pixel position is calculated and converted to the filament temperature, T_{SiC}.

Once the filament temperature T_{SiC} is known, it is corrected for radiative heat loss to obtain the gas temperature T_{g} [208]:

$$T_g = \frac{\varepsilon\sigma(T_{SiC}^4 - T_\infty^4)}{h} + T_{SiC}, \tag{E.2}$$

where T_∞ is the ambient temperature and h is the convective heat transfer coefficient given by:

$$h = \frac{\mathrm{Nu}\, k_{gas}}{d_{SiC}}. \tag{E.3}$$

Here, k_{gas} is the gas thermal conductivity and d_{SiC} is the filament diameter (14 µm in this case). A range of expressions is given in literature for the Nusselt number Nu depending on flow conditions (natural or forced convection, Reynolds number Re) and object geometry (cylinder diameter and aspect ratio). An equation for forced convection over a cylinder perpendicular to the flow direction that was previously used for correcting SiC filament measurements is [208, 297]:

$$\mathrm{Nu}_{90} = a\mathrm{Re}^n. \tag{E.4}$$

The subscript 90 indicates the perpendicular flow direction. The constants a and n depend on the range of the Reynolds number, Re. In the present study, the following values were used: $a = 0.565$ and $n = 0.136$ when $0.03 \leq \mathrm{Re} \leq 0.09$ and $a = 0.800$ and $n = 0.280$ when $0.09 \leq \mathrm{Re} \leq 0.61$ [297].

The above expression is suitable in the flame centreline where the gas flow is truly perpendicular to the filament orientation. Away from the centre, the filament can be seen as an inclined or tilted cylinder heated by forced convection. In this study, the expression for Nu_{90} was corrected for the inclination angle Φ [248]:

$$\mathrm{Nu}_\Phi = \mathrm{Nu}_{90}(\sin^2\Phi + F^2\cos^2\Phi)^{0.5n_1}. \tag{E.5}$$

Possible values for the constants F and n_1 are tabulated in [248, 375]. Values of $F = 0.2$ and $n_1 = 0.5$ were used here because they were reported for small diameter cylinders with high aspect ratios. The remaining parameters required for the temperature correction (Re, k_{gas}, Φ) were obtained from the 2D simulation.

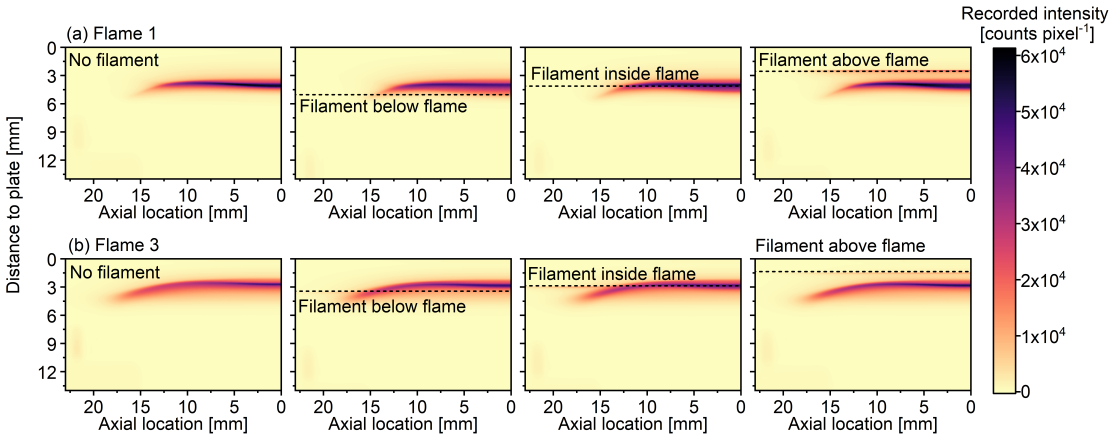

Fig. E.1 Recorded CH* chemiluminescence from the undisturbed flames (leftmost column) and from the flames with a SiC filament inside their centre at different distances from the plate.

The temperature profiles of each flame were measured three times. The spatial location of each measurement was determined from the imaged filament to ensure temperatures at the same spatial positions were averaged.

E.1.1 Flame disturbance by SiC filament

Intrusive techniques always pose the risk that they disturb the flame such that the measurements are not representative of the undisturbed flame. To investigate how the filament disturbs the flame, images of the CH* chemiluminescence were taken with and without a filament inside the flame (Fig. E.1). It should be noted that Abel inversion was not applied here because rotational symmetry is broken when the filament is present.

Placing the 14 µm SiC filament into the flame has no major effect on the flame shape or position (Fig. E.1). In fact, the changes are too small to clearly see them in Fig. E.1. The location of the flame front is undisturbed when the filament is inside the flame as can be observed when plotting the recorded intensity over the distance to the plate (Fig. E.2). The only slight difference between flames with and without the filament can be seen when the filament is positioned upstream of the flame (i.e., in the pre-heat zone of the flame). In such cases, it is noted that the flame attached to the filament and caused the flame to become slightly stretched, leading to disturbance of temperature measurements in the pre-heat zone. This is in agreement with previous studies where thermocouples were used in these type of flames [345]. It can also be observed that the flame disturbance is less when the flow velocity is increased (compare Flame 1 and 3 in Fig. E.1).

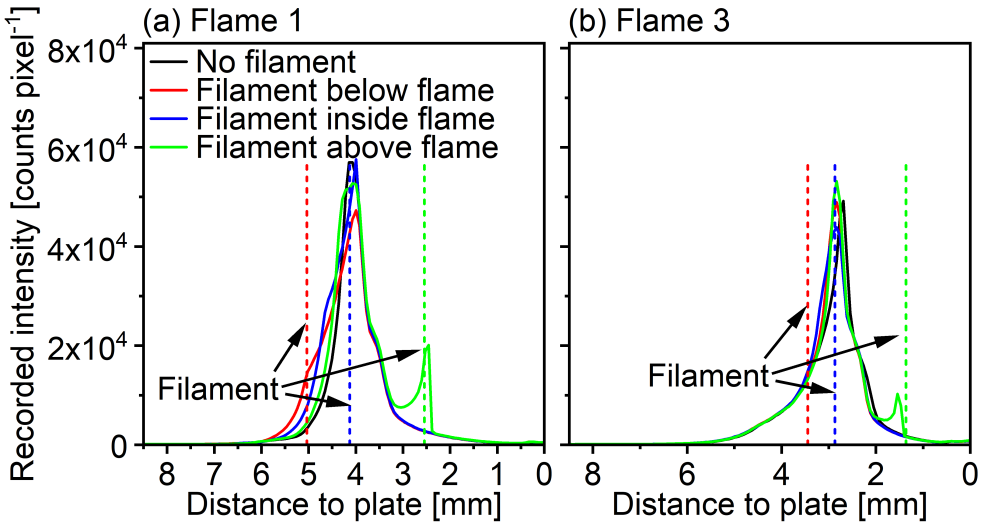

Fig. E.2 Line profiles extracted from Fig. E.1 to highlight how the presence of the SiC filament influences the flames.

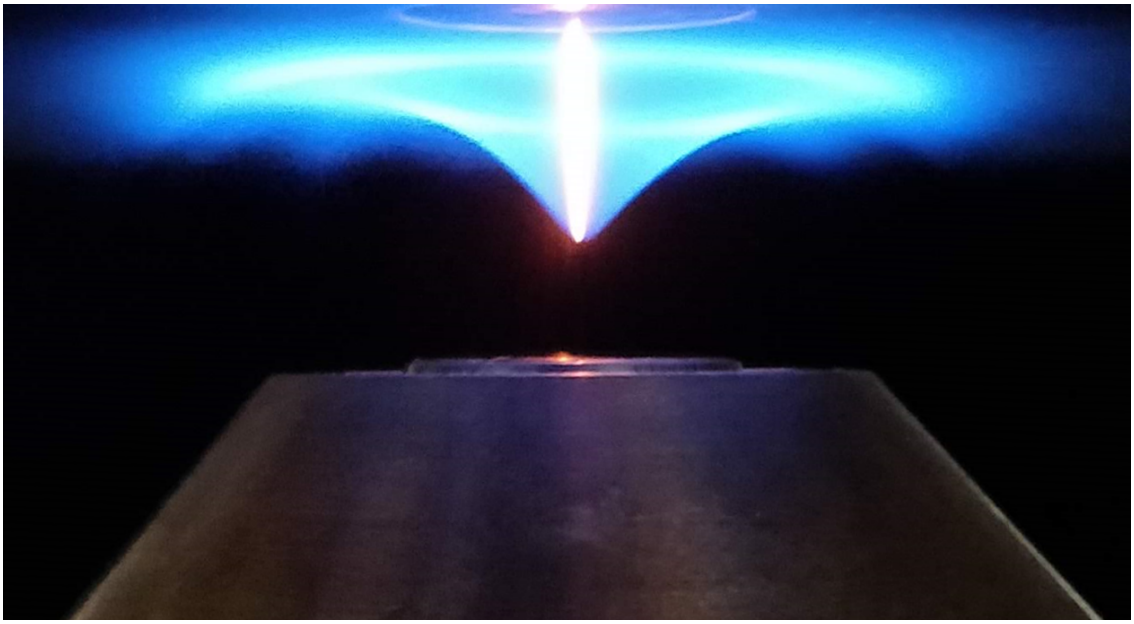

Fig. E.3 Photograph of the flame disturbance when placing the SiC filament vertically into the flame.

It is also interesting to note that measuring the centreline temperature directly by positioning the filament vertically into the flame proved impractical due to the significant flame disturbance (Fig. E.3).

Appendix F

Additional figures

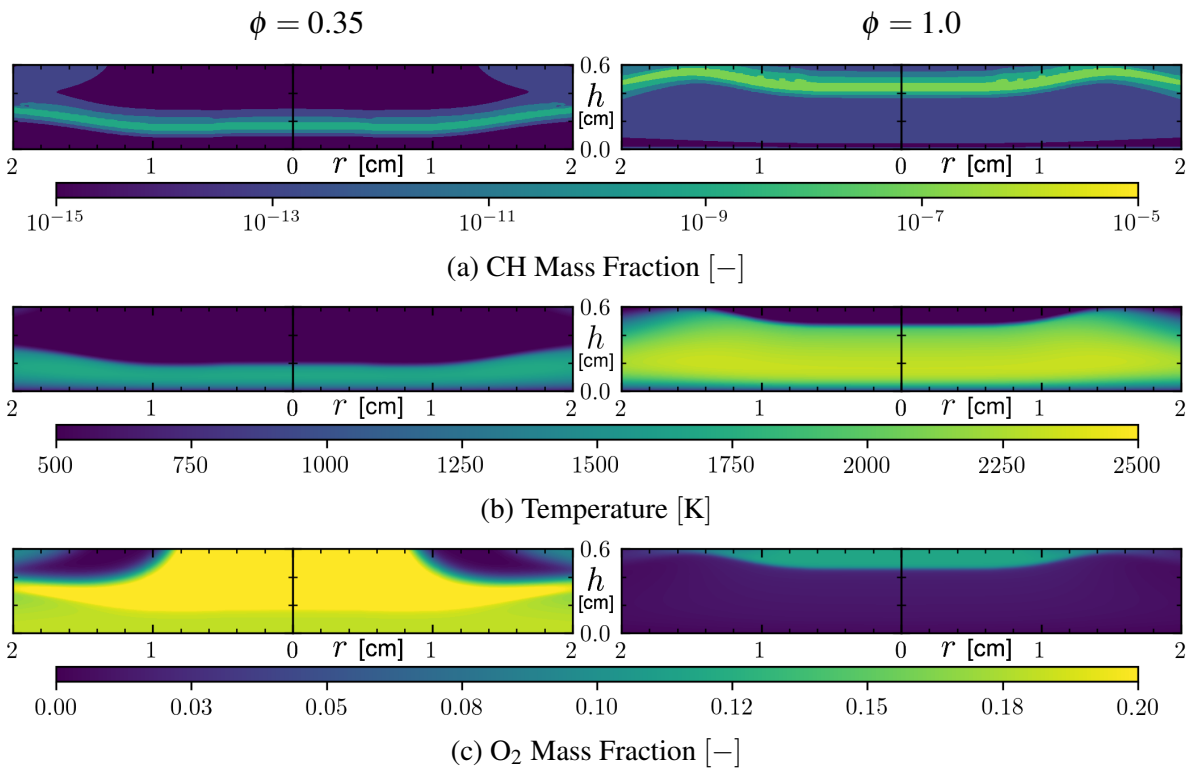

(a) CH Mass Fraction $[-]$

(b) Temperature [K]

(c) O_2 Mass Fraction $[-]$

Fig. F.1 2D fields of (a) CH mass fraction $[-]$, (b) temperature [K] and (c) O_2 mass fraction $[-]$ for the $\phi = 0.35$ (left) and $\phi = 1.0$ (right) flames without TTIP.

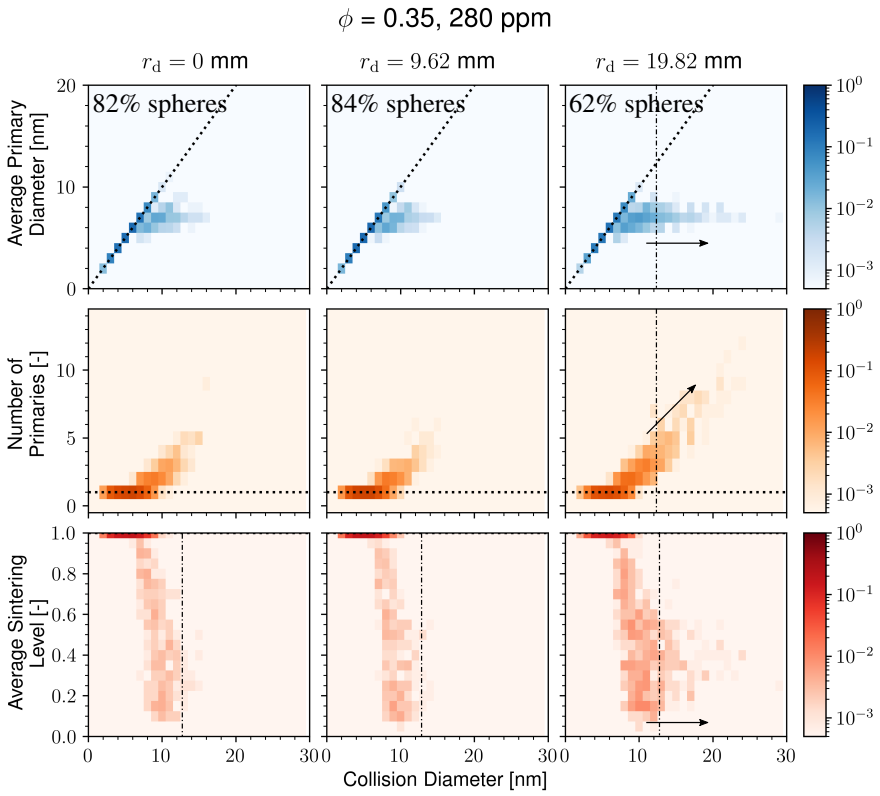

(a) Part 1: Lean flame with 280 ppm TTIP.

Fig. F.2 Joint distributions of average primary diameter, number of primaries, and average sintering level with collision diameter at different deposition radii, r_d. The averages are arithmetic means are taken over the primary particles within each aggregate. The fraction of particles that are spherical are reported as a percentage. The dotted black line corresponds to spherical particles, while the dot-dash lines (column 3) mark the collision diameter of large aggregates that form at large deposition radii.

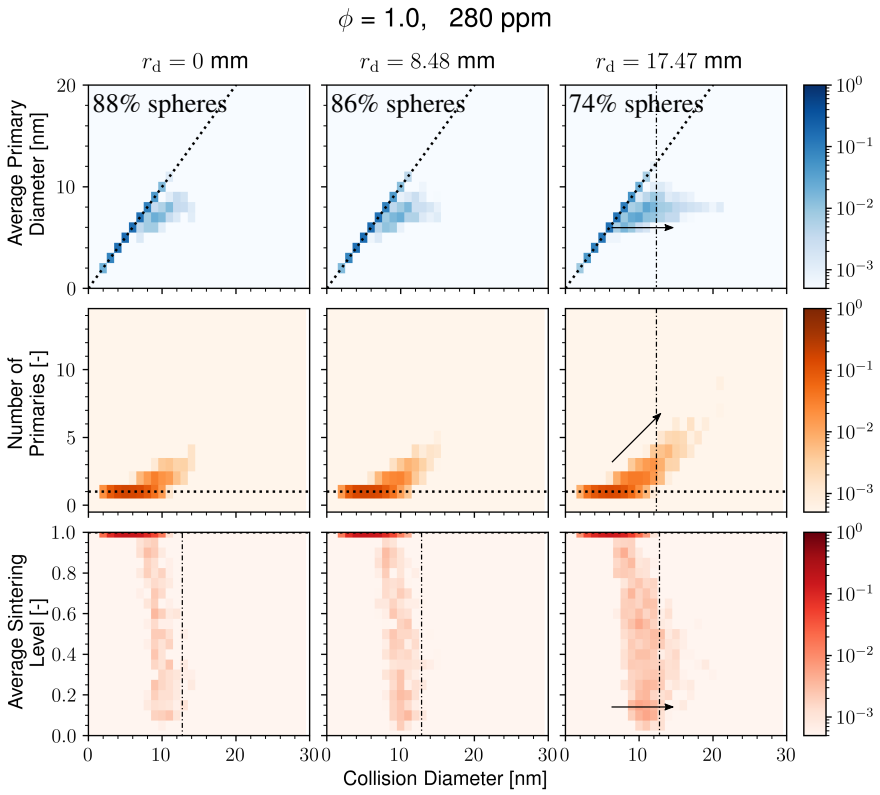

(b) Part 3: Stoichiometric flame with 280 ppm TTIP.

Fig. F.2 Cont.

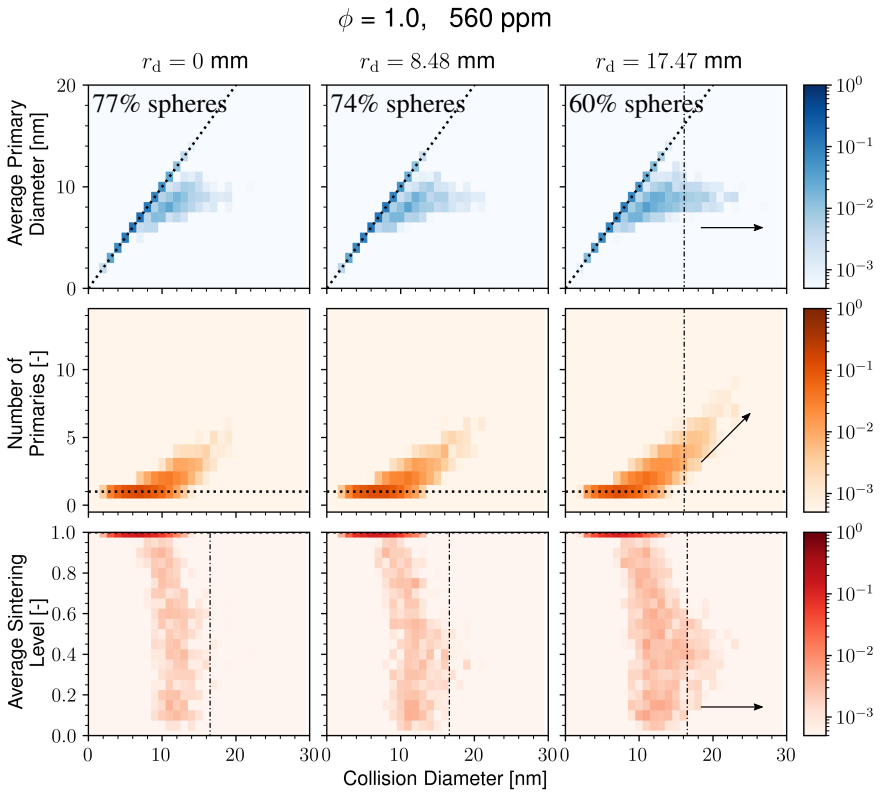

(c) Part 4: Stoichiometric flame with 560 ppm TTIP.

Fig. F.2 Cont.